Planar Laser Induced Fluorescence Imaging and Monte Carlo Simulations of Pulsed Laser Ablation

Thesis by

Dale L. Capewell

In Partial Fulfillment of the Requirements

for the Degree of

Doctor of Philosophy

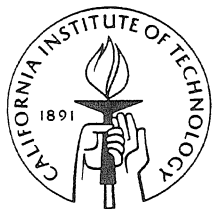

Pasadena, California

1997

(Submitted 24 Oct 1996)

Acknowledgements

For me this experience has felt like a long ultra-marathon on steep terrain in which I went out too fast, went off course a few times, and then struggled at the end to reach the finish line. Looking back, I often walked when I could have run but was uncertain whether I'd have the strength to continue. In fact I often lay face down in the dust crying like an infant and wishing that death would come to relieve my suffering. I do, however, recall moving at times with power and grace and I choose to remember most clearly these brief periods. Now that I have completed my mission at Caltech, it may be several years before I acquire the necessary perspective to fully appreciate what I have accomplished.

As in any long run, the contibutions of the many handlers are vital but often go unnoticed as the buckles and plaques are awarded. My deepest gratitute is to my wife, Dr. Selmer Wong, who has tirelessly endured my angst and offered a positive outlook when it was needed most. Thanks also to my mother, who has become a counselor and friend, and to John, who will now spend years trying to one-up this. I would also like to thank both Dr. Pete Sercel and Dr. Stephanie Leifer for living life with intensity, enthusiasm, and laughter. They are like family to me, and continue to be a source of inspiration.

My gratitude extends to my research advisor Dr. Dave Goodwin for laying before me all the necessary equipment and ideas to complete this project. I am equally indebted to Dr. Phil Paul at Sandia National Laboratories for his invaluable expertise in acquiring the data presented in this dissertation, and to Dr. Viet Nguyen for his help in the lab.

I would like to acknowledge the many runners I have encountered along the trail. Among these are Sven Khatri, Ashok Tripathi, Steve Sanders, Jimmy Yee, Yan Speth, Ho Seon Shin, Andrew Bailey, Bob Kirkwood, Nick Glumac, and many others. Thanks for the talks, the lunches, the encouragement, the chess, and the

e-mail. Thanks also to Frank Cosso for his engineering skills, and to Rodney for his machining prowess.

This race is over. Ooh Rahh. I certainly didn't win it but I hung in there have learned a lot. I wish all of the runners still on the trail the best of luck. I will now hobble to the shower and then try in vain to get some rest.

Abstract

The first reported planar laser-induced fluorescence (PLIF) images depicting the relative ground-state, neutral density of Si within a pulsed laser ablation (PLA) plume as it expands into vacuum and 10 mTorr Ar are presented. Because of the high flow speeds in PLA plumes and the narrow bandwidth of typical lasers, several images acquired with the laser detuned incrementally must be superimposed to produce images which compensate for Doppler shifts. Density profiles of Si along the axis of symmetry as a plume expands into Ar at pressures of 0-150 mTorr demonstrate the influence of a background gas and substrate on the expanding plume in the interval $0 < t < 5\mu$s. In-flight production of SiO along the contact as an Si plume expands into 1.0 Torr air is demonstrated in the first reported images of a reactive intermediate species produced during PLA.

The expansion of Si into both 10 mTorr and 100 mTorr Ar is investigated using the technique of Direct Simulation Monte Carlo (DSMC), with a simple ablation model used to generate the Si plume. As a consequence of the rapid displacement of background gas, i.e. the snowplow effect, the plume divides into two components, one which travels nearly collisionlessly toward the substrate and one which interacts more strongly with the gas. At 10 mTorr, collisions between fast component Si atoms and Ar atoms during the period $t < 250$ ns are responsible for most of the energy transfer from Si to Ar. This results in the creation of a fast (15 eV), collisionless Ar component which impacts the substrate shortly after the fast Si component arrives, but does not result in thermal heating. At 100 mTorr, the energy transfer from the plume to the Ar gas occurs on a μs time scale and is attributed primarily to thermal heating. The energy of the fast Ar component decreases to about 5 eV.

Finally, the DSMC technique is employed to study the expansion of Si into both 10 mTorr and 100 mTorr O_2. The chemical reaction Si + O_2 $\rightarrow$ SiO + O is investigated, including rotational and vibrational excitation the diatomic molecules O_2 and SiO.

At both pressures, SiO first appears along the sides of the expanding plume and, at 100 mTorr, appears only along the contact front between the Si and O_2. This result compares well will PLIF data. An examination of the O_2 rotational temperature indicates that the background gas is heated along a conical surface whose tip is located at the ablation spot as the plume expands.

Collectively, these simulations demonstrate the potential of the DSMC method to provide quantitative information about the reactive expansion of a wide variety of PLA plumes into rarified background gas mixtures, and study the particle flux onto a substrate when parameters such as background gas pressure and composition are varied.

Contents

List of Figures

Chapter 1 Introduction

1.1 Background

Wide interest in the physical vapor deposition (PVD) technique commonly known as pulsed laser deposition (PLD) began about a decade ago, when it was discovered that complex multi-element superconducting films of good quality such as $YBa_2Cu_3O_{7-\delta}$ could be deposited by irradiating a target with laser pulses, obtaining a film with a stoichiometry similar to that of the target [1, 2]. These results are consistent with previous work which suggested that the evaporation occurring during pulsed laser ablation of many complex materials is congruent, that is, the stoichiometry of the target is preserved in the plume. Although this might seem surprising, especially for target materials such as $Hg_{1-x}Cd_xTe$ which have been shown to exhibit grossly incongruent thermal evaporation [3, 4], this unique PLD property can be understood by considering that the rates of heating and cooling within a target subjected to high energy laser pulses of less than 100 ns duration are usually rapid compared with typical millisecond segregation rates [5]. Although small differences among the sticking probabilities for different target species are observed to produce small stoichiometric differences between the target and film, this can be compensated for by enriching the target with species which would otherwise be deficient in the film, or by including these species in a background gas. Both of these methods are effective, for example, in increasing the concentration of Hg in $Hg_{1-x}Cd_xTe$ films grown by PLD [5].

Research has revealed that the composition of high-T_c superconducting films can be controlled by varying the target-substrate distance, background gas pressure, deposition angle, and laser beam energy. In fact, recipes for growing *in situ* crystalline YBCO films are available [6, 2]. Although recipes for depositing YBCO films using the more conventional techniques of chemical vapor deposition (CVD), plasma-enhanced chemical vapor deposition (PECVD), and coevaporation of the metallic constituents

[7], PLD is far simpler and easier to control. The technique is therefore likely to remain an important method for growing YBCO films for a wide variety of applications.

Extensive efforts to apply PLD to the deposition of non-superconducting materials have also met with success. By 1990, a wide variety of semiconductors (e.g., GaAs, GaP, GaSb, InAs, InBb), oxides (e.g., Al_2O_3, SiO_x, MgO, $BaTiO_3$), ferromagnetic materials (e.g., γ-Fe_2O_3), organic compounds, and superlattices (e.g., HgTe-CdTe) of good quality had been successfully deposited onto substrates using PLD. Several varieties of pulsed lasers were employed for this work, including excimer lasers, ruby lasers, Nd:glass lasers, Nd:YAG lasers, and N_2 lasers as well as a few CW lasers including CO_2 lasers and argon ion lasers [5]. The excimer laser, which combines a high energy UV output with a high pulse repetition rate, has become the preferred choice for an even wider range of PLD applications, including the recent deposition of ferroelectric films and heterostructures ($PbZr_xTi_{1-x}O_3$) for use as nonvolatile random access memory [8].

The apparatus typically used for PLD consists of a target and substrate enclosed within a vacuum chamber fitted with a transparent window enabling an excimer laser beam to be directed onto a solid target. A schematic diagram depicting this arrangement is shown in Figure 1.1 with a real experiment to the right. As shown, the interaction of the laser with the target generates a plume of ablated target material which expands toward the substrate and adsorbs. As depicted, the substrate and target are often rotated, enhancing film uniformity and increasing the surface area of a solid target which is exposed to the laser's radiation.

In addition to congruent evaporation, the PLD method of growing thin films has demonstrated many other advantages not shared by alternative deposition methods. In contrast to molecular beam epitaxy (MBE), the power for PLD is supplied from outside the vacuum chamber so there is no need for resistively heating the target material. This not only increases the efficiency with which power is coupled to the target, but also minimizes the ambient chamber temperature and therefore minimizes outgassing. Further, because the target holder is not resistively heated, highly reactive materials such as rare-earth metals can be evaporated by PLD without reacting with

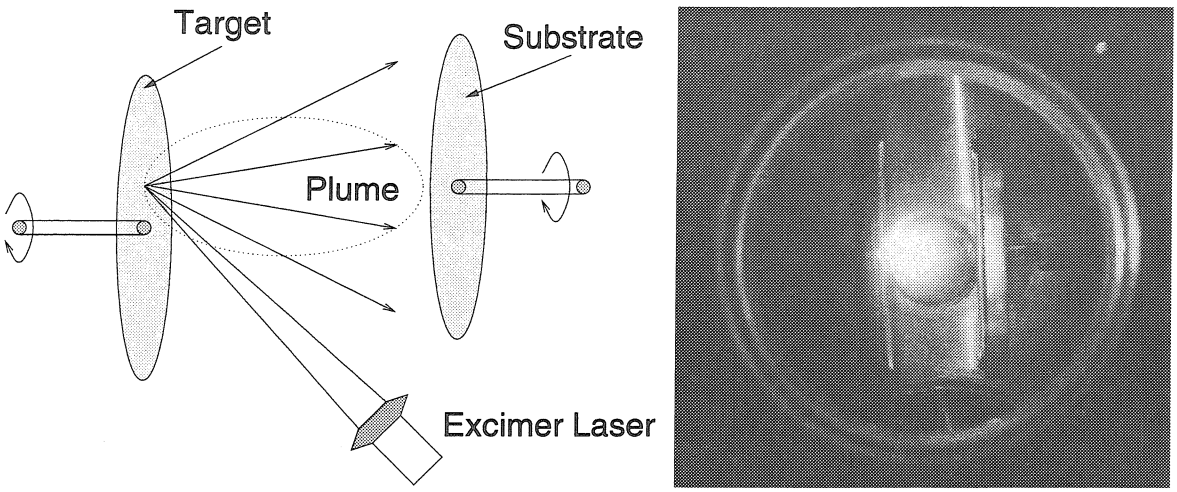

Figure 1.1: Typical arrangement used for pulsed laser deposition (PLD), showing the target, substrate, and focused laser beam used to generate the plume.

it. In the case of PLD with a reactive background gas such as O_2, concerns about burning out hot filaments or initiating electrical discharges are eliminated. Because of the ease with which solid targets can be interchanged, the same facility can be used to deposit a wide variety of films with few adjustments in between. In fact, a rotating target holder with different materials has allowed complex multi-layered heterostructures to be fabricated *in situ* using PLD [9].

Although several of the advantages of PLD are a consequence of the method's simplicity, others result from observed properties of the plume. Unlike MBE, the material ejected during laser ablation is forward-directed, maximizing the amount of target material available for deposition onto the substrate. In a production environment this efficient utilization of target material may translate into reduced costs, especially for the deposition of expensive target materials. The forward-directed behavior of ablation plumes may also be utilized to fabricate recessed features on a substrate more easily than with alternative techniques.

It has been widely observed that in addition to being forward-peaked, pulsed laser ablation (PLA) plumes are also highly ionized above a threshold laser intensity. Using a variety of techniques, the ionization fraction of the plume incident onto a substrate is estimated [5] at about <0.5% for a 50 MW/cm^2 laser intensity, 10% for intensities near 500 MW/cm^2, and nearly 100% for intensities exceeding 5000 MW/cm^2. The

kinetic energy of the ions, measured using time-of-flight (TOF) analysis of ion probe data, is typically 10-100 eV. The high energy ionic component of the plume has been credited with improving the quality of deposited films. It has been observed, for example, that while epitaxial growth of ZrO_2 films occurs under certain experimental conditions, an amorphous film results under identical conditions when an electric field is used to deflect the ions away from the substrate [10]. The role of the energetic ions in this case may be to anneal the initially amorphous film, allowing subsequent epitaxial growth.

In many cases, the increase in mobility of target atoms on the substrate may explain improvements in film quality during PLD. An experiment comparing Ge films grown on Si by both MBE and PLD has revealed that films grown by PLD at 300^o C are epitaxial while those grown by MBE at that same temperature are polycrystalline [5]. Since Ge films grown by MBE are epitaxial only if the substrate temperature is increased to 350^o C, the important difference in this case may be the improved mobility of Ge atoms on the substrate during PLD. Improvements in diamond-like carbon (DLC) films observed when an ArF laser is used instead of a KrF laser [11] may also be explained using this argument. Although these improvements may be due in part to the observed increase in the atomized carbon fraction in the plume, the carbon atoms in the plume are observed to be more energetic when the ArF laser is used for ablation.

In other applications, interactions between background gas molecules and high energy target atoms may be responsible for certain film properties. The use of background of O_2 in the deposition of both silicon dioxide films [12, 13, 14, 15] and YBCO films [16], for example, indicate that chemistry occurs during PLD. Since the high impact energies during PLD make it much easier for reactants to overcome the activation energy barrier, both in-flight oxidation and oxidation at the substrate may be enhanced in comparison to MBE. Experiments have also shown that highly doped p-type ZnTe films can be grown by ablation of ZnTe into a background gas of N_2 [17]. Since the bond strength of N_2 is about 10 eV, a plasma source is ordinarily used to generate atomic N during growth of these films by MBE. During PLD, however, this

energy is provided by the plume, which perhaps accelerates a few N_2 molecules to more than 10 eV during collisions. Upon subsequent impact with the substrate, these molecules might then dissociate and incorporate into the ZnTe film. Recent growth of SiN films and TiN films by ablating Si or Ti into N_2 may be explained similarly [18, 19].

Despite the many advantages of PLD, several disadvantages have also been recognized. Among these are the difficulty in scaling the process to large diameter substrates, and the presence of excessive particulates in PLD films. Efforts to address the former by rotating the substrate and/or by rastering the substrate side-to-side have successfully led to the deposition of films onto 3-inch wafers with a uniformity comparable to that of MBE. The effectiveness of physical substrate manipulation is limited to small substrates, however, because the substrate will inevitably obstruct the path of the laser beam en route to the target as its size increases. The problem of particulates in the plume is currently a much more serious handicap for the PLD process. Evidence of globules on films which are consistent with solidification of molten droplets have been widely reported [20, 5]. These globules, which have dimensions ranging from a few nanometers to a few tens of microns, significantly reduce the quality of the desired film. As with the creation of energetic ions in the plume, splashing of molten droplets from the target occurs above a threshold laser intensity and are believed to be produced when the target becomes superheated, that is when a region beneath the surface melts before the surface becomes vaporized. Efforts to combat the presence of particulates in the plume have included the invention of a both a rotating vane particle filter [21] and a synchronized electromagnetic shutter filter [22], and attempts to spin the target at high RPM to reject particulates using centrifugal force [5]. Despite these efforts, the density of particles incorporated into typical films grown by PLD remains a problem.

The extensive experimental success growing films using PLD certainly outweighs the current limitations. Efforts to understand the basic physics of ablation may lead to currently unforeseen solutions to many of its problems, making this technique more attractive for commercial use. Research into the fundamentals of the process using

plume diagnostics and computer modeling has only recently begun. Since it is now generally believed that PLA may be regarded as a simple thermal process only at low laser intensity (i.e. < 1 MW/cm^2) [5], future research will focus on how the plume becomes ionized, accelerated, and heated at higher laser fluence, and how the plasma interacts with a background gas during its expansion. Most important for the deposition of films, however, are questions about how the ionized plume then interacts with the substrate. If PLD is to become as widely used as CVD, comprehensive models capable of reproducing in simulation quantitative properties of films observed experimentally under the same choice of laser fluence, gas pressure, target and gas stoichiometry, substrate temperature, etc. must be developed. For this goal to be realized, much more progress in plume diagnostics and modeling is necessary.

1.2 Diagnostics applied to PLA

Several diagnostic techniques are available to study the gas dynamics, chemistry, and plasma physics relevant to expanding PLA plumes. These diagnostics are often single-point measurements which measure the density of some plume species at a fixed position as a function of time. If the assumption is made that plume particles travel collisionlessly from the ablation spot on the target, whose dimensions are negligible, and originate from that point during a negligibly brief duration of time, then the time of flight (TOF) required for a particle to reach the probe can be used to infer its velocity. Data acquired from the probe can therefore be used to infer the velocity distribution function describing the ensemble of plume particles to which the probe is sensitive. For example, consider a small volume of Maxwellian gas described by the velocity distribution function

$$f(v_x, v_y, v_z) = \frac{1}{\pi^{3/2} v_p^3} e^{-(v_x^2+v_y^2+v_z^2)/v_p^2}, \tag{1.1}$$

where $v_p = (2kT/m)^{1/2}$. The fraction of atoms with a velocity in the range v_x to $v_x + dv_x$, v_y to $v_y + dv_y$, and v_z to $v_z + dv_z$ is given by $f(v_x, v_y, v_z)dv_x dv_y dv_z$. If

the boundary is instantaneously removed, and the gas expands collisionlessly into vacuum, then the density $n(x, y, z)$ may be determined by making the substitution $dx = dv_x/t$, $dy = dv_y/t$, $dz = dv_z/t$. Along the coordinate z axis, the density is easily shown to be

$$n(z,t) = \frac{N}{\pi^{3/2} v_p^3} \frac{1}{t^3} e^{-z^2/v_p^2 t^2}, \tag{1.2}$$

constituting the signal for a density sensitive probe. The time-dependent signal from a TOF probe generally depends on the velocity distribution function selected to describe the initial ensemble, and whether the probe is sensitive to density or particle flux. TOF signal generally takes the approximate form [23]

$$S(z,t) \propto z^{n-3} t^{-n} e^{-(z-ut)^2/v_p^2 t^2} \tag{1.3}$$

where u is a flow velocity parameter in the velocity distribution and $n \geq 3$.

Because PLA plumes are quite luminous in the visible spectrum, single-point time-of-flight (TOF) measurements sensitive to emission are among the first TOF data reported. Some of this work suggests that particles liberated during PLA expand into vacuum like those from a supersonic nozzle, which are described by the velocity distribution function [24]

$$f(v_z) = A v_z^3 e^{-(v_z-u)^2/v_p^2}. \tag{1.4}$$

where A is a normalization constant and u is a stream velocity. The fit parameters v_p and u can be related to the Mach number for the expansion, given by $M = (u/v_p)(2/\gamma)^{1/2}$.

Despite apparently good fits to data, TOF profiles sensitive to emission are potentially misleading. This is because TOF analysis usually assumes the number of particles to which the probe is sensitive remains constant in time, and emission spectroscopy is sensitive only to the population of atoms in excited states. For an equilibrium gas, a Boltzmann relationship is maintained among state populations by collisional and radiative energy exchange, keeping the population in any excited state constant. As a PLA plume expands and the collision rate decreases, however, colli-

sions are eventually unable to offset radiative de-excitation, so the number of excited atoms must diminish. Neglecting this in the TOF analysis may introduce error in the flow velocity and temperature ($T = mv_p^2/2k$) parameters in equation 1.4, especially for excited atoms which have rapid spontaneous decay rates.

Similar caution must be exercised when comparing the time-integrated emission signal from multiple atomic transitions in order to estimate the plume temperature [25]. If a Boltzmann distribution is assumed to govern the density of excited states, then the signal S_{21} from a transition described by upper-state energy E_2 and degeneracy g_2 with a spontaneous emission rate to some lower state A_{21} satisfies

$$S_{21} \propto g_2 A_{21} e^{-E_2/kT}. \tag{1.5}$$

The temperature of the plume can therefore be determined by acquiring emission signal from several transitions and then computing the slope of a line defined by

$$ln\left(\frac{S_{21}}{g_2 A_{21}}\right) = (-1/kT)E_2 + C. \tag{1.6}$$

If however the collision rate is not much greater than the spontaneous emission rate of each transition, a Boltzmann relationship cannot safely be assumed. Even with this considered, it remains unclear whether the unsteady initial conditions during PLA populate excited states according to a Boltzmann distribution. The temperature parameter calculated using this technique may therefore have little meaning.

Because emission signal is abundant and easy to acquire, 2-D images of PLA plumes are also commonly reported [25]. These images are unfortunately difficult to interpret because emission signal intensity cannot be easily related quantitatively to either plume temperature or total plume density. Further, the signal is usually gathered from the full depth of the 3-D plume and projected on a 2-D plane, so the data cannot be interpreted as emission from a cross section of the plume as the images might suggest. Also, because emission spectroscopy is only sensitive to excited atoms, it cannot show properties of the bulk of the plume, which probably resides in

the ground state and may have a significantly different distribution than the excited populations. Emission images are quantitatively useful, however, for identifying hot regions of a plume, and for indicating the presence of some atomic or molecular species by their unique spectroscopic signatures.

As with emission spectroscopy, ion probes are sensitive to what may be a small fraction of the total plume density, although it has been suggested that above a fluence of about 3 J/cm^2 (about 100 MW/cm^2 assuming a 30 ns pulse), ions constitute a major portion of the ablated material [26]. Also, as for TOF measurements sensitive to emission, TOF measurements sensitive to ions are subject to time dependence in the velocity distribution function, in this case due to in-flight recombination and charge exchange. This also applies to mass spectroscopic TOF experiments sensitive to ions, which have suggested that ions expand into vacuum during PLA similarly to the way excited atoms expand, like atoms from a supersonic nozzle [27].

Often during PLD a background gas fills the space between the target and substrate, resulting in significantly different plume behavior than when the plume expands into vacuum. For example, Geohegan has observed using an ion probe that a PLA plume splits into two components in the presence of a background gas [28, 29, 30, 31]. The fast component expands as if in vacuum while the slow component is attenuated by the gas. Data from ion probes combined with optical spectroscopy have been used to show that initially the attenuation is consistent with a drag model, defined by the time-dependent radial position [30]

$$R(t) = C(1 - e^{-\beta t}). \tag{1.7}$$

After a shock structure forms, the attenuation becomes more consistent with a shock model, defined by [32]

$$R(t) = Ct^{2/5}. \tag{1.8}$$

The variables C and β in these expressions are numerical constants.

Laser induced fluorescence (LIF) has gained wide popularity as an *in situ* diagnostic for measuring the relative spatial density of atomic and molecular species relevant

to the deposition of YBCO [33, 34, 35, 36, 37, 38], diamond-like carbon films [39, 40], and other films. In general, the technique employs a laser beam to pump atoms or molecules residing within the interaction volume, here defined as the region of the plume illuminated by laser energy, from a specific lower state to a specific upper state on a time scale which is fast compared to the typical speed of the plume atoms. The subsequent fluorescence from the excited atoms as they decay back into the initial state (resonant LIF) or into some third state (non-resonant LIF) is gathered using an arrangement of lenses which focus the signal onto some frequency discriminating detector. The number of signal photons gathered is directly proportional to the density of excited atoms at some point of interest $\vec{x}$ in the interaction volume. Figure 1.2 shows a typical LIF experimental arrangement.

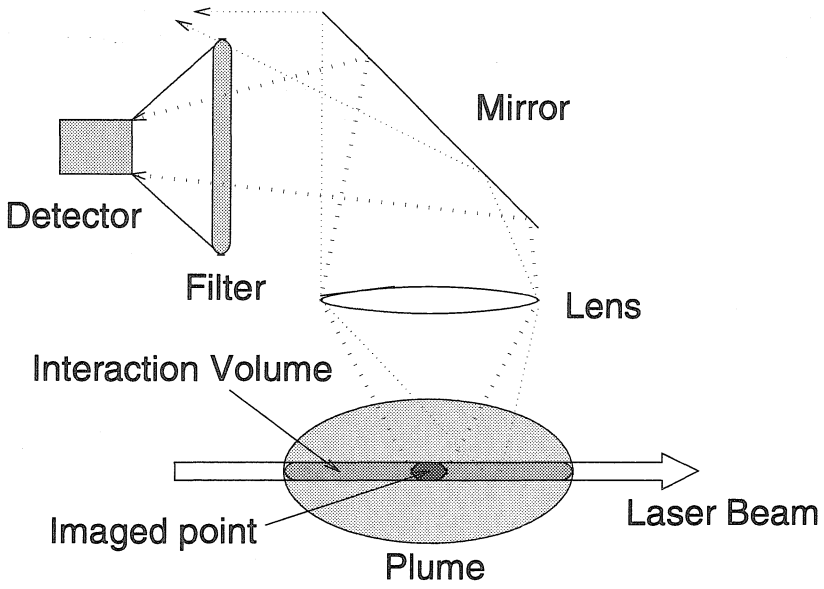

Figure 1.2: Typical experimental arrangement used to make single-point LIF measurements.

The density of atoms in the upper state can be described using a population rate equation of the form [41]

$$\dot{N}_2 = R_{12}N_1 - R_{21}N_2 - \sum_m A_{2m}N_2 - QN_2, \tag{1.9}$$

which generally includes rates for absorption (R_{12}), stimulated emission (R_{21}), spon-

taneous emission (A_{2m}), and collisional quenching (Q). Both the absorption and stimulated emission rates depend on the laser intensity while the spontaneous emission rates and collisional quenching rate do not. If the time dependence of the resonant laser intensity and the initial population of each state are known or assumed, then the rate equation 1.9 can be solved for $N_2(t)$ in terms of $N_1(0)$, the population in the lower state prior to pumping. By varying the time delay between plume creation and pump laser activation, the time dependence of density at a point $\vec{x}$ in the plume can be obtained. Figure 1.2 provides a schematic diagram showing a typical LIF scheme with the transition rates labeled. Details concerning the interaction of laser energy with a two-level atom, and the derivation of equation 1.9 are provided in Appendix A.

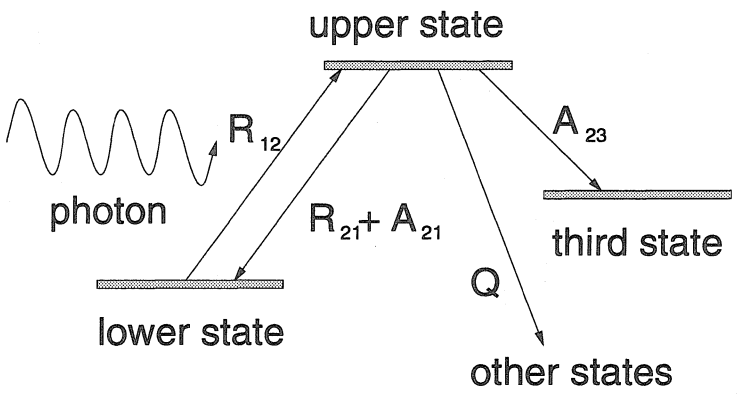

Figure 1.3: Generalized LIF scheme showing absorption, both resonant and non-resonant fluorescence, and collisional quenching.

The LIF technique offers several advantages over the alternative *in situ* diagnostics previously described. As an optical diagnostic LIF is minimally intrusive, interacting with the particles on an electronic level without altering the macroscopic properties of the flow. This may not be as true for diagnostics which employ physical probes. Also, because the LIF technique is based on a resonant interaction that occurs when a laser's photon energy matches the unique energy level spacing of a particular transition within a specific atomic or molecular species, it is both species- and state-selective. An LIF diagnostic can therefore probe the neutral, ground-state population within a plume, whose relative spatial density may differ substantially from that of excited

state populations or that of ions. This is important when comparing LIF data to data acquired from ion probes or from emission spectroscopy. To illustrate this point, Figure 1.4 provides a direct comparison of the signal obtained at a single point, a distance of 1.0 cm from the target along the axis of symmetry of the plume, using these three diagnostic techniques. Details concerning the acquisition of these data are discussed later. The data reveal how the density of ions, excited neutral atoms,

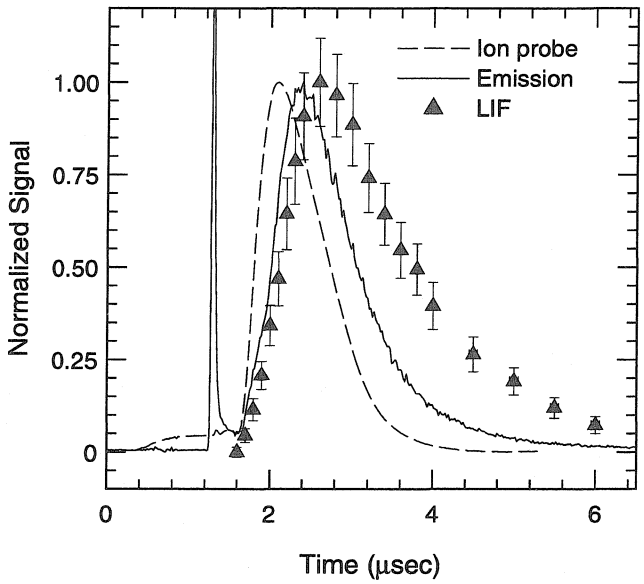

Figure 1.4: LIF, emission, and ion probe TOF profiles acquired from a copper plume a distance of 1.0 cm from the target.

and ground-state neutrals at single point differ as a function of time. The peak in the ion trace precedes that for excited-state neutrals. The peak in the LIF trace suggests that the bulk of ground-state neutrals arrives even later. Since each profile is normalized to its own maximum, Figure 1.4 cannot be used to compare the relative populations of the different species. A two order-of-magnitude increase in emission signal when the pump laser is activated strongly suggests that the fraction of plume atoms in the excited state is very small. Because the energy required to ionize a copper atom is even greater than the energy required to excite it, it might seem reasonable to assume that the density of ions in the expanding plume is also small. The laser intensity used to generate the plume from which the data in Figure 1.4 is acquired is near 10 J/cm^2 and therefore exceeds the threshold intensity when a

Cu plume is expected to be significantly ionized [26]. Even so, information about the relative density of ground-state neutrals obtained using LIF therefore provides valuable insight into the time-dependent behavior of the plume, supplementing data obtained using either ion probes or emission spectrometry.

Only recently have pulsed laser ablation (PLA) plumes been examined using planar LIF (PLIF) [42, 43, 44, 45, 46, 47]. This special application of the LIF technique employs a cylindrical lens to spread the pump laser beam into a thin sheet that passes through a selected cross section of the plume. By resolving the LIF signal spatially over the thin interaction volume, a planar image showing the relative density of atoms or molecules in the initial state immediately prior to the pump laser pulse can be constructed. A CCD camera can be used for signal detection, with a gated microchannel plate intensifier to increase its sensitivity. A schematic diagram depicting a typical planar PLIF setup is shown in Figure 1.2.

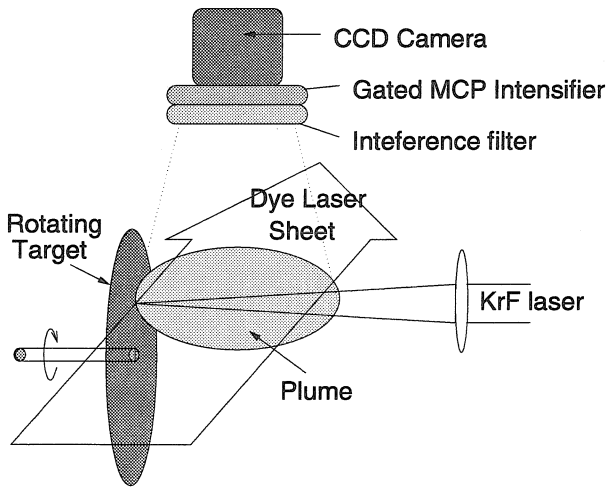

Figure 1.5: Typical experimental arrangement used to do PLIF imaging on a PLA plume.

A PLA plume expanding into vacuum is a particularly challenging system because the bandwidth of a typical dye laser is much too narrow to resonantly excite all the atoms in the plume. The TOF profiles in Figure 1.4, as well as other TOF studies [48, 49, 38, 25] suggest a characteristic particle velocity near 3 km/s, with a non-negligible fraction of particles traveling more than 10 km/s. The resonant frequency of a particle traveling at 10 km/s along the direction of pump laser propagation, whose

stationary resonant frequency is near 41,000 cm^{-1}, is Doppler-shifted by about 1.0 cm^{-1}. To effectively pump such a fast atom using a laser whose spectral peak is tuned to the stationary resonance frequency would therefore require a FWHM of about 2.0 cm^{-1}. The FWHM spectral bandwidth of a typical dye laser is only a small fraction of this value. Any PLIF image obtained using such a spectrally narrow laser at a fixed frequency is therefore velocity-biased, neglecting atoms with resonant frequencies outside the laser bandwidth. This effect is negligible when performing a single-point LIF experiment along the axis of an expanding PLA plume (assuming the laser beam is oriented perpendicular to the direction of expansion), because symmetry ensures a small radial velocity component along the plume axis and therefore a small Doppler shift. In contrast, the radial velocities of particles far off axis in a collisionlessly expanding plume are certainly large enough to require consideration of Doppler shifts.

To date, no Doppler-corrected PLIF images depicting relative ground-state, neutral density within a PLA plume expanding into vacuum have appeared in the literature. In this work, the first such images are presented. These images are produced by superimposing several PLIF images, each obtained at a different magnitude of pump laser detuning from the stationary resonance frequency. Since this is analogous to pumping with a broadband laser, the resulting image includes the contribution of all plume atoms, independent of radial velocity. Care is taken in the analysis of the PLIF data to correctly compensate for variations in the laser intensity across the width of the laser sheet. In acquiring some of the data, the laser intensity used is sufficiently low that the PLIF signal varies linearly with laser intensity. PLIF images in this case are normalized to the laser intensity profile to produce images that depict relative ground-state, neutral Si density. The remainder of the data is acquired using a laser intensity sufficiently great to produce power broadening of the PLIF signal. For these data, the three-level population rate equations for the selected PLIF scheme are solved to determine the nonlinear dependence of PLIF signal on laser intensity, after first demonstrating that the plume expands collisionlessly and that the PLIF signal itself may be used to estimate the laser intensity used for its acquisition.

At high background gas pressure, the rapid deceleration of the expanding plume

reduces the flow speed of the slow plume component significantly. Assuming a 0.14 cm^{-1} FWHM laser bandwidth and a resonance frequency near 41,000 cm^{-1}, atoms or molecules with a radial speed less than about 500 m/s are excited when the laser is tuned to the stationary resonance frequency. In this regime, the relative density of any plume species may be obtained by processing a single image. In this work, SiO produced as Si expands into air at 1 Torr is detected using PLIF imaging. The images shown are believed to be the first PLIF images reported which indicate in-flight chemistry during PLA.

1.3 Modeling of PLA

Early efforts to understand the pulsed laser ablation process focus on the heating of the target by the laser, and almost independently, the gas dynamics of the expanding plume. When a target is irradiated by a laser, many regimes may be identified, depending on laser fluence and on relationships among target material properties and laser frequency. For example, if the optical absorption depth of the material at the laser wavelength is much smaller than the thermal diffusion length, then surface heating rather than bulk heating occurs [50, 5, 51]. If the target material is a metal or a semiconductor with a bandgap less than the laser's photon energy, then laser heating is significantly different than if a ceramic or glass is irradiated due to the presence or absence of conducting electrons [5]. These issues complicate the use of the heat flow equation to model target heating.

Early models describing the gas dynamics of an expanding plume consider a uniform density 1-D gas in thermal equilibrium expanding into vacuum [52]. This approach results in an analytical solution describing the plume in terms of an adiabatic expansion, with the target boundary treated assuming either recondensation or specular reflection. If the boundary condition at the target surface changes abruptly after the effusive pulse, the solution to this problem is non-trivial. Analytical work by Kelly [53] recognizes that the distribution function describing a gas produced by thermal effusion is half-Maxwellian, and that the region near the target requires special treat-

ment. The problem of steady-state, 1-D effusion is understood, and an analytical solution has been derived using the method of moments [54]. This solution describes a transition region, commonly refered to as a Knudsen layer, where the distribution function evolves from a half- to a full-Maxwellian. Kelly uses this solution as a boundary condition for the plume during the effusion period, and specular reflection thereafter, to produce a solution describing the distribution function of the plume after a period of 1-D unsteady adiabatic expansion (UAE). An assumption that the plume subsequently expands collisionlessly into 3-D leads to a solution for the time- and space-dependent plume density [23, 55, 56]. This solution offers an explanation for the tendency for PLA plumes to become forward-peaked and high effusion rates, a property discussed later in more detail when this solution is compared to results of DSMC simulations of pulsed effusion into vacuum.

The analytical solution for steady-state effusion assumes an infinitesmal mean free path, and depends on the existence of a well-defined steady state back-scattered particle flux onto the target. For sufficiently low effusion rates, the mean free path is not small enough to justify the use of a fluid model, and without sufficient collisions, a steady back-scattered flux onto the target will not exist. Even if the plume is sufficiently collisional, some time is required for steady-state back-scattered flux to develop. It is therefore not obvious over what range of pulse durations and/or effusion rates the steady-state results are applicable to pulsed effusion. Properties of the distribution function within the region near the effusing surface have been examined in detail by Sibold and Urbassek [57, 58, 59] using 1-D DSMC simulations and comparing profiles of density, temperature, and flow velocity to results predicted analytically for steady-state effusion. This work demonstrates that the number of atoms per area, i.e. the number of monolayers liberated per pulse, may be used as a dimensionless parameter to determine whether a steady-state Knudsen layer ever forms, and on what time-scale it develops. This work is extended here, focusing on the back-scattered particle flux.

Recently models have been developed which combine the current understanding of target heating with that of plume formation and expansion [60, 61, 50, 62]. The in-

fluences of photo-ionization, inverse Bremsstrahlung absorption, and electron-impact ionization within the plume during the laser pulse are included in numerical simulations to determine what role, if any, the laser beam couples directly to the plume to promote ionization and heating. These models all predict plasma breakdown, a rapid ionization of the plume, and rapid heating of the resulting plasma. Many details concerning this process, however, remain unclear. For example, it is not known whether acceleration of the ions in the plasma by ambipolar diffusion is important, perhaps necessary to explain the apparent splitting of plumes into two components described earlier. Additionally, the importance of ion sputtering from the target after plasma breakdown has yet to be investigated using these models.

1.4 The Direct Simulation Monte Carlo (DSMC) Method

The Direct Simulation Monte Carlo (DSMC) method, developed by Bird [63] for the purpose of studying rarified flows for aerospace applications, has recently been applied to the problems of steady-state and pulsed effusion in both 1-D and 2-D, axisymmetric geometry [57, 58, 64, 65, 59, 66, 67, 68, 69]. Because the method is not based on numerical solutions of the fluid equations, it provides an opportunity to test whether a steady-state Knudsen layer develops during pulsed effusion over a wide range of effusion rates, and to test the validity of the collisionless expansion model, upon which TOF data analysis often depends. Recently a Monte Carlo simulation technique has been used to study effusive plume expansion into a rarified gas (0.1-200 mTorr), focusing on the dependence of energy flux and particle flux incident onto a substrate [68] on gas pressure. This type of work is important because detailed, time-resolved information about the gas dynamics near the substrate may be valuable as input for models of surface kinetics, perhaps leading to a better understanding of the role of target ions, target neutrals, and gas molecules on film properties and deposition rates. In Chapter 6, the DSMC method is employed to study these issues.

Since details concerning the DSMC method are provided in Appendix B, only an overview of the method is presented here.

In short, the method is equivalent to solving the Boltzmann equation directly, following the trajectories of individual simulation particles, each one representing as few as one or as many as several million real atoms or molecules. Collisions among these particles are treated statistically. Since each collision is constrained to conserve both kinetic energy and momentum, these quantities are automatically conserved for the simulated gas. While continuum models include transport properties for a gas explicitly by employing viscosity, diffusion, and thermal conductivity coefficients in flow equations, transport properties are implicitly included in DSMC simulations by the choice of collision cross sections. Simulations of flows in simple situations where analytical solutions to the flow equations are available, such as the flow between two rotating cylinders or the flow between two parallel plates at different temperature, have been used to calibrate the collision cross sections for many atoms and molecules. Variations in the transport properties with temperature can be closely approximated using the Variable Hard Sphere (VHS) method, which establishes a functional relationship between the relative velocity v_r of a given collision pair and the collision cross section $\sigma(v_r)$. Once analytical solutions are matched for simplified flows using a certain set of fit parameters for the collision cross sections, the DSMC method can easily be applied to flows involving complex geometry or complex boundary conditions.

The DSMC method is superior to numerical solutions of the flow equations in simulations involving rarified flows, flows which include strong shocks, and flows where the distribution function describing the gas particles may be non-Maxwellian. Continuum models assume an infinitesimal mean free path, so they are inherently unrealistic for problems where the scale length of the flow or of any gradients in the flow may be small compared to λ, the mean free path. Defining the Knudsen number (Kn) by $Kn = \lambda/L$ with L being the smaller of the flow dimension or the dimension of flow's most extreme gradients, continuum models are effective in systems with $Kn < 0.2$ [63]. In contrast, the DSMC method is valid over the full range of Knudsen number. Since the mean free path for a typical gas at 300 K exceeds 5.0 mm for pressures less

than about 10-20 mTorr, ablation into a background gas at this low pressure with a typical target-substrate spacing of a few centimeters cannot be treated accurately using continuum modeling. If details concerning the shock that forms as the plume expands is of interest, its millimeter length scale and the restriction $Kn < 0.2$ suggest that continuum modeling should not be used for pressures less than about 100 mTorr.

Unlike numerical solutions of the fluid equations, the DSMC method may be used to model systems with non-Maxwellian distributions (e.g. effusion). Although simulations of pulsed effusion have suggested that the distribution function describing an effusion plume often becomes Maxwellian within a few mean free path lengths of the effusive surface, the temperature components parallel and perpendicular to the target are not necessarily the same, and the particle flux onto a substrate during pulsed effusion is seldom thermal [59, 58]. DSMC simulations therfore provide important details about the particle flux, momentum flux, and energy flux incident onto a substrate that cannot be obtained using continuum models. Accurate and detailed estimates of these quantities might offer valuable insight into the kinetics of film deposition.

Figure 1.6 shows a flow chart which outlines the implementation of the DSMC method in a typical computer program. Simulation particles, each representing several million real particles, are generated in phase space with initial positions and velocities consistent with some distribution function $f(\vec{v}, \vec{x})$ of interest. Once generated, particles are moved according to $\vec{x}(t + \Delta t) = \vec{x}(t) + \vec{v}(t)\Delta t$ with each time step. The time step must be much smaller than the mean time between collisions, but not so small as to make the code computationally inefficient. If a particle is found to be outside the simulation boundaries when its position is updated, an appropriate boundary condition is implemented to return the particle to the simulation volume with an appropriate velocity or remove it from the simulation. Boundary conditions may include specular reflection, diffuse reflection, redeorption, or recondensation. Each surface may have a time-dependent sticking probability which is different for each species.

At each time step, particles are assigned into spatial cells whose dimensions must be selected to be smaller than or comparable to the mean free path, and then a

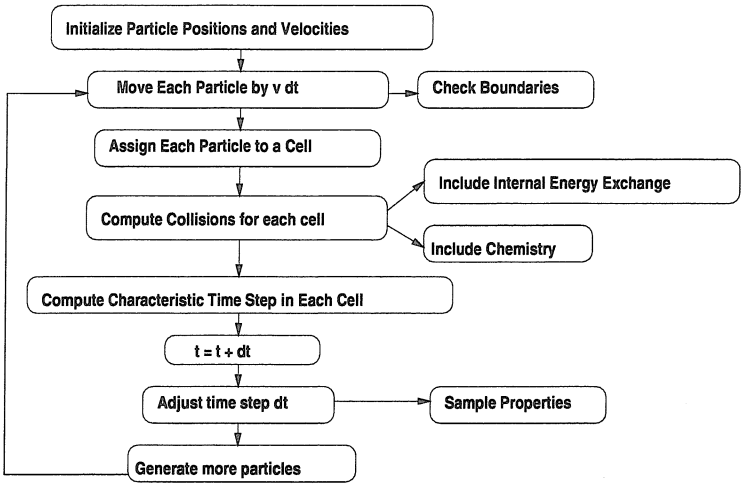

Figure 1.6: Flow chart for a typical DSMC simulation.

number of collision pairs are selected within each cell, using the acceptance-rejection method developed by Bird [63]. For monatomic species collisions are elastic, so the translational energy shared by the collision pair is conserved. For polyatomic species, the Larsen-Borgnakke method may be used to include rotational and vibrational internal energy exchange [70, 63]. Reaction cross sections may also be introduced to allow bi-molecular reactions consistent with Arrhenius reaction rates [63]. To ensure that the cell dimensions and time step are sufficiently small, the mean free path within each cell may be estimated by $\lambda = 1/\sqrt{2}\sigma n$ where σ is the average cross section of randomly selected collision pairs, and n is the density in the cell. A cell's characteristic time step is then the mean free path divided by the average relative velocity among selected collision pairs in that cell. For computational efficiency, the time step may be allowed to increase during the simulation, so long as it remains well below the minimum characteristic time step.

After a specified number of time steps, the flow may be sampled, saving density, radial and axial flow velocity, and radial and axial kinetic temperature in each cell for each species. On a faster time scale, data describing the flux of particles onto the substrate, defined by the boundary opposite the target, may be recorded for each species. Additionally, the plume's energy and momentum may be monitored, along with density and temperature at fixed points in the simulation volume. Each

simulation may be repeated several times, until running averages of the flow properties have negligible statistical noise.

A technique has been developed [70] for use within the DSMC method to treat energy exhange among rotational, vibrational, and translational modes in polyatomic gases such as O_2 and SiO during collisions. Additionally, Bird has developed a method to treat bi-molecular chemical reactions such as $Si + O_2 \rightarrow SiO + O$ by deriving a functional form for reaction cross sections which statistically result in chemistry that is consistent with Arrhenius reaction rates in the continuum limit. In this way, the formation of reaction products during the expansion of a target material into a background gas may be observed in simulation. Information obtained may be useful in understanding reactive processes observed experimentally during PLA. What are believed to be the first simulations of Si expanding into a rarified background gas containing O_2 are presented here.

Chapter 2 Doppler-corrected PLIF imaging of a PLA plume expanding into vacuum

2.1 Introduction

In this chapter, PLIF images acquired from a PLA plume expanding into vacuum using a typical excimer-pumped dye laser are processed to produce planar images depicting relative atomic density within a cross section of the plume. This requires compensating for Doppler shifts because the narrow bandwidth of the laser limits its ability to resonantly illuminate the rapidly expanding plume uniformly. For a given peak laser frequency, only a small region of the plume is resonantly illuminated. An image acquired by a spectrally flat, broadband laser can be simulated, however, by superimposing several images taken at closely spaced pump laser detuning frequencies. Images constructed by superimposing up to 15 individual images are presented, each image acquired by incrementally detuning the pump laser from the resonant frequency of a stationary Si atom in steps of 0.18 cm^{-1} (5.4 GHz), a spacing slightly greater than the 0.14 cm^{-1} (4.2 GHz) FWHM of the laser.

Care is required, however, to correctly compensate the images produced by such a superposition for any variations in the pump laser intensity that might exist across the width of the sheet. It can be shown that for a sufficiently low pump laser intensity and/or a sufficiently brief laser pulse, the LIF signal, which is directly proportional to the upper state population, increases linearly with laser intensity. In this regime, the superimposed images must be corrected by normalizing to the laser intensity profile, a function describing the intensity variation along the width of the sheet. Although this regime is desirable, it is often difficult to acquire data with an acceptable signal-to-noise ratio using a laser intensity which can safely be regarded as linear, and it is often not obvious during an experiment that the laser intensity is nonlinear. For the

special case of PLIF imaging on PLA plumes which expand into vacuum, the PLIF images contain valuable information that can be used to estimate the laser intensity and allow them to be corrected even if the laser intensity is nonlinear.

A schematic showing a typical experimental arrangement used to acquire PLIF images was shown in Figure 1.2. As described, a pump laser beam, shaped into a thin sheet, bisects the plume and the resonant atoms within the interaction volume subsequently fluoresce. A photograph of the experimental arrangement used for this work is shown in Figure 2.1. The vacuum chamber and its associated windows and feedthroughs, normally maintained at Caltech, was temporarily transported to the Combustion Research Facility at Sandia National Laboratories in Livermore, CA where the lasers, optics, and imaging equipment are maintained. The data presented is therefore a collaborative effort between Caltech and Sandia National Laboratories.

The vacuum chamber consists of a custom-designed 12-inch diameter spherical stainless steel vacuum chamber (Huntington Mechanical Labs, Inc.). Attached is a Varian V250 macro torr pump (part 969-9008) controlled by a Varian controller (part 969-9523). Pressure in the chamber is monitored using a Bayard-Alpert ion gauge from Physical Electronics, Inc. (part 6057672) with a DGC 111 digital ion gauge controller (part 60506000), or a Varian silicon transducer (part 6543-25-010) and WV100-2 manometer (part 6522-08-410), depending on chamber pressure. Ports through which the input UV laser beam and PLIF signal must pass are fitted with UV-grade fused silica. A 3-inch diameter n-type Si (100) wafer is mounted inside the chamber on a custom target holder which is attached to a rotary motion feedthrough with AC motor drive from MDC (part 670002-01). A second 3-inch Si wafer is mounted directly opposite the target on a similar rotary feedthrough. Target and substrate positions are measured using calibrated linear feedthroughs, also from MDC (part 665503).

In these experiments, 0.5-3.0 μs delay separates the creation of the plume, achieved by irradiating an Si target with a focused KrF laser, and the illumination of the interaction volume with the pump laser. The pump laser is generated using a Lambda Physic EMG 201 MSC excimer laser operating with XeCl (308 nm output) to pump

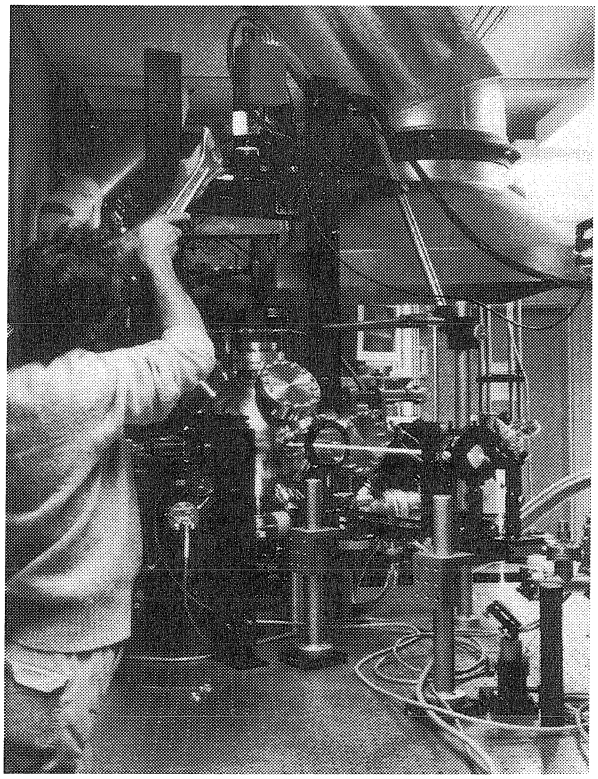

Figure 2.1: Experimental apparatus used for PLIF imaging of Si. A multiple exposure is used to show the path of the pump laser sheet into the chamber.

coumarin 480 dye in a modified Lumonics Hyper Dye 300 laser assembly, whose output is doubled in BBO and then shaped and focused using a -50 mm cylindrical lens, a 500 mm spherical lens, and 750 mm spherical lens into a sheet with a waist thickness near 200 μm. A portion of the resulting fluorescence signal is gathered by a lens and focused onto a single-microchannel plate-intensified CCD camera oriented perpendicular to the laser sheet. The intensifier is triggered off the pump laser pulse and the camera is filtered by a 10 nm FWHM interference filter centered at 290 nm. This filter is ideal for gathering fluorescence from the $^1P^0\ 4s \rightarrow {}^1D\ 3p^2$ Si transition at 288.158 nm while eliminating scattered pump laser light and UV radiation originating from the ablation spot following the creation of the plume.

Using this arrangement, a 512 x 239 pixel digital image is created to represent the 4.0 cm x 3.0 cm rectangular area near the target through which the plume travels. This configuration provides a spatial resolution near 0.12 mm, which is sufficiently small to produce detailed images, while still slightly larger than the characteristic distance traveled by atoms moving at 10^4 m/s with an excited-state lifetime near 10 ns. To increase the signal-to-noise ratio even further, each image is averaged over 40 shots and then digitally filtered to remove a small amount of background emission from the plume. This same CCD camera, intensifier, and similar experimenatal arrangements have been used previously to successfully generate detailed images of a wide variety of combustion-related systems [71, 72, 73, 74].

To determine the nonlinear dependence of PLIF signal on pump laser intensity, a three-level model is introduced and applied to the specific case of PLIF on Si, pumping the ^{3}P 3p^2 $\leftarrow$ ^{1}P^0 4s transition and gathering signal from the ^{1}P^0 4s $\rightarrow$ ^{1}D 3p^2 transition. This model is very sensitive to the magnitude of the pump laser intensity. In contrast to PLIF imaging using linear laser intensity, knowledge of the relative intensity across the sheet is therefore insufficient to deduce relative density from PLIF signal strength. An additional measurement which provides the laser's average pulse energy is also necessary, accounting for losses introduced by the optics and chamber window.

To aid in the measurement of the pump laser intensity, the PLIF data itself is

examined. The PLIF data, which consist of thin linear streaks whose positions are displaced from the plume's axis by a distance which varies linearly with pump laser detuning, suggest that the plume expands collisionlessly from the target. It can be shown that for a plume which originates instantaneously from a dimensionless point and collisionlessly expands into vacuum that the fluorescence spectral linewidth can be related to the width of the PLIF signal streaks. Since the three-level model can be used to calculate fluorescence linewidth as a function of laser intensity, qualitative estimates of laser intensity can be inferred from the width of the PLIF signal. Because the plume originates from an ablation spot with a non-zero width, the width of the PLIF signal depends on the width of the ablation spot as well as the bandwidth of the pump laser, making the analysis slightly more complex. Despite this, estimates of laser intensity determined by this method allow images obtained by superimposing several individual images to be corrected for variations in laser sheet intensity, producing what are believed to be the first reported PLIF images depicting ground-state, neutral density within a cross section of a PLA plume expanding into vacuum.

2.2 A three-level model describing the PLIF imaging of Si

There are two primary reasons why a three-level, non-resonant LIF scheme is generally preferable to the two-level, resonant scheme described in Appendix A. First, if the photons constituting the LIF signal are to be gathered by a detector during the laser pulse, then scattered laser radiation cannot be filtered from the resonant signal. Non-resonant fluorescence, however, is at a different frequency then the pump frequency, so a narrow bandpass filter can be employed to eliminate unwanted scattered light, significantly increasing the signal-to-noise ratio. Second, if atoms are pumped from the atomic ground state and the linestrength of the transition is sufficiently large, a high density plume may be optically thick for both the pump laser sheet and the resonant signal as it propagates through the plume en route to the detector.

Even if the pump laser sheet is of sufficient intensity to saturate the upper state and therefore suffer no attenuation as it propagates through the plume, the incoherent PLIF signal would still be subject to attenuation if the scale length for re-absorption is small compared to the width of the plume. Such attenuation would be spatially and temporally dependent, making data analysis extremely difficult. Although the Si plumes used in these experiments are not optically thick at the 243.877 nm ^{3}P 3p^2 $\leftarrow$ ^{1}P^0 4s transition wavelength ($A_{12} = 7.4$ x 10^5 s^{-1}), the problem of scattered laser light is still minimized using a three-level, non-resonant LIF scheme. The specific scheme used for PLIF imaging of an Si plume in these experiments is shown schematically in Figure 2.2.

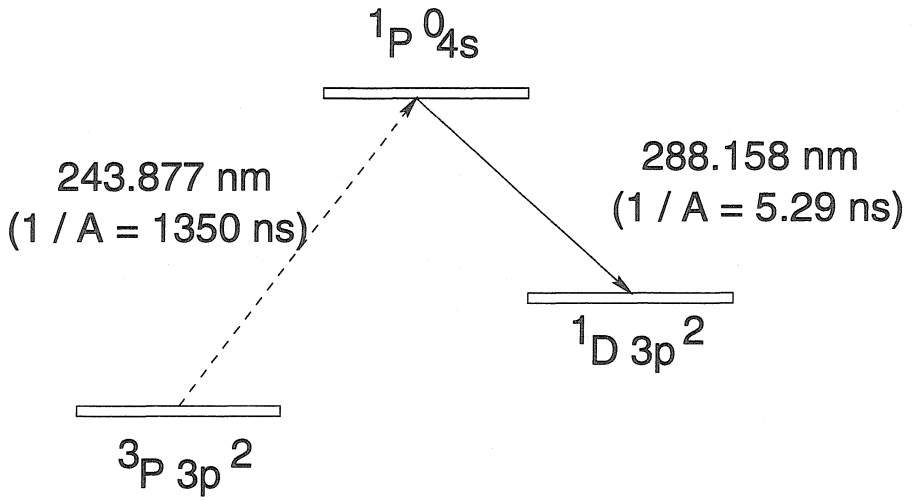

Figure 2.2: LIF scheme used to acquire PLIF images depicting the relative density of Si in a PLA plume. The dotted line represents a weak transition disallowed by Hund's selection rules.

Level (1) is chosen to be the ^{3}P 3p^2 electronic ground state under the assumption that the ablation process populates this state significantly more than any other state, allowing the acquired PLIF images to be interpreted as the relative density of the bulk of the Si plume. The $^1P^0$ $4s$ state is selected as level (2) because of its accessibility using the available coumarin 480 dye and BBO doubling crystal, and because it has at least one non-resonant level to which it is connected by a non-zero linestrength. Fluorescence into the ^1D $3p^2$ state (level 3) is detected because the linestrength of the $^1P^0$ $4s \rightarrow {}^1D$ $3p^2$ transition is more than an order of magnitude greater than the

linestrength of the alternative $^1P^0\ 4s \rightarrow {}^1S\ 3p^2$ transition.

The rate equations for this three-level LIF system are given by

$$\dot{N}_2(t) = R_{12}N_1 - A_2N_2 \tag{2.1}$$

and

$$\dot{N}_1(t) = A_{21}N_2 + R_{21}N_2 - R_{12}N_1, \tag{2.2}$$

where A_2 is a sum over all allowed rates for the decay out of the upper state, that is

$$A_2 = \sum_m A_{2m}, \tag{2.3}$$

and the stimulated emission rate R_{21} and aborption rate R_{12} are given by

$$R_{21}(\nu) = \frac{g_1}{g_2}R_{12}(\nu) = \frac{c^2}{8\pi h\nu_{21}^3}I_0A_{21}S(\nu), \tag{2.4}$$

where I_0 is the intensity of the laser, g_2 and g_1 are the degeneracies of the uppper and lower states, and $S(\nu)$ is an appropriate lineshape function (see Appendix A for details). Although these equations allow for the removal of atoms or molecules from the two level system, they ignore thermal processes that would tend to replenish the lower state and deplete the upper state. Rates for these processes are assumed to be much smaller than either the stimulated emission rate or the spontaneous emission rate and are therefore ignored. Knowing the time-dependent function $N_2(t)$, the LIF signal for this system is then given by the time integral

$$\int_0^\infty A_{23}N_2(t)dt. \tag{2.5}$$

For the three-level Si system chosen for this work, the depletion of the upper state by spontaneous emission is rapid, occurring with a characteristic time of $1/A_2 = 5.3$ ns so that the upper limit on the integral in equation 2.3 could actually be reduced to about 40 ns without affecting the result. In the 5.3 ns lifetime of the upper state the fastest atoms or molecules, traveling at the extreme velocity of 10 km/s, are displaced

by only 0.05 mm, which is still less than half the $\approx$ 0.12 mm spatial resolution of the CCD camera used to image the planar interaction volume. This rapid decay of the upper state is therefore convenient, because the gate width on the microchannel plate intensifier can be made arbitrarily large ($\approx$ 50 ns in these experiments) without spatially smearing the PLIF images.

Solving equations 2.2 and 2.1 for $N_2(t)$, assuming $N_2(0) \approx 0$, gives

$$N_2(t) = N_1^0 \frac{(k_+ - R_{12})(R_{12} - k_-)}{(R_{21} + A_{21})(k_+ - k_-)}(e^{-k_- t} - e^{-k_+ t}), \tag{2.6}$$

where

$$k_\pm = \frac{\eta \pm \sqrt{\eta^2 - 4R_{12}A_{23}}}{2} \tag{2.7}$$

with $\eta = R_{21} + R_{12} + A_2$.

Shown on the left in Figure 2.3 are solutions for the upper state population fraction as a function of time for laser intensities ranging from 0.1-1000 kW/cm^2. A temporal step function pulse profile is assumed, with a duration of 28 ns, measured using a fast response (< 200 ps rise time, < 250 ps fall time) photodiode. The LIF scheme parameters used in equation 2.6 are obtained from a NIST database [75], specifically, A_{23} = 1.89 x 10^8 s^{-1}, A_{21} = 7.4 x 10^5 s^{-1}, λ_{21} = 243.877 nm, $g_1 = 1$, and $g_2 = 3$.

The graph to the right in Figure 2.3 shows the time integral of the upper state population, a function directly proportional to the LIF signal. Clearly evident is the threshold for saturation at $I_s \approx$ 10 kW/cm^2.

Shown on the left in Figure 2.4 are solutions for the upper state population fraction as a function of time for laser intensities ranging from 0.1-5 kW/cm^2, and to the right, the time integral of the upper state population. The LIF signal appears linearly dependent on pump laser for intensities less than about 1 kW/cm^2, about an order of magnitude less than the threshold value for saturation.

Since the pump laser sheet used to illuminate the plume consists of a $\approx$28 ns, 0.5 mJ/pulse, manipulated into a sheet $\approx$ 6.0 cm wide with a focused waist of $\approx$ 200 μm, the average intensity over the cross section of the sheet can be estimated to be near 100 kW/cm^2. It is therefore unacceptable to assume, based on this rough

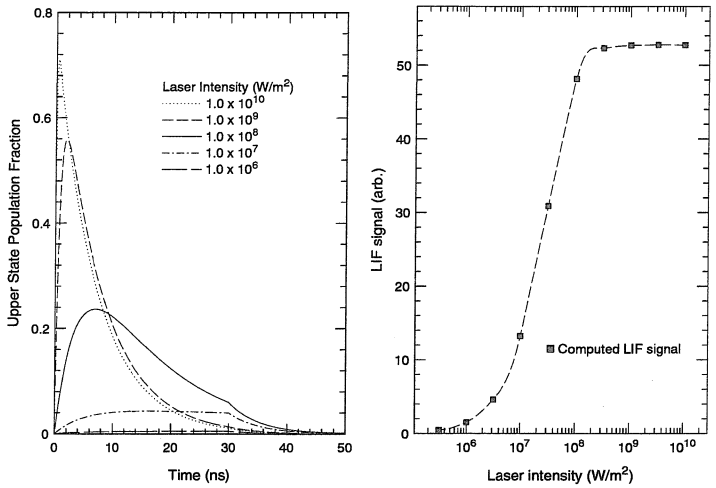

Figure 2.3: (Left) Fraction of Si atoms in the upper state vs. time for pump laser intensities ranging from 0.1 - 100 kW/cm^2, assuming the three-level model used in these experiments. (Right) Time integral of the upper-state fraction vs. laser intensity. The threshold for saturation is near 10 kW/cm^2.

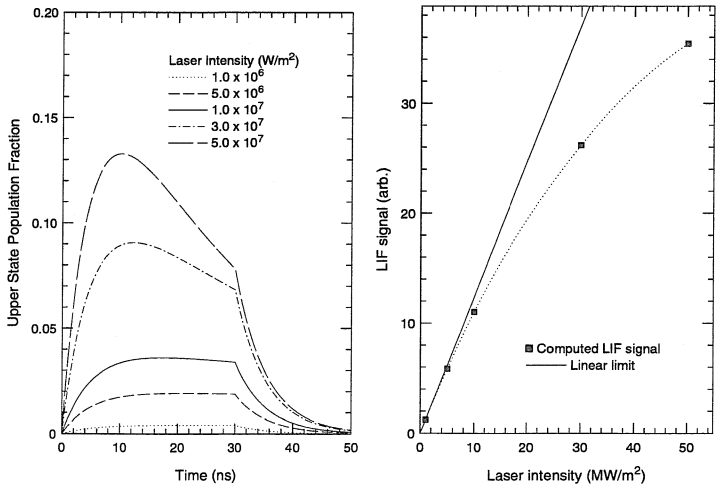

Figure 2.4: (Left) Fraction of Si atoms in the upper state vs. time for pump laser intensities ranging from 0.1-5 kW/cm^2, assuming the three-level model used in these experiments. (Right) The time integral of the upper state fraction, a linear function for intensities below $\approx$ 1 kW/cm^2.

estimate, that the laser intensity used to acquire the PLIF images in this work is linear, being about two orders of magnitude greater than the threshold intensity for nonlinear behavior. This measurement was taken outside the vacuum chamber, however, and beam cropping by the 3.0 cm input window and attenuation by the thin film of Si deposited on its inner side certainly imply that the laser intensity reaching the plume is much lower. Use of this measurement as a parameter in the three-level rate equations is therefore unreasonable, both because of the uncertainty in the measurement and because of inconsistencies that arise in the analysis of the PLIF data when this value for laser intensity is assumed. In an effort to provide some independent measurement of laser intensity from the PLIF data, the following sections discuss how the laser's spectral linewidth, the solution for $N_2(t)$ given in equation 2.6, and the spatial dimensions of the PLIF images can be used to produce a more convincing estimate of the pump laser intensity, and more accurately correct the PLIF data.

2.3 Measurement of the pump laser linewidth

A detailed understanding of the PLIF images acquired from a PLA plume using a spectrally narrow pump laser requires an accurate measurement of the linewidth of the pump laser. In this work, two Burleigh wavemeters, models WA-5500 and WA-4500, are employed to measure the width of the doubled and undoubled laser lineshapes, respectively, by examining the the interference fringes produced by the etalon in either device. The spacing between fringes is used automatically by Burleigh software to determine the wavelength of the input laser, but the linewidth must be determined manually. This is accomplished by considering that the lineshape of each fringe results from a convolution integral between the laser lineshape function and a second lineshape function determined by physical properties of the instrument. In order to determine the laser linewidth by measuring the width of an etalon fringe, the lineshape functions appropriate for the laser and instrument must be assumed or known, and the FWHM of the instrument lineshape function must also be assumed

or known.

A FWHM value appropriate for the lineshape function introduced by the WA-4500 wavemeter can be measured using a single-mode HeNe laser as an input. Since the linewidth of this laser is much narrower than the 0.039 ± 0.002 cm^{-1} measured width of the etalon fringe (an average over 50 shots), the width can safely be attributed to the width of the lineshape function for the instrument. The full widths of the observed lineshape, measured from 5 to 50% of maximum are shown in Figure 2.5, compared with both a Gaussian profile and Lorentzian profile with the same FWHM. The data suggests that the lineshape contributed by the instrument is nearly Gaussian, the wings apparent in the data resulting from the contribution of a narrow Lorentzian lineshape in the convolution integral. The manufacturer's specification for spectral resolution is given as 0.05 cm^{-1}, and is therefore interpreted as closely approximating the FWHM of the Gaussian lineshape that becomes convolved with the laser lineshape function to produce the observed etalon fringe lineshape.

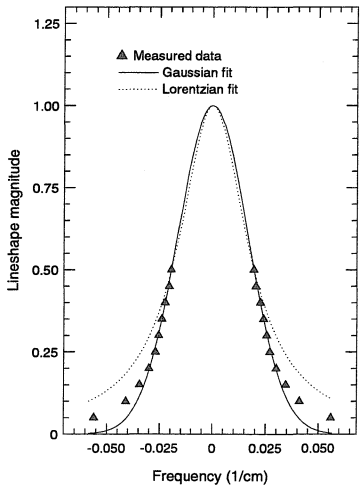

Figure 2.5: Measured lineshape function appropriate for a Burleigh wavemeter, model WA-4500. Lineshape appears nearly Gaussian, with wings introduced by its convolution with a negligibly narrow Lorentzian lineshape appropriate for a single mode HeNe laser.

Using the output of the XeCl pumped dye laser as an input to the WA-4500 produces fringes whose width is 0.087 ± 0.009 cm^{-1}. If the lineshape of the laser is assumed to be Lorentzian, the resulting convolution integral produces a Voight profile

with the measured fringe width if the laser FWHM is 0.070 ± 0.001 cm^{-1}. The three normalized lineshapes involved in the convolution integral are shown to the left in Figure 2.6.

The fringes produced when the doubled output from the dye laser is put into the WA-5500 have a FWHM value of 0.39 ± 0.01 cm^{-1}. Because no spectrally narrow UV source with a wavelength near 244 nm is readily available, the manufacturer's specification for spectral resolution for the WA-5500 (0.33 cm^{-1}) is assumed to be nearly accurate for the FWHM of the lineshape function appropriate for this instrument. A Gaussian lineshape function with a FWHM of 0.32 cm^{-1} can be convolved with a Lorentzian to produce a Voight lineshape with the measured fringe linewidth if the Lorentzian has a FWHM of 0.14 ± 0.01 cm^{-1}. This linewidth, about twice the width of the undoubled laser linewidth, is consistent with the result expected when two identical Lorentzian lineshapes are convolved. The three normalized lineshapes involved are shown to the right in Figure 2.6.

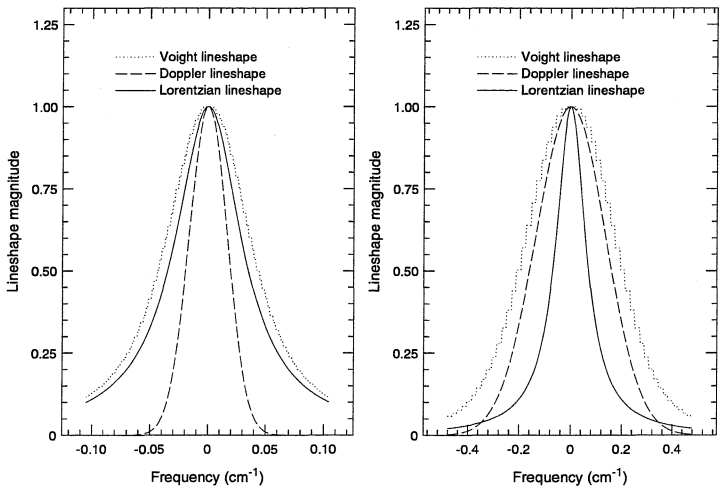

Figure 2.6: Lineshape functions involved in generating the Voight profiles describing the fringes produced by wavemeter etalons, convolutions of a laser lineshape (Lorentzian) with an instrument lineshape (Gaussian). (Left) XeCl excimer pumped dye laser output. (Right) Dye laser output doubled in BBO.

2.4 The relationship between LIF signal linewidth and PLIF image intensity for a collisionless plume

The population rate equations that describe the distribution functions of the upper and lower states of the three-level system used in this work to image an Si plume are

$$\dot{f}_2(t,\nu) = R_{12}(\nu)f_1(t,\nu) - A_2 f_2(t,\nu) \tag{2.8}$$

and

$$\dot{f}_1(t,\nu) = (A_{21} + R_{21}(\nu))f_2(t,\nu) - R_{12}(\nu)f_1(t,\nu), \tag{2.9}$$

where $f_2(t,\nu)d\nu$ and $f_1(t,\nu)d\nu$ are the fractional population densities for the upper and lower states, respectively, that is, the fraction of the population density of the state that is resonant at a frequency between ν and $\nu+d\nu$. The upper state population density can in turn be evaluated from the integral

$$N_2(t,\vec{x}) = \int_{-\infty}^{\infty} f_2(t,\vec{x},\nu)d\nu \tag{2.10}$$

The LIF signal $\mathcal{S}(\vec{x})$, proportional to the integral of $N_2(t,\vec{x})$ over time, can be written as

$$\mathcal{S}(\vec{x}) \propto \int_0^{\infty} N_2(t,\vec{x})dt = \int_0^{\infty} f_1^0(\vec{x},\nu)P(\nu)d\nu \tag{2.11}$$

where $f_1^0(\vec{x},\nu)$ describes the lower state population just prior to the activation of the pump laser, and where the function $P(\nu)$ is obtained from the integral

$$\int_0^{\infty} \frac{(k_+ - R_{12})(R_{12} - k_-)}{(R_{21} + A_{21})(k_+ - k_-)} \left[\left(\frac{1}{A_2} - \frac{1}{k_-} \right) e^{-k_- t} + \frac{1}{k_-} - \left(\frac{1}{A_2} - \frac{1}{k_+} \right) e^{-k_+ t} - \frac{1}{k_+} \right] dt. \tag{2.12}$$

The frequency dependence of $P(\nu)$ comes from the functions $R_{12}(\nu)$ and $R_{21}(\nu)$, which are each proportional to $I(\nu) = I_0\mathcal{L}(\nu)$ where $\mathcal{L}(\nu)$ and I_0 are the lineshape and intensity of the laser, respectively. The function P_ν can be normalized and

interpreted as a fluorescence lineshape function, shown at the left in Figure 2.7 for laser intensities ranging from 0.1-1000 kW/cm^2. For linear laser intensities, this lineshape function reduces to $\mathcal{L}(\nu)$, the spectral lineshape of the pump laser, having a FWHM of 0.14 cm^{-1} in these experiments. For laser intensities greater than 1 kW/cm^2, the fluorescence lineshape becomes significantly power broadened. To the right in Figure 2.7, the linewidth $\delta\nu_P(I_0)$ of $P(\nu)$ is plotted as a function of laser intensity I_0, again assuming a laser FWHM of 0.14 cm^{-1}.

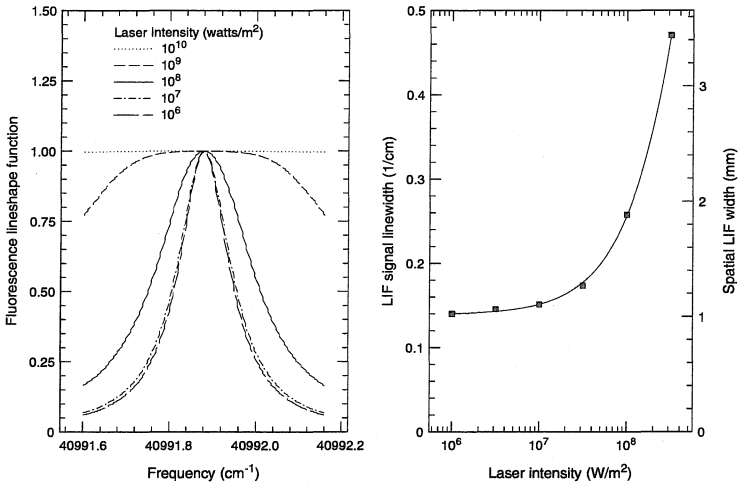

Figure 2.7: (Left) Fluorescence lineshape functions for pump laser intensities of 0.1-1000 kW/cm^2. (Right) Fluorescence linewidth as a function of laser intensity. Power broadening is significant for intensities exceeding about 1 kW/cm^2.

For a plume which originates from a dimensionless point beginning at time $t = 0$, and then expands collisionlessly, the resonant frequency of all atoms at any point in the interaction volume a distance r off axis is given by

$$\nu'_{21} = \nu_{21}(1 + \frac{r}{ct}), \tag{2.13}$$

and therefore

$$f_1^0(\vec{x}, \nu) = N_1^0(\vec{x})\delta\left(\nu - \nu_{21}(1 + \frac{r}{ct})\right). \tag{2.14}$$

This relationship is true regardless of the velocity distribution function $f(\vec{v})$ which describes the ensemble of plume atoms at the moment the collisionless expansion

begins. Substituting this expression into equation 2.11 gives

$$\mathcal{S}(\vec{x}) \propto N_1^0(\vec{x}) P\left(\nu_{21}(1+\frac{r}{ct})\right). \tag{2.15}$$

This spatially dependent function describes the PLIF image intensity at any position $\vec{x}$ within a planar interaction volume that passes through the axis of symmetry of a collisionlessly expanding plume, generated using a laser of arbitrary average intensity with an arbitrary intensity profile across the sheet. If the density of the plume varies negligibly over the width $\delta\nu_P$ of $P(r)$, then the PLIF image intensity would appear as a linear streak in the z direction whose center is offset from $r = 0$ to a position

$$r = ct\frac{\Delta}{\nu_{21}}, \tag{2.16}$$

where $\Delta = |\nu_{21} - \nu_0|$. The spatial FWHM of the streak would be given by

$$\delta x = ct\frac{\delta\nu_P}{\nu_{21}}, \tag{2.17}$$

which is independent of the magnitude of laser detuning Δ. A diagram showing how this resonant region might appear is shown in Figure 2.8.

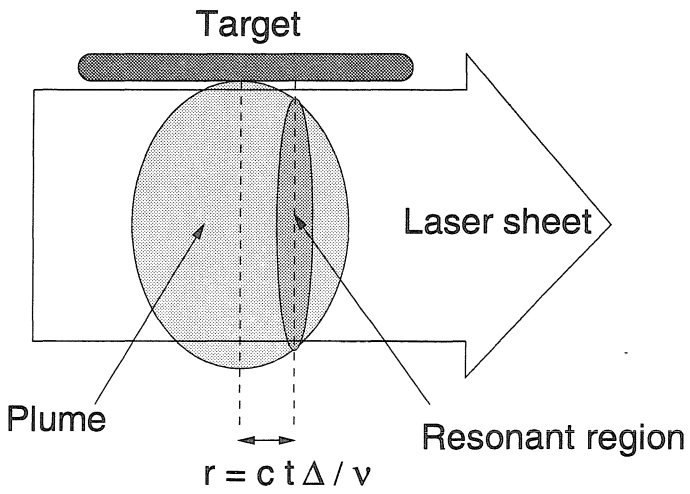

Figure 2.8: Schematic diagram showing the resonant region within an expanding PLA plume when a pump laser sheet, positively detuned from the plume atoms' stationary resonant frequency, enters from the left. The region is a linear streak whose position is given by equation 2.16.

These results suggest that if the frequency of the pump laser were continuously scanned near the stationary resonance frequency, the PLIF image streak would translate along the direction of propagation of the laser and maintain a constant spatial width related to the spectral width of $P(\nu)$ by equation 2.17. It will be shown in the following section of this chapter that the radial position of image streaks acquired using PLIF imaging are dependent on laser detuning as predicted by equation 2.16 and that the widths of the PLIF streaks are independent of detuning, thereby supporting the claim that the plume expands collisionlessly from the target. In this chapter, however, attention is focused on the significance of the width of the PLIF image streaks.

For the case of a pump laser intensity which is linear, $\delta\nu_P$ reduces to $\delta\nu_0$, the width of the laser, becoming independent of laser intensity. The width of a PLIF image streak acquired in this regime should therefore also be independent of laser intensity even if $I_0(z)$ varies appreciably across the sheet. For the case of a nonlinear pump laser intensity which varies as a function of z, however, the spatial width of the PLIF image streak should also depend on z due to the dependence of the power broadened linewidth on laser intensity.

2.5 PLIF data acquired from a typical Si PLA plume

Shown in Figure 2.9 are PLIF images of silicon taken 1.0 μs following the ablation of a silicon target into vacuum by a KrF excimer laser at a fluence near 2 J/cm^2/pulse. The dimensions of each image frame are 4.0 cm x 3.0 cm and are depicted to scale, with the target at the top. The images shown result when the pump laser, which enters the field of view from the left and bisects the plume, is detuned from stationary resonance by +1.08 cm^{-1}, +0.72 cm^{-1}, +0.36 cm^{-1}, 0 cm^{-1}, -0.36 cm^{-1}, and -0.72 cm^{-1}. The accuracy of the pump laser detuning is ensured by sampling a fraction of the dye laser output using a Burleigh pulse wavemeter (model WA-4500) calibrated by the 632.8

nm output of a small internal HeNe laser. Each image is essentially a vertical streak with a horizontal position moving left to right with an increase in laser frequency.

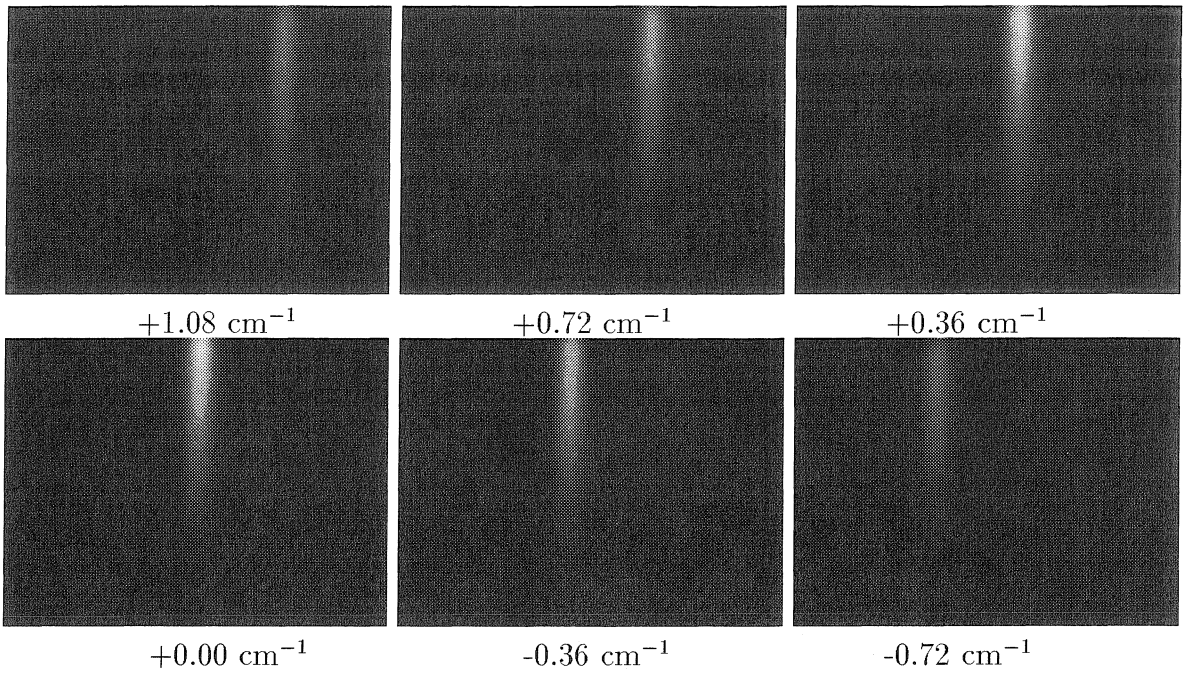

Figure 2.9: 4.0 cm x 3.0 cm PLIF images of expanding Si plume after 1.0 μs using 0.14 cm^{-1} bandwidth pump laser at various detunings from stationary resonance. The target is at the top, and the laser sheet enters the field of view from the left.

Although the images shown in Figure 2.9 are spaced by 0.36 cm^{-1} of detuning, data are actually acquired with spacings of 0.18 cm^{-1}, an increment slightly greater than the FWHM of the pump laser. In all, 15 such images are acquired, 7 on either side of the stationary resonance frquency. It is interesting at this point to present the resulting image when all of the individual images are superimposed, given at top in Figure 2.10 despite the fact that an interpretation of the image remains incomplete.

2.5.1 Evidence that the plume expands collisionlessly from the target

Shown to the left in Figure 2.12 is a plot showing the dependence of the PLIF streak center position, defined as the radial location of maximum intensity when integrated along z, on pump laser detuning. The dependence appears linear, and the slope is

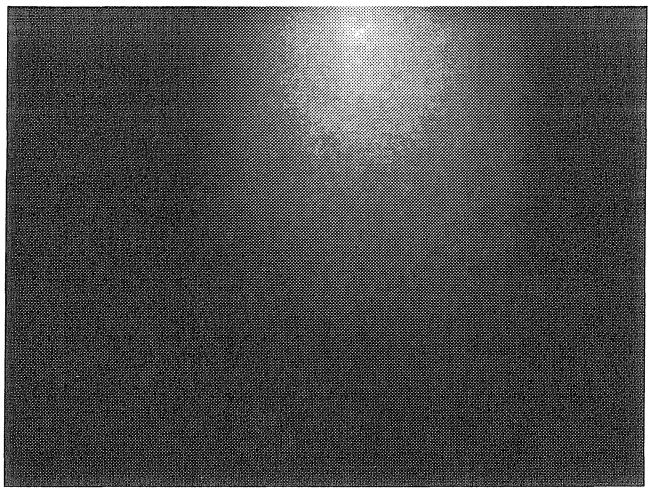

Figure 2.10: 4.0 cm x 3.0 cm PLIF image generated by superimposing 15 individual images, including those in Figure 2.9, each spaced by 0.18 cm^{-1} of detuning. Data corresponds to a delay of 1.0 μs.

consistent with that predicted by equation 2.16, which was derived assuming that the plume expands collisionlessly. By arguments identical to those used to derive equation 2.16, it might be expected that if the laser sheet were directed normal to the target plane, and that the plume in fact expands collisionlessly, PLIF images would appear as horizontal streaks with positions given by

$$z = ct\frac{\Delta}{\nu_{21}}. \tag{2.18}$$

An experiment was conducted to test this hypothesis. Shown in Figure 2.11 are images taken 2.0 μs after the ablation laser pulse, corresponding to pump laser detunings of -1.02 cm^{-1}, -.54 cm^{-1}, and +0.54 cm^{-1} from stationary resonance. The target in these images is actually 5.0 mm above the field of view, whose dimensions are 4.0 cm x 3.0 cm as before. The images produced using negative detuning, which resonates with atoms having velocities directed away from the target, in fact produce horizontal streaks as predicted. The right side of these images appears cropped because the laser sheet is cropped by the input window on the vacuum chamber. The center position of the streaks is plotted against laser detuning to the right in Figure 2.12, a function which appears linear with a slope consistent with equation 2.18.

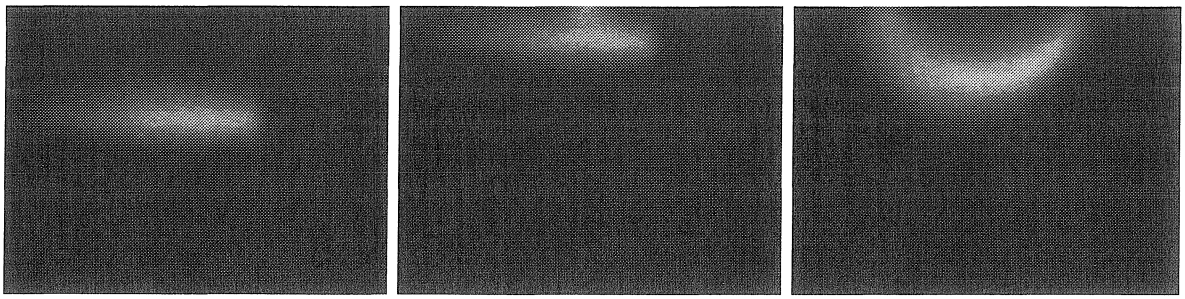

-1.02 cm^{-1} -0.54 cm^{-1} +0.54 cm^{-1}

Figure 2.11: 4.0 cm x 3.0 cm PLI images of an Si plume expanding into vacuum after 2.0 μs using a 0.14 cm^{-1} bandwidth pump laser at various detunings from stationary resonance. Target is 5.0 mm above the field of view, and the laser sheet enters from the bottom.

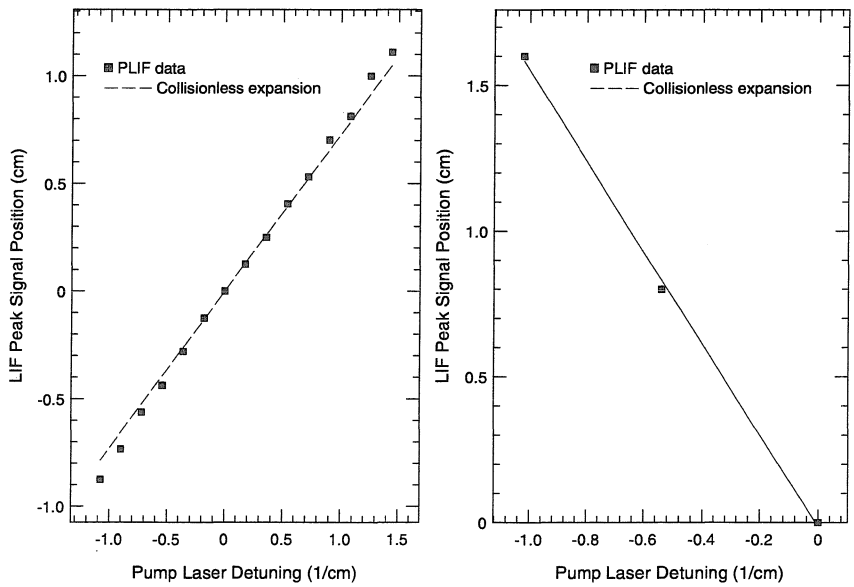

Figure 2.12: (Left) Center position of vertical PLIF streaks as in Figure 2.9 vs. pump laser detuning. (Right) Center position of the horizontal PLIF streaks in Figure 2.11 vs. pump laser detuning. Dependences are linear with slopes consistent with the collisionless expansion of the plume from the target.

An interesting observation is made when the pump laser is positively detuned from stationary resonance. The collisionless expansion model would predict no PLIF signal in this regime, since all the atoms are traveling away from the target and positive detuning is resonant with atoms moving toward the target. Instead, circular rings of PLIF signal are observed, centered on the location of the ablation spot, as seen to the right in Figure 2.11. These rings are believed to result from diffuse reflection of the laser sheet off the highly reflective target surface resonantly exciting the outward traveling Si atoms. If this explanation is correct, the rings should disappear if a smaller target were used instead of a 3-inch wafer but this hypothesis was not tested.

2.5.2 Use of PLIF streak widths to estimate pump laser intensity

Assuming that the plume expands collisionlessly from the target, the width of the PLIF streaks shown in Figure 2.9 might be expected to relate to the fluorescence linewidth according to equation 2.17, after inserting a time delay of 1.0 μs. The width of a PLIF streak may be determined by examining the normalized magnitude of the PLIF signal as a function of radial position at some fixed distance from the target. Figure 2.13 shows the result, a distance of 5.1 $\pm$ 0.1 mm from the target for detunings of +1.08 cm^{-1}, +0.72 cm^{-1}, +0.36 cm^{-1}, 0 cm^{-1}, -0.36 cm^{-1}, and -0.72 cm^{-1}. The width of the PLIF streak a distance of 5.1 mm from the target for each magnitude of detuning appears to be the same, about 2.3 mm. This independence of the LIF streak width on detuning further supports the claim that the plume expands collisionlessly from the target, allowing it to be used to relate the width of the PLIF streaks in Figure 2.9 to the fluorescence linewidth. This results in a fluorescence FWHM of 0.31 cm^{-1}, more than twice the width of laser lineshape function. According to the current model, PLIF streaks acquired using a linear laser intensity would only be 1.0 mm wide.

It is tempting to conclude that the extra width is simply the result of power broadening, which is seen in the graph in Figure 2.7 to stretch a 1.0 mm streak width

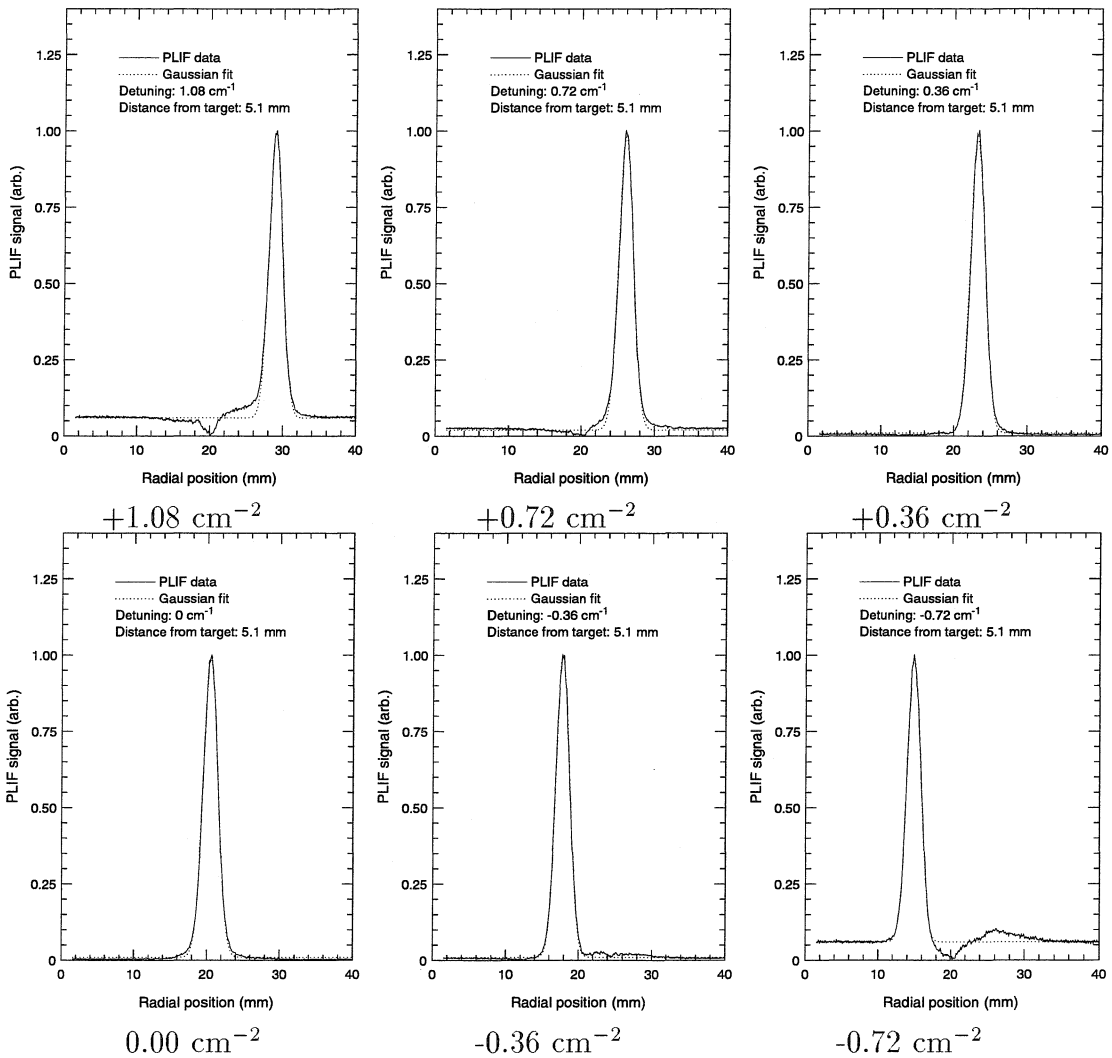

Figure 2.13: Normalized PLIF intensity of images in Figure 2.9 along a cross section 5.1 $\pm$ 1.5 mm from the target. Data is described reasonably well by Gaussian lineshape functions with a width near 2.3 mm, independent of detuning.

to 2.3 mm at a laser intensity 10-11 kW/cm^2. If such power broadening is in fact the cause of the extra PLIF streak width, however, the width should vary as a function of z in a way that is consistent with the variation in laser intensity across the sheet. Shown to the left in Figure 2.14 is the laser intensity profile used to acquire the images in Figure 2.9. This profile is measured using a small ($\approx$ 1.0 mm) photodiode positioned at several points across the width of the laser sheet. The data fits well to a Gaussian lineshape with a FWHM of 2.1 cm, centered 0.63 cm outside the field of view. To the right in Figure 2.14 are linewidth profiles, calculated using the current three-level model assuming a laser FWHM of 0.14 cm^{-1} and the laser intensity profile on the left of Figure 2.14, for average intensities ranging from .316 - 31.6 kW/cm^2. The current model requires that a laser intensity large enough to widen the PLIF streaks to the observed value of 2.3 mm should also produce a significant variation in PLIF streak width along the z direction.

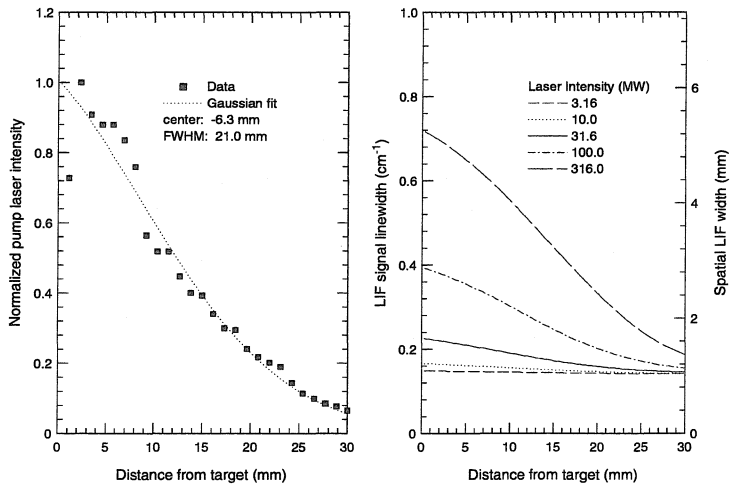

Figure 2.14: (Left) Normalized laser sheet intensity as a function of axial position, measured using a photodiode. (Right) Calculated fluorescence linewidth profiles for average intensities ranging from 0.316 to 31.6 kW/cm^2 assuming the intensity profile to the left and a laser FWHM of 0.14 cm^{-1}.

Shown in Figure 2.15 are cross sections of the PLIF streak along the axis of the plume (0 cm^{-1} detuning) for several positions spaced by 3.4 $\pm$ 0.8 mm away from from the target. The data for each cross section fits well to a Gaussian profile, with no significant variation in the width as a function of distance from the target. Clearly, in

the current model, there is no solution that satisfies both the experimentally observed PLIF linewidth of 2.3 mm and its apparent independence of z.

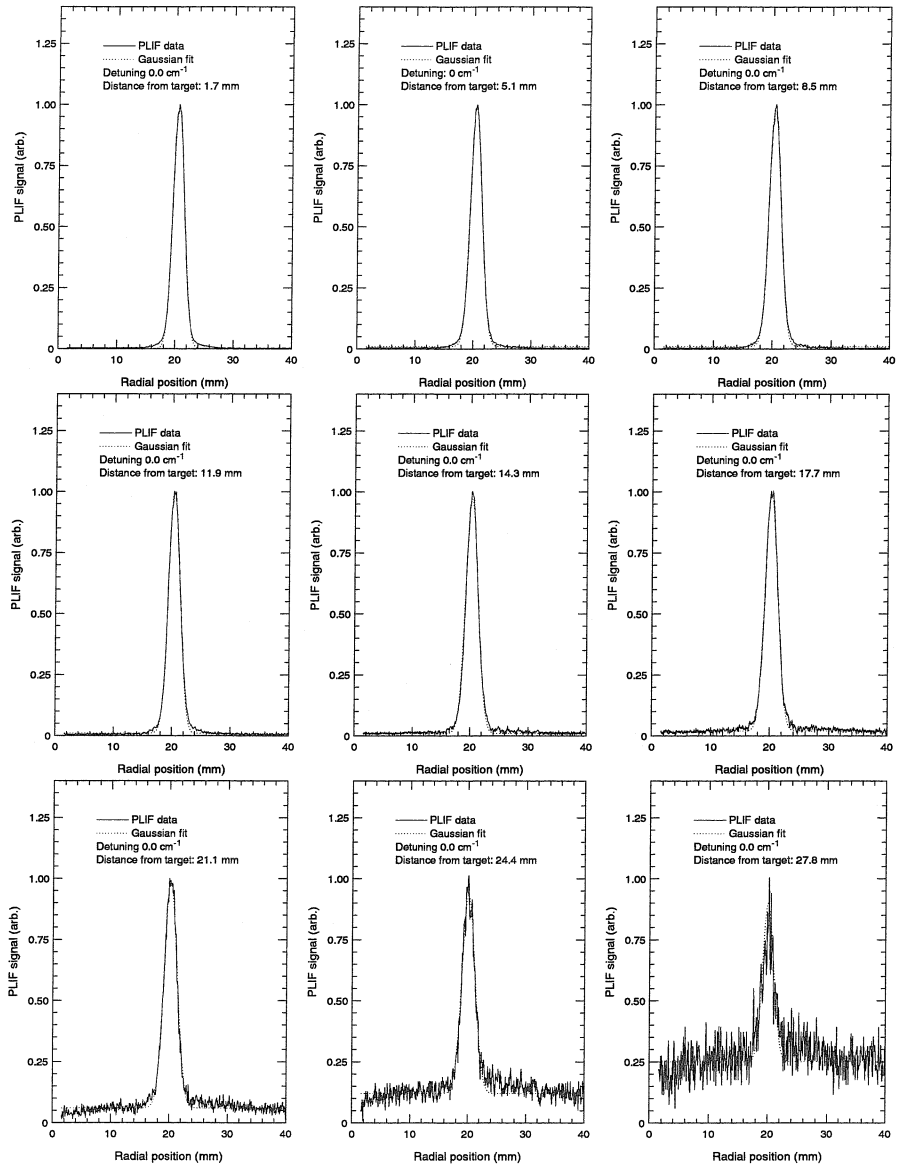

Figure 2.15: Cross sections of the PLIF streak acquired using 0 cm^{-1} detuning for several distances from the target, spaced by 3.4 $\pm$ 0.8 mm. Lineshapes appear Gaussian with no significant variation in width.

This problem can be resolved, however, by considering the effect of the non-zero width of the target spot on the PLIF signal. The fact that a PLA plume does not in fact originate instantaneously from a dimensionless point complicates the connection between PLIF streak width and laser intensity. The spatial width of the spot from

which the plume is created, and the duration of the excimer pulse used to create the plume require the distribution function $f_1^0(\vec{x},\nu)$, describing the particles at any point in space, to be modified to read

$$f_1^0(\vec{x},\nu) = N_1^0(\vec{x}) \int_0^\infty \int_{-\infty}^\infty \delta\left(\nu - \nu_{21}(1 + \frac{r - r_0}{c(t - t_0)})\right) \mathcal{T}(t_0)\mathcal{R}(r_0) dr_0 dt_0, \qquad (2.19)$$

where $\mathcal{T}(t_0)\mathcal{R}(r_0)dt_0 dr_0$ describes the fraction of plume particles originating from a distance off axis between r_0 and $r_0 + dr_0$ during the time interval t_0 to $t_0 + dt_0$. The PLIF signal then becomes

$$\mathcal{S}(\vec{x}) \propto N_1^0(\vec{x}) \int_0^\infty \int_{-\infty}^\infty P\left(\nu_{21}(1 + \frac{r - r_0}{c(t - t_0)})\right) \mathcal{T}(t_0)\mathcal{R}(r_0) dr_0 dt_0. \qquad (2.20)$$

In these experiments, it can be shown that the characteristic width of the function $\mathcal{T}(t_0)$ is negligible, resulting in spatial widening of $\mathcal{S}(\vec{x})$ by less than a few percent. The width of the function $\mathcal{R}(r_0)$, however, cannot be ignored. Letting $\mathcal{T}(t_0) \to \delta(t_0)$, equation 2.20 becomes

$$\mathcal{S}(\vec{x}) \propto N_1^0(\vec{x}) \int_{-\infty}^\infty P\left(\nu_{21}(1 + \frac{r - r_0}{ct})\right) \mathcal{R}(r_0) dr_0. \qquad (2.21)$$

If $\mathcal{R}(r_0)$ is also sufficiently narrow, then the limit $\mathcal{R}(r_0) \to \delta(r_0)$ applies, and equation 2.21 reduces to equation 2.15 as it must. In the opposite limit, however, where the half-width of the target spot $\delta_\mathcal{R}$ is large, equation 2.21 becomes

$$\mathcal{S}(\vec{x}) \propto N_1^0(\vec{x}) \mathcal{R}(r - ct\frac{\Delta}{\nu_{21}}). \qquad (2.22)$$

This equation suggests a PLIF image streak centered at $r = ct\Delta/\nu_{21}$ consistent with equation 2.16, but with a width $\delta_\mathcal{R}$, assuming as before that the density is nearly constant over that region. Data acquired in this limit would impair any effort to use the width of a PLIF image streak to ascertain whether the laser intensity used to obtain it were nonlinear and if so, provide a quantitative estimate of its magnitude. The measured PLIF streak widths in this case could only serve to determine an upper

bound on the laser intensity.

Depicted to the left in Figure 2.16 is the dependence of PLIF streak linewidth on laser intensity, for laser spot widths ranging from 0.5 - 2.0 mm, assuming the lineshape function $\mathcal{R}(\vec{x})$ is Gaussian as the measured PLIF streak profiles suggest. PLIF images with a width near 2.3 mm, weakly dependent on laser intensity, are consistent with this modified model over a narrow range of ablation spot widths and laser intensities.

It is possible the average laser intensity used to acquire the data in Figure 2.9 is in fact linear, i.e. < 1 kW/cm^2, and that the ablation spot has a FWHM near 1.6 mm. This is entirely consistent with the observed data, athough it implies that laser intensity is two orders of magnitude lower than the rough estimate obtained by measuring the laser intensity and the dimensions of the sheet directly. It is also possible, however, that the laser intensity in weakly nonlinear and that dependence of the PLIF streak width on laser intensity is simply hidden by the experimental uncertainty inherent in the PLIF streak width measurements. Shown to the right in Figure 2.16 are linewidth profiles calculated by assuming several average laser intensities and spot widths which result in profiles that pass through the measured PLIF streak width data taken from the image in Figure 2.9 at several magnitudes of detuning. This figure shows clearly that the calculated profiles for average intensities less than about 5 kW/cm^2 pass roughly within the error bars of the measured PLIF streak widths, and lie well outside for average laser intensities greater than this limit.

2.5.3 Correction of the PLIF image in Figure 2.9 for laser sheet intensity variation

Previously given, in equation 2.21, was the solution for the PLIF signal $\mathcal{S}(\vec{x})$ resulting when a relatively narrow linewidth laser pumps atoms residing within a cross sectional sheet passing through the axis of symmetry of a collisionless PLA plume generated nearly instantaneously from a Gaussian ablation spot. If several images acquired with the pump laser's spectral peak detuned by different amounts from the

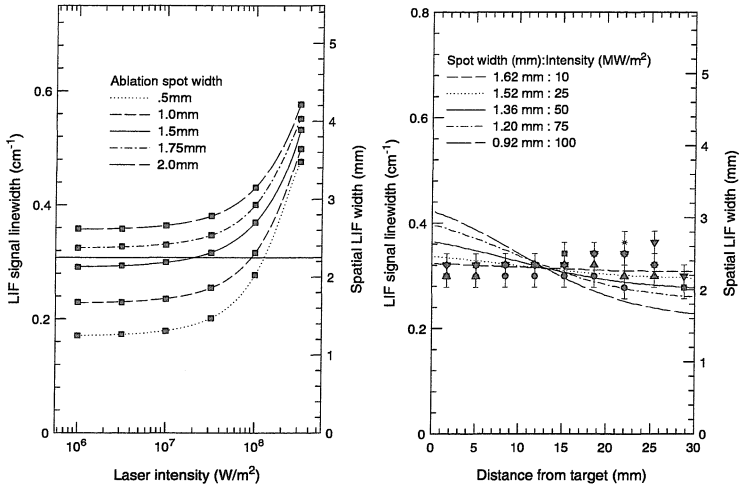

Figure 2.16: (Left) LIF signal linewidth vs. laser intensity for ablation spot widths ranging from 0.5 - 2.0 mm, assuming a pump laser FWHM of 0.14 cm^{-1}. A linewidth near 2.3 mm, independent of laser intensity, is only possible for laser intensities < 5 kW/cm^2. (Right) Calculated linewidth profiles for intensities between 1-10 kW/cm^2. The variation of PLIF streak width with distance from the target becomes measurable within the experimental error for average intensities exceeding 5 kW/cm^2.

atoms' stationary resonance frequency are superimposed, the resulting signal can be described by

$$\sum_j \mathcal{S}_j(\vec{x}) \propto N_1^0(\vec{x}) \sum_j \int_{-\infty}^{\infty} P\left(\nu_{21}(1+\frac{r-r_0}{ct}), \Delta_j\right) \mathcal{R}(r_0) dr_0, \tag{2.23}$$

where the function $P(\nu, \Delta)$ is defined in equation 2.12. In this work, the spectral peaks of the pump laser are spaced around the stationary resonance frequency of the pump transition by a fixed value $\delta\nu_t$, so that the detuning can be described by $\Delta_j = j\delta\nu_t$ with $-N \leq j \leq N$, where N is some positive integer. The spatial density of the ground state atoms prior to the application of the pump laser pulse $N_1^0(\vec{x})$ is then given by

$$N_1^0(\vec{x}) \propto \sum_{j=-N}^{j=N} \mathcal{S}_j(\vec{x}) \frac{1}{\mathcal{F}(\vec{x})} \tag{2.24}$$

with the function $\mathcal{F}(\vec{x})$ defined by

$$\mathcal{F}(\vec{x}) = \int_{-\infty}^{\infty} \sum_{j=-N}^{j=N} P\left(\nu_{21}(1+\frac{r-r_0}{ct}), j\delta\nu_t\right) \mathcal{R}(r_0) dr_0. \tag{2.25}$$

Normalizing the superposition of PLIF images to the function $\mathcal{F}(\vec{x})$ therefore produces an image which depicts the relative density of the ground state atoms immediately prior to the pump laser pulse.

In an effort to simplify this normalization function, the radial dependence of the sum appearing in the integral in equation 2.25 can be examined more closely. Shown to the left in Figure 2.5.3 is the sum for $N = 7$, as used in these experiments, for laser intensities ranging from 1-10 kW/cm^2. Although there appears to be noticeable ripple in the function for all laser intensities, the amplitude of the spatial oscillation is only a few percent of the average value, which is nearly flat over the spatial region where PLIF signal exists. Neglecting the ripple, which is eliminated by the convolution integral with $\mathcal{R}(r)$ anyway, eliminates any radial dependence in the normalization function, allowing it to be expressed as

$$\mathcal{F}(z) = \langle \sum_{j=-N}^{j=N} P\left(\nu_{21}(1 + \frac{r - r_0}{ct}), j\delta\nu_t\right)\rangle_r, \tag{2.26}$$

where $\langle\rangle_r$ denotes a spatial average over the region where PLIF signal exists (e.g. $r \leq$ 1 cm for a 1 μs old plume). A plot of $\mathcal{F}(z)$ vs laser intensity is given to the right in Figure 2.5.3.

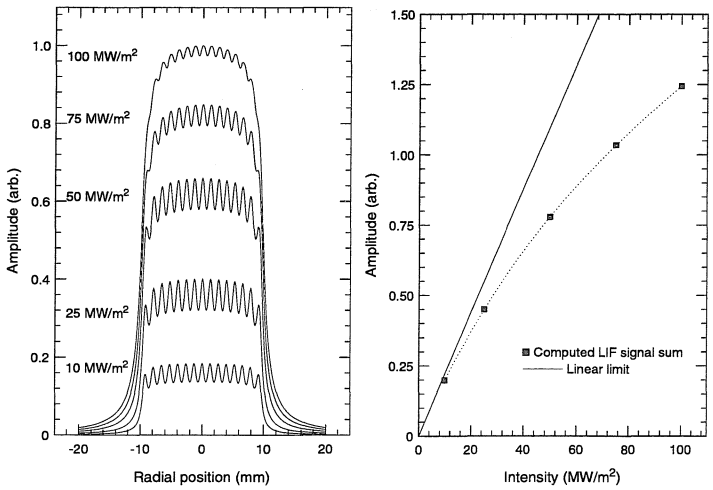

Figure 2.17: (Left) The sum appearing in equation 2.25 for laser intensities ranging from 1-10 kW/cm^2. The average amplitude in the central region is roughly flat over a width of nearly 2.0 cm. (Right) Amplitude of the central region average as a function of laser intensity.

Shown at the top in Figure 2.18 is a corrected image obtained from the image in Figure 2.9, assuming a linear laser intensity, i.e. < 1 kW/cm^2. Beneath is shown the image resulting when the upper bound value of average laser intensity of 5 kW/cm^2 is assumed. The image quality far from the target in either case is poor, resulting from the combination of low laser intensity and low PLIF signal in that region. The correction, being greatest where laser intensity is lowest, appears to be amplifying the noise. The portion of the image showing the plume, however, is believed to be a faithful representation of the density of Si, without velocity bias.

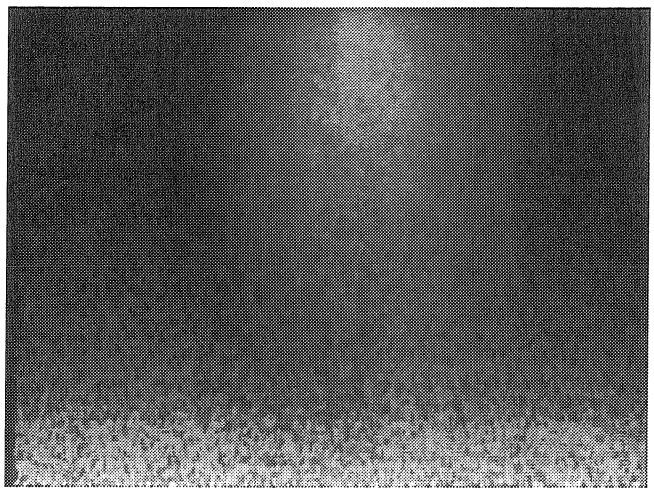

1 kW/cm^2

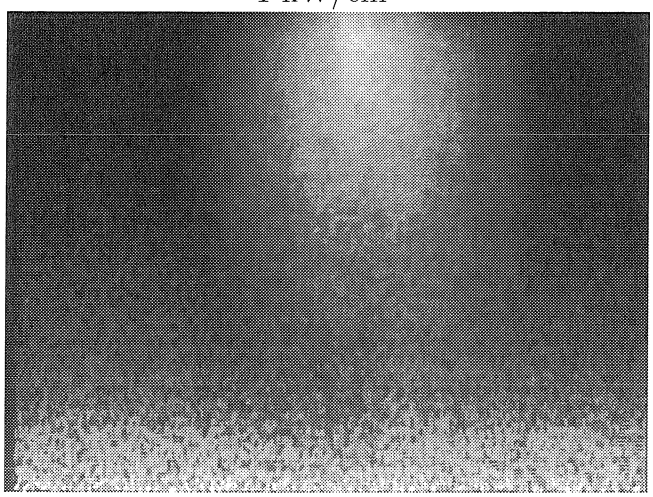

5 kW/cm^2

Figure 2.18: Corrected PLIF image assuming linear (top) and nonlinear (bottom) average pump laser intensity.

2.6 PLIF data acquired from a typical Si PLA plume using an improved laser sheet

In an effort to minimize the amplification of noise that occurs when the PLIF signal from regions of low density is corrected for weak laser intensity, a set of images similar to those seen in Figure 2.9 are acquired using a more intense laser sheet with less variation along its width, placing the highest intensity region where the lowest PLIF signal is anticipated. The data shown in Figure 2.19 correspond, as before, to pump laser detunings of +1.08 cm^{-1}, +0.72 cm^{-1}, +0.36 cm^{-1}, 0 cm^{-1}, -0.36 cm^{-1}, and -0.72 cm^{-1}.

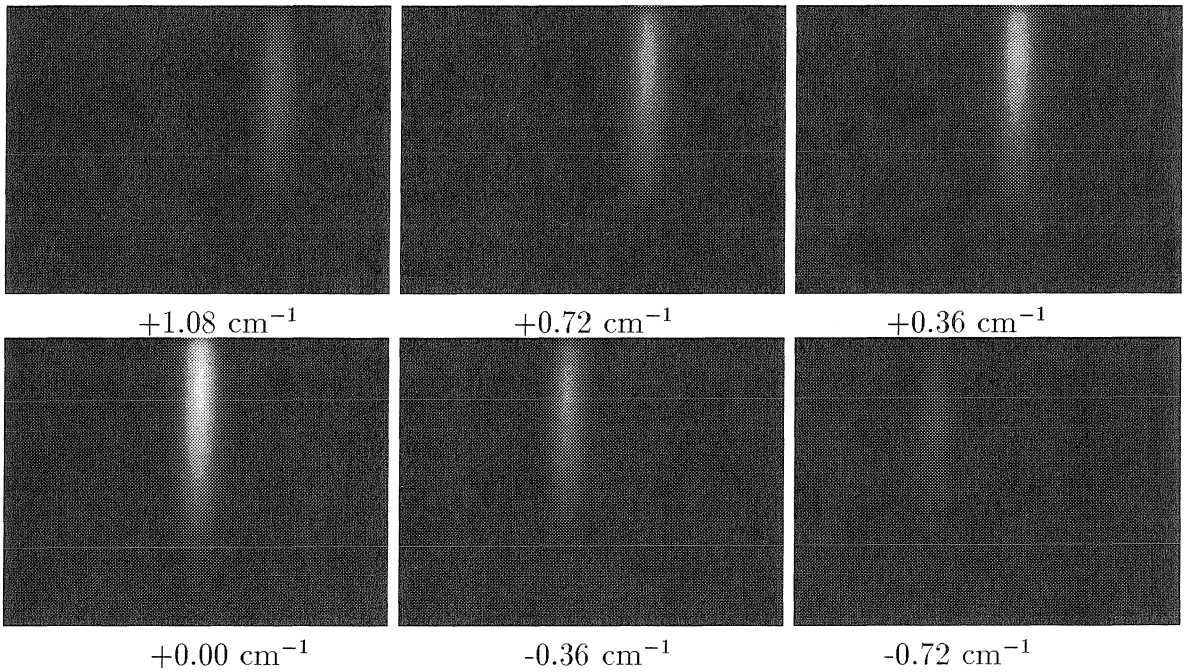

Figure 2.19: 4.0 cm x 3.0 cm PLIF images of expanding Si into vacuum, similar to those in Figure 2.9 but with an improved laser sheet.

Figure 2.20 shows the superposition of 15 individual images, similar to that appearing in Figure 2.10. Although the differences between these two uncorrected images are subtle, a close inspection reveals that the image in Figure 2.20 is more elongated. Since the images describe the same plume, this difference aids in making the laser sheet intensity correction and verifying that the correction is reasonable.

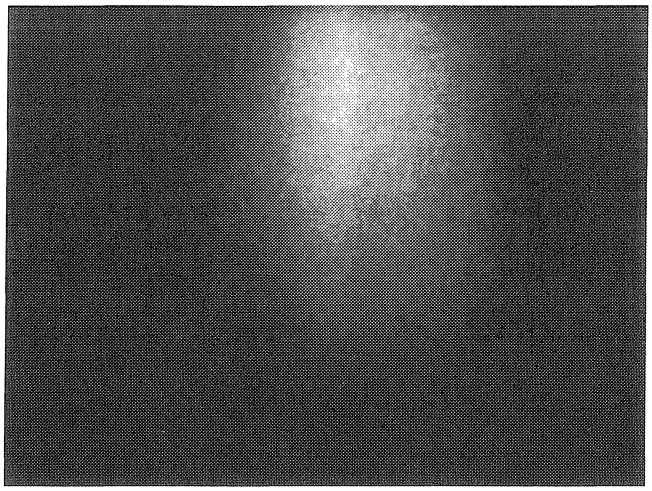

Figure 2.20: 4.0 cm x 3.0 cm PLIF image generated by superimposing 15 individual images, including those in Figure 2.19, each spaced by 0.18 cm^{-1} of detuning.

Shown in Figure 2.21 are cross sections of the PLIF streak along the axis of the plume (0 cm^{-1} detuning) for several positions spaced by 3.4 $\pm$ 0.8 mm away from from the target. The data for each cross section fits well to a Gaussian profile as before, however, a significant increase in width is observable as the distance from the target increases. In fact, the width about 2.8 mm near the target increases by nearly 30% to about 3.6 mm a distance of 3.0 cm away. This apparent increase in width is consistent with the laser intensity profile appearing in the lower-right corner of Figure 2.21 if the laser intensity is nonlinear. The average laser intensity used to acquire the images in Figure 2.19 can then be estimated by comparing streak width data with computed widths assuming various spot widths, laser intensities, and the laser sheet profile shown in Figure 2.21. The result is given in Figure 2.22. A reasonable fit is obtained by assuming a spot width of 1.9 mm and an average laser intensity near 10 kW/cm^2.

An alternative method can also be employed to estimate the laser intensity used to acquire the PLIF images seen in Figure 2.19, and verify the value of 10 kW/cm^2 suggested by the variation in line width and the known laser intensity profile. It can be shown that for a plume which expands collisionlessly, the normalized density profile along any two axial contours should be identical. Any variation between two normalized PLIF signal profiles along two different contours is therefore caused by

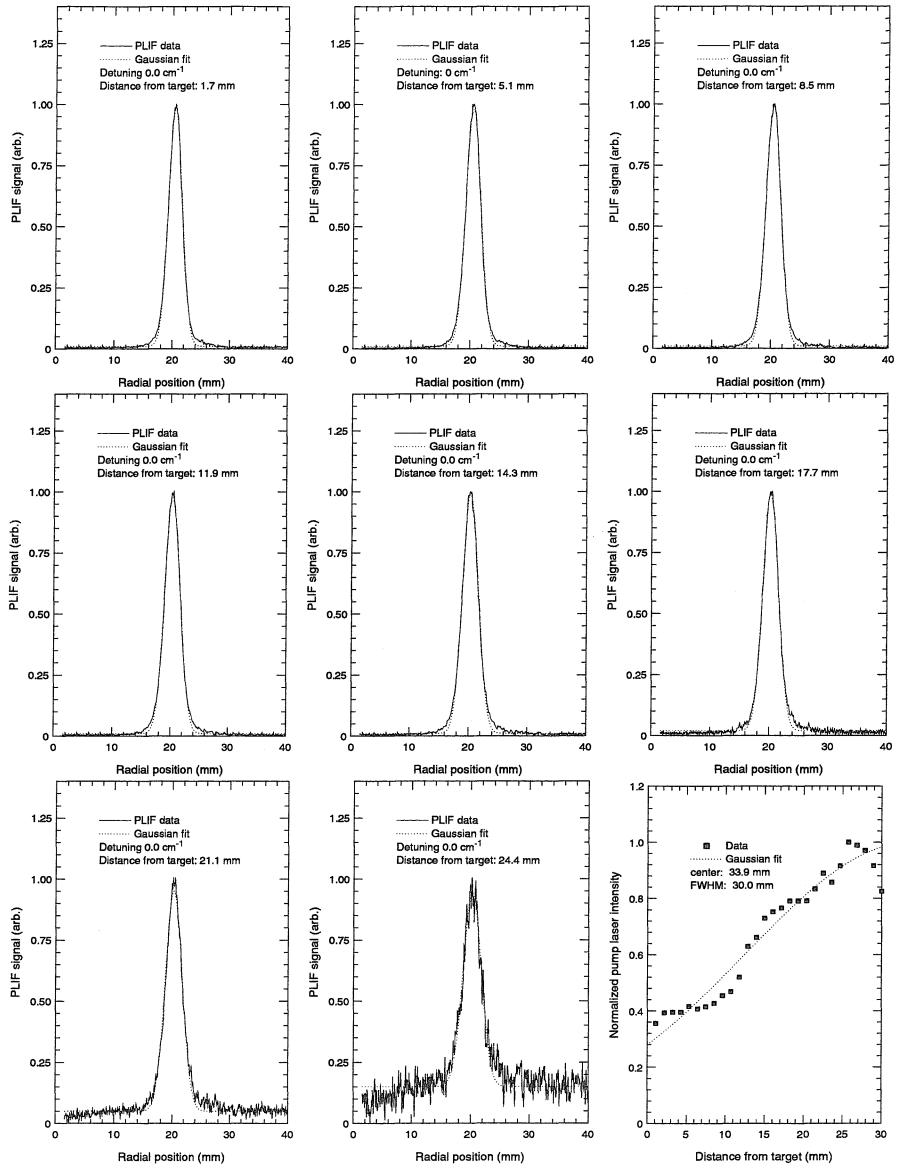

Figure 2.21: Cross sections of the PLIF streak acquired using 0 cm^{-1} detuning for several distances from the target, spaced by 3.4 $\pm$ 0.8 mm. Lineshapes appear Gaussian with a slight increase in width as the distance from the target increases. Laser intensity profile used to acquire the data is shown in the lower-right corner.

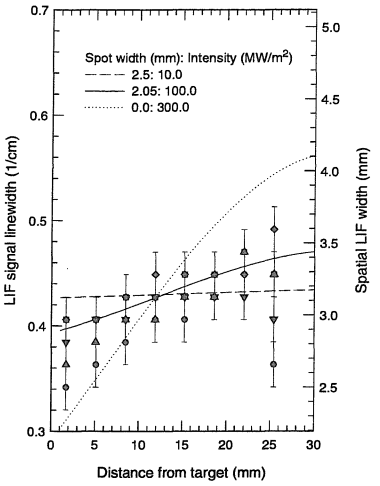

Figure 2.22: Calculated linewidth profiles for intensities between 1 and 30 kW/cm^2. Different symbols correspond to data taken at different magnitudes of detuning. The variation of PLIF streak width with distance from the target is consistent with a laser spot width of 1.9 mm and an average laser intensity near 10 kW/cm^2.

differences in the resonant laser intensity used to illuminate the atoms along the two contours. Shown in Figure 2.23 are two PLIF streaks whose center positions (ridgelines), defined by

$$r = ct\frac{\Delta}{\nu_{21}}, \tag{2.27}$$

are marked as white lines. As previously discussed, Δ is the magnitude of laser detuning and ν_{21} is the resonant frequency of the stationary Si atoms. Although the positions of these streaks differ by about 5.2 mm (0.72 cm^{-1} detuning), the axial profiles along the two contours appear nearly identical. This is expected since the ridgeline of each PLIF streak corresponds to the pump laser's spectral peak, so the laser intensity profiles along the two PLIF streak ridgelines are identical even though the plume density certainly is not. This data further validates the the collisionless expansion model.

At the top of Figure 2.24 two contours taken from the same PLIF streak, chosen to be the one acquired at 0 cm^{-1} detuning, are shown. One contour is taken along the ridgeline, but the other is taken along the edge of the PLIF streak, about 2.1 mm from the ridge. Such a distance corresponds to a detuning of about 0.28 cm^{-1} from the peak in the pump laser spectral lineshape. The normalized PLIF signal profiles along

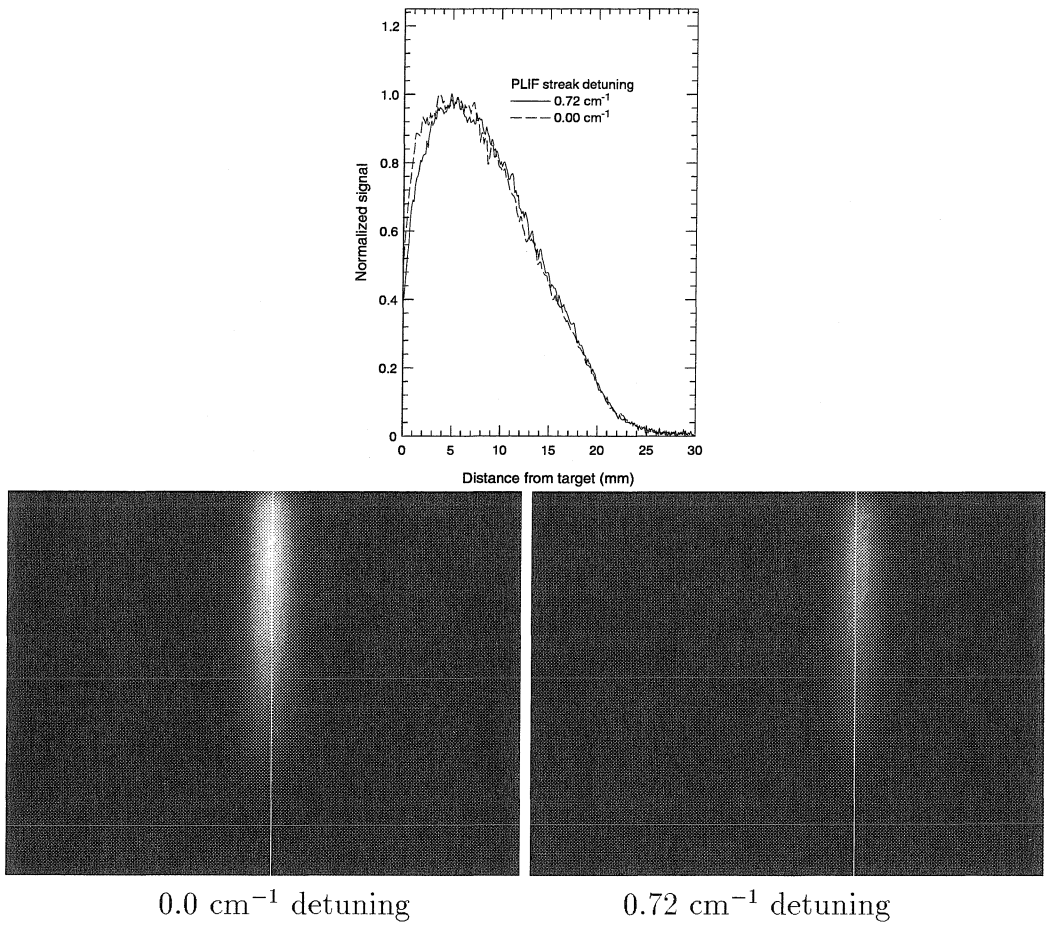

Figure 2.23: PLIF streaks acquired using 0.00 cm^{-1} and 0.72 cm^{-1} detuning at 1.0 μs time delay with ridgeline contours shown as white lines. Normalized density profiles along these contours appear nearly identical, validating the collisionless expansion model.

the two contours differ significantly even though the data in Figure 2.23 suggests that the normalized density does not. The difference can be explained by assuming the resonant laser intensity along the ridgeline is nonlinear. Since the pump laser has a FWHM of only 0.14 cm^{-1}, the laser intensity illuminating the contour taken along the PLIF streak's edge is less than 6% of the intensity illuminating the ridgeline. The resonant intensity illuminating the edge is therefore linear, even if the average resonant intensity illuminating the ridgeline is as high as 10 kW/cm^2. The Si density profile can therefore be inferred from the profile taken along the PLIF streak's edge by normalizing it to the laser intensity profile given in Figure 2.21. The result is shown in Figure 2.24, and compared with the density profile deduced by correcting the PLIF streak profile taken along the ridgeline for nonlinear laser intensity whose average value along the contour is 10 kW/cm^2. These two profiles are much more similar than the two signal profiles, suggesting that the rate equation model used to correct for nonlinear laser intensity is reasonable, that the analysis is self-consistent, and that the Si density can be deduced despite the use of nonlinear pump laser intensity.

The image superposition shown in Figure 2.20 can be corrected for the nonlinear laser intensity used to acquire the data using the method discussed in the previous section. The resulting image, shown in Figure 2.25, is significantly better than the ones depicted earlier in Figure 2.18 due to the improvements in the laser sheet. On close inspection of the image, it appears to consist of two distinct components, one rounded and the other more like a forward-directed jet. This observation has also been made elsewhere [6], and the jet is attributed to a secondary ejection process (e.g. ion sputtering), while the rounded component is attributed to thermal avaporation. The cause of this phenomenon may be nonuniformity in the excimer laser intensity over the width of the ablation spot.

2.7 Summary

The image presented in Figure 2.18 is believed to be the first reported image depicting ground-state, neutral Si density within a narrow cross-section of an ablation

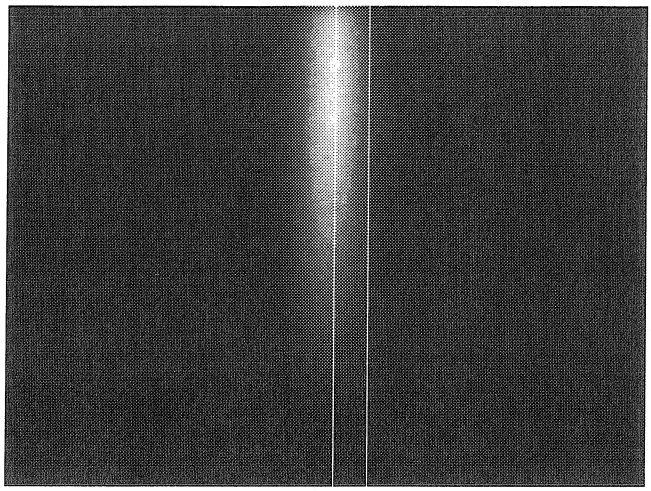

Figure 2.24: (Top) PLIF streak with ridgeline and edge contours shown as white lines. (Bottom) Normalized PLIF signal profiles taken along ridgeline and edge contours. An Si density profiles is obtained for each by correcting the PLIF signal for laser intensity.

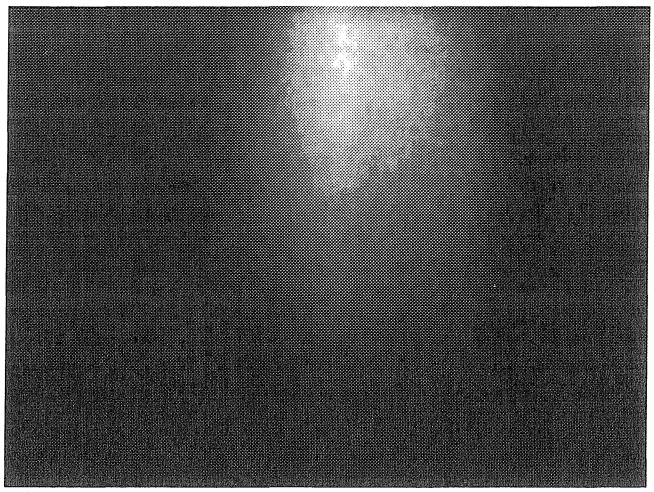

Figure 2.25: Image generated by correcting data seen in Figure 2.20 for nonlinear laser intensity. The image can be interpreted as the density of ground-state, neutral Si along a cross section of a PLA plume, 1.0 μs after its creation by a KrF laser.

plume, generated using a KrF excimer laser, as it expands into vacuum. The image is produced by superimposing several individual images, acquired using a 0.14 cm^{-1} FWHM bandwidth laser detuned from the stationary resonant frequency in increments of 0.18 cm^{-1}, and correcting for nonlinear laser intensity. For the purpose of correcting the image, a set of population rate equations describing a three-level model are solved, using parameters appropriate for the 243.877 nm $^3P\ 3p^2 \leftarrow {}^1P^0\ 4s$ pump transition and the 288.158 nm ${}^1P^0\ 4s \rightarrow {}^1D\ 3p^2$ fluorescence transition. Values for laser intensity, on which the equations strongly depend, are estimated using information contained in the acquired PLIF data, e.g. the spatial width of the signal and its variation with distance from the target, and the difference between normalized signal along ridgeline and edge contours of a single PLIF streak. This analysis is based on evidence that the plume expands collisionlessly from the ablation spot.

Chapter 3 The influence of a background gas and substrate on a PLA plume

3.1 Introduction

In this chapter the influence of a background gas and substrate on an Si plume are studied using PLIF imaging. A typical Si plume expanding into vacuum (10^{-5} Torr) is first studied by examining normalized density profiles taken along contours of constant radius and along contours of constant axial position. Similarity among several such profiles after a delay of 1.0 μs suggests that the plume expands collisionlessly from the target.

Next, normalized density profiles along similar contours are taken from an Si plume expanding into 10 mTorr of argon, a typical pressure for PLD [13, 16]. As with the case of vacuum, profiles taken from this plume suggest that the collisionless expansion model remains valid, although the background gas has the apparent effect of slowing down the atoms at the leading edge of the plume. Although these two observations may seem contradictory, they are self-consistent if the interaction of the plume with the background gas occurs primarily during the earliest phase of expansion, when the plume is within a few millimeters of the target, and the subsequent expansion is nearly collisionless. A second consequence of the plume's interaction with background gas appears to be a significant reduction in the relative Si density near the substrate for $0 < t < 3.0$ μs. These observations suggest that the time-integrated flux of Si onto the substrate might be reduced by the introduction of a background gas, and that the energy of the Si atoms incident onto the substrate may also be reduced. The pressure dependence of these quantities might be valuable in estimating rates of film depostion.

In an effort to further quantify trends in Si density profiles related to background

gas pressure, a series of PLIF images are acquired from an Si plume expanding into argon at pressures between 0 and 150 mTorr, looking at time delays between 1.0 and 5.0 μs. These data confirm the monotonic drop in Si density near the substrate as a function of pressure for times less than about 3.0 μs, but reveal an interesting increase in Si density near the substrate at longer delay times. This evidence of enhanced density above the substrate is believed to be the first reported. These data are later compared with simulation results to estimate the sticking probability for Si onto an unheated Si(100) substrate.

Finally, the occurrence of gas-phase chemistry as an Si plume expands into air at a pressure near 1.0 Torr is demonstrated. SiO, possibly resulting from the reaction $Si + O_2 \rightarrow SiO + O$, is detected by pumping the $Q_1(35) + R_1(42)$ transitions in the $A^1\Pi \leftarrow X^1\Sigma^+(0,0)$ system of SiO at 235.25 nm. Fluorescence into a 260 $\pm$ 10 nm bandwidth is gathered using an interference filter, and a 1.0 mm thick piece of Schott UG1 glass to help reject scattered excimer light at 248 nm. The gathered signal includes most of the (0,4) band as well as portions of the (0,3) and (0,5) bands. After subtracting a significant background resulting from spontaneous emission within this bandwidth, and correcting for variations in the laser sheet intensity, images depicting relative SiO density are obtained, suggesting that a ring of SiO forms along the contact front between the plume and background gas. Unlike the PLIF imaging done previously on Si expanding into vacuum and Ar at pressures up to 150 mTorr, the symmetry of the PLIF signal about the plume's axis is not affected by pump laser detuning, suggesting that the flow velocity of the SiO is sufficiently small that Doppler shifts may be ignored. The images presented here are believed to be the first reported PLIF images of any intermediate species produced by gas-phase chemistry during PLA.

3.2 Time evolution of a typical ablation plume expanding into vacuum

Shown in Figure 3.1 are time sequence images showing the density of ground-state, neutral Si density within a cross section of a typical PLA plume as it expands into vacuum. Time delays of 1.0 μs, 2.0 μs, 3.0 μs are presented. The images shown are corrected for nonlinear laser intensity using the method described in the previous chapter, and then processed using a median filter to smooth the noise. Although each image is normalized to its own maximum, the intensity of the fluorescence is actually much weaker as the time delay increases.

Normalized density profiles are a convenient way to help visualize a PLA plume, and provide a standard for comparing different plumes. In Figure 3.2 a schematic diagram of a plume is shown, sliced along contours of constant radius and along contours of constant axial position z. The upper row in Figure 3.3 shows the normalized density profiles taken from the plume in Figure 3.1 along contours of fixed radii at r = -2.8 mm, 1.0 mm, 4.9 mm, and 8.7 mm $\pm$ 1.9 mm at time delays of 1.0 μs, 2.0 μs, and 3.0 μs. These data are produced by averaging over 49 radial pixels (about 3.8 mm) to reduce noise. The lower row in this same figure depict the normalized density profiles of the same plume along contours of fixed axial position z = 1.5 mm, 7.5 mm, and 13.5 mm $\pm$ 1.5 mm for the same set of time delays. These data result after averaging over 24 axial pixels, about 3.0 mm.

Several significant observations can be made from these data. First, the axial density profiles suggest that Si atoms have axial velocities as great as 20 km/s (60 eV), with a much slower bulk velocity near 3 km/s (1-2 eV). The highest radial velocity is about 10 km/s (15 eV). The characteristic velocity v of a thermal system can be defined in terms of the system temperature using $v = (kT/k)^{1/2}$, thus if v = 3 km/s then $T \approx$ 61,000 K. This suggests that the plume originates from a very hot source.

Second, both the axial and radial profiles taken at 1.0 μs appear to be independent of the position of the contour. Since the plume has a characteristic dimension near 1.0

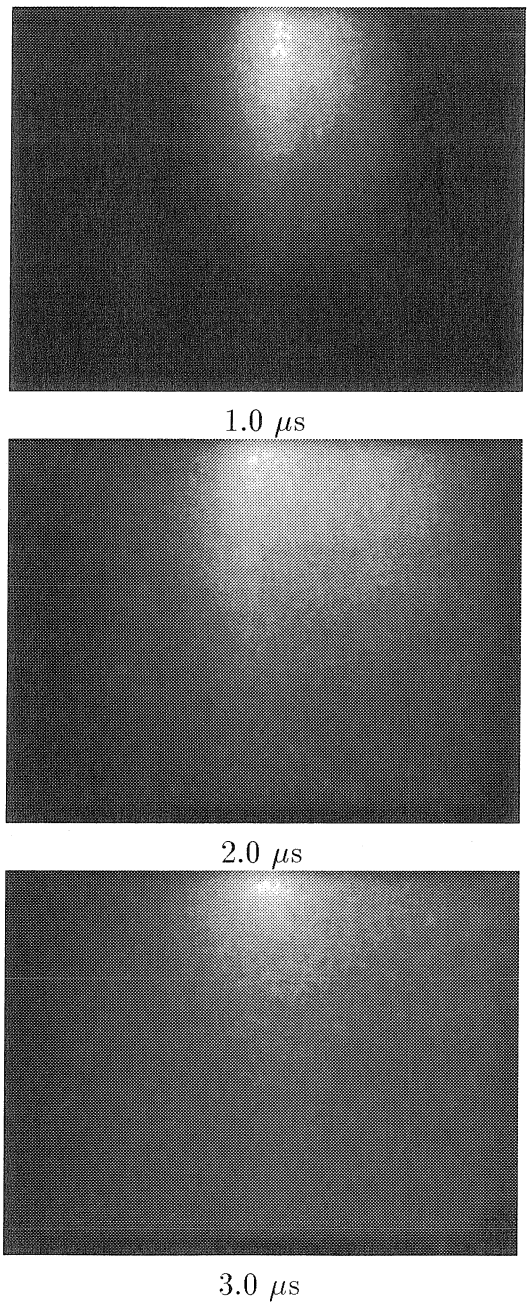

Figure 3.1: Time sequence images of ground-state, neutral Si density within a cross sectional sheet of a PLA plume expanding into vacuum.

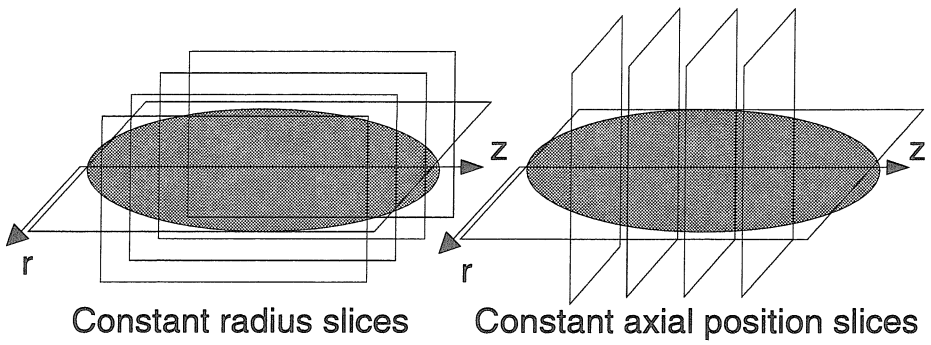

Figure 3.2: Schematic diagram showing how the PLIF sheet may be sliced to produce normalized density contours at fixed radius or axial position in cylindrical geometry.

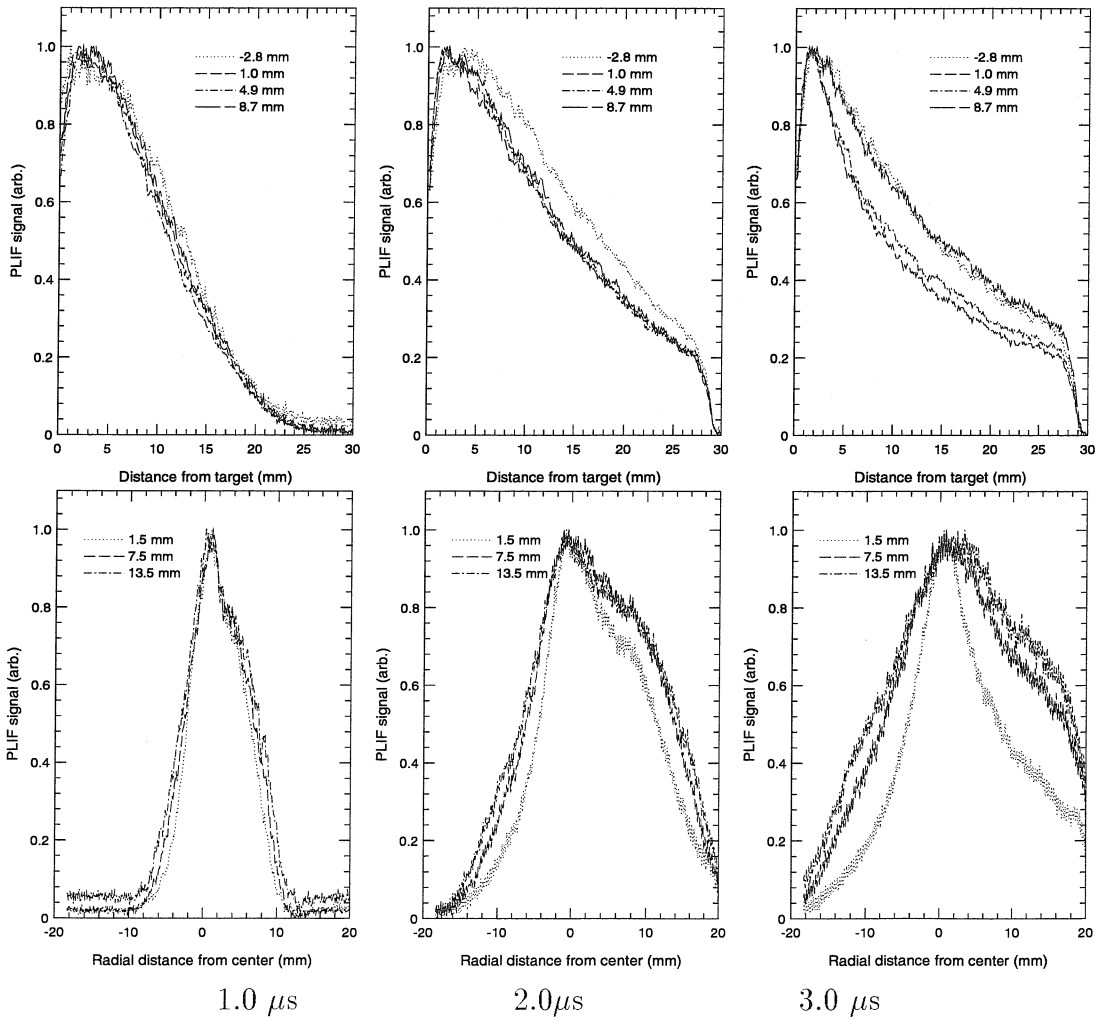

Figure 3.3: (Upper row) Normalized density profiles along contours of constant radii r = -2.8 mm, 1.0 mm, 4.9 mm, and 8.7 mm ± 1.9 mm. (Lower row) Normalized density profiles along contours of constant axial position z = 1.5 mm, 7.5 mm, 13.5 mm, and 18.5 mm ± 1.5 mm for the same set of time delays.

cm after 1.0 μs, the contours selected in Figure 3.3 sample the full width and length of the plume. The independence of profiles on position therefore strongly suggest that the plume expands collisionlessly from the ablation spot after being generated during a brief period satisfying $t_p \ll 1.0$ μs. Curiously, however, the contours taken at later times differ significantly. Although this observation might be used to refute the collisionless expansion model, it only demonstrates the presence of a very small, slow, collisional component of the plume that lingers near the target. This component may result from either an interaction of a few back-scattered plume atoms with the boundary, or from a small amount of effusion from the target after the laser pulse. Because these atoms are slow and near the origin, the rate of change in volume they occupy is much smaller than the rate of change in volume occupied by the faster atoms further from the target. Since PLIF signal is proportional to density, the contribution from the slowest atoms begins to dominate at later times even if these atoms constitute only a very small fraction of the total number of atoms in the plume.

Finally, the sudden drop in signal intensity near $z = 2.8$ cm is due to the presence of a substrate, visible at the bottom of the later images in Figure 3.1. Although no comparative data is presented, PLIF images were acquired both with and without the substrate present. The normalized density profiles in each case appear nearly identical in the region between target and substrate for $t < 3.0$ μs. Data is presented later which indicates a enhancement of density near the substrate after 3.0 μs.

3.3 Time evolution of a typical ablation plume expanding into 10 mTorr of argon

Shown in Figure 3.4 are time sequence images showing the density of ground-state, neutral Si within a cross section of a typical PLA plume as it expands into a background gas of argon at 10 mTorr. Time delays of 1.0 μs, 2.0 μs, 3.0 μs are presented as in the previous section. Normalized density profiles from this plume are provided in Figure 3.5.

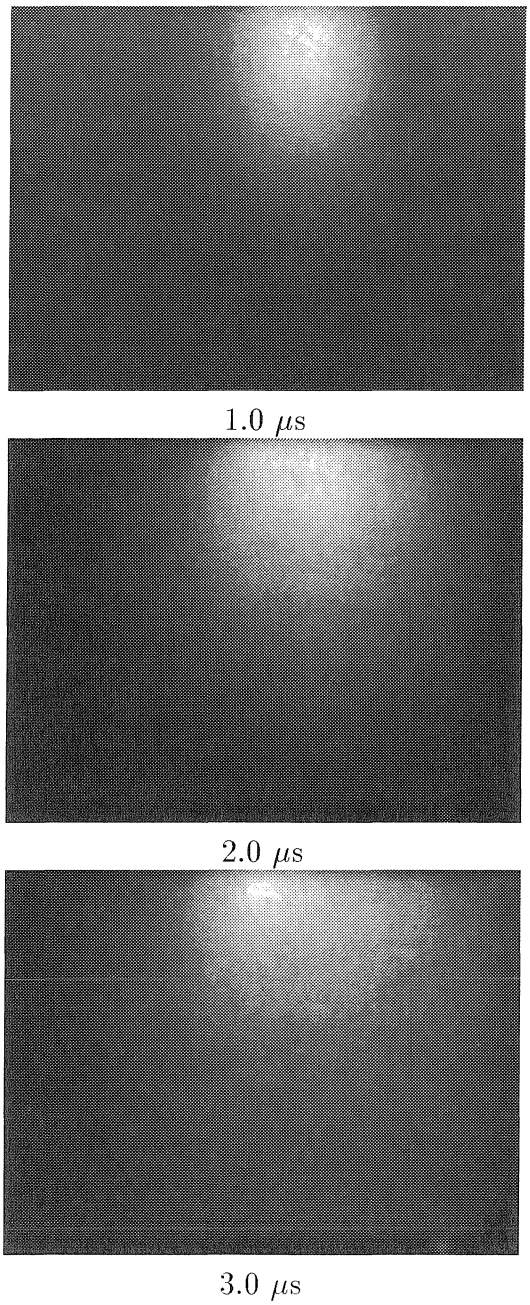

Figure 3.4: Time sequence images of ground-state, neutral Si density within a cross sectional sheet of a PLA plume as it expands into 10 mTorr of argon.

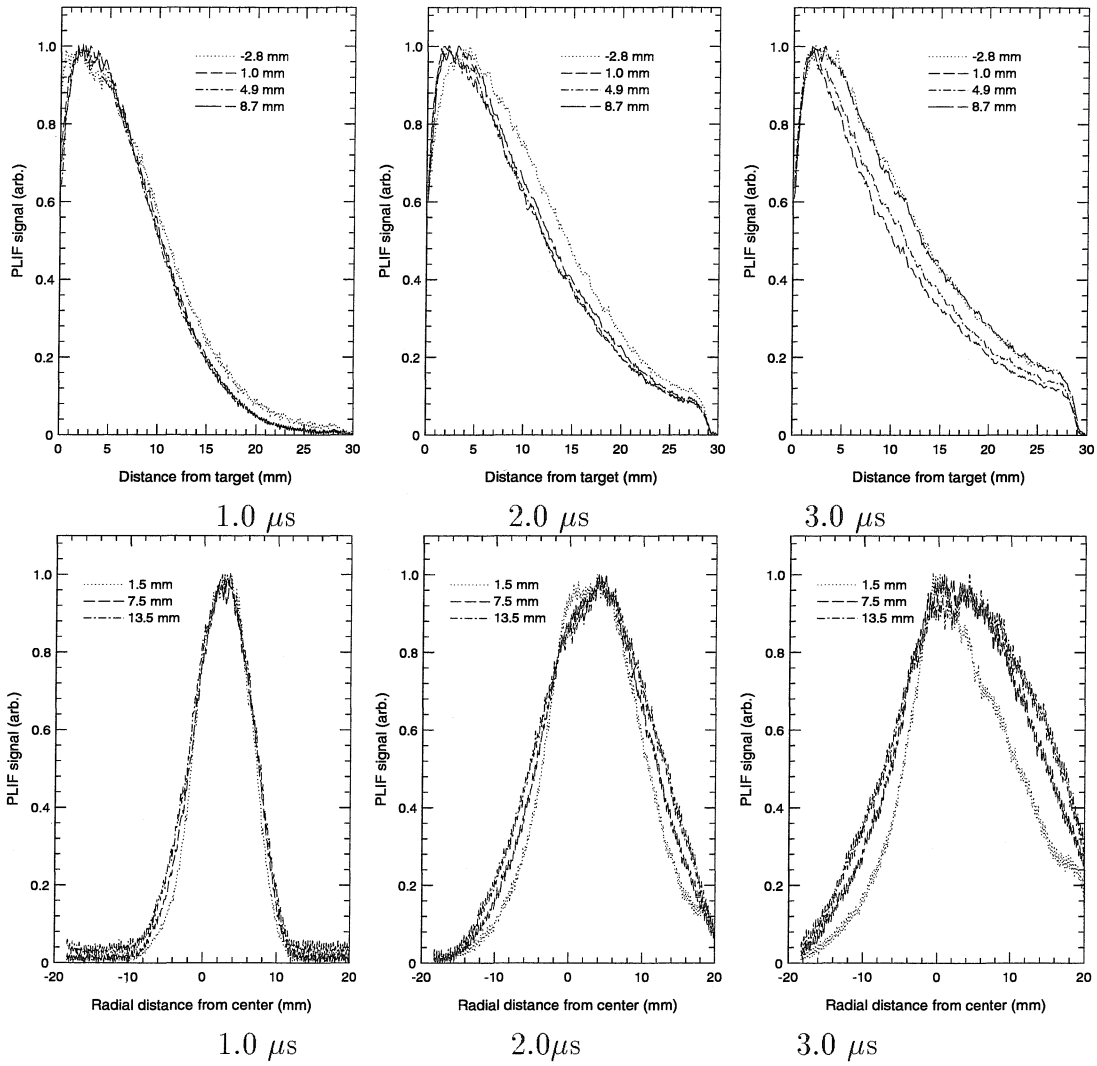

Figure 3.5: (top row) Normalized density profiles along contours of constant radii r = -2.8 mm, 1.0 mm, 4.9 mm, and 8.7 mm ± 1.9 mm. (bottom row) Normalized density profiles along contours of constant axial position z = 1.5 mm, 7.5 mm, and 13.5 mm ± 1.5 mm.

Curiously, the apparent independence of profiles taken at 1.0 μs on contour position suggests that the plume expands collisionlessly, even in the presence of a background gas. Although it might be tempting to conclude that the background gas has no effect on the expanding plume, this conclusion can be refuted by comparing the normalized density profiles taken along the axis (r = 0) of the two plumes seen in Figures 3.1 and 3.4 as is done in Figure 3.6. The background gas appears to affect the

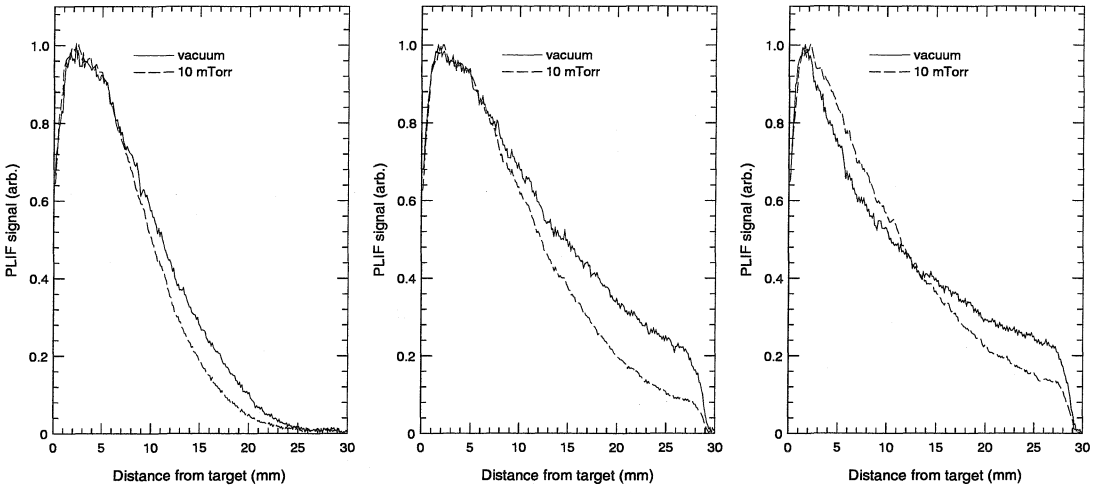

Figure 3.6: Normalized density along the axis of two PLA plumes, one expanding into vacuum and the other into 10 mTorr of argon.

fast atoms on the leading edge of the plume without significantly affecting the slow atoms nearer the target. Since the similarity among the normalized density profiles appearing in Figure 3.5 at t = 1.0 μs suggest collisionless expansion, the interaction of the plume with the background gas must only be significant near the vicinity of the ablation spot. This is plausible if the expanding silicon compresses the background gas into a high density layer along the contact front, and the peak density in this layer occurs early and diminishes rapidly in time. In this case only the atoms along the plume's leading edge are influenced by the presence of the gas, and only while the gas density along the contact front is large.

A second apparent consequence of the presence of the background gas, important perhaps for PLD, is that by 2.0 μs the density of Si near the substrate is about 60% lower, and about 40% lower after 3.0 μs. To help visualize the difference between the

vacuum and 10 mTorr conditions, Figure 3.7 shows enhanced images of Si density near the substrate after 2.0 μs. Each image is normalized after cropping the PLIF signal at 31.4% of maximum. The expansion into vacuum results in more Si near the substrate at all radial positions and not just on axis, suggesting perhaps that over the lifetime of the plume, the total flux of Si onto the substrate is reduced when the plume expands into a background gas. A reduction in particle flux, and a reduction in kinetic energy of the plume atoms, might be important for both the rate of deposition and the quality of films deposited by PLD.

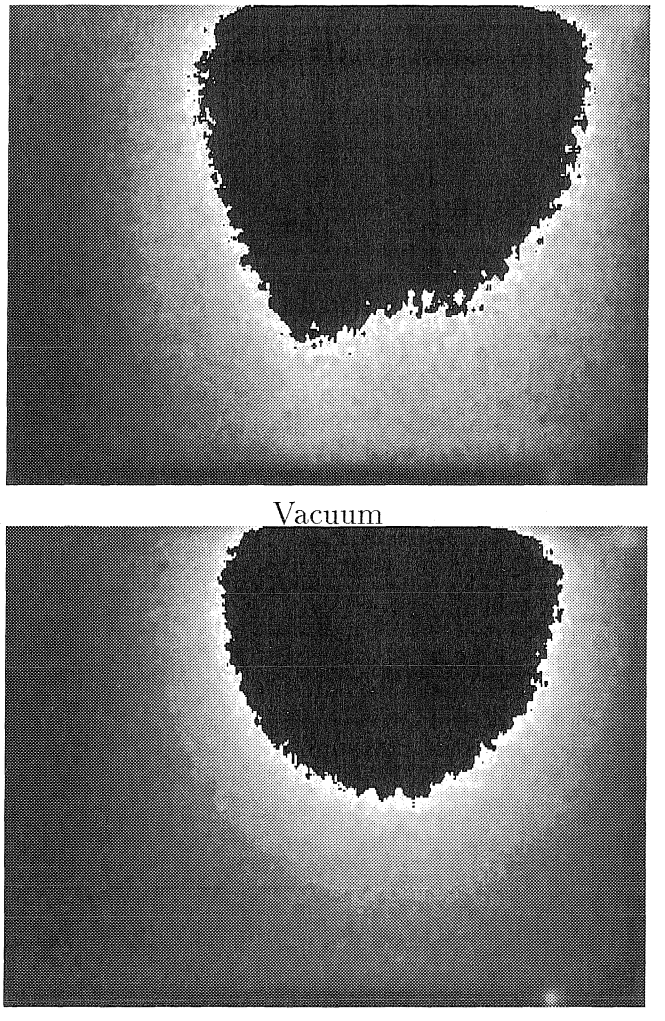

Figure 3.7: Images of an Si plume expanding into vacuum and 10 mTorr Ar after 2.0 μs. The relative density above a threshold value appears black in each image, enhancing the resolution near the substrate where the density is greater for ablation into vacuum.

3.4 A study of Si density on axis during ablation into argon over a wide range of pressure

For the purpose of examining the plume's density on axis, a superposition of images, presented in the previous section, is not required. The spread in radial velocities for atoms within about 1.0 mm of the axis is sufficiently small to resonantly excite them using a 0.14 cm^{-1} bandwidth pump laser tuned to the stationary resonance frequency. In an effort to more accurately quantify the dependence of the normalized density profile of Si along the axis of symmetry of the expanding plume on background gas pressure and time, several PLIF streaks are acquired with the pump laser tuned to stationary resonance, setting time delays from 0.5 μs to 5.0 μs and pressures from 0 to 150 mTorr. To simplify the analysis of this data, the energy of the pump laser is reduced until the PLIF signal satisfied the criteria for linearity previously established.

Shown to the left in Figure 3.8 is a PLIF streak acquired from an Si plume expanding into vacuum using a 1.0 μs time delay, contours along the ridgeline and edge highlighted. To the right are the normalized density profiles along these contours. The similarity suggests that the laser intensity everywhere is linear.

In Figure 3.9 slices of the PLIF streak appearing in Figure 3.8 along constant axial positions of 1.5 mm, 4.5 mm, 7.5 mm, 11.5 mm, 14.5 mm, 17.5 mm, and 20.5 mm are shown. The laser intensity profile used to acquire the image appears at the bottom of this figure. A constant PLIF streak width near 2.2 mm despite significant variation in laser intensity corroborates the claim that the laser intensity is linear.

Having established that the PLIF streak appearing in Figure 3.8 was acquired using linear laser intensity, the normalized density profile along the axis may be obtained by normalizing the signal to the laser sheet profile. The results for time delays from 1.0 to 5.0 μs appear in Figure 3.10 in steps of 0.5 μs, each graph comparing profiles taken at background gas pressures of 0 mTorr, 30 mTorr, 60 mTorr, 90 mTorr, and 150 mTorr. The time sequence appears from top to bottom, then left to right. The left edge of each graph is actually 2-3 mm from the target surface, explaining the absence of a peak in any of the profiles. This presents no significant problem, how-

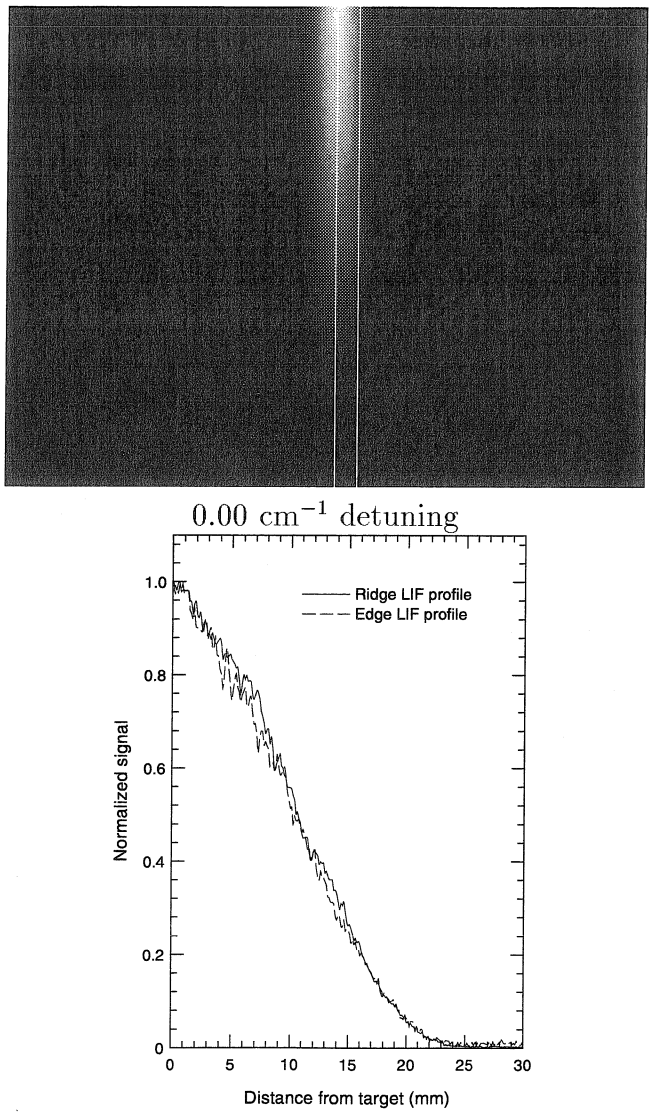

Figure 3.8: Similarity between normalized density profiles along edge and ridgeline contours of the PLIF streak shown indicates linear laser intensity.

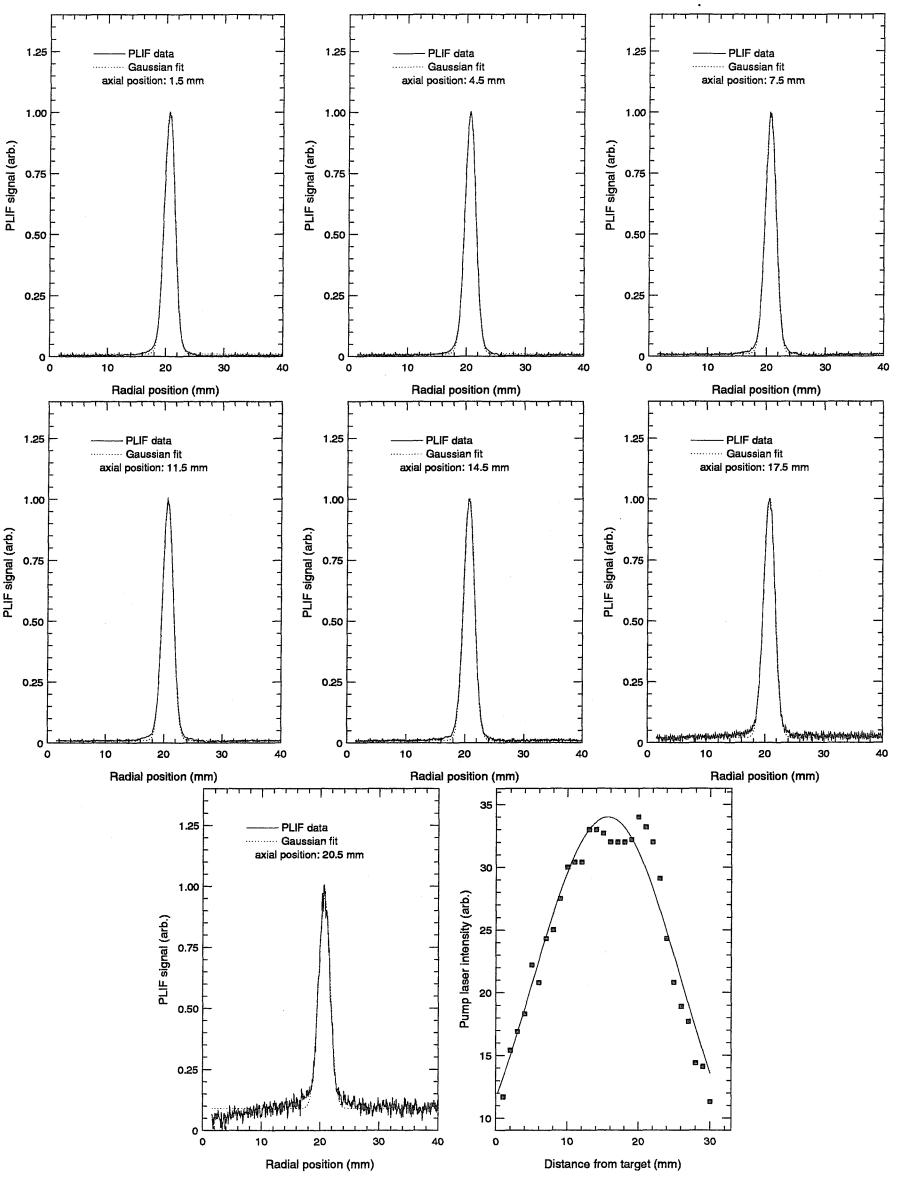

Figure 3.9: Slices of the PLIF streak appearing in Figure 3.8 along contours of constant axial positions between 1.5 mm and 20.5 mm. A constant width near 2.2 mm despite significant variation in laser intensity implies linear laser intensity.

ever, because similar normalized density profiles obtained from ablation into vacuum and into 10 mTorr argon presented in the previous section revealed no appreciable difference for $z < 3$ mm, at least for times less than 2.0 μs. For longer time delays, the density at $z = 3$ mm appears to be slightly greater for higher pressure, an effect which might introduce some error since all of the profiles are compared after normalizing them to their maximum value. This error is small, however, and is neglected.

One very interesting feature of these profiles is the apparent buildup in Si density at the substrate after 3.0 μs. Believed to be the first observation of the pressure dependence of this effect using PLIF imaging, these data offer information about the sticking probability of Si onto the unheated Si (100) substrate used in these experiments.

For Ar pressures of 0-150 mTorr the PLIF streaks acquired at 0.0 cm^{-1} detuning indicate that, for the purpose of imaging, Doppler shifts remain important, although less so as the pressure increases. This conclusion is evident in Figure 3.11 where streaks acquired after a 2.0 μs delay are compared for Ar pressures of 0-150 mTorr. Each image represents a 1.9 cm x 1.4 cm area near the target. At higher pressure the plume appears more rounded and less cropped at the sides, suggesting that more of the Si atoms are resonant with the pump laser. When the pressure is increased to 1 Torr, the rounded appearance of the image contrasts dramatically with the PLIF streaks acquired from plumes expanding into vacuum and more closely resembles the images produced by the superposition of several PLIF streaks acquired at different magnitudes of detuning (see Figure 3.1). One apparent difference, however, is a buildup in Si density near the contact front. The rounded appearance of the plume strongly suggests that the expansion of the plume is sufficiently slowed by a 1 Torr background gas after 2.0μs that Doppler effects are negligible. For a laser linewidth of 0.14 cm^{-1} and a resonance frequency near 41,000 cm^{-1} this requires that the characteristic velocitity of plume atoms be less than about 500 m/s. Since the size of the plume suggests an *average* leading-edge expansion plume near 5 km/s, the plume must expand rapidly during the first 1 μs, and expand much more slowly after that, as suggested later in this chapter and elsewhere [30].

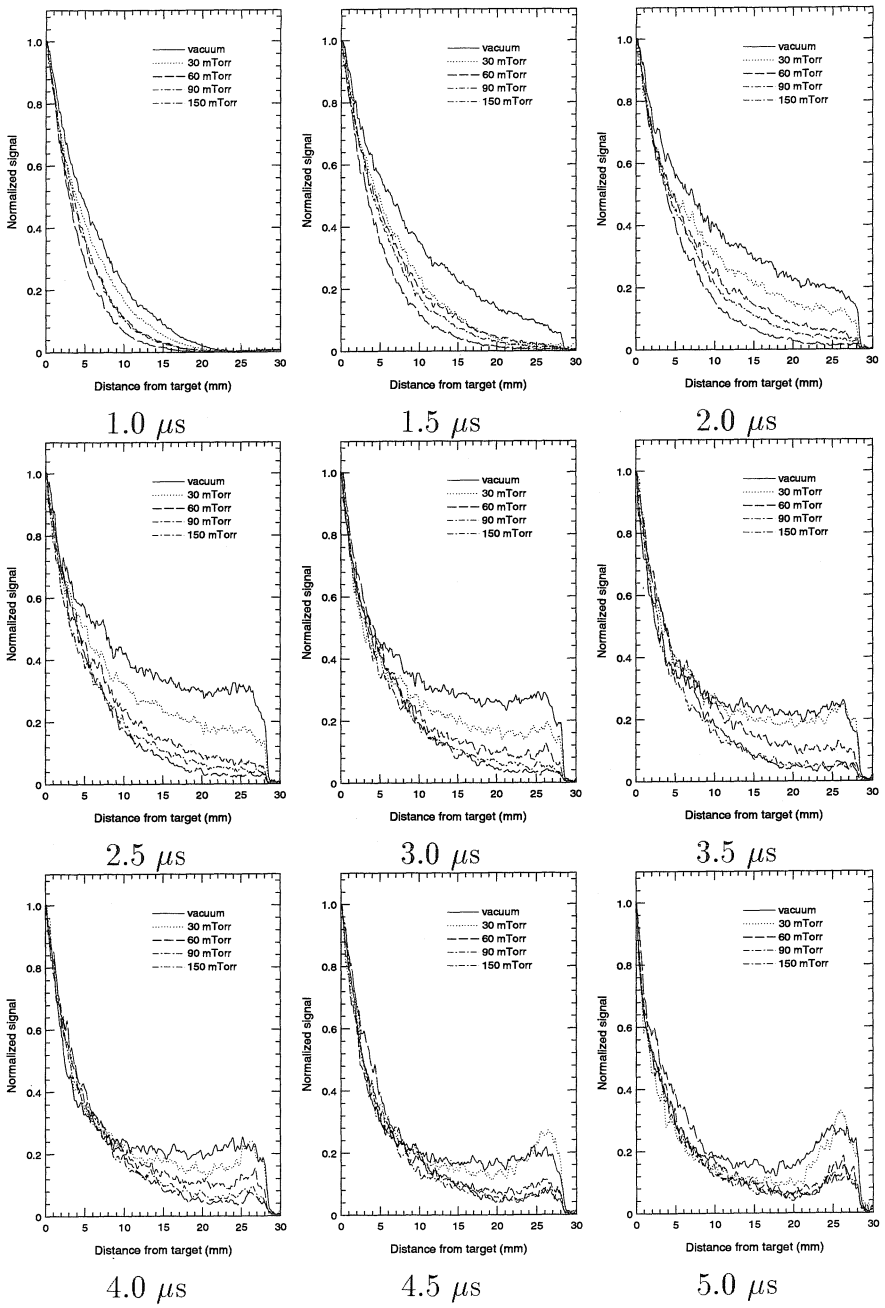

Figure 3.10: Time sequence profiles showing relative ground-state, neutral Si density along the axis of an ablation plume expanding in argon at various pressures and delay times.

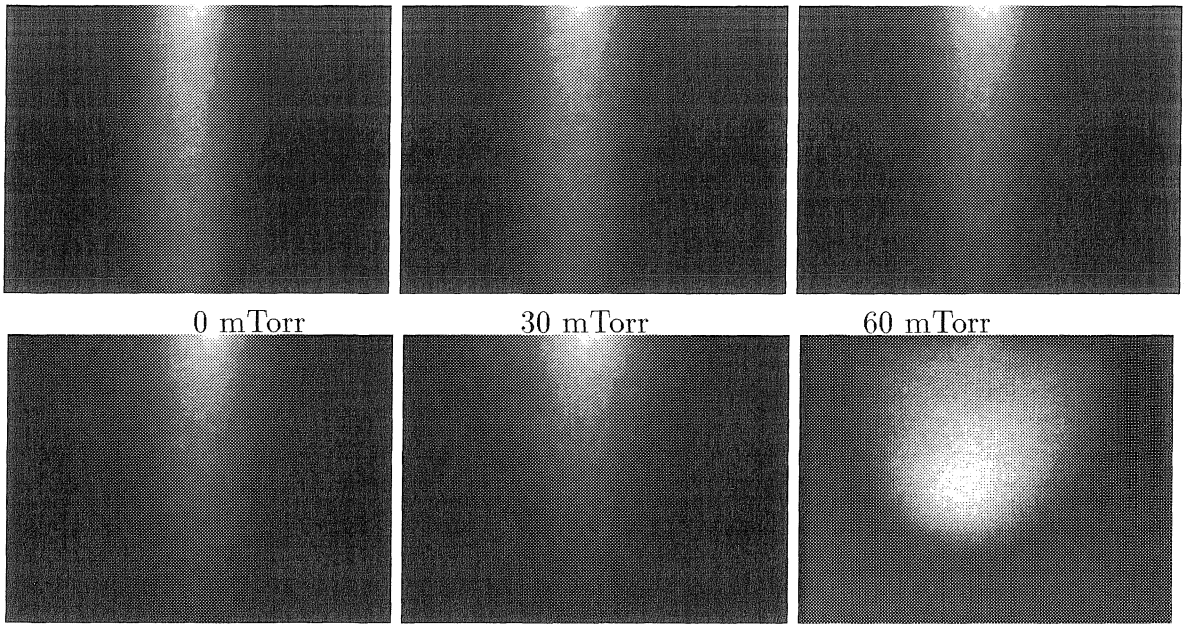

Figure 3.11: PLIF streak acquired at 0.0 cm^{-1} detuning after a 2.0 μs delay for various gas pressures. The plume appears less cropped on the sides as pressure increases, suggesting slower expansion speeds.

3.5 Evidence of gas-phase chemistry during ablation of Si into air

Recently oxide films such as SiO_x and GeO_2 have been successfully deposited onto a substrate using PLD by ablating Si or Ge into a background gas containing O_2 [14, 76, 12, 77]. Despite this experimental success, the primary mechanism for oxidation of the target material remains remains unclear. One possibility is that Si or Ge deposited onto the substrate reacts with O_2 in the gas, a second possibility is that SiO_2 or GeO_2 is ablated from a target whose surface becomes oxidized between laser pulses, and a third possiblity is that Si or Ge reacts with O_2 in flight. An understanding of the chemistry in simple systems such as these are important because it could potentially lend insight into the chemistry occurring when more complex materials are ablated into background gases, aiding perhaps in the identification of relevant parameters for controlling growth rate and/or film stoichiometry.

Shown on the left Figure 3.5 is an image showing the average emission signal from

40 shots, gathered using a gated micro-channel plate intensified CCD camera and a 260 ± 10 nm bandwidth interference filter with a 1.0 mm thick piece of Schott UG1 glass to help reject scattered excimer light at 248 nm. The intensifier gate is triggered 2.4 μs after Si is ablated into a 1.0 Torr background of air, and gathers signal for 50 ns. The image area represents the 1.9 cm x 1.4 cm region near the target, which is at the top of the image. The contact front between Si and air is clearly visible and the signal appears to be greatest along the forward edge of this front. Assuming that the emission signal is due to $3d\ ^1P^0 \rightarrow 3p^2\ ^1S$ transitions in Si (g_2A_{21} = 2.2 x 10^9) at 263.128 nm, the signal indicates the presence of Si in an excited state 7.0 eV above ground, which then might suggest high temperature at the forward edge of the plume. This interpretation is only approximate, however, because the emission signal also depends on Si density. A useful comparison can be made to the image of relative density of Si acquired from the Si plume expanding into 1 Torr Ar using PLIF, shown earlier in Figure 3.11.

To the right in Figure 3.5, is a second image showing the signal gathered during a 50 ns period which, as before, begins after a delay of 2.4 μs. During the first 30 ns of this period, a 235.25 nm pump laser sheet passes through the plume, a wavelength which excites the $Q_1(35)$ + $R_1(42)$ transitions in the $A^1\Pi \leftarrow X^1\Sigma^+(0,0)$ system of SiO. The complete PLIF scheme believed to be responsible for the enhanced signal is shown schematically in Figure 3.13. As shown, fluorescence into the 260 ± 10 nm bandwidth is gathered, including most of the (0,4) band as well as portions of the (0,3) and (0,5) bands. Although several transitions are apparent as the pump laser frequency is varied, the choice of 235.25 nm appears to maximize the signal. A numerical model which assumes a Boltzmann distribution of rotational levels prior to the pump laser pulse, and rapid rotational energy transfer (RET) among rotational levels in the excited state, predicts a maximum in signal at this wavelength if the rotational temperature of the SiO is near 2500 K. Although this estimate is only approximate, it implies that the SiO temperature is well above the 300 K temperature of the air.

The Doppler width of the fluorescence signal from an equilibrium SiO gas at

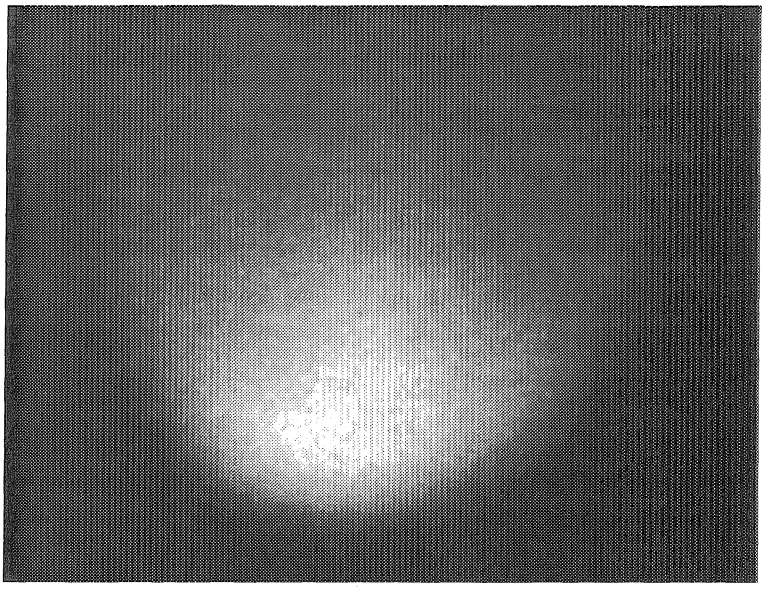

Si emission

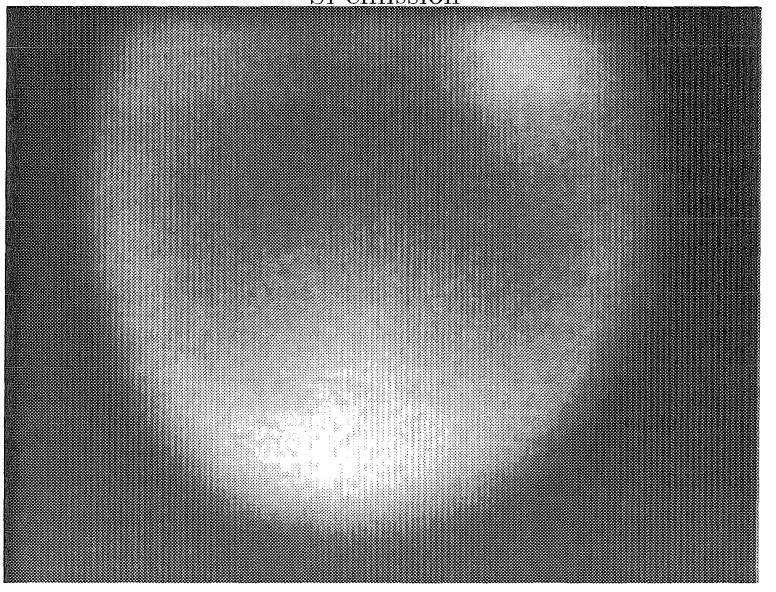

Si emission + SiO PLIF

Figure 3.12: (top) Emission from a 2.4 μs old Si plume in the 260 $\pm$ 10 nm bandwidth as it expands into 1.0 Torr air. (bottom) Emission + SiO PLIF signal obtained after pumping the $Q_1(35) + R_1(42)$ transitions in the $A^1\Pi \leftarrow X^1\Sigma^+(0,0)$ system of SiO at 235.25 nm.

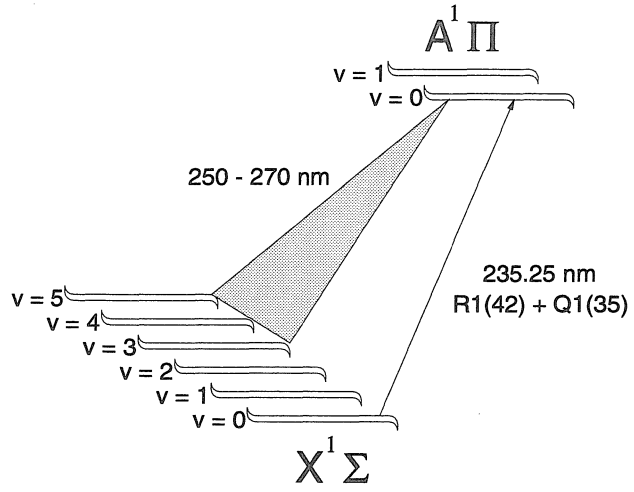

Figure 3.13: PLIF scheme used to acquire images of SiO density within an Si plume expanding into air.

2500 K is about 0.24 cm^{-1}, which is significantly greater than the 0.14 cm^{-1} laser linewidth. The Voight linewidth appropriate when both the Doppler width of the gas and the Lorentzian linewidth of the laser are combined is therefore about 0.32 cm^{-1}. This is the linewidth of the fluorescent signal $\delta\nu_s$, which negates Doppler shift effects caused by radial flow speeds v_r of the plume which satisfy $v_r \ll c\delta\nu_s/\nu_0$ where $\nu_0 = 42{,}500$ cm^{-1} denotes the frequency of the transition. The expansion speed is therefore negligible if $v_r \ll 2.2$ km/s. Even if the SiO temperature is only 300 K, the fluorescence linewidth is still about 0.18 cm^{-1}, negating expansion speeds satisfying $v_r \ll 1.2$ km/s.

In order to produce images showing the relative density of SiO, the contribution to the gathered signal from emission must be subtracted from the signal gathered during the laser pulse. The result must then be corrected as before for variations in laser sheet intensity. Although a set of population rate equations could be solved using a method analogous to that used to determine the threshold for nonlinear intensity for PLIF imaging of Si, for PLIF imaging of SiO it is assumed that the 1-10 kW/cm^2 pump laser intensity used in these experiments is sufficiently low to ensure that the PLIF signal is linear. This assumption is based on the expectation that RET among rotational levels during the pump laser pulse is sufficiently rapid to prevent saturation of the upper state. Making this assumption, the emission-subtracted image can be

corrected simply by normalizing the data to the laser sheet profile. Resulting images obtained after 1.0 μs, 1.5 μs, and 3.75 μs are shown in Figure 3.5. These images may be interpreted as relative density maps of SiO, believed to be the first reported PLIF images showing reactive intermediate species during PLD.

A plot of the contact front position vs. time, taken from the emission data that was subtracted from the signal to produce the images shown in Figure 3.5, suggests that the expansion speed is only about 500 m/s after a delay of 1.0 μs, with an average expansion speed near 8 km/s before that. PLIF images acquired after 1 μs may therefore be treated by neglecting the Doppler shifts associated with the plume's expansion speed. The data is compared to theory assuming both a shock wave expansion model and a drag model [30]. A reasonable fit is obtained to the drag model (equation 1.7) using $C = 1.35$ cm and $\beta = 1.0$ s^{-1}.

The data appearing in Figure 3.5 suggest that SiO is not produced in detectable quantity until about 1.0 μs. After that, SiO appears along the contact front between the Si and air, and not in the region believed to be occupied only by Si atoms. This data rules out the possibility that the detected SiO is simply ablated from an oxidized Si target, because this would result in the presence of SiO wherever Si is present. Instead, the presence of SiO only along the leading edge strongly suggests the occurrence of gas-phase chemistry where Si and air are mixed. The 1 μs delay before SiO appears may be related to the time scale for heating by the expanding plume, and high temperatures may be necessary to overcome the activation energy for whatever reaction produces it.

Curiously, the SiO density appears greatest at the sides of the plume near the target rather than at the forward edge of the plume where emission data might suggest that the temperature is greatest. It remains uncertain why this aspect of the SiO distribution is observed. It is possible that the SiO produced along the contact front near the axis quickly dissociates, but because the dissociation energy of SiO is about 8.3 eV this is unlikely unless the temperature in this region is several thousand degrees. At temperatures sufficient to dissociate the SiO, a cornucopia of chemical reactions involving Si, O, and N must be considered, making a thorough

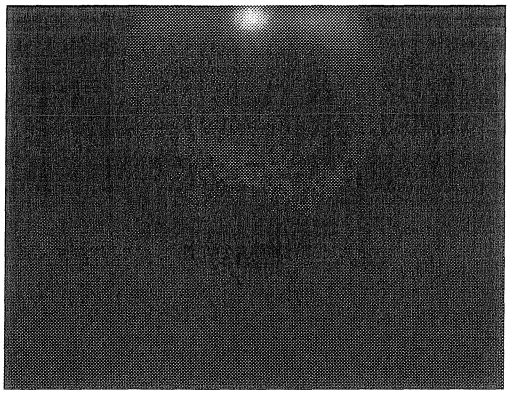

1.0 μs

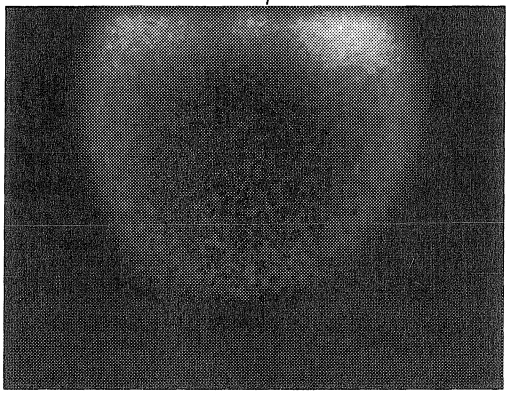

1.5 μs

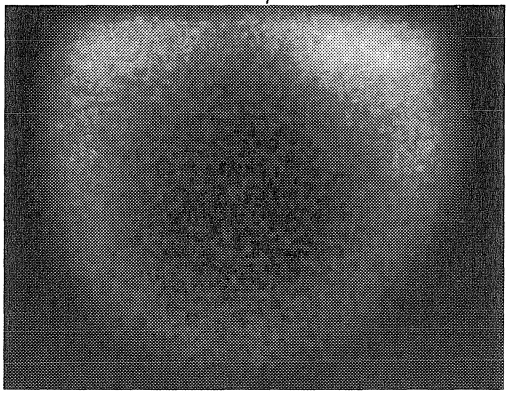

3.75 μs

Figure 3.14: Images of SiO density, obtained by PLIF, along the contact front of an Si plume expanding into air.

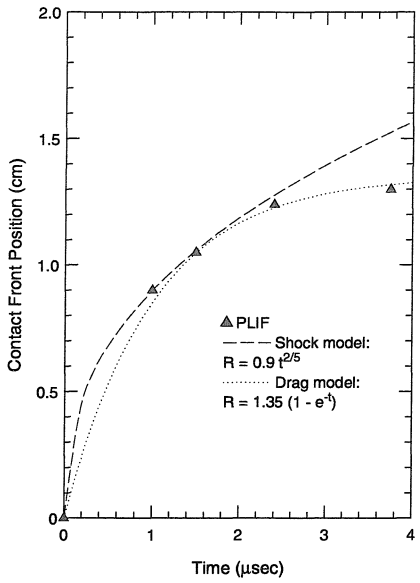

Figure 3.15: Position of the contact front as Si expands into 1 Torr air.

understanding of the chemistry along the contact front quite complex. It is also possible that the fluorescence signal is Doppler-broadened. Neglecting the linewidth of the laser and the Doppler-shifts associated with the expansion velocity of the plume, the PLIF signal originating from some point $\vec{x}$ in the interaction volume should satisfy [41]

$$S(\vec{x}) \propto n(\vec{x}) \left(\frac{mc^2}{2\pi kT\nu_0^2} \right)^{1/2} \tag{3.1}$$

where m is the mass of an SiO molecule. In this case the signal is therefore not simply proportional to the SiO density, but also depends inversely on the square root of the temperature. If the temperature around the perimeter of the contact front is not constant, then the PLIF signal would appear attenuated in regions of high temperature. Since the temperature profile along the contact front is not known, it is difficult to compensate for this effect. A third possiblity is that because the emission signal along the contact front on axis is signicantly larger than the PLIF signal, the apparent absence of signal there is an artifact of the background subtraction procedure.

Curiously, a similar experiment attempted using pure O_2 instead of air produced no detectable SiO PLIF signal. This result also remains unclear. It is possible that

the presence of N_2 suppresses reactions which would otherwise rapidly convert SiO to more stable SiO_2 molecules. For example, if SiO is produced by the bi-molecular reaction $Si + O_2 \rightarrow SiO + O$, then the resulting high energy O atoms may participate in the reaction $SiO + O \rightarrow SiO_2$, or the reaction $O + O_2 \rightarrow O_3$ which is then followed by $O_3 + SiO \rightarrow SiO_2 + O$. Each of these pathways for converting SiO to SiO_2 would be supressed by collisional quenching of the high energy atomic oxygen in the presence of a large N_2 partial pressure. This hypothesis could be tested by looking for SiO_2 in the plume, however, this was not investigated further.

3.6 Summary

PLIF imaging has been used in this chapter to produce Doppler-corrected images of Si expanding into both vacuum (10^{-5} Torr) and 10 mTorr Ar. In both cases, the plume is described well by a collisionless expansion model, evidenced by an independence on position of the normalized density profiles taken along parallel contours of the plume. For expansion into 10 mTorr Ar, however, collisions appear to slow the leading edge of the plume significantly. These observations are self-consistent if the interaction of the plume with the background gas occurs primarily during the earliest phase of the plume's expansion, while the plume is within a few millimeters of the target. This is consistent with a model whereby the background gas is initially compressed to high density along the contact front, forming a wall which slows the expansion of the leading edge and then quickly subsides, leaving the plume to expand nearly collisionlessly to the substrate.

Normalized axial density profiles along the axis of Si plumes expanding into Ar pressures of 0 - 150 mTorr after time delays of 0.5 - 5.0 μs reveal an interesting increase in Si density near the substrate after 3.0 μs. The pressure dependence of this enhanced density above the substrate is believed to be the first reported. When compared with simulation results, this data can be used to estimate the sticking probablity for Si onto an unheated Si(100) substrate.

Lastly, evidence of gas-phase chemistry as an Si plume expands into air at 1.0

Torr is reported. SiO is detected by pumping the $Q_1(35) + R_1(42)$ transitions in the $A^1\Pi \leftarrow X^1\Sigma^+(0,0)$ system of SiO at 235.25 nm. Fluorescence into a 260 $\pm$ 10 nm bandwidth is gathered, including most of the (0,4) band as well as portions of the (0,3) and (0,5) bands. Images of SiO density are obtained after subtracting background emission and correcting for variations in the laser sheet intensity. These images are believed to be the first reported PLIF images of any reactive intermediate species produced by gas-phase chemistry during PLA.

Chapter 4 DSMC simulations of pulsed effusion into vacuum

4.1 Introduction

In this chapter the Direct Simulation Monte Carlo (DSMC) method is introduced and applied to the problem of pulsed thermal effusion of Si into vacuum. Although the effusion rate and source temperature during effusion are normally related thermodynamically by the vapor pressure of the target material, they are treated here as independent. This model is simplistic, but is serves as a good starting point for examining qualitative properties of plumes, and for comparison to previous analytical and numerical work on pulsed thermal effusion.

The density of plume atoms near a surface immediately following an effusive pulse of duration t_p can be estimated by dividing the total number of particles effused by the characteristic volume of the plume. Assuming a 1-D expansion and no backscattering, the result is

$$n_s = \frac{\pi^{1/2} N_m d_m \rho}{v_p t_p}, \tag{4.1}$$

where d_m is the thickness per monolayer of the target material, N_m is the number of monolayers effused per pulse, ρ is the number density of the target material, and $v_p = (2kT_s/m)^{1/2}$. The mean free path $\lambda = 1/\sqrt{2}\sigma n_s$ expected near the target surface at this density is therefore

$$\lambda \approx \frac{v_p t_p}{(2\pi)^{1/2} \sigma \rho d_m N_m}, \tag{4.2}$$

where σ is the characteristic collision cross section.

If $d_p \approx \pi^{1/2} v_p t_p/2$ is used to describe the characteristic axial width of the plume after the laser pulse, then the ratio of d_p to the mean free path can be used as a dimensionless parameter α to characterize effusion plumes over a wide range of

effusion rates, specifically

$$\alpha = \frac{\pi}{\sqrt{2}} \sigma \rho d_m N_m, \tag{4.3}$$

which is *independent of the effusion temperature.* Since Si has 8 atoms per cubic cell in a diamond lattice with a cell width of 0.543 nm and 4 monolayers per cell [78], the number density and monolayer thickness can be estimated as 5.0 x 10^{28} atoms/m^3 and 1.36 x 10^{-10} m, respectively. Using a Lennard-Jones collision diameter of 2.91 x 10^{-10} [79] suggests that $\alpha \approx 4\ N_m$ for silicon. The parameter α is therefore comparable to the parameter $Z \approx 4N_m$ intoduced by Sibold and Urbassek to parameterize their simulations [59]. their work suggests that the ratio of the duration of the pulse to the characteristic collision time during the effusion period is also a useful parameter. If the characteristic collision time is approximated by $2\lambda/\sqrt{\pi}v_p$ then this parameter is also α.

It will be seen that for simulated plumes resulting from low effusion rates ($\alpha \ll 1$), the normalized density profiles taken along contours of constant radius from the axis of symmetry, and along contours of constant axial position, compare well with profiles derived assuming a collisionless expansion model and the initial half-Maxwellian velocity distribution function. The interaction of plume particles with the target is insignificant in this range of effusion rates, evidenced by the independence of the results on the boundary condition at the target (e.g. recondensation or specular reflection).

For moderate effusion rates ($\alpha \approx 1$), the plume becomes more forward-peaked, the normalized density profiles differing significantly from those predicted assuming the collisionless expansion of atoms described by the initial half-Maxwellian. The leading edge of the axial profile resembles that predicted assuming a collisionless expansion while the rest resembles that predicted by the collisionless expansion of a Maxwellian gas whose temperature and center-of-mass velocity are determined assuming momentum and energy conservation. Radial density profiles near the target also resemble the predictions based on this assumption. Little variation among profiles along parallel contours validate the collisionless expansion model, indicating that although the early collisional phase of the plume plays an important role in determining the degree of

forward-peaking, the width of this region is small. The non-zero width of the effusion spot already imposes the restriction $|\vec{x}| >> r_s$ (where $\vec{x}$ is any position where density is measured) on the collisionless expansion model anyway, so no further restriction is necessary as long as the width of the collisional region is not much greater than r_s. Like the results obtained for $\alpha \ll 1$, the results in this range of effusion rates are nearly independent of the boundary condition at the target.

At even higher effusion rates ($\alpha \gg 1$), the simulated plume is observed to become even more forward-peaked. This phenomenon has been quantified by expressing the amplitude of the peak in off-axis TOF profiles in the form $cos^p(\theta)$, where the angle θ is measured relative to the axis of symmetry of the plume [55, 23, 56], or by expressing the thickness of film deposition in the same form [80]. An analytical model offers an explanation of plume forward-peaking and relates the parameter p to the presumed Mach number describing the plume immediately after the expansion, when it is assumed to become instantaneously collisionless. A schematic diagram depicting the three regimes described using using this model is provided in Figure 4.1.

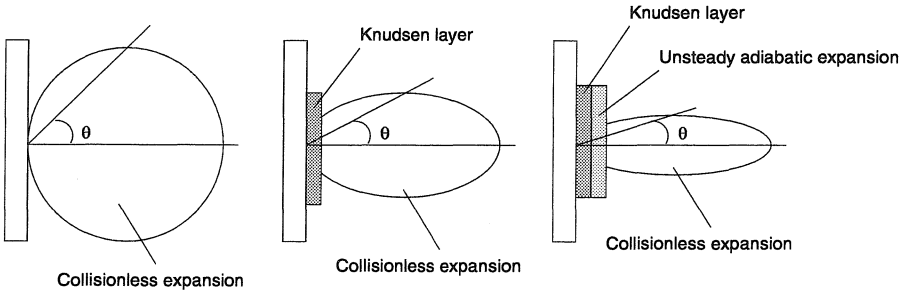

Figure 4.1: Three regimes of PLA into vacuum described analytically. (left) Half-Maxwellian. (Center) Shifted-Maxwellian resulting from Knudsen layer formation. (right) Shifted-Maxwellian resulting from unsteady adiabatic expansion after Knudsen layer formation.

Although the results of DSMC simulations in this range of effusion rates might appear consistent with the analytical model when the degree of forward-peaking of the plume is examined, the normalized density profiles along contours of fixed radius or fixed axial position do not match well to those predicted by the model. It will be shown that this discrepancy results primarily from a breakdown in the assumption that the Knudsen layer is in steady state. Although Kelly justifies the use

of the steady-state Knudsen layer solution, citing DSMC simulation results which suggest the velocity distribution function of the plume particles transitions from a half-Maxwellian to a shifted-Maxwellian after only 3-4 collisions per particle [23], this is not sufficient to claim that the Knudsen layer is in steady state. Simulations by Sibold and Urbassek which focus on the plume's temperature components near the target surface suggest that a pulse duration greater than about 200 mean collision times is necessary (equivalent to $\alpha > 200$) before the steady-state Knudsen layer solution becomes valid [58], requiring effusion of about 50 monolayers of Si. This result is independent of the source temperature. A similar result is obtained here, focusing on the time-dependent back-scattered particle, momentum, and energy flux and comparing them to the steady-state 1-D solutions. Since effusion of only a few monolayers is sufficient for a plume to exhibit strong forward-peaking, it is unnecessary, and in fact incorrect, to base a model describing forward-peaking on the assumption that a steady-state Knudsen layer exists during the effusive pulse.

The analytical model also assumes 1-D gas dynamics. A second plume parameter, defined by $\beta = d_p/r_s$, may be introduced to estimate the significance of the radial expansion during the laser pulse, a 1-D expansion approximation during this period being reasonable if $\beta \ll 1$. Unlike α, this parameter depends on the choice of effusion temperature, specifically $\beta \propto T^{1/2}$. The assumption $\beta \ll 1$ is therefore valid only for sufficiently low temperature, and the influence of the radial expansion of the plume during the laser pulse may be significant. It will be shown using DSMC simulation that the steady-state values for the back-scattered particle, momentum, and energy flux onto the target, quantities which have been calculated analytically for 1-D effusion [54], are slightly different than theory predicts. This difference is explained by a breakdown in the $\beta \ll 1$ assumption.

Since TOF analysis often assumes the plume expands collisionlessly, it is useful to estimate how far from the target a probe must be to safely make this assumption. If d_c is the characteristic dimension of the plume when it becomes collisionless, the signal acquired by a probe placed at position $\vec{x}$ can be analyzed using the collisionless expansion approximation if $\vec{x} >> d_c$. If the expansion of a plume following the laser

pulse occurs in 1-D, however, the characteristic dimension of the plume increases at exactly the same rate as the density decreases, keeping the ratio $d_p/\lambda = \alpha$ constant. Collisionless expansion, presumed to begin when $\lambda \gg d_p$, can therefore not begin for a plume decribed by $\alpha \geq 1$ unless the plume expands into 3-D and the density decreases faster than the characteristic plume dimension increases. Some assumption about the 3-D expansion behavior must therefore be made. One simple assumption is that the plume expands spherically, occupying a volume $4\pi d_c^3/3$ when $\lambda \approx d_c$ is satified. In this case, it is straightforward to show that

$$d_c \approx \frac{r_s}{2}(3\alpha)^{1/2}. \tag{4.4}$$

Perhaps a better approximation for the characteristic shape of the plume is an ellipse as is suggested schematically in Figure 4.1. A geometric argument can be used to show that if the density has angular dependence like $cos^n(\theta)$ then d_c becomes

$$d_c \approx \frac{r_s}{2}(3\alpha)^{1/2}\left(\frac{1/2^{1/n}}{1-1/2^{1/n}}\right)^{1/4}. \tag{4.5}$$

which reduces to equation 4.4 for $n = 1$. The parameter n is dependent on α, and for the Si effusion simulations presented in this chapter satisfies $n \approx \alpha$ for $\alpha \geq 1$. Equation 4.5 therefore reduces to

$$d_c \approx r_s\alpha^{1.6} \tag{4.6}$$

For example, assuming an effusion spot radius of 1 mm, the signal acquired by a probe more than 1 cm from the target may be treated assuming collisionless expansion, if less than about 1-4 monolayers are effused. If 10 monolayers are effused however, d_c increases to about 30 cm. This breakdown in the assumption of collisionless expansion must be considered when analyzing TOF data within a few centimeters of the target for high effusion rates.

DSMC simulations, which are are not limited by assumptions of 1-D expansion or

abrupt transitions from collisional to collisionless flow, provide a more accurate way to study plume properties during pulsed effusion than approximate analytical solutions currently available. The simulation results presented in this chapter demonstrate the ability of the DSMC method to effectively bridge the gap between the collisionless limit and the continuum limit often encountered in the study of rarified gas dynamics, and to provide credible data in situations such as PLA where good analytical solutions are unavailable.

4.2 Simulation parameters required to model pulsed thermal effusion using DSMC

The azimuthal symmetry of a typical PLA experiment suggests the use of a 2-D, axisymetric cylindrical cell grid consisting of concentric cylindrical shells. In such a grid, atoms located within $r \pm \Delta$ and $z \pm \Delta$ occupy the same cell, independent of their azimuthal coordinates. The DSMC method requires the dimension Δ of each cell be smaller than or comparable to the mean free path of particles in that cell for all time. Equation 4.2 suggests that the mean free path within an Si plume during the laser pulse is about 50 ${N_m}^{-1}$, assuming an effusion temperature of 100,000 K, while simulations indicate a mean free path about twice as large. This difference is believed to result because average relative velocity between collision pairs is smaller than the center-of-mass velocity $\sqrt{\pi}v_p/2$ used to estimate λ. Assuming then that the mean free path for Si effused for 30 ns satisfies $\lambda \approx 100{N_m}^{-1}$ μm, a simulation with $N_m = 10$ requires a cell width near 10 μm.

To uniformly divide a cylindrical space 3.0 cm in length and 1.5 cm in radius would then require 4,500,000 total cells which is impractical for monitoring flow properties once the plume expands beyond a few millimeters from the target. To illustrate this point, consider that once the plume occupies more than about 5% of the cylindrical volume containing it, the average cell population is less than one particle, assuming a total of 250,000 simulation particles. Since the density in the plume is determined

by dividing the number of simulation particles in a cell by the cell volume, the density would appear unrealistically quantized, and the average of hundreds of separate simulations would be necessary to smooth the statistical noise. More particles could certainly be used, but this solution is computationally inefficient. Instead, a high resolution grid might be treated as a network of subcells embedded in a lower resolution grid whose cell width is 0.5 mm, 50 times larger than the width of each subcell. Collisional pairs could be computed within the subcell network, while density, temperature, and flow velocity are computed by sampling each low-resolution cell. Since only 900 cells would divide the cylindrical space between the target and substrate, the average cell population would be about 5000 times greater than in the subcell network so fewer runs would be necessary to produce statistically meaningful densities. The low resolution cell grid would still maintain enough resolution, however, to generate good images. A diagram depicting a typical cell and subcell grid networks is provided in Figure 4.2.

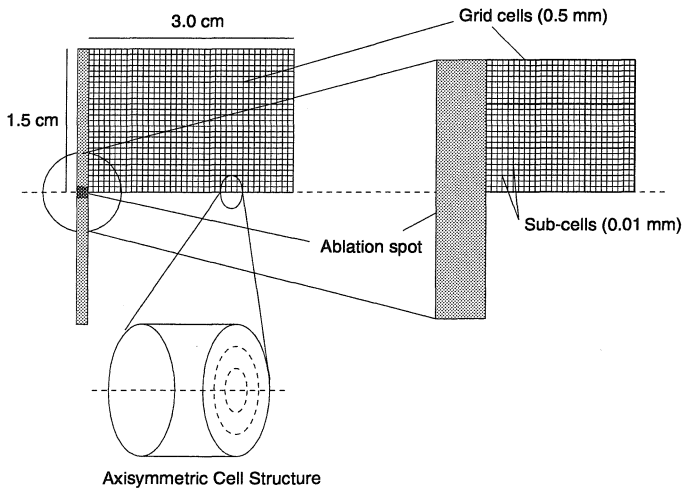

Figure 4.2: Typical cell grid used to study pulsed thermal effusion into vacuum using DSMC. Each cell is a cylindrical shell 0.5 mm thick and 0.5 mm length, subdivided into 2500 subcells, each with a 10.0 μm dimension.

In general, the time step for any DSMC simulation must satisfy

$$t_{step} \ll \lambda / v \tag{4.7}$$

where v is the characteristic velocity of atoms in the simulation. Equation 4.2 can be used again here, to re-write equation 4.7 as

$$t_{step} \ll \frac{\sqrt{2}t_p}{\pi\sigma\rho d_m N_m} \approx \frac{t_p}{10N_m} \tag{4.8}$$

Assuming a laser pulse lasting 30 ns, an initial time step of about $0.3/\mathrm{N}_m$ is used, although for optimal computational efficiency, the time step in the simulation is allowed to increase or decrease, subject to the constraint that equation 4.7 remains satisfied. This is accomplished by measuring the density in each cell and calculating the mean cross section of selected collision pairs at each time step to estimate the mean free path. A measurement of the mean relative velocity of the selected collision pairs then determines the characteristic time step in each cell. The minimum time step used for the simulation is chosen to be 10% of the smallest characteristic time step measured. The time step should not be allowed to increase during the effusion period, however, until the subcell directly over the target surface becomes fully occupied, otherwise an unrealistically low density measurement results in an unrealistically large characteristic time step for the subcell. The time step should therefore not be adjusted until $t \approx 2\Delta/\sqrt{\pi}v_p$ where Δ is the width of the subcell near the target. For a 10 μm subcell, this means $t \approx 1.0$ ns. After that, density measurements in the subcells should be accurate, however it does no harm to keep the time step fixed during the entire effusion period and only allow it to increase afterward. Shown in the table below is a list of the parameters used for the simulations presented in this chapter. Modeling effusion at higher effusion rates efficiently requires a more powerful computer than the HP 700/RX used for this work.

N_m	Δt (ns)	Δx (mm)	Subcells/cell
0.0316	10.0	0.5	1
0.1	3.0	0.5	1
0.316	1.0	0.5	3
1.0	0.3	0.5	10
3.16	0.1	0.5	25
10.0	0.03	0.5	50

In order to simulate conditions of expansion into vacuum, the boundary conditions at the substrate and surrounding surface are recondensation, that is, particles are simply removed from the simulation. Since the atoms incident onto these surfaces are effectively collisionless anyway, this condition is nearly identical to having no boundary at all. At the target, particles also recondense for $t < t_p$, as assumed in the derivation of the analytical solution for steady state effusion [54], but for $t > t_p$, both recondensation and specular reflection are investigated.

As described in Appendix B, the DSMC method used here employs the VHS technique to determine the collision cross section for the Si, a parameter which depends on the relative velocity of each collision pair selected. The calculation of the parameter requires knowledge about the temperature dependent viscosity of Si at some reference pressure. This function generally satisfies

$$\mu(T) = \mu_{ref}(T/T_{ref})^{\omega} \tag{4.9}$$

where ω is obtained by fitting equation 4.9 to available data, which is available for many elements and molecules [79]. The parameters used for Si in these simulations are μ_{ref} = 7.09 x 10^{-6} Pa s at 300 K and ω = 0.93.

4.3 A comparison of DSMC results and theory for low effusion rates ($\alpha \ll 1$)

4.3.1 Theory

The distribution function appropriate for an ensemble of particles generated by thermal effusion from a surface at temperature T_s oriented in the x, y plane is given by the *half*-Maxwellian

$$f(\vec{v},0) = \frac{n_s}{\pi^{3/2} v_p^3} e^{-\frac{(v_x^2+v_y^2+v_z^2)}{v_p^2}}, \tag{4.10}$$

where $v_p = (2kT_s/m)^{1/2}$, n_s is the effusion gas density at the $z = 0$ surface, and velocities are defined in the ranges $0 < v_z < \infty$ and $-\infty < v_x, v_y < \infty$. The number of atoms effused per unit area per unit time in the velocity range v_x to $v_x + dv_x$, v_y to $v_y + dv_y$, v_z to $v_z + dv_z$ in the z direction from the surface is then given by $f(\vec{v},0)v_z dv_x dv_y dv_z$, so that the total number of particles N_p desorbed in a time t_p from a small area A is

$$N_p = A t_p \int_{-\infty}^{\infty}\int_{-\infty}^{\infty}\int_{0}^{\infty} f(\vec{v},0)Q(\vec{v})dv_z dv_y dv_x = \frac{v_p t_p n_s A}{2\pi^{1/2}}, \tag{4.11}$$

where $Q(\vec{v}) = v_z$. The total momentum and energy are determined by taking higher moments, integrals of the form in equation 4.11 but with $Q = mv_z^2\hat{z}$ and $Q = mv_z(v_x^2 + v_y^2 + v_z^2)/2$. The results are

$$P = N_p m\sqrt{\frac{\pi k T_s}{2m}} \tag{4.12}$$

and

$$E = 2N_p k T_s. \tag{4.13}$$

The velocity distribution among the N_p particles, assuming no collisions occur after desorption, is simply

$$P(\vec{v}) = A t_p v_z f(\vec{v},0) = \frac{2N_p}{\pi v_p^4} v_z e^{-\frac{(v_x^2+v_y^2+v_z^2)}{v_p^2}}. \tag{4.14}$$

If the effusion is limited to a small region located at the coordinate origin $(x, y, z = 0)$, the effusion pulse is brief, and the expansion of the gas into vacuum is collisionless, then the position of each particle can be approximated by $x_i = v_i t$. This step defines the collisionless expansion model, and for the velocity distribution function in equation 4.14 results in the density

$$n(x, y, z) = \frac{2N_p}{\pi v_p^4} \frac{z}{t^4} e^{\frac{-(x^2+y^2+z^2)}{v_p^2 t^2}}. \tag{4.15}$$

The *normalized* density profile along any constant radius $r = (x^2 + y^2)^{1/2}$ contour for this plume at some time t then satisfies

$$\mathcal{N}(z) = \sqrt{2} \frac{z}{v_p t} e^{\frac{1-(z/v_p t)^2}{2}} \tag{4.16}$$

which is independent of radial position. This independence is useful because it suggests that any two profiles along parallel contours are identical, providing a good way to test the collisionless expansion assumption. The normalized density profile along any contour of constant z satisfies

$$\mathcal{N}(r) = e^{-(\frac{r}{v_p t})^2}, \tag{4.17}$$

which is independent of axial position.

Relevant to the deposition of films by PLD is the flux of atoms onto a substrate, assumed to be located at $z = D$. This quantity is given by

$$F(r, t) = n(r, D) \frac{D}{t} = \frac{2N_p}{\pi v_p^4} \frac{D^2}{t^5} e^{\frac{-(r^2+D^2)}{v_p^2 t^2}}. \tag{4.18}$$

Assuming a sticking probability equal to 1, the surface density of the film deposited on the substrate can be obtained by integrating $F(r, t)$ over time. This gives

$$F(r) = \frac{2N_p D^2}{\pi v_p^4} \int_0^\infty \frac{1}{t^5} e^{\frac{-(r^2+D^2)}{v_p^2 t^2}} dt = \frac{N_p D^2}{\pi (r^2 + D^2)^2}. \tag{4.19}$$

Similarly, the rate at which atoms impact the substrate can be obtained by integrating $F(r,t)$ over the substrate surface, giving

$$F(t) = \frac{4N_pD^2}{v_p^4t^5}e^{-D^2/v_p^2t^2}\int_0^R re^{-r^2/v_p^2t^2}dr = \frac{2N_pD^2}{v_p^2t^3}e^{-D^2/v_p^2t^2}\left(1-e^{-R^2/v_p^2t^2}\right), \quad (4.20)$$

where R is the radius of the substrate. The total fraction of effused atoms which eventually deposit onto the substrate can be determined most easily by integrating $F(r)$ over the substrate surface. The result is

$$F = 2N_pD^2\int_0^R \frac{rdr}{(r^2+D^2)} = N_p\frac{R^2}{D^2+R^2}. \quad (4.21)$$

The energy per particle incident onto the substrate is also of interest for PLD. The axial energy per particle, as a function of radius, is given by

$$E_{perp}(r) = \frac{1}{F(r)}\int_0^\infty F(r,t)\frac{mD^2}{2t^2}dt = mv_p^2\frac{D^2}{r^2+D^2},. \quad (4.22)$$

and the radial energy per particle can be otained using

$$E_{para}(r) = \frac{1}{F(r)}\int_0^\infty F(r,t)\frac{mr^2}{2t^2}dt = mv_p^2\frac{r^2}{r^2+D^2}.. \quad (4.23)$$

The angular dependence of density, defined in terms of θ, an angle measured from the axis of symmetry of the plume, is easily obtained by letting $z = R\cos(\theta)$ and $r = R\sin(\theta)$, where R is the distance from the effusion spot measured in *spherical* coordinates. The density can then be written as

$$n(R,\theta) = \frac{2N_p}{\pi v_p^4t^4}Re^{-(\frac{R}{v_pt})^2}cos(\theta), \quad (4.24)$$

demonstrating that for a fixed value of R, $\mathcal{N}(\theta) \propto cos(\theta)$. Equilavently, an inspection of equation 4.19 reveals that this angular dependence becomes evidenced in the surface density of the deposited film as $F(r) \propto cos^2(\theta)$.

Although the plume is expected to expand collisionlessly if $\alpha \ll 1$, flow speed may

be defined by $\vec{u} \equiv \langle \vec{v} \rangle$ and temperature components perpendicular and parallel to the target surface may be defined by $T_{perp} \equiv m(\langle {v_z}^2 \rangle - {u_z}^2)/k$ and $T_{para} \equiv m(\langle {v_r}^2 \rangle - {u_r}^2)/k$, where $\langle\rangle$ denotes an average over all the simulation particles in a given cell. It is straightforward to show that for a collisionless expansion of particles originating simultaneously from a dimensionless point, $\vec{u} = \vec{x}/t$ and $T_{para}(\vec{x}) = T_{perp}(\vec{x}) = 0$ for all $\vec{x}$.

4.3.2 DSMC results

Shown in Figure 4.3 are time-sequence images depicting the density of Si, assuming thermal effusion at a rate consistent with a time-integrated effusion of 0.0316 monolayers/pulse from an effusion spot having a time-independent temperature of 100,000 K. Times from 0.5 to 3.0 μs are shown incremented by 0.5 μs.

To the left in Figure 4.4 is a normalized density profile of the plume along a contour of constant radius (r = 0 mm) taken after 1.0 μs, compared to a theoretical profile calculated assuming collisionless expansion and the initial half-Maxwellian distribution function given in equation 4.10. Two other theoretical profiles are also shown, however these become relevant only at higher effusion rates. To the right in Figure 4.4 is another normalized density profile, taken along a contour of constant axial position (z = 4.5 mm). Again, the DSMC result compares well with the profile predicted assuming collisionless expansion of the initial half-Maxwellian atoms. The target boundary condition for this simulation is recondensation although the results are the same if specular relection is assumed instead. This indicates negligible backscattering (0.1% by 9.0 μs), which expected if the plume is collisionless.

The collisionless nature of the expansion is directly evident in Figure 4.5, which shows both the axial and radial components of the flow velocity $\vec{u}$ within each cell after a time delay of 2.0 μs. The perpendicular plume temperature after 2.0 μs is also shown. A constant value is consistent with collisionless expansion, the magnitude of 25 K being an inevitable artifact of using cells with non-zero dimension.

Information about the particle flux and average energy per particle onto the sub-

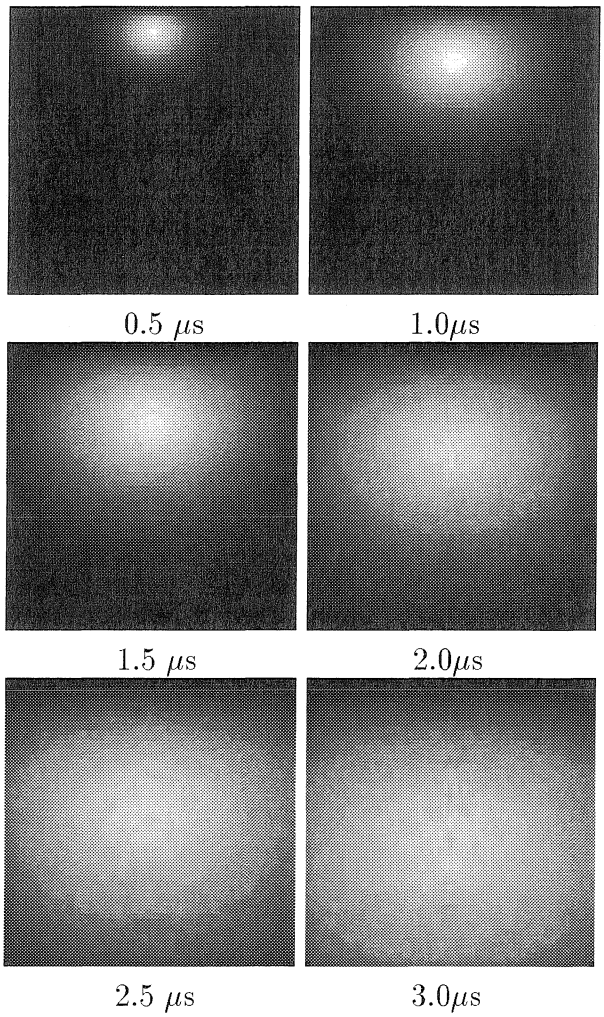

Figure 4.3: Time-sequence images of Si density resulting from the effusion of 0.0316 monolayers as the plume expands into vacuum.

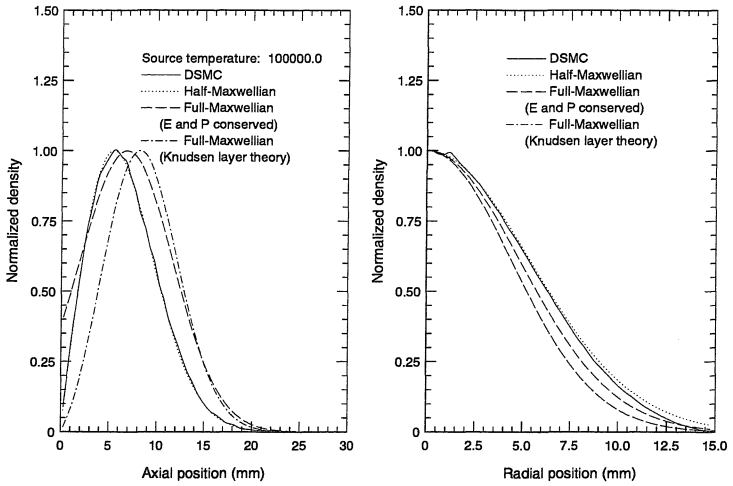

Figure 4.4: Normalized density profile along (left) a constant radius contour, and (right) along a constant axial position contour for the 1.0 μs old plume appearing in Figure 4.3. Profiles are consistent with the collisionless expansion model, assuming the initial half-Maxwellian velocity distribution function.

strate is shown in Figure 4.6. Each of the functions is consistent with theory developed earlier. For the specific condition $R = D/2$ used in this simulation equation 4.21 suggests that only 20.0% of the atoms effused impact the substrate. This is consistent with the value of 19.4% observed in simulation. Most of the remaining atoms escape to the sides of the substrate.

4.4 A comparison of DSMC results and theory for moderate effusion rates ($\alpha \approx 1$)

4.4.1 Theory

The evolution of the velocity distribution function describing an ensemble of thermally desorbed gas atoms is of fundamental importance to the problem of pulsed laser ablation. Because any velocity distribution function which is non-Maxwellian will evolve into a Maxwellian distribution on a time scale dictated by the collision rate among particles in the ensemble, it is expected that collisions during the initial phase of a plume's expansion will tend to re-configure the distribution function into a *shifted-*

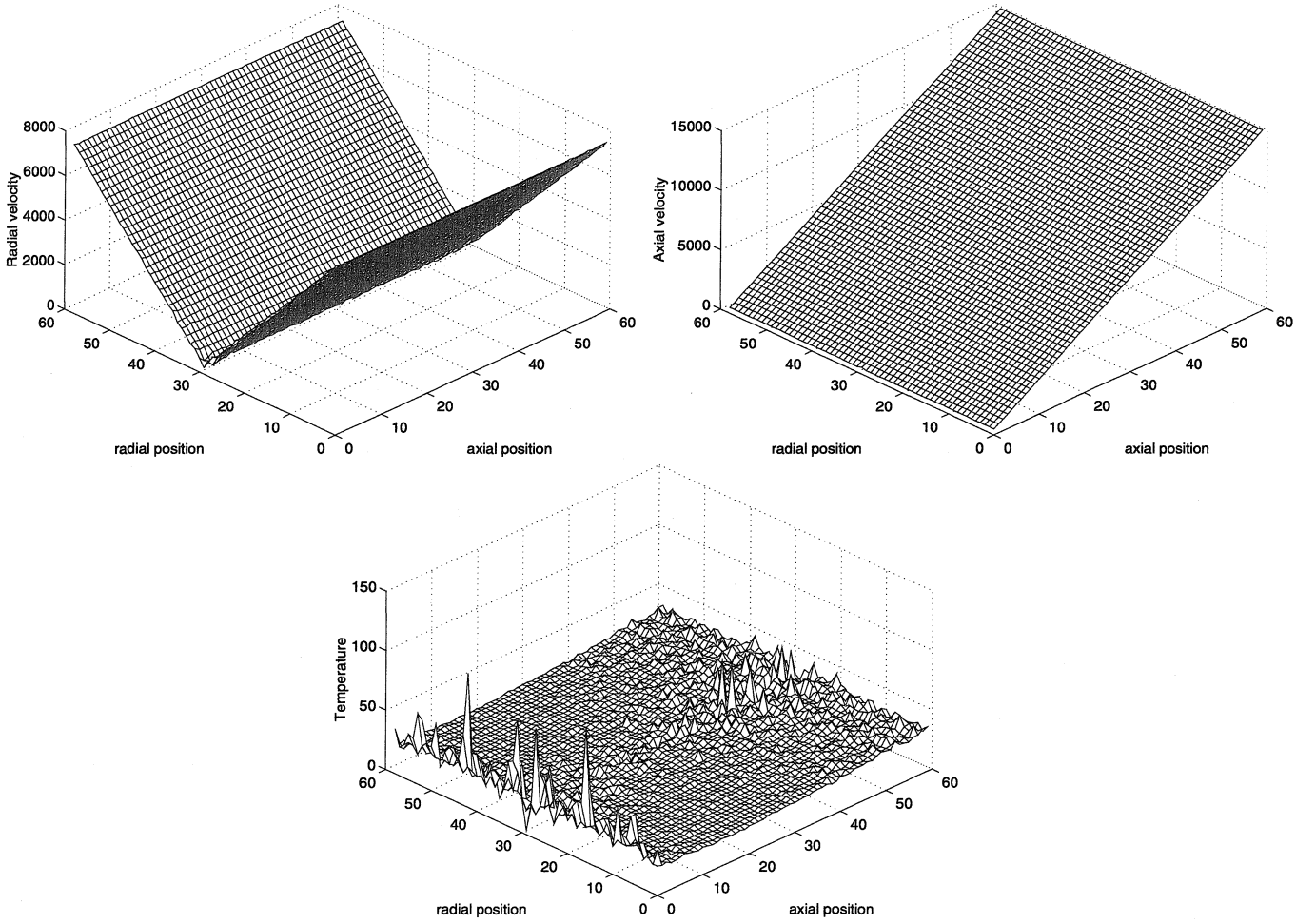

Figure 4.5: (Upper left) Radial flow speed within a 2.0 μs old 0.0316-monolayer Si plume expanding into vacuum. (Upper right) Axial flow speed. (Bottom) Perpendicular temperature. Data indicates a collisionless expansion.

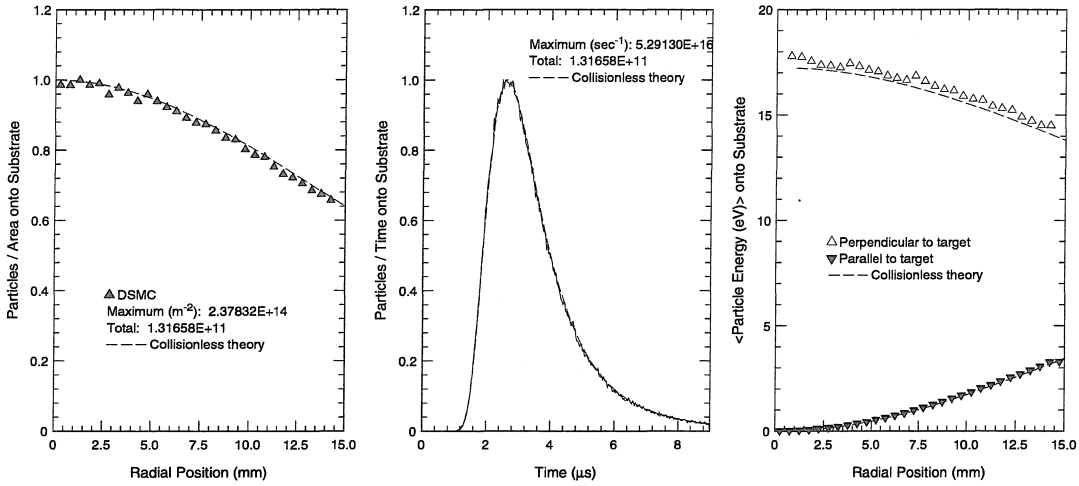

Figure 4.6: (Left) Particle density on the substrate as a function of radial position for a nearly collisionless effusion plume. (Center) Impact rate as a function of time. (Right) Average axial and radial energy per particle incident onto the substrate.

Maxwellian form, defined by

$$f(\vec{v},\vec{x}) = n(\vec{x})\left(\frac{m}{2\pi kT}\right)^{3/2} e^{\frac{-m(v_x^2+v_y^2+(v_z-u)^2)}{2kT}} \tag{4.25}$$

with $-\infty < v_x, v_y, v_z < \infty$.

A formal analysis of *steady-state* effusion, matching moments of the Boltzman equation [54], is the basis of a popular ablation model [23, 55]. In brief, the analysis introduces a shifted-Maxwellian profile f_k^+ given by

$$f_k^+(\vec{v}) = \frac{n_k}{\pi^{3/2}v_{pk}^3} e^{-\frac{-(v_x^2+v_y^2+(v_z-u_k)^2)}{v_{pk}^2}} \tag{4.26}$$

to describe the fluid emerging from the Knudsen layer with flow properties u_k, T_k, and n_k. To account for back-scattering onto the target, a second shifted-Maxwellian f_k^- is introduced which is identical to f_k^+ except that it is only defined for $-\infty < v_z < 0$. A solution $f(\vec{v},0) + \beta^- f_k^-(\vec{v})$ is then assumed for the distribution function at $z = 0$, where $f(\vec{v},0)$ is defined in equation 4.10 and β^- is a free parameter whose magnitude

is greater than unity. Three moment equations of the form

$$\int Q(\vec{v}) f_k^+(\vec{v}) d\vec{v} = \int_{v_z>0} Q(\vec{v}) f(\vec{v},0) d\vec{v} + \int_{v_z<0} Q(\vec{v}) \beta^- f_k^-(\vec{v}) d\vec{v} \tag{4.27}$$

can be formed with the four unknown quanties, u_k, T_k, n_k, and β^-. If the flow speed beyond the Knudsen layer is estimated by the sound speed $u_k \approx (\gamma k T_k/m)^{1/2}$ then the remaining unknowns can be determined. The results show that $\beta^- = 6.324$, $T_k = 0.6691 T_s$, and $u_k = 1.0560(kT_s/m)^{1/2}$. The particle flux and energy flux incident onto the target, obtained from the term in equation 4.27 involving f_k^-, indicate that 18.4% of the atoms recondense, carrying 9.0% of the energy. The 15.7% increase in momentum is a consequence of the recondensation of particles with *negative* velocities back-scattered onto the target.

According to this model, the remainder of the particles emerge from the Knudsen layer and expand collisionlessly, resulting in a plume density given by

$$n(x,y,z) = \frac{2N_k}{\pi v_p^4} \frac{z}{t^4} e^{\frac{-(x^2+y^2+(z-u_k t)^2)}{v_p^2 t^2}}, \tag{4.28}$$

where $v_p = (2kT_k/m)^{1/2}$. The normalized axial density profile for this plume satisfies

$$\mathcal{N}(z) = Cze^{\frac{-(z-u_k t)^2}{v_p^2 t^2}}, \tag{4.29}$$

where C is a constant determined by evaluating the density at $z = t(u+(u^2+2v_p^2)^{1/2})$. The normalized radial density profile satisfies

$$\mathcal{N}(r) = e^{-r^2/v_p^2 t^2}. \tag{4.30}$$

The particle flux onto the substrate in this case satisfies

$$F(r,t) = \frac{2N_k}{\pi v_p^4} \frac{D^2}{t^5} e^{\frac{-(r^2+(D-u_k t)^2)}{v_p^2 t^2}}, \tag{4.31}$$

and the impact rate onto the substrate is therefore

$$F(t) = \int_0^R 2\pi r F(r,t)dr = \frac{2N_p D^2}{v_p^2 t^3} e^{-(D-u_k t)^2/v_p^2 t^2} \left(1 - e^{-R^2/v_p^2 t^2}\right). \tag{4.32}$$

The surface density of the film, obtained by integrating $F(r,t)$ over time, is more difficult to determine analytically, but may instead be computed numerically. The same is true for the average energy of particles onto the substrate.

The angular dependence of plume density can examined by considering that

$$n(R,\theta) = \frac{2N_k}{\pi v_p^4 t^4} Rcos(\theta) e^{\frac{-(R^2 sin(\theta)^2 + (Rcos(\theta) - u_k t)^2)}{v_p^2 t^2}} \tag{4.33}$$

where R is again the distance from the effusion spot, measured using spherical coordinates. If R = constant, then

$$n(\theta) \propto cos(\theta) e^{-\zeta(1-cos(\theta))}, \tag{4.34}$$

where

$$\zeta = \frac{u_k R m}{k T_k t}. \tag{4.35}$$

The angular dependence of this plume is more complex than the simple $cos(\theta)$ dependence of a collisionless effusion plume. By inspection of equation 4.34, it is apparent that the function $n(\theta)$ decreases more rapidly with θ than before. Defining angle θ_H when the plume density drops to half its value on-axis, the angular dependence may be approximated by $cos^n(\theta)$ with

$$n = 1 + \zeta \frac{cos(\theta_H) - 1}{ln(cos(\theta_H))}. \tag{4.36}$$

Forward-peaking will also be evidenced in a more rapid decrease in the film surface density $F(r) \propto cos^{n+1}(\theta)$ with increasing radius.

It is not obvious *a priori* whether a steady-state Knudsen layer is an appropriate assumption for pulsed effusion. It is possible that early collisions result in a transition

from a half-Maxwellian to a shifted-Maxwellian distribution function, but without a steady-state Knudsen layer and without back-scattering onto the target during the transition. In this case, the ensemble of N_p atoms described by the distribution function equation 4.25 has a total momentum given by

$$\int_{-\infty}^{\infty} (m\vec{v}) f(\vec{v}) d\vec{v} = N_p m u \hat{z} \tag{4.37}$$

and total energy given by

$$\frac{1}{2}\int_{-\infty}^{\infty} m v^2 f(\vec{v}) d\vec{v} = \frac{3}{2} N_p k T + \frac{1}{2} N_p m u^2. \tag{4.38}$$

If the interaction of the plume with the target boundary is ignored during the transition, then both the total momentum and total energy of the plume will be conserved as the distribution function evolves from equation 4.10 to equation 4.25. Equating the momenta in equations 4.37 and 4.12 and the energy in equations 4.38 and 4.13 give

$$u = \sqrt{\frac{\pi k T_s}{2m}} = 1.2533\sqrt{\frac{k T_s}{m}} \tag{4.39}$$

and

$$T = \frac{8-\pi}{6} T_s = 0.8097 T_s. \tag{4.40}$$

If this shifted-Maxwellian gas, initially a thin sheet near the target surface, then expands collisionlessly, the density $n(x, y, z)$ satisfies

$$n(x, y, z) = \frac{N_p}{\pi^{3/2} v_p^3} \frac{1}{t^3} e^{\frac{-(x^2+y^2+(z-ut)^2)}{v_p^2 t^2}}, \tag{4.41}$$

where $v_p = (2kT/m)^{1/2}$. The normalized profiles are given by

$$\mathcal{N}(z) = e^{-(z-ut)^2/v_p^2 t^2} \tag{4.42}$$

and

$$\mathcal{N}(r) = e^{-r^2/v_p^2 t^2}. \tag{4.43}$$

The flux onto the substrate in this case is described by

$$F(r,t) = \frac{N_p D}{\pi^{3/2} v_p^3 t^4} e^{\frac{-(r^2+(D-ut)^2)}{v_p^2 t^2}} \tag{4.44}$$

and the impact rate is

$$F(t) = \frac{N_p D}{\pi^{1/2} v_p t^2} e^{\frac{-(r^2+(D-ut)^2)}{v_p^2 t^2}} . \tag{4.45}$$

The function $F(r)$ and the average particle must again be solved numerically.

The fraction of atoms in this shifted-Maxwellian gas having negative velocities is given by

$$\int_{-\infty}^{0} \left(\frac{m}{2\pi kT}\right)^{1/2} e^{\frac{-m(v_z-u)^2}{2kT}} dv_z = .082 \tag{4.46}$$

This calculation suggests that about 8.2% of the atoms are back-scattered onto the target, if the plume expands collisionlessly after the transition from a half- to a shifted-Maxwellian distribution.

4.4.2 DSMC Results

Shown in Figure 4.7 are time-sequence images depicting the density of 1.0 monolayer Si plume. Times from 0.5 to 3.0 μs are shown incremented by 0.5 μs. A qualitative comparison of these images with the ones shown in Figure 4.3 reveals that the plume is narrower or forward-peaked.

To the left in Figure 4.8 is a normalized density profile of this plume taken along a contour of constant radius (r = 0 mm), compared to those predicted assuming different models. One model assumes collisionless expansion, another assumes a transition to a shifted-Maxwellian with both energy and momentum conserved followed by collisionless expansion, and a third assumes collisionless flow from a steady-state Knudsen layer. To the right is a similar profile, taken along a contour of constant axial position (z = 1.5 cm) compared with profiles derived assuming the same three models. Both the radial and axial density profiles closely resemble those predicted assuming the collisionless expansion of a shifted-Maxwellian gas whose temperature and flow speed result from momentum and energy conservation and not those predicted from Knud-

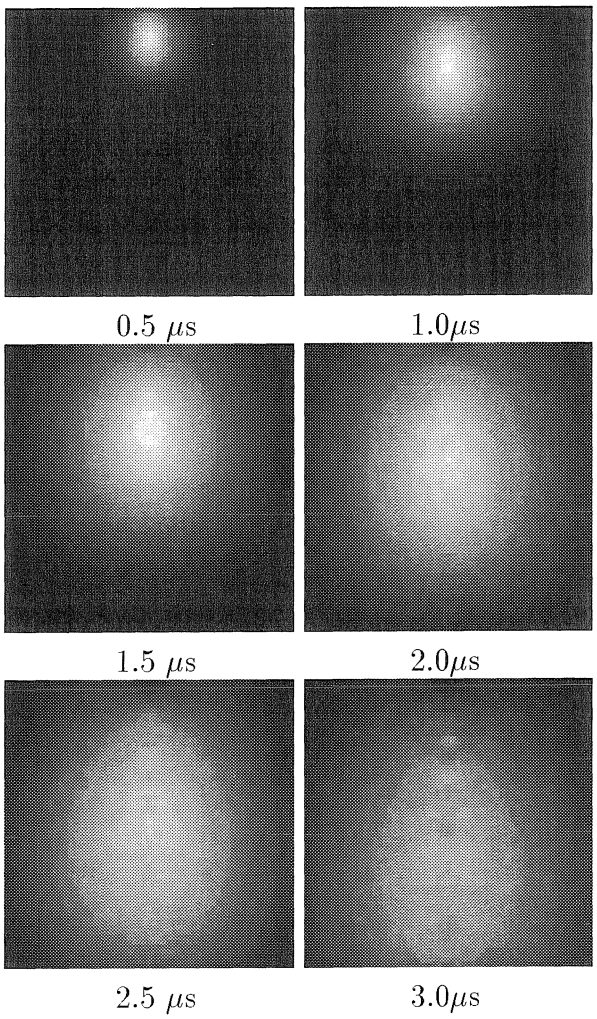

Figure 4.7: Time-sequence images of Si density in a plume generated by the effusion of 1.0 monolayers in 30 ns as it expands into vacuum.

sen layer theory. This is not surprising, however, since only 1.5% of the simulation particles carrying only 0.8% of the plume's energy recondense at the target during the interval $0 < t < 30$ ns. These values are far less than 18.4% and 9.0%, respectively, predicted from Knudsen layer theory.

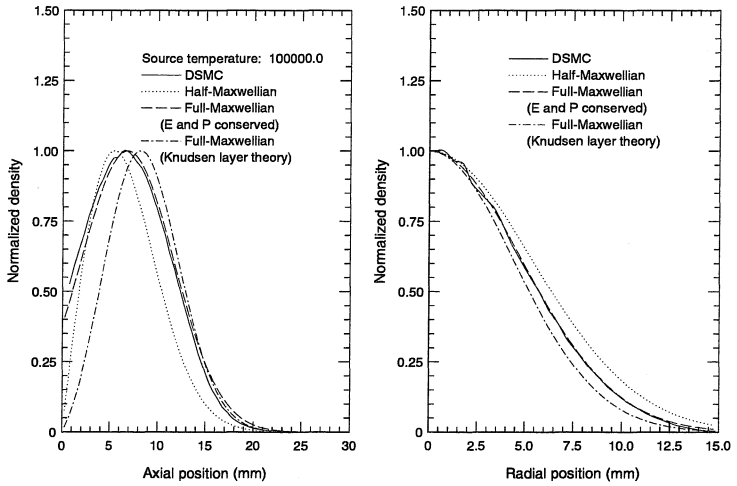

Figure 4.8: Normalized density profile along constant radius (r = 0 mm) contour, and along constant axial position (z = 1.5 cm) contour from the 1.0 μs old 1.0-monolayer plume appearing in Figure 4.7. Profiles are consistent with the collisionless expansion of shifted-Maxwellian atoms with energy and momentum conserved.

Figure 4.9 shows the surface density of the film and the average energy per particle as functions of radial position. Also shown is the impact rate as a function of time. Each of these plots is consistent with a transition to a shifted-Maxwellian while conserving momentum and energy and not the steady-state Knudsen layer model. In this simulation, 25.1 percent of the atoms deposit onto the substrate and 5.4% are back-scattered into the target after 9 μs.

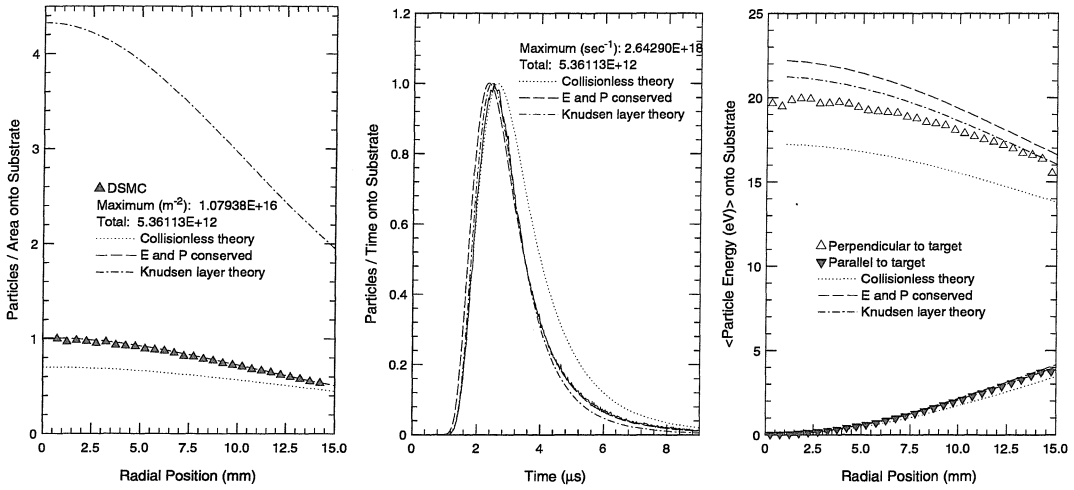

Figure 4.9: (Left) Particle density on the substrate as a function of radial position for 1.0 monolayer plume. (Center) Impact rate as a function of time. (Right) Average axial and radial energy per particle incident onto the substrate.

4.5 A comparison of DSMC results and theory for high effusion rates ($\alpha \gg 1$)

4.5.1 Theory

If one assumes, as before, that a Knudsen layer is in steady state during pulsed effusion, then a plume with a sufficiently small mean free path can be modeled by assuming a region of 1-D unsteady adiabatic expansion exists between the Knudsen layer and the collisionless expansion region. The shifted-Maxwellian distribution function describing atoms which emerge into the collisionless region takes the form

$$f_M(\vec{v},\vec{x}) = \frac{n(\vec{x})}{\pi^{3/2}v_p^3} e^{-\frac{(v_x^2+v_y^2+(v_z-u_M)^2)}{v_p^2}}, \tag{4.47}$$

where $v_p = (2kT_M/m)^{1/2}$. This 1-D problem has been solved analytically [55, 56], producing the relations

$$T_M = T_k \left(\frac{4}{3+M}\right)^2 \tag{4.48}$$

and

$$u_M \approx u_k \frac{4M}{3+M}. \tag{4.49}$$

The quantity M is the Mach number, the ratio of the flow velocity to the sound speed at the position where the plume is considered to begin its collisionless expansion. In this model, a plume which proceeds directly to a collisionless expansion after Knudsen layer formation, without a period of adiabatic expansion, is described using M = 1.0. The normalized density profiles of the plume are then described using equations 4.29 and 4.30 with the parameters $u_M > u_k$, $T_M < T_k$ instead. The degree of forward-peaking in this case is given by equation 4.34, but with ζ having a value $M(3+M)/4$ times greater than in equation 4.35. According to this model, the increase in forward-peaking with an increase in α is explained in terms of an increasing Mach number as the plume expands.

4.5.2 DSMC results

Figure 4.10 shows the best fit parameter n to the relation $n(\theta) \propto cos^n(\theta)$ for the simulated effusion of 1.0 monolayers and 3.16 monolayers. This expression was introduced earlier and used to describe the degree of forward-peaking in plumes. The complexity of equation 4.34 indicates that this fit is only approximate, however, it effectively quantifies forward-peaking when the best fit parameter n is plotted as a function of the number of monolayers effused. The density of each plume is sampled at a fixed *spherical* radius of 1.5 cm at $t = 1.0\mu$s. The parameter n, equal to 1 for collisionless effusion, increases from 4 to 50 as the number of monolayers effused increases from 1.0 to 10.0. A good approximation to this data is $n(\alpha) \approx \alpha$.

Earlier results suggest that a plume expansion model which assumes a steady-state Knudsen layer does not fit DSMC data for $\alpha \approx 1$. This is evidenced by poor fits to normalized density profiles, and to radial-dependent particle flux and energy profiles. It was observed that the DSMC data fits much better to predictions assuming both energy and momentum conservation, and no back-scattering as the distribution function transforms into a shifted-Maxwellian. DSMC simulations focusing on the back-scattering during a 30 ns pulse reveal why this is true. Shown in Figure 4.11 are plots showing the rates at which particle number, momentum, and energy are back-

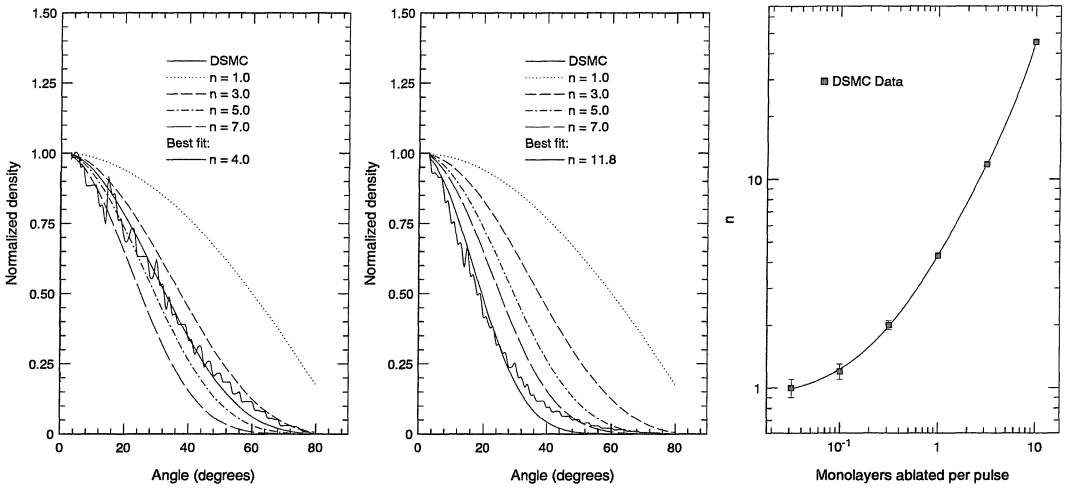

Figure 4.10: (Left) Relative density along a contant radius contour in *spherical* coordinates for a 1.0-monolayer plume. Simulation data is acquired 1.5 cm from the ablation spot after a delay of 1 μs and compared with profiles of the form $cos^n(\theta)$. (Center) Relative density along the same contour for a 3.16-monolayer plume. (Right) Parameter n as a function of the number of monolayers desorbed. Simulation data indicates a rapid increase in forward-peaking when more than a fraction of a monolayer is desorbed.

scattered onto the target as functions of time assuming desorption of 1.0 to 316.0 monolayers. Each is expressed as a percentage of the corresponding rate leaving the target surface.

The maximum observed back-scattered number flux near 14.8% is slightly less than the predicted value of 18.4% from 1-D, steady-state Knudsen layer theory. This is because the dimensionless parameter β for this simulation is about 0.2 and doesn't quite satisfy the requirement that $\beta \ll 1$ necessary to assume 1-D gas dynamics. Similar simulations with a smaller value of β (e.g. a larger spot radius and/or a lower surface temperature) result in a back-scattered particle flux closer to 18.4 percent. More importantly, the asymptotic values are not achieved by the end of the pulse, except for the effusion of more than $\approx$ 30 monolayers. Even if the back-scattered flux achieves steady state by the end of the pulse, the contribution from the early effusion period does not appear negligible for the effusion of less than 316 monolayers in 30 ns. Only above this rate is it reasonable to assume that a fully-formed Knudsen layer exists during the entire effusion period. This result is consistent with the findings of

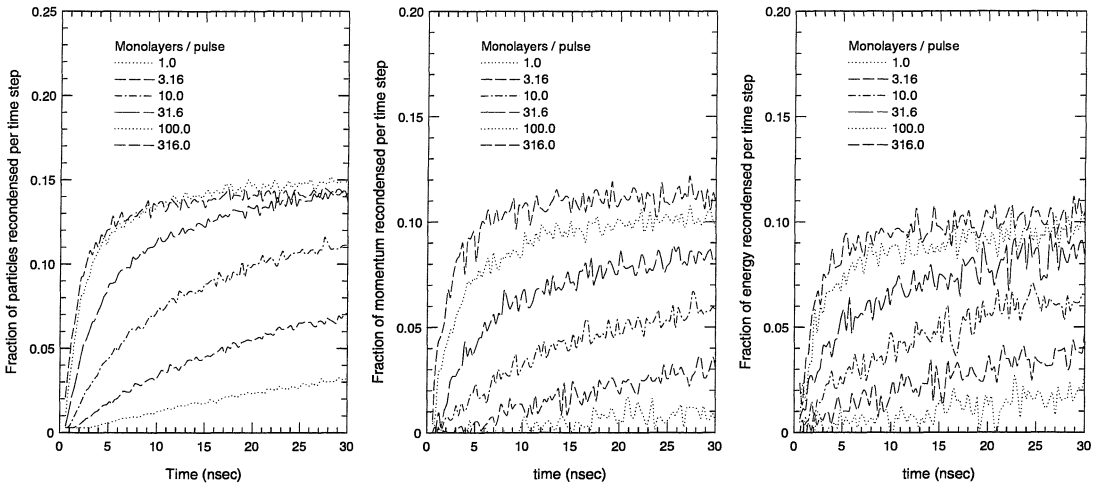

Figure 4.11: Rates at which particle number, momentum, and energy are back-scattered onto the target vs. time during a 30 ns pulse.

Sibold and Urbassek [58] who compare the parallel and perpendicular temperatures to determine whether a Knudsen layer reaches steady state during pulsed effusion. They estimate that about 20 monolayers are necessary. The main point here is that forward-peaking always occurs before a steady-state Knudsen layer forms, regardless of effusion temperature, so any description of forward-peaking which assumes the existence of a steady-state Knudsen layer is misleading.

An additional problem with the analytical model is the assumption that a 1-D adiabatic expansion occurs after the flow emerges from the Knudsen layer, and that the scale length of this expansion is small. Equation 4.6 defines the collisional scale for effusion plumes, equal to about 6.0 cm for pulsed effusion of 3.16 monolayers from a 1.0 mm radius effusion spot. Since this is about 60 times the radius of the effusion spot, a 1-D expansion model is not justified. Because equation 4.6 suggests that the axial dimension of the plume during its collision period can exceed the effusion spot radius for for the effusion of more than about 0.25 monolayers, radial expansion cannot be neglected for any plume which exhibits forward-peaking. Also, since 6.0 cm is twice the target-substrate spacing distance, a collisionless expansion model is invalid inside the volume.

Figure 4.12 shows a set of radial profiles acquired from 1.0 μs old plume generated by the effusion of 3.16 monolayers ($\alpha \approx 12$) along parallel contours spaced evenly by

3.0 mm. The profiles are significantly different, those near the target being narrower and non-Gaussian. Far from the target the radial profiles have a Gaussian form, as equation 4.30 predicts, and the temperature parameter suggested is near T_k, but this parameter has little physical meaning since the collisionless expansion model used to derive equation 4.30 is invalid. The non-Gaussian appearance of the radial density profiles near the target, which becomes even more apparent at higher effusion rates, indicate that radial expansion of the plume cannot be ignored. Very near the target and close to the plume axis, the expansion seems analogous to the gas dynamics of an infinitely long cylindrical volume of gas contained within $0 < r < r_{spot}$, whose bounding surface is removed to allow the gas to expand radially into vacuum. Although a solution for this problem is not available in closed form, insight into its qualitative behavior can be obtained by examining the analytical solution to a one-dimensional adiabatic expansion of a gas with zero initial flow velocity into vacuum in Cartesian geometry. If the boundary at $z = 0$ of a fixed volume of gas existing between $-l < z < 0$ and having a uniform density n_0 and sound speed $a_0 = \gamma k T_0/m$ is removed at $t = 0$, the density some later time $0 < t < l/a_0$ satisfies [55]

$$n(z) = \frac{n_0}{4}\left(3 - \frac{z}{a_0 t}\right)^3. \tag{4.50}$$

In contrast to a Gaussian profile, this function diminishes rapidly with z near $z = 0$ and satisfies $d^2n(z)/dz^2 > 0$ for all z. This is qualitatively similar to the way the radial dependence of density along fixed z contours behaves near the target.

Curiously, an excellent fit is obtained still to the axial density profile in Figure 4.12 by using a collisionless expansion profile with flow velocity and temperature parameters in a shifted-Maxwellian derived assuming that both momentum and energy are conserved, that is, $u = 6798$ m/s and $T = 80{,}970$ K. Although these parameters are reasonable for describing the velocity distribution for the plume at $t \approx t_p$ since only a small fraction of the particles recondense during the effusion period, 4.42 is not justified because the expansion cannot safely be approximated as collisionless.

In Figure 4.13 the radially-dependent particle flux and average energy per particle

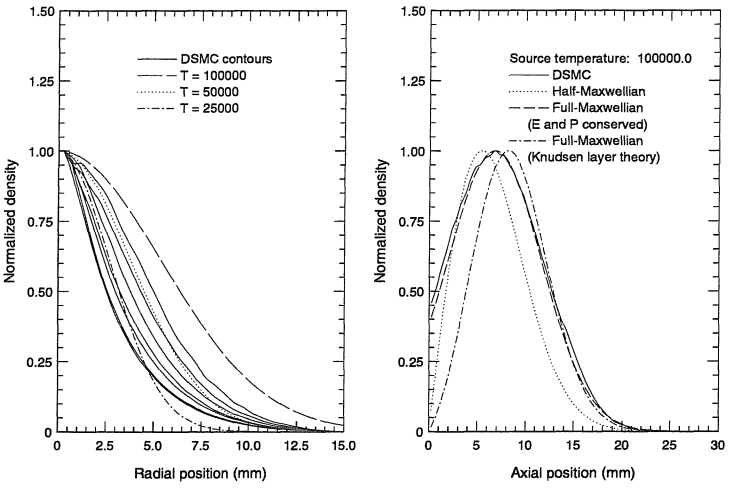

Figure 4.12: (Left) Normalized density profiles along constant z contours spaced by 3.0 mm for a 1.0 μs old plume generated assuming effusion at rate of 3.16 monolayers in 30 nsec. The breakdown of the collisionless expansion approximation is evident. (Right) Normalized density profile along a constant radius (r = 0 mm) contour. Curiously, the collisionless expansion model describes this profile well.

incident onto the substrate are shown, and compared to theory. One might conclude from this data alone that the expansion model which assumes a steady-state Knudsen layer is correct, closely predicting the particle flux and average energy that are observed in simulation. Because the normalized density profiles do not match those predicted using this model, however, this is regarded as coincidence. For this simulation 33.1% of the effused atoms are deposited onto the substrate and 11.7% are back-scattered into the target after 9 μs.

The particle flux and average energy per particle incident onto the substrate for a 10-monolayer plume are shown in Figure 4.14. Assuming that all the incident particles stick, the increase in forward-peaking is seen to result in a significant increase in the surface density of the film on-axis, and a more rapid drop in surface off-axis. Acceleration of the plume during the expansion is evidenced by an increase in the average energy per particle. Applying the steady-state Knudsen layer model to these data would indicate a Mach number near 2.58, or a plume temperature T_M = 50,000 K and a flow speed u_M = 82,000 m/s at the instant collisionless expansion begins. It is easy to show, however, that these parameters do not produce normalized density profiles which match the DSMC data. For this plume, 46.9% of the effused atoms

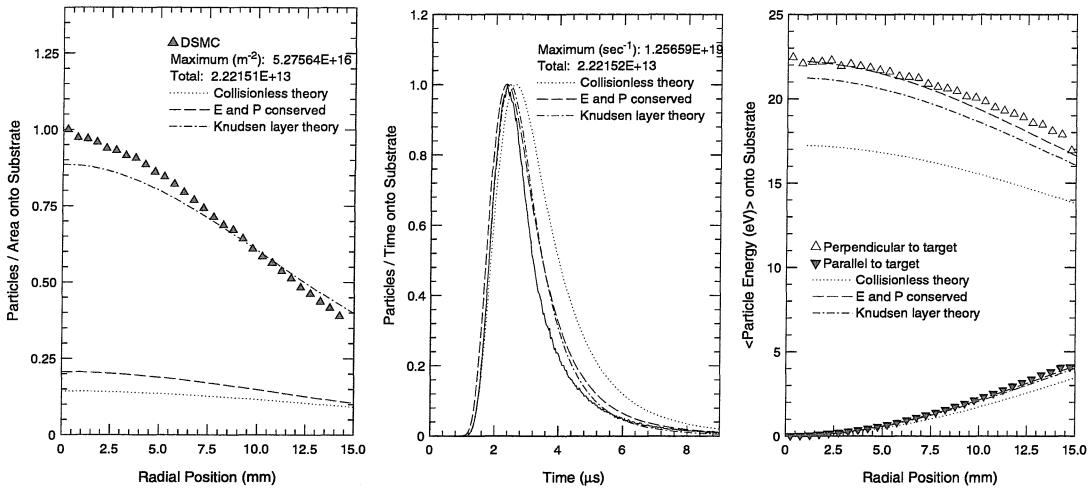

Figure 4.13: (Left) Particle density on the substrate as a function of radial position for a 3.16-monolayer plume. (Center) Impact rate as a function of time. (Right) Average axial and radial energy per particle incident onto the substrate.

deposit onto the substrate and 17.7% are back-scattered onto the target after 9.0 μs.

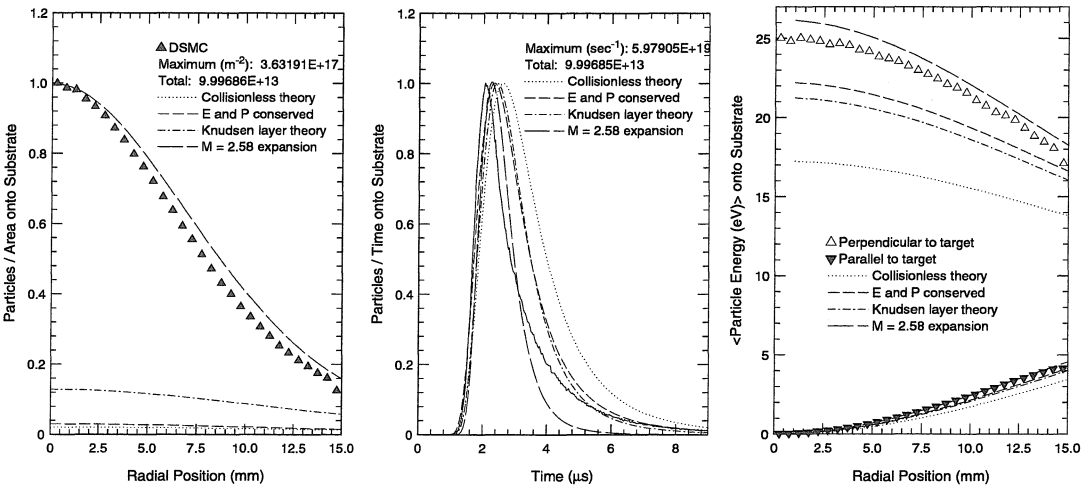

Figure 4.14: (Left) Particle density on the substrate as a function of radial position for a 10-monolayer plume. (Center) Impact rate as a function of time. (Right) Average axial and radial energy per particle incident onto the substrate.

For high effusion rates ($\alpha > 1$), where the back-scattered flux onto the target is significant, the density profiles are strongly dependent on the choice of boundary condition at the target. In fact, the density at $z = 0$ nearly doubles when specular reflection occurs for $t > t_p$, shifting the peak in the normalized profile much closer to the target and slowing down the leading edge of the plume. In Figure 4.15 two

axial density profiles (r = 0.0 mm) from a 10-monolayer plume are compared, one obtained assuming specular reflection at the target for $t > t_p$ and the other assuming recondensation. Recondensation at the effusion spot for $t < t_p$ is assumed in both cases. To help visualize the difference that the target boundary condition produces, Figure 4.16 compares time sequence images of a 10-monolayer plume after 1.0, 2.0, and 3.0 μs for both boundary conditions. Despite these apparent differences in the appearance of plume density images, the choice of target boundary condition produces no significant differences in particle and energy flux onto the substrate.

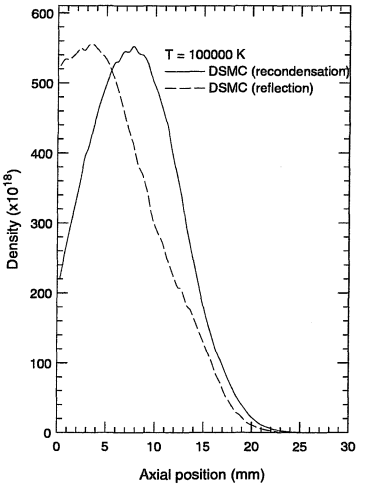

Figure 4.15: A comparison of density profiles assuming either recondenstion or reflection at the target for $t > t_p$. Each profile is from the axis of a 10.0 monolayer plume after a 1 μs delay.

4.6 Summary

In this chapter, general properties of pulsed effusion plumes are investigated using DSMC simulations. It is shown that a dimensionless parameter α can be defined and used to characterize the forward-peaking in the plume due to collisions. This parameter, proportional to the number of monolayers effused, is independent of the effusion temperature. The angular dependence of plume density is shown in simulation to approximately satisfy $n(\theta) \propto cos^{\alpha}(\theta)$. A second dimensionless parameter, β, is defined and used to estimate the validity of a 1-D expansion during the laser

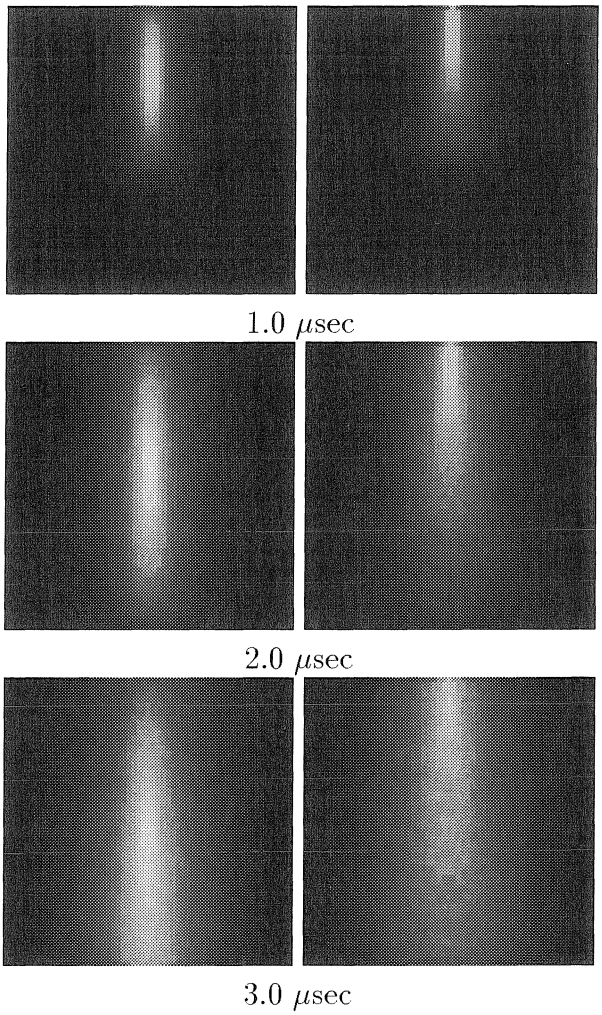

Figure 4.16: Time-sequence images of Si density as a 10-monolayer effusion plume expands into vacuum. Effects of the target boundary condition for $t > t_p$ are compared: (left column) recondensation, (right column) specular reflection.

pulse. Finally, a characteristic scale length d_c, dependent on α and proportional to the effusion spot size, is defined and used to estimate the size of the expanding plume when it becomes collisionless.

Although plume forward-peaking has been predicted analytically by assuming a period of 1-D adiabatic expansion following the formation of a steady-state Knudsen layer, the density profiles assuming this model do not match well to those produced in DSMC simulations. Differences are believed to result from the breakdown of several assumptions made in the analytical model, including the assumption of 1-D adiabatic expansion, the assumption of subsequent collisionless expansion, and the assumption that the Knudsen layer is in steady state. Use of a 1-D expansion model during the effusive pulse requires that $\beta \ll 1$. The breakdown of this assumption is evidenced by a decrease in the asymptotic values of back-scattered flux onto the target when effusion occurs from very small areas at very high temperatures. Use of a 1-D adiabatic expansion model after the effusive pulse requires that $d_c \leq r_s$ where $d_c \approx r_s \alpha^{1.6}$. The breakdown of this assumption for $\alpha > 1$ is evidenced by non-Gaussian radial density profiles. The most serious problem with the analytical model, however, is the assumption that the Knudsen layer is in steady state during the effusive pulse, which requires that sufficient collisons occur to transform the half-Maxwellian distribution function into a shifted-Maxwellian *and* that the back-scattered particle and energy flux maintain specific steady-state values throughout the pulse. This assumption is tested by DSMC simulations which focus of the back-scattered particle flux, energy flux, and momentum flux during the 30 ns effusion period and compares the results to those predicted analytically. Simulation results suggest that about 30 monolayers must be effused before the back-scattered flux reaches steady state, and more than 300 monolayers must be effused if the transient time to reach steady state is negligible. This result is independent of the effusion temperature.

Lastly, the influence of the target boundary condition at high effusion rates is examined. For a reflecting boundary, the maximum plume density occurs near the target. If recondensation is assumed instead, the peak density occurs further from the target. The choice of target boundary condition appears to have little effect, however,

on the radial or temporal particle and energy flux onto the substrate.

Chapter 5 The development of an ablation model and a comparison of PLIF data with DSMC results for ablation into vacuum

5.1 A target heating model for pulsed effusion

A thorough understanding of the ablation process must begin by considering the laser-target interaction. The physics involved when a solid surface is irradiated by a laser of 10-500 MW/cm^2 intensity is, however, not well understood. It is unfortunate that the results of extensive research on inertial plasma fusion, focusing on the influence of much higher laser intensities (I $>$ 10^9 MW/cm^2 [81]) are not generally applicable to PLA. Since the details of this problem closely depends on the choice of target material and laser fluence, attention is focused here on irradiation of Si by a KrF laser.

A photon from a KrF laser (248 nm) has an energy of 5.0 eV, well above the Si bandgap energy of 1.11 eV, thus photon absorption by Si atoms would place electrons high into the conduction band, and subsequent relaxation processes would heat the bulk of the crystal. If the laser intensity were sufficiently high, the surface would become highly conductive. The reflectivity of an Si surface has been measured at this photon energy, using a Kramers-Kronig analysis to determine the index of refraction and absorption coefficient. Published values [82] of n = 1.68 and k = 3.58 suggest a measured reflectivity $R_s = 0.675$, where

$$R_s = \frac{(n-1)^2 + k^2}{(n+1)^2 + k^2}, \tag{5.1}$$

and a skin depth, given by $d = \lambda/2\pi k$, near 11 nm. Neglecting heat diffusion into the target bulk and heat loss from the target surface, the fraction of the laser energy which is not reflected will be deposited into a thin layer of thickness d. The temperature in

this layer following the pulse can be approximated using

$$T \approx \frac{1}{C}\left(\frac{Q_l(1-R_s)t_p}{\rho d} - H\right), \tag{5.2}$$

assuming the specific heat C (J/kg-K) is constant. Here ρ is the mass density (kg/m^3) of Si and H is the heat of fusion per unit mass (J/kg). The specific heat for a solid can be approximated using the Debye model [78] which predicts

$$C(T) = \frac{9k}{m}\left(\frac{T}{\theta}\right)^3 \int_0^{\theta/T} \frac{x^4 e^x}{(e^x-1)^2}. \tag{5.3}$$

For Si, the Debye temperature θ is 645 K [78]. At high temperature ($T \gg \theta$) the specific heat asymptotically approaches a value near 880 J/kg K, which is consistent with known experimental data [83]. Extrapolating the experimental value to higher temperatures and using H = 1.644 x 10^6 J/kg [84], a modest laser fluence of 1.0 J/cm^2 results in a temperature near 100,000 K for the 11 nm layer of Si at the target surface.

This target heating model can be improved by including thermal diffusion into the target bulk during the laser pulse. Because the characteristic heating depth is significantly smaller than the diameter of the ablation spot, radial heat flow at the edges of the ablation spot may be ignored and one-dimensional heat flow is a reasonable approximation. In this case the temperature everywhere satisfies

$$\frac{\partial T}{\partial t} = \frac{\partial}{\partial x}\left(\alpha \frac{\partial T}{\partial x}\right), \tag{5.4}$$

where $\alpha(T)$ is the diffusivity (m^2 s^{-1}).

An analytical solution is available for the problem of steady irradiation of a semi-infinite slab if the diffusivity and thermal conductivity κ (W m^{-1} K^{-1}) are both constant [85]. The temperature $T(x,t)$ in this case satisfies

$$T(x,t) = T(x,0) + \frac{Q_l(1-R_s)}{\kappa}\left(\frac{\alpha t}{\pi}\right)^{1/2} e^{-x^2/4\alpha t} - x\mathrm{erfc}\left(\frac{x}{2\sqrt{\alpha t}}\right), \tag{5.5}$$

while the surface temperature $T(0,t)$ is described by

$$T(0,t) = T(0,0) + \frac{2Q_l(1-R_s)}{\kappa}\left(\frac{\alpha t}{\pi}\right)^{1/2}. \tag{5.6}$$

The thermal diffusivity of solid Si over a wide range of temperatures is known [83], and this data can be fit to a polynomial of the form

$$\alpha = \sum_0^4 C_n T^{-n}, \tag{5.7}$$

with $C_0 = -1.311082 \times 10^{-7}$, $C_1 = 1.296482 \times 10^{-2}$, $C_2 = 1.978210$, $C_3 = 4.770785 \times 10^2$, and $C_4 = 4.655855 \times 10^4$. These parameters produce an asymptotic value near 1.2 x 10^{-5} m^2/s as the melting temperature is approached. Using this value in the relation $\kappa = C\rho\alpha \approx 24.6$ W $m^{-1}K^{-1}$, and substituting into equation 5.6 gives $T(0,$ 30 ns) = 3100 K. Equation 5.6 predicts this estimate to increase linearly with laser intensity.

Recent models of target heating include the latent heat of fusion in the energy balance [86, 50, 61]. Serious concern about melting can be understood by considering how much power is required to sustain a traveling melt front in an Si target. If such a front travels at the upper-bound speed of sound in a typical solid ($v_s \approx 5$ km/s) [84], then the power per area required to sustain the front is $P/A = \rho H v_s/m \approx 1.9$ GW/cm^2 which is 1-2 orders of magnitude greater than typical PLA laser intensities. A melt front traveling at only 86 m/s would consume all the energy of a laser pulse with a fluence of 1 J/cm^2, resulting in a total melting depth of 2.6 μm. This might suggest that the maximum surface temperature attainable is the melting temperature, and that superheating above 1685 K is impossible. This simplification assumes an infinite diffusivity, however, so it is not obvious whether or not this regime is applicable.

To study this question, a computer code has been developed which numerically solves equation 5.4, employing a finite-differencing method with the laser's intensity included as a source term [85]. Specifically, equation 5.4 is approximated in the

target volume by dividing it into a number of cells which are labeled by some index j. Neglecting melting or freezing, the change in temperature for a cell in the target bulk at time t is given by

$$\Delta T_j(t) = \frac{\Delta t \alpha}{\Delta x^2} \left(T_{j+1} - 2T_j + T_{j-1}\right)(t), \tag{5.8}$$

and the change in the surface temperature at time t is given by

$$\Delta T_0(t) = \frac{2\Delta t \alpha}{\Delta x^2} \left(T_1 - T_0 + \frac{Q\Delta x}{\kappa}\right)(t), \tag{5.9}$$

where $Q = Q_l(1 - R_s) - Q_{vap} - Q_{rad}$ denotes the net intensity (W/m^2) onto the surface. This net intensity includes the laser intensity Q_l, thermal radiation losses estimated using $Q_{rad} = \sigma T_0(t)^4$ where σ is Stefan-Boltzmann constant, and losses due to the latent heat of vaporization carried from the surface by evaporation $Q_{vap} = qP_v(t)/mv_p(t)\pi^{1/2}$, where P_v is the vapor pressure of Si at the temperature $T_0(t)$, q is the heat of vaporization per atom, and $v_p = (2kT_0(t)/m)^{1/2}$. Additionally, κ denotes the thermal conductivity ($W\ m^{-1}K^{-1}$) of silicon at the temperature $T_0(t)$ of the surface cell.

The vapor pressure of silicon at $T_0(t)$ may be estimated by solving the Clausius-Clapeyron equation

$$\frac{dP_v}{dT} = \frac{qP}{kT^2} \tag{5.10}$$

to produce an equation which gives the temperature dependence of the vapor pressure over a range of temperatures where q is assumed nearly constant. The result is

$$P_v(t) = P_0 e^{-q/kT_1(t)}. \tag{5.11}$$

This equation can be fit to tabulated vapor pressure data for Si [84] to produce the parameters $P_0 = 1.85 \times 10^{15}$ Pa and $q = 8.35 \times 10^{-19}$ J/atom. Since the available vapor pressure data is available for molten Si up to 2560 K, extrapolation of this fit is employed for higher temperatures. This seems reasonable as long as $kT \ll q$ or

$T \ll 12{,}500$ K.

The target is described using a 1000-point grid with a cell width of 10 nm, the temperature in each cell initialized to 300 K. This width is chosen based on the physical requirement that each cell be much larger than the cubic lattice spacing of 0.543 nm [78]. Comparable to the skin depth of Si at 248 nm, this cell width justifies the treatment of laser energy deposition onto the target as surface heating. Having selected the cell width, a time step of 0.1 ps is then used because it easily satisfies the stability requirement [85] $\Delta t \ll \Delta x^2/\alpha$, and also because a smaller time step has no apparent effect on the outcome.

The temperature-dependent diffusivity and heat conductivity parameters for Si are calculated for each grid cell using equations 5.7 and 5.3, respectively. Although extrapolation of these functions beyond 1685 K is risky, especially since a phase change in Si occurs at that temperature, thermodynamic parameters appear asymptotic with increasing temperature, suggesting that they are nearly constant for $T > 1685$ K. As long as the true values are approximately continuous across the phase transition, and do not vary much with increasing temperature, the extrapolation is reasonable.

Melting is included in the model by checking at each time step whether $T_j + \Delta T_j$ exceeds T_m, the melting temperature. If so, the temperature of cell j is set to T_m and a specific energy $C(T_j + \Delta T_j - T_m)$ becomes available for melting. The fraction of the material in the cell melted during the time step is then given by $C(T_j + \Delta T_j - T_m)/H$. During subsequent time steps, the fraction of material melted in this cell increases until the fraction melted exceeds unity, at which time the cell temperature again increases normally according to equation 5.8 or 5.9. A similar procedure is used to treat freezing if the calculated temperature changes are negative.

Shown in Figure 5.1 are the results of the computer simulation described for laser fluences from 0.5 to 8 J/cm^2. From these data, two important problems for this model, as it relates to PLA, may be identified. The first is that the peak target surface temperature is much too low to explain the ≈ 1 cm/μs characteristic velocity of plume atoms estimated using PLIF imaging of Si plumes and single-point diagnostics of Cu plumes presented earlier. For effusion at only 3800 K, the peak surface

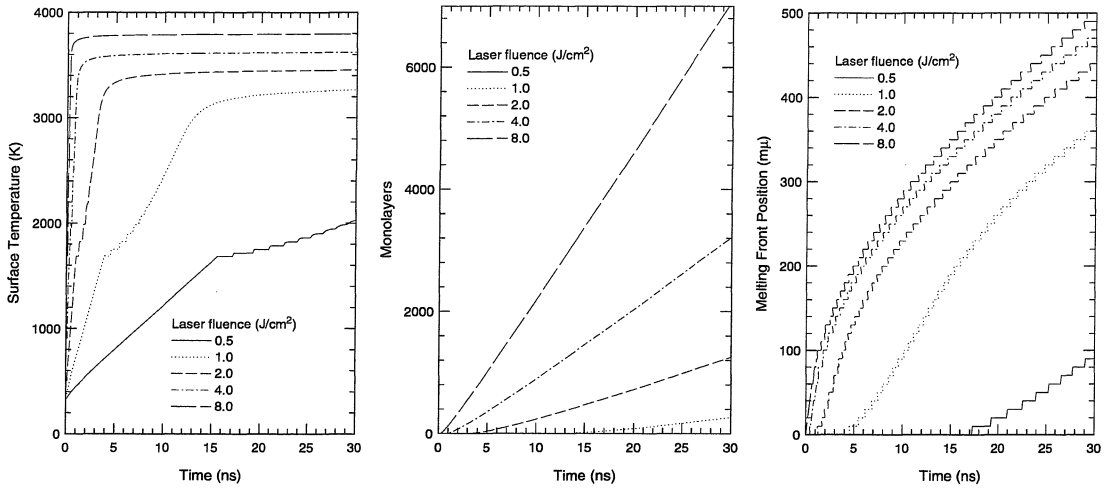

Figure 5.1: (Left) Target surface temperature, (Center) total number of monolayers effused, and (right) melt front position as functions of time using a 1-D target heating model.

temperature shown in Figure 5.1 for a fluence of 8 J/cm^2, the characteristic velocity is only 1.5 mm/μs. Efforts have been made to estimate the plume temperature near the target surface using emission spectroscopy [25], and the results of a similar experiment are presented here. If the early plume is described as a Maxwellian gas at some temperature T, then the density fraction in some arbitrary excited state (2) is given by

$$n_2(z,t) = \frac{n(z,t)g_2}{Z} e^{-E_2/kT}, \tag{5.12}$$

where $Z = \sum_i g_i exp(-E_i/kT)$ is the partition function for the atom and $n(z,t)$ is the density of the plume at the point from which the emission signal is collected. The rate of spontaneous emission from state (2) to some lower state (1) is given by $A_{21}n_2(z,t)$, so that the fluorescence signal gathered from a point z in the plume can be written as

$$S_{21}(z,t) = Cn(z,t)g_2A_{21}e^{-E_2/kT}, \tag{5.13}$$

where C is some constant which includes Z. An integral of the emission signal over time gives

$$S_{21} = \int_0^\infty S_{21}(t)dt = Cg_2A_{21}e^{-E_2/kT}, \tag{5.14}$$

which can be re-arranged to give

$$ln\left(\frac{S_{21}}{g_2 A_{21}}\right) = \left(\frac{-1}{kT}\right) E_2 + ln(C). \tag{5.15}$$

This equation suggests that if the quantity $ln(S_{21}/g_2A_{21})$ is plotted vs. E_2 for several different emission transitions from the plume, then the result should be linear, with a slope given by $-1/kT$. Shown in Figure 5.2 is the result for emission gathered from a Cu plume, using time-integrated LIF signals similar to the one in Figure 1.4, but acquired at a distance only 1.0 mm from the target. Signal from four different transitions are included, two 4d $^2D \rightarrow$ 4p $^2P^0$ transitions at 515.324 nm ($g_2A_{21} = 4.7\times 10^8$ sec^{-1}) and 521.820 nm ($g_2A_{21} = 5.8\times 10^8$ sec^{-1}), one 4p $^2P^0 \leftarrow$ 4s ^2S transition at 324.754 nm ($g_2A_{21} = 4.1\times 10^8$ sec^{-1}), and a 4d' $^4G \rightarrow$ 4p' $^4F^0$ transition at 330.795 nm ($g_2A_{21} = 5.1\times 10^8$ sec^{-1}). A least-square linear fit to the data produces a temperature parameter of 23,700 K, which is much lower than the surface temperature estimated by fitting TOF profiles to the collisionless expansion theory. This temperature is still much greater than the critical temperature of copper however. Also, the treatment of state populations using a Boltzmann distribution implicitly assumes that the collision rate among atoms is much greater than the spontaneous decay rates. After the plume expands to a distance 1.0 mm from the target this assumption may not be valid. Consequently, the populations in all the excited states may be lower than they would be for a more collisional gas in equilibrium at the same temperature. The temperature $T = 23{,}700$ K may therefore be interpreted as a lower bound on the maximum plume temperature prior to collisionless expansion.

The second problem is that the number of monolayers effused during a 30 ns laser pulse is much greater than typical values measured experimentally. For example, a measurement of this quantity for an Si target irradiated by a 300 mJ/pulse KrF laser was made by examining the target under an SEM after 61,200 pulses. A 3-inch wafer is rotated so that the ablation spot traced out a 1.8 mm wide annulus of 2.5 cm radius, etched to an average depth near 50 μm. A scanning electron micrograph of a cross section of this ablated annulus is shown in Figure 5.1. These data suggest that about

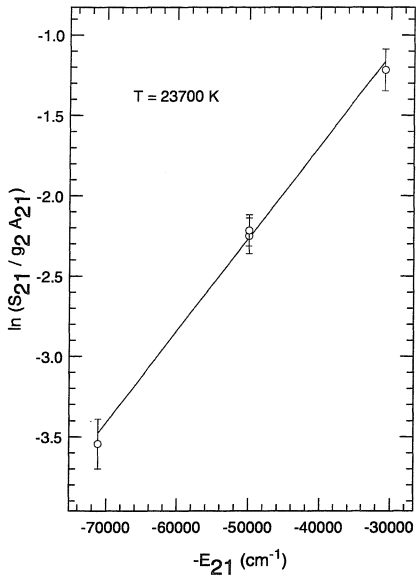

Figure 5.2: Emission signal from four different transitions plotted against the upper-state energy as described in equation 5.15. A linear fit suggests a Boltzmann population of excited states, and the slope of the line may be used to infer a plume temperature.

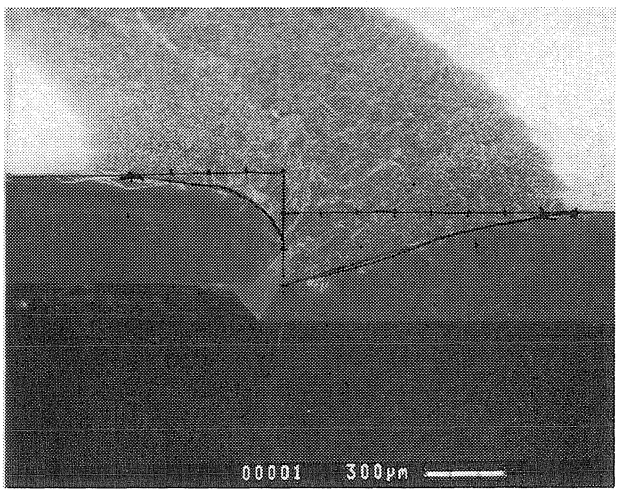

Figure 5.3: SEM photograph showing a cross section from the annulus of an Si target ablated by a KrF laser.

7.0 x 10^{20} total atoms are liberated, or 1.2 x 10^{16} atoms/pulse. Since the ablation spot is rectangular with dimensions near 1.8 mm x 1.5 mm, an ablation rate of 630 monolayers/pulse at a fluence near 10 J/cm^2 is implied. Since some of this material may have been removed in the form of particulates [20], this figure represents an upper bound. Figure 5.1 shows that the time-integrated number of effused monolayers is about 7000 for a slightly lower fluence of 8 J/cm^2, about an order of magnitude higher than the measured value. Measurements of Si film thickness by Rutherford Back-scattering Spectrometry (RBS) after several pulses of a KrF laser at a lower fluence of 2 J/cm^2 suggest an ablation rate of only 10 monolayers/pulse, while the model predicts 1200 monolayers desorbed at this fluence.

5.2 An investigation of plume heating by the laser

Direct evidence that PLA plume particles are more energetic than can be explained by thermal effusion and indirect evidence that the number of monolayers desorbed during PLA is much less than the number estimated assuming thermal effusion using a target heating model suggests that laser energy is being absorbed by the plume, and that this absorption reduces target surface heating and therefore restricts further effusion. This reasoning depends on whether mechanisms exist for atoms in an expanding plume produced by thermal effusion to become heated to high temperature during a 30 ns laser pulse, and also shield the target surface from further heating. It has been suggested [5, 87] that inverse-Bremsstrahlung (IB) absorption is sufficient to produce these desired effects, and recent models [60, 61, 88, 89] which include IB absorption support this hypothesis. To further corroborate this important aspect of PLA, and investigate the consequences of plume heating by the laser, an order-of-magnitude calculation is provided here, followed by results of a simple computer model.

5.2.1 Order-of-magnitude plausibility test for plasma breakdown by inverse-Bremsstrahlung absorption

The density of an Si plume created by thermal effusion can be estimated at the target surface using the relation $n_c = P_v/kT$. Using equation 5.11 for the vapor pressure P_v and assuming a surface temperature of 3000 K, the density near the target is about 8 x 10^{24} m^{-3}, about 0.01% the density of solid Si. At a surface temperature of 3000 K about 10 monolayers of Si desorb every nanosecond.

The Saha equation, given by [90]

$$\frac{n_i}{n_n} \approx 2.4 \times 10^{21} \frac{T^{3/2}}{n_i} e^{-U/kT}, \tag{5.16}$$

can be used to estimate the density of ions n_i in an equilibrium plasma at temperature T. In this equation, U is the ionization energy per atom and n_n is the density of the neutral atoms. Using U = 8.149 eV for Si, and a temperature of 3000 K, the plasma density can be estimated at 8 x 10^{18} m^{-3}. Since the 5.0 eV energy per photon for a KrF laser slightly exceeds the 4.85 eV work function of Si [84], photo-ionization might be expected to produce more electrons in the plume than the Saha equation predicts. This contribution to the free electron density, however, is ignored here.

The absorption coefficient (m^{-1}) for inverse-Bremsstrahlung absorption by the free electrons in this weakly ionized plasma is given by [25]

$$\alpha = 3.69 \times 10^{10} \frac{Z^3 n_i^2}{T^{1/2}\nu^3}(1 - e^{-h\nu/kT}) \tag{5.17}$$

A KrF laser (248 nm) and a plasma density of 8 x 10^{18} therefore suggest an absorption length $1/\alpha$ near 3.5 cm. Since the characteristic width of the plume, given by $d_p = t_p(\pi kT/2m)^{1/2}$, is about 35 μm, free electrons in the plume are expected to initially absorb about 0.1% of the laser power. If the laser intensity is about 33 MW/cm^2 (1 J/cm^2 in 30 ns), the electrons could therefore be heated to 100,000 K in only 15 ps, a time that is very short compared to the duration of the laser pulse.

Since inverse-Brehmsstrahlung absorption directly heats the free electrons in the

plasma, it is important to estimate the rate at which electron energy is transferred to the bulk of the plume, and determine whether or not this rate is also rapid. A rough estimate of the relaxation time for energy transfer from the electrons to the ions is given by [91]

$$t_{eq} = 5.87 \times 10^6 \frac{\lambda_e \lambda_i}{n_i ln\Lambda} \left(\frac{T_e}{\lambda_e} - \frac{T_i}{\lambda_i} \right)^{3/2} \tag{5.18}$$

where λ_e and λ_i are the ratios of the electron and ion masses to the proton mass, respectively, and T_e and T_i are the temperatures of the electrons and ions. The plasma parameter Λ is defined by $\Lambda = 12\pi n_i \lambda_D^3$ where $\lambda_D = (\epsilon_0 k T_e / n_i e^2)^{1/2}$ is the Debye length. For this plasma the Debye length is about $\lambda_D \approx 1.5$ μm so $\ln\Lambda \approx 6.8$. The relaxation time in this case simplifies to

$$t_{eq} \approx 1 \times 10^9 \frac{T_e^{3/2}}{n_i} \tag{5.19}$$

If $T_e = 3000$ K and $n_i = 8$ x 10^{18} m^{-3}, then $t_{eq} \approx 20$ μs, implying that energy transfer to the ions is much slower than the rate at which electrons are heated.

It seems likely that an unbounded plasma with a hot electron component and a cooler ion component would experience charge separation leading to ambipolar diffusion [90] which accelerates the ions. The electrons are also likely to transfer energy to the ions through collisionless collective processes [91] such as electrostatic instabilities which have a characteristic time scale given by $1/\omega_p$, where $\omega_p \approx 9 n_i^{1/2}$ is the plasma frequency. For a plasma density of $n_i = 8$ x 10^{18} m^{-3}, the time scale of energy transfer may therefore be much smaller, closer to 40 ps. If the ion-neutral energy transfer rate is then estimated using the relation $t_{eq} = 1/\sqrt{2}\sigma n v_p$, where σ denotes the impact cross section and v_p denotes the characteristic thermal speed, the neutrals are heated by the ions on a 100 ps time scale, comparable to that for electron-ion energy exchange. This calculation assumes a Lennard-Jones diameter of 2.9×10^{-10} m [79], $n \approx 8 \times 10^{24}$ m^{-3}, and T = 3000 K. It therefore seems reasonable, when considering a 1-10 ns time scale of the plume's expansion, to assume that the energy absorbed by the electrons is transferred instantaneously to the plasma bulk. Making this assumption, a plasma described by $n = 8$ x 10^{24} m^{-3}, $n_i = 8$ x 10^{18} m^{-3},

and T = 3000 K, would be heated at a rate near 10 K/ns. Although this rate of plume heating may initially be slow, the Saha equation is strongly temperature-dependent. Small increases in plume temperature produce dramatic increases in the ion density, which then result in even larger increases in the IB absorption rate. It is therefore conceivable that once the plume begins to absorb even a very small fraction of the laser's energy, it may become highly ionized and heated to high temperature.

If the characteristic absorption length $1/\alpha$ becomes smaller than the width of the plume, the target surface would be shielded from further laser heating, causing a rapid decline in the target surface temperature and effusion rate. If plasma breakdown occurs within the first few nanonseconds of the laser pulse, the total number of monolayers effused would be significantly lower than the number predicted earlier using the target heating model. In this case, the temperature of the plume would likely become limited by radiative losses which would inhibit further increase. If the plume becomes highly ionized, the characteristic absorption length may be much smaller than the width of the plume. This might suggest all of the laser's energy is absorbed within the plume's leading edge and thermal equilibrium throughout the plume is not a reasonable assumption. The self-collision time for the electrons, given by [91]

$$t_c = 1 \times 10^6 \frac{T_e^{3/2}}{n_i} \left(\frac{m_e}{m_p} \right)^{1/2}, \tag{5.20}$$

is 25,000 times faster than the electron-ion relaxation time, however, so the electron temperature remains effectively constant over the width of the plume. If the plasma density is approximated as uniform, the energy transfer from the free electrons to the ions and neutrals therefore occurs uniformly over the plume volume.

5.2.2 A simple 1-D computer model to investigate plasma breakdown

Plasma breakdown and its consequences can be investigated by including IB absorption in the 1-D effusion plume generated in the target heating model. If the density

of the plume is approximated as uniform, it can be estimated at time t by defining a characteristic width determined assuming momentum conservation, that is

$$d_p(t) = \int_0^t u(t')dt', \tag{5.21}$$

where

$$u(t) = \frac{1}{2N_p(t)m}\int_0^t P_v(t')dt' \tag{5.22}$$

is the velocity of the plume's center-of-mass and

$$N_p(t) = \frac{1}{(2\pi km)^{1/2}}\int_0^t \frac{P_v(t')}{T_0(t')^{1/2}}dt' \tag{5.23}$$

is the total number of particles per area in the plume. The temperature of the plume can be approximated assuming energy conservation and a shifted-Maxwellian velocity distribution, that is

$$T_p(t) = \frac{1}{3k}\left(\frac{2E_p(t)}{N_p(t)} - mu^2(t)\right), \tag{5.24}$$

where the energy per area in the plume $E_p(t)$ is given by

$$E_p(t) = \frac{(2\pi k)^{1/2}}{m}\int_0^t P_v(t')T_0(t')^{1/2}dt' + \int_0^t P_{IB}dt' - \int_0^t P_{EM}dt'. \tag{5.25}$$

The quantity $P_{IB}(t)$ denotes the power transferred per area to the plume via inverse-Bremsstrahlung absorption and $P_{EM}(t)$ denotes the radiative losses per unit area.

For a uniformly dense plasma in equilibrium, the Saha equation can be used to estimate the ion density n_i, which in turn can be used to estimate the inverse-Bremstrahlung coefficient α. Accounting for absorption from both the incident and reflected laser light, the IB power absorbed per unit area can be estimated using

$$P_{IB}(t) = \frac{Q_l}{N_p(t)}(1 - e^{-\alpha(t)d_p(t)})(1 + R_s e^{-\alpha(t)d_p(t)}). \tag{5.26}$$

The radiative losses per area are modeled as emissive, using $P_{EM} = \epsilon\sigma T_p^4$ with an emissivity ϵ proportional to the plume density.

Shown in Figure 5.4 are plots describing plume properties as a function of time, assuming laser fluences of 0.5-8 J/cm^2. Plasma breakdown is seen to occur when the

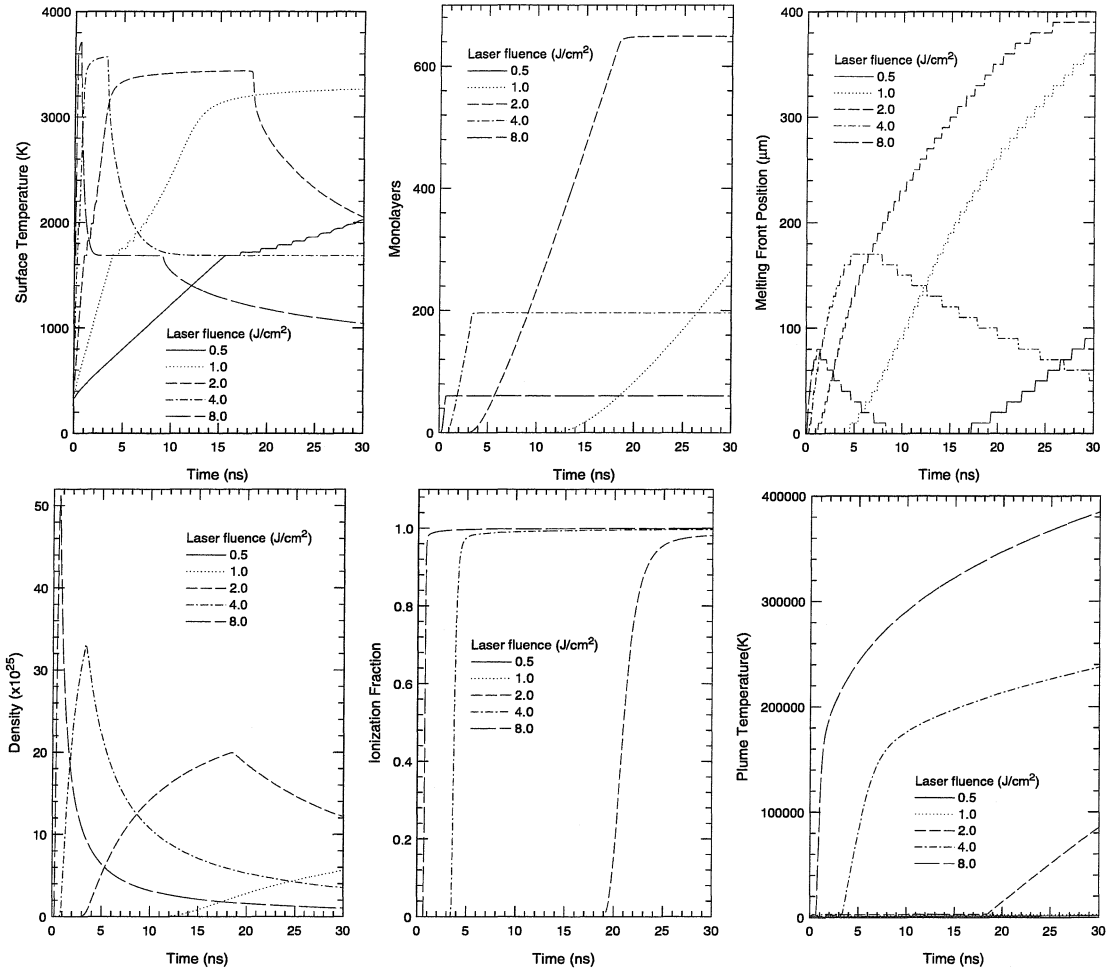

Figure 5.4: Properties of an Si target and 1-D plume predicted using a simple target heating model with IB absorption in a 1-D plume. (Top row) Target surface temperature, total monolayers effused, and melt front location. (Bottom row) Plume density, ionization fraction, and temperature.

temperature of the target surface reaches about 3400-3600 K. Depending on the laser fluence, this can occur at any time during the pulse, or not at all, as is observed for a laser fluence less than 2.0 J/cm^2. When breakdown does occur, it is rapid. This is evidenced by a transition from ≈ 0 to 100% ionization within 1.0 ns, during which time the total plume density remains nearly constant. Following breakdown, the plume temperature increases rapidly, asymptotically approaching some upper bound as the plume's radiative energy losses, which presumably increase with plume temperature,

negate the absorbed laser power. Target shielding following breakdown produces an abrupt drop in the effusion rate, resulting in a total desorption which decreases with increasing laser fluence. At 2.0 J/cm^2 the 640 monolayers effused is much less than what the value predicted without plasma breakdown, but still much higher than is observed experimentally. Spatial variation in both plume density and laser intensity might be responsible for localized regions of high energy deposition, causing plasma breakdown far sooner than can be predicted using this simple model. This could significantly decrease the number of monolayers effused before target shielding effectively terminated further effusion. At 8.0 J/cm^2 the 60 monolayers predicted to be desorbed is about an order of magnitude lower than the value estimated experimentally. Because the target surface exhibits evidence of cone formation [92] when viewed through a scanning electron microscope (SEM) (see Figure 5.1), ion sputtering following plume breakdown may be responsible for the bulk of the plume atoms at this high fluence and not thermal effusion.

The important suggestion made by these simulations is that although the characteristic velocity of particles created by thermal effusion from a laser-heated target surface is much lower than what is often observed experimentally, it is reasonable to assume that plume heating via IB absorption explains plume expansion from a source whose temperature parameter is 100,000 K or greater. Simulations also suggest that while target heating and thermal effusion throughout a 30 ns laser pulse at a fluence > 1 J/cm^2 results in the desorption of far more monolayers per pulse than is observed experimentally, target shielding following plasma breakdown could significantly decrease the number of monolayers desorbed, bringing this parameter within an order-of-magnitude of experimentally observed values as well.

5.2.3 A model for DSMC simulations of expanding plumes

While thermal effusion from a surface with a time-dependent temperature may be easily treated using the DSMC method, it is difficult to explicitly include IB absorption within an expanding plume using this technique. Since DSMC treats the plume as an

ensemble of particles whose interactions are treated statistically using cross sections, knowledge of cross sections for collision-induced ionization, multi-photon ionization, recombination, charge exchange, photon absorption by free electrons, and collisional energy exchange among multiple species must be known. Alternatively, the results of the simple 1-D target-heating model may be used to make simplifying assumptions about the plume during the laser pulse, and then simulate only the subsequent plume expansion into vacuum or a background gas using the DSMC method.

Shown in Figure 5.5 is a schematic diagram depicting three phases of plume evolution: target heating and thermal effusion, plume heating, and finally plume expansion. Assuming that at least one monolayer is desorbed prior to breakdown, the plume may be described in the first phase using a shifted-Maxwellian distribution function of the form

$$f(\vec{v}) = \frac{n_0}{\pi^{3/2} v_p^3} e^{-\frac{v_x^2 + v_y^2 + (v_z - u)^2}{v_p^2}}, \tag{5.27}$$

where $v_p = (2kT/m)^{1/2}$. The parameter T in this distribution will be slightly less than the estimated 3400-3600 K peak target temperature immediately prior to breakdown, and the parameter u will be close to $v_p \approx 1.5$ km/s. As breakdown and plume heating occur, the flow speed u should remain nearly constant while T increases rapidly. During this phase, radiation losses, which increase rapidly with temperature, eventually restrict further increase in T. The distribution function appropriate for the hot plume is again given by equation 5.27, however since $v_p \gg u$, u may be neglected. The plume may be modeled after the heating phase as an equilibrium gas of uniform density and temperature occupying a thin $\approx 200\mu$m disc near the target surface.

The third phase, plasma expansion after laser heating, may be treated using the same DSMC method employed earlier to study effusion from a hot source. This is evident if an imaginary boundary at $z = 0$ is considered to separate the plume from vacuum as expansion begins. The particle flux in the velocity range v_i to $v_i + dv_i$ crossing this boundary is given by $v_z f(\vec{v}) dv_x dv_y dv_z$, where

$$f(\vec{v}) = \frac{n(t)}{\pi^{3/2} v_p^3} e^{-\frac{v_x^2 + v_y^2 + (v_z)^2}{v_p(t)^2}}. \tag{5.28}$$

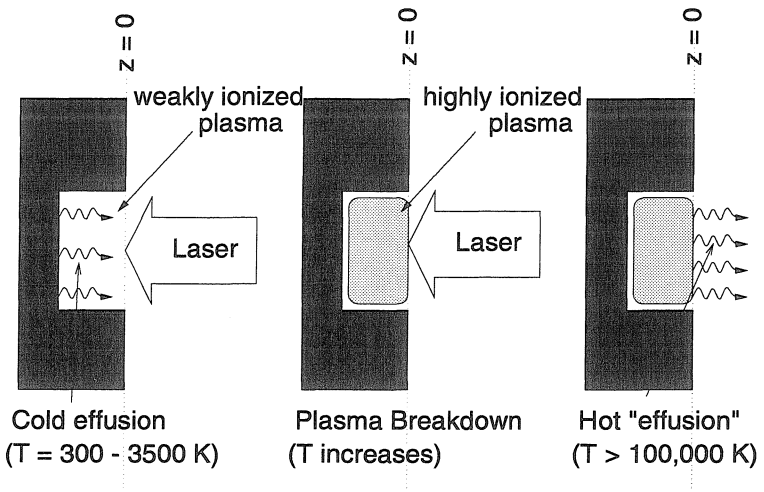

Figure 5.5: Schematic diagram showing how plume creation may be modeled as a hot effusion process following plasma breakdown.

The density $n(t)$ and $v_p(t) = (2kT(t)/m)^{1/2}$ are two free time-dependent parameters describing the plasma to the left of the boundary, which is assumed to remain in equilibrium as atoms cross the boundary.

Any of several models may be used to determine $T(t)$ and $n(t)$ which describe the plasma during this expansion phase. The simplest is to assume that these functions are constant, as they would be for real effusion from a hot surface. This model is not consistent however with two important physical constraints: the density of the plasma to the left of the imaginary boundary must decrease appropriately as atoms cross into vacuum, and the energy flux across the boundary must result in a corresponding decrease in energy in the plasma remaining on the left. Assuming a monatomic plasma, the energy density is given by $3nkT/2$ and the average energy per particle crossing the boundary is $2kT$, so energy balance requires

$$\frac{3}{2}(\dot{n}kT + nk\dot{T}) = 2kT\dot{n}, \tag{5.29}$$

or equivalently, $3n\dot{T} = T\dot{n}$. This equation is easily solved to give

$$T(t) = (T_0 - T_f)\left(\frac{n(t)}{n_0}\right)^{1/3} + T_f. \tag{5.30}$$

If the plasma on the left of the boundary is modeled as an ideal gas, then the particle flux across the boundary is given by $n(kT/2\pi m)^{1/2}$, so that

$$\dot{n}(t) = \frac{-n}{d}\left(\frac{kT}{2\pi m}\right)^{1/2} = \frac{-1}{d}\left(\frac{kT_0}{2\pi m}\right)^{1/2}\frac{n^{7/6}(t)}{n_0^{1/6}}, \tag{5.31}$$

where d is the width of the plasma. The solution to this equation is easily shown to be

$$n(t) = n_0\left[1 + \frac{t}{6d}\left(\frac{kT_0}{2\pi m}\right)^{1/2}\right]^{-6}, \tag{5.32}$$

so that the plume temperature satifies

$$T(t) = (T_0 - T_f)\left[1 + \frac{t}{6d}\left(\frac{kT_0}{2\pi m}\right)^{1/2}\right]^{-2} + T_f \tag{5.33}$$

Because the width of the plume after heating can be approximated by $d \approx t_p(2kT_0/m)^{1/2}$, the characteristic time for the decay of $n(t)$ is about t_p, the duration of the laser pulse.

It is straightforward to show that as long as equation 5.29 is satisfied, the density of atoms in velocity space after all the plasma atoms cross the imaginary boundary is independent of $n(t)$. This suggests that as long as $n(t)$ drops a rate that is smaller than or comparable to the collision rate among atoms that have crossed the boundary, any choice of $n(t)$ will result in similar gas dynamics in the expanding plume. For the purpose of simplicity, one might therefore consider the case when atoms cross the boundary at a rate which is constant in time during a period t_p. In this case, $n(t)$ is given by

$$n(t) = n_0\left(1 - \frac{t}{t_p}\right) \tag{5.34}$$

and $T(t)$ then must satisfy

$$T(t) = (T_0 - T_f)\left(1 - \frac{t}{t_p}\right)^{1/3} + T_f. \tag{5.35}$$

5.3 DSMC simulation of PLA into vacuum

DSMC results for thermal effusion at 100,000 K presented earlier demonstrate that a normalized axial density profile within a 1-10 monolayer effusion plume is consistent with one derived assuming momentum and energy conservation as the distribution function evolves into a shifted-Maxwellian, and then a subsequent collisionless expansion. Although the normalized density profiles are expected to be more complex if a time-dependent effusion temperature such as that in equation 5.35 is used, the parameters T_0 and T_f may be determined by comparing the axial profiles obtained using DSMC simulation to those obtained experimentally using PLIF imaging. Earlier DSMC results also show that the degree of forward-peaking, evidenced in the normalized radial density profiles, increases rapidly with the number of monolayers effused in the range of 1-10 monolayers per pulse. A comparison of both axial and radial normalized density profiles obtained by PLIF imaging with those computed using DSMC simulation allows the second free parameter, the number of monolayers desorbed per pulse, to be determined.

Shown in Figure 5.6 is a PLIF image depicting the density of a typical Si plume after a 1.0 μs delay as it expands into vacuum. Above are normalized density profiles along constant axial contours and along contant radius contours. It was argued earlier that the independence of these profiles on position strongly suggest collisonless expansion, which was observed in earlier DSMC simulations of effusion to be valid only for $\alpha \approx 1$ or less, that is less than a few monolayers desorbed per pulse.

The 1 cm/μs characteristic velocity of the plume's leading edge suggests that the creation of the plume may be described as a hot effusion process with a source temperature near 150,000 K. Figure 5.7 shows the effusion plumes which result from this assumed temperature, with the radial density profiles compared to PLIF data shown beneath each. A 0.1 monolayer plume is clearly too wide while a 10.0 monolayer plume is much too narrow, suggesting that about 1-3 monolayers are desorbed.

Shown to the left in Figure 5.8 is a plot comparing the normalized axial density of this PLA plume with profiles of the form in equation 4.42, assuming surface tem-

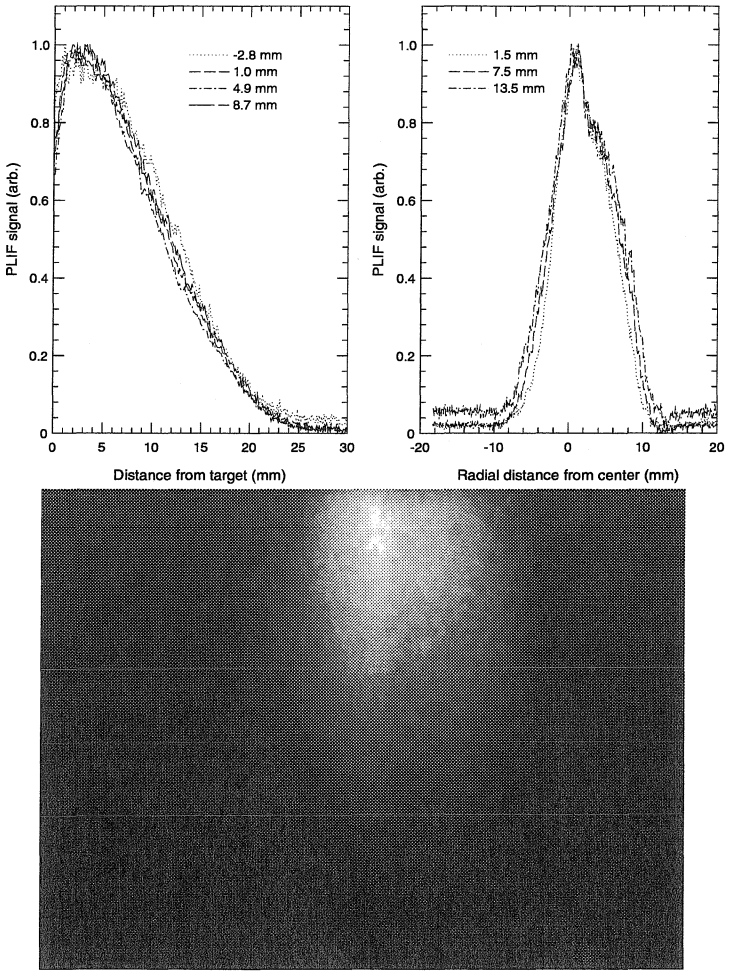

Figure 5.6: PLIF image showing the density of a 1.0 μs old plume expanding into vacuum. Above are normalized density contours which suggest collisionless expansion.

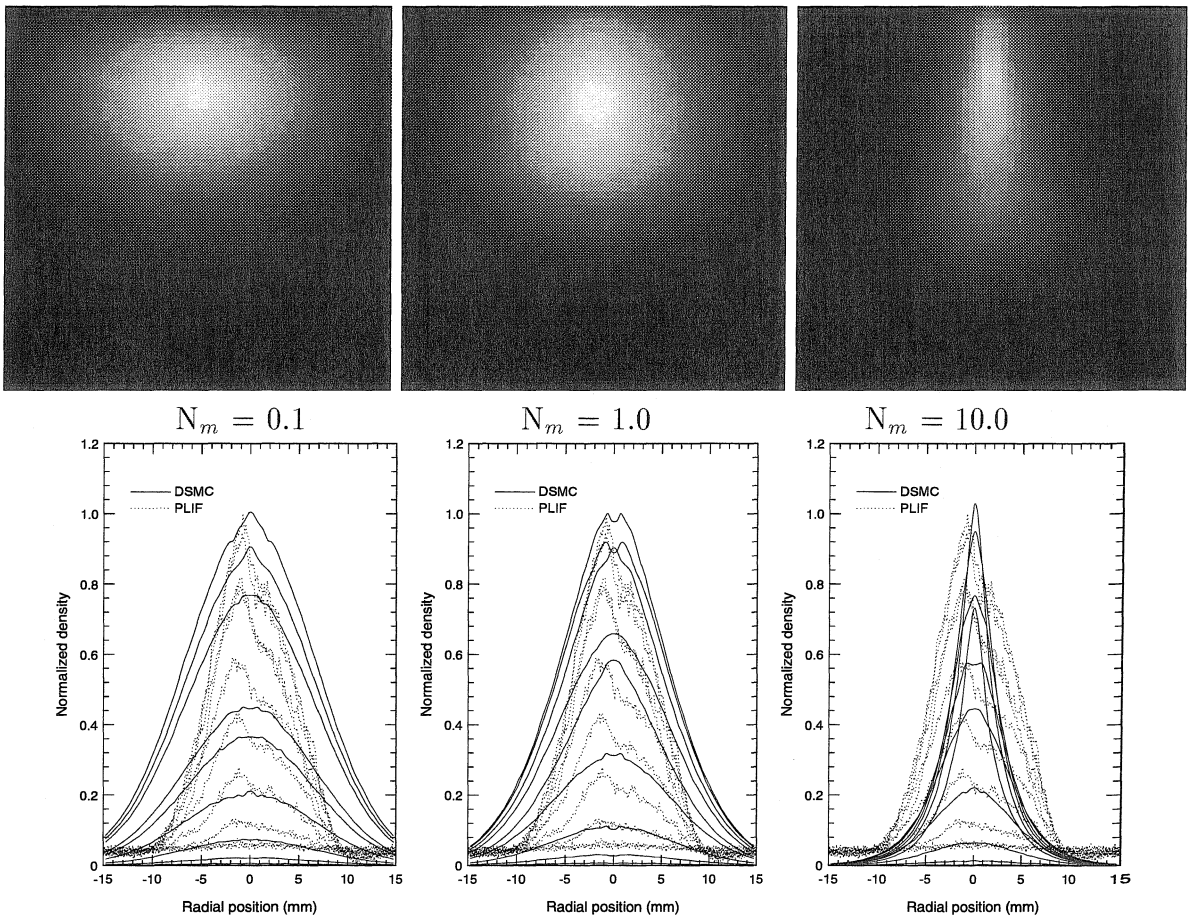

Figure 5.7: Simulated pulsed effusion plumes assuming a source temperature of 150,000 K. Each is 1 μs old and beneath each are a set of radial density profiles spaced by 3 mm, compared to profiles obtained from the PLIF image in Figure 5.6.

peratures of 15,000 K and 150,000 K. Both fits are poor, however, they indicate that the leading edge of the plume is in fact consistent with effusion at about 150,000 while the density peak is more consistent with about an order of magnitude cooler temperature. Based on results presented earlier, it is tempting to consider whether the shift of the density peak toward the target is simply a consequence of the boundary condition at the target. To the right of Figure 5.8 are the normalized density profiles obtained in simulation when 2.0 monolayers are desorbed and the target is diffusely-reflecting after the laser pulse. The peak is nearer the target as expected, but only for profiles near the axis. Dissimilarity among the profiles indicates that this plume's gas dynamics cannot be described as a collisionless expansion, in contrast to the plume observed experimentally. This result suggests that the target boundary condition must be recondensation, and that the temperature parameter must be time-dependent as suggested earlier.

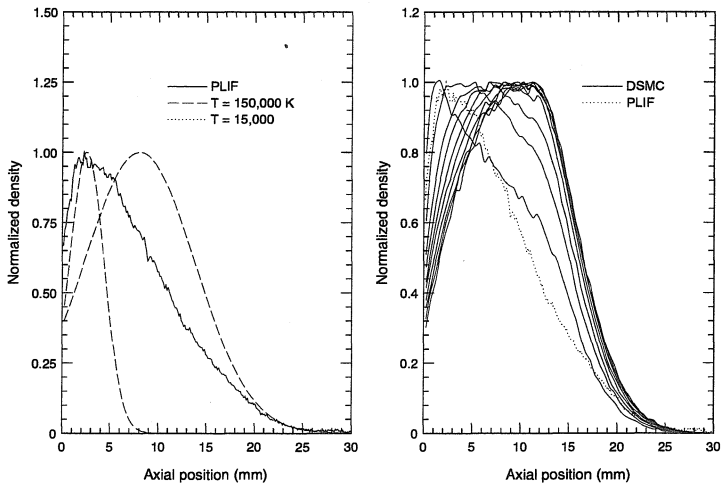

Figure 5.8: (Left) PLIF data showing normalized axial density compared with theoretical profiles assuming Knudsen layer source temperatures of 15,000 K and 150,000 K. (Right) DSMC profile resulting from effusion of 2.0 monolayers, assuming a diffusely-reflecting target.

In an effort to reproduce the density profiles in Figure 5.6 *and* the apparent collisionless expansion, simulations employing a source temperature described by the function

$$T_s(t) = T_0 - (T_0 - T_f)\left(\frac{t}{t_p}\right)^n \tag{5.36}$$

are observed to be successful, if atoms back-scattered onto the target recondense there. A model described earlier offers a physical argument for using a source temperature given by

$$T_s(t) = (T_0 - T_f)\left(1 - \frac{t}{t_p})\right)^{1/3} + T_f. \tag{5.37}$$

which is shown in Figure 5.9 to be very similar to equation 5.36 when the parameters $T_0 = 200,000K$, $T_f = 300K$, and $n = 3.8$ are used. This indicates that although $T_s(t)$ in equation 5.36 is entirely empirical, its use can be justified by physical arguments. Also in this same figure are comparisons of simulated density profiles to experimental PLIF data, demonstrating a reasonable fit. Figure 5.10 provides a comparison of PLIF images with simulation images using this fitting procedure, showing qualitative agreement.

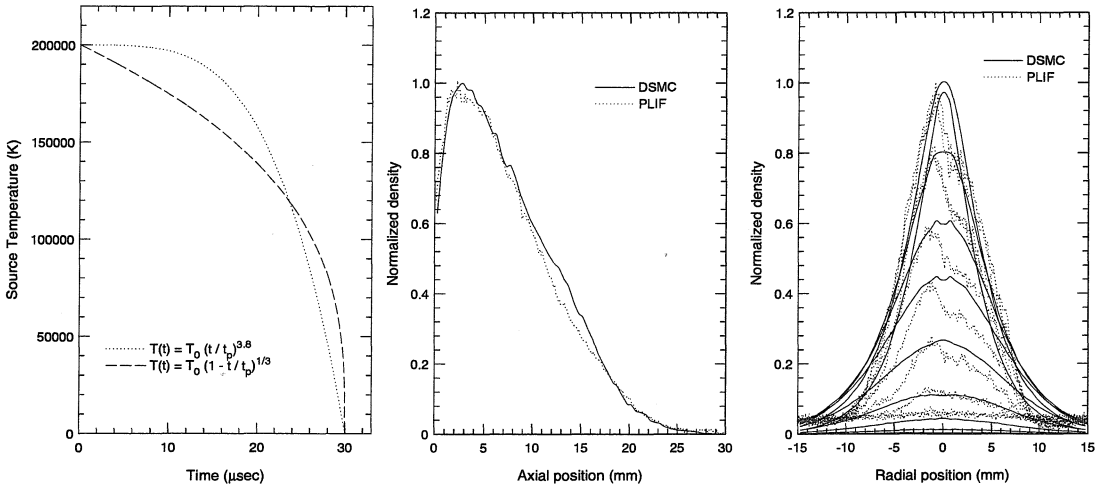

Figure 5.9: (Left) Source temperature vs. time used to fit PLIF data. (Center) Axial density profiles from DSMC and PLIF compared. (Right) Radial density profiles from DSMC and PLIF compared.

5.4 Time-of-flight (TOF) profiles

It is interesting to examine TOF profiles from simulated plumes expanding into vacuum, and compare the results to typical experimental TOF profiles. For this purpose, the data presented in Figure 1.4 are formally introduced here. This figure shows data

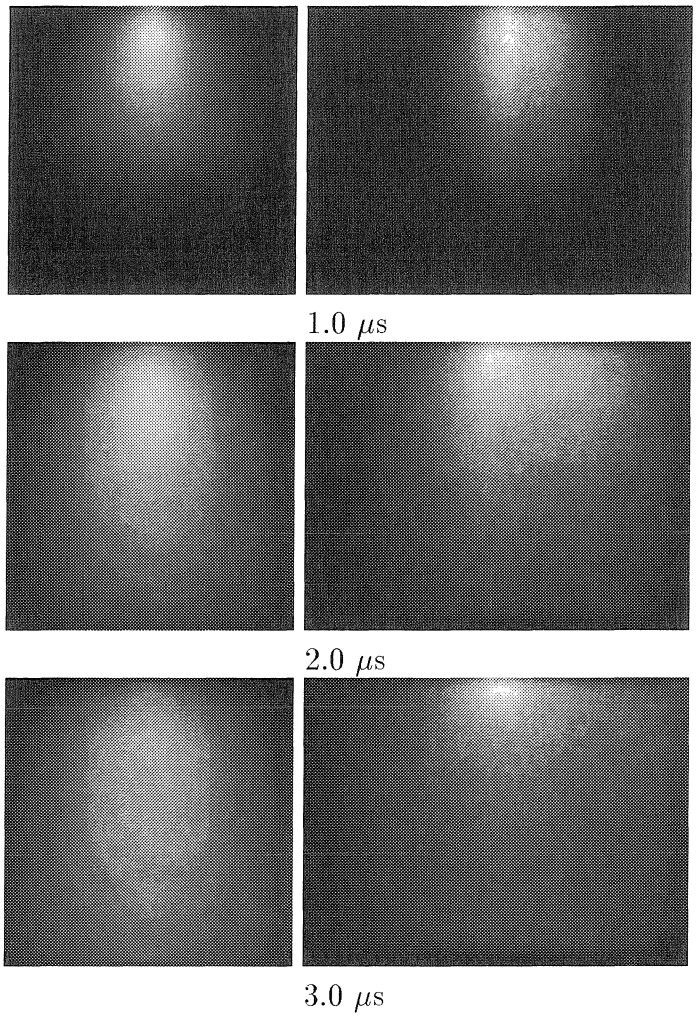

Figure 5.10: A comparison of a simulated 2.0 monolayer plume (left column) with PLIF images of a real Si plume (right column), assuming a time-dependent source temperature and recondensation at the target.

acquired using emission spectroscopy, single-point LIF, and an ion probe, all acquired from a position 1.0 cm from the target, along the axis of the plume. The plume is generated by ablation of Cu into vacuum using a 30 ns KrF laser pulse at a fluence near 10 J/cm^2. The ion probe trace is acquired using a 0.5 mm diameter tungsten wire shielded in ceramic up to the 2.0 mm tip. The probe is biased to -60 volts and the flow of ion current from the plasma is monitored by measuring the voltage across a 1.0 ohm resistor, the signal filtered using a low pass RC filter. Data is acquired on a LeCroy 9310M oscilloscope and transfered to a 486 computer using a GPIB interface made by National Instruments. The emission trace is acquired using a 1/8 m monochromator (Oriel model 77250-M), centered near 510.5 nm with a bandwidth near 20 nm, and a photo-multiplier. Three 4d $^2D \rightarrow$ 4p $^2P^0$ transitions lie within this bandwidth [93, 94], one at 515.324 nm ($g_2A_{21} = 4.7 \times 10^8$ s^{-1}), another at 521.820 nm ($g_2A_{21} = 5.8 \times 10^8$ s^{-1}), and the third at 522.007 nm ($g_2A_{21} = 0.95 \times 10^8$ s^{-1}). An additional contribution may come from the 4p $^2P^0 \rightarrow$ 4s^2 ^2D transition at 510.554 nm ($g_2A_{21} = 5.1 \times 10^6$ s^{-1}). A schematic diagram showing these transitions is shown in Figure 5.11. The emission spike appearing at $t = 1.28$ μs marks the moment when

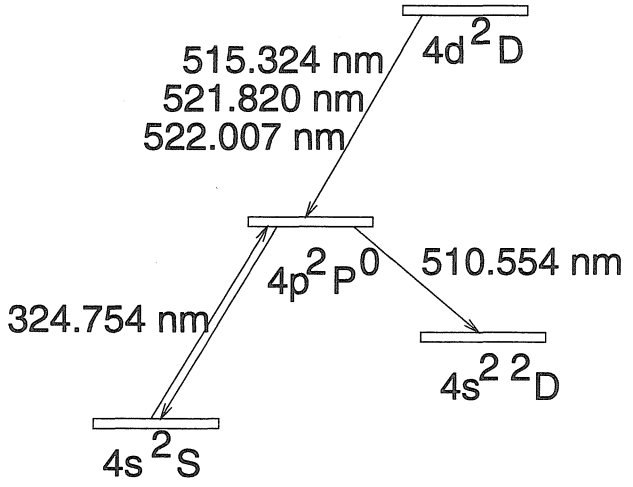

Figure 5.11: Electronic transitions in Cu relevant for emission spectroscopy and LIF.

the laser light arrives at the target, demonstrating a small delay between the KrF laser trigger and the beginning of the light pulse. The LIF data is acquired by exciting the 4s $^2S \leftarrow$ 4p $^2P^0$ transition at 324.754 nm using the ouput of a Nd-YAG

pumped DCM dye laser doubled in KDP, and then gathering fluorescence from 4p $^2P^0 \rightarrow 4s^2\ ^2D$ at 510.554 nm using the monochromator and photo-multiplier previously described. Resonant fluorescence at 324.754 nm is a much stronger signal, but data acquired at this wavelength suggests that this signal is attenuated significantly by the plume and is therefore not proportional to Cu density. For each time delay, the PMT signal from 100 shots are time-integrated on the interval $0 < t < 30$ ns and averaged. The uncertainties shown are statistically determined from the variance in the measurements.

TOF profiles are usually fit to function of the form

$$S(t) = \frac{K}{t^n} e^{-m(z_0 - ut)^2/2kTt^2}, \tag{5.38}$$

where K is a normalization constant, and z_0 is the distance of the probe from the target. This function, introduced earlier in equation 1.3, can be derived assuming the collisionless expansion of atoms described by the velocity distribution function

$$f(v) \propto v^{n-3} e^{-m(v_z - u)^2/2kT}. \tag{5.39}$$

It is straightforward to show that the temporal peak in $S(t)$ occurs at

$$t_m = \frac{z_0}{nv_p^2} \left((u^2 + 2nv_p^2)^{1/2} - u \right), \tag{5.40}$$

so that for a given value of T, chosen to fit the width of the profile, the best fit parameter u can be calculated to fit the peak by using

$$u = \frac{z_0^2 - nv_p^2 t_m^2/2}{z_0 t_m}. \tag{5.41}$$

The value $n = 4$, based on the assumption that a steady-state Knudsen layer forms, is commonly used to fit TOF profiles acquired from PLA plumes [23, 35, 49]. In Figure 5.12, the temporal peaks of 0.82 μs, 1.12 μs, and 1.32 μs for ions, excited neutrals, and ground-state neutral TOF profiles, respectively, are used to

determine best fit flow speed parameters assuming $n = 4$, and temperatures from 50,000 K to 500,000 K. Good fits are obtained to both emission and LIF data, however, the emission profile suggests a plasma temperature near 150,000 K while the LIF data suggests a temperature closer to 500,000 K. The fit to the LIF data is actually insensitive to further increases in the temperature parameter, and the fact that u becomes more negative as T increases indicates that the fit parameters do not relate to physical properties of the plasma. The occurence of a negative flow speed parameter using equation 5.38 with $n = 4$ has been observed elsewhere [39] during the study of carbon plumes used in the deposition of diamond-like films.

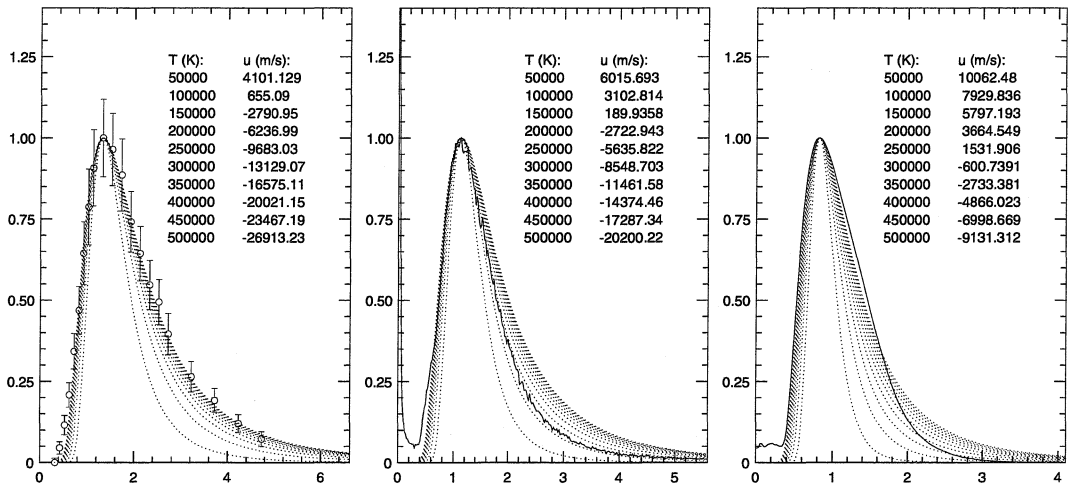

Figure 5.12: (Left to right) LIF, emission, and ion probe TOF profiles fit to theory (n = 4) assuming the collisionless expansion of shifted-Maxwellian Cu atoms.

Others have chosen $n = 6$ to fit both emission and mass spectrometry TOF profiles. This choice is based on the assumption that the plume expands as if emerging from a supersonic nozzle [27, 24]. This choice suggests, however, an even greater temperature and a more negative flow speed for the LIF data appearing in Figure 5.12.

One might assume instead that the laser-heated plume, a hot Maxwellian gas with negligible flow speed, expands collisionlessly. In this case the TOF profile requires the parameter $n = 3$. Figure 5.13 shows the results when this asumption is made. In this case the best fit temperature for the LIF data is 100,000 - 150,000 K and the flow speed parameter is small and positive, consitent with the $u << v_p$ assumption

implicit in the model previously described. The emission data also suggests a plasma temperature near 100,000, although a much greater positive flow speed parameter is suggested.

The difference between these profiles can be explained by assuming a decay in the excited state population as the plume expands. This is expected to occur as the collision rate among the expanding plume atoms becomes smaller than the spontaneous emission rate, preventing collisions from maintaining a Boltzmann distribution among excited states. Figure 5.14 demonstrates how a correction term of the form e^{At} may be used to transform the emission profile so that it more closely matches the LIF profile. A good fit is obtained using the value $A = 7 \times 10^5$ s^{-1}, which is several orders of magnitude smaller than spontaneous decay rates of the transitions which contribute to the emission signal. A similar correction may be applied to the TOF profile acquired using an ion probe, the result shown in Figure 5.14 obtained using a decay rate of 1.9×10^6 s^{-1}. These results demonstrate the consequences of using diagnostics other than LIF which are not sensitive to the ground-state neutral population in the plume.

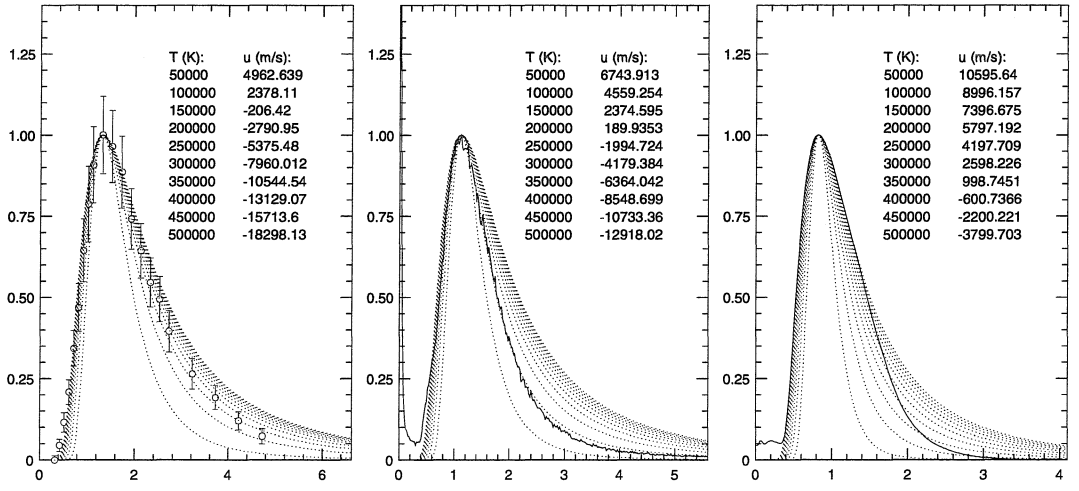

Figure 5.13: (Left to right) LIF, emission, and ion probe TOF profiles fit to theory (n = 3) assuming the collisionless expansion of shifted-Maxwellian Cu atoms.

Shown in Figure 5.15 is a TOF profile acquired 1.0 cm from an Si target, compared with theoretical profiles of the form in equation 5.38 with $n = 3$. A reasonable fit is obtained assuming a plasma temperature near 150,000 K. For comparison, if $T_s(t)$

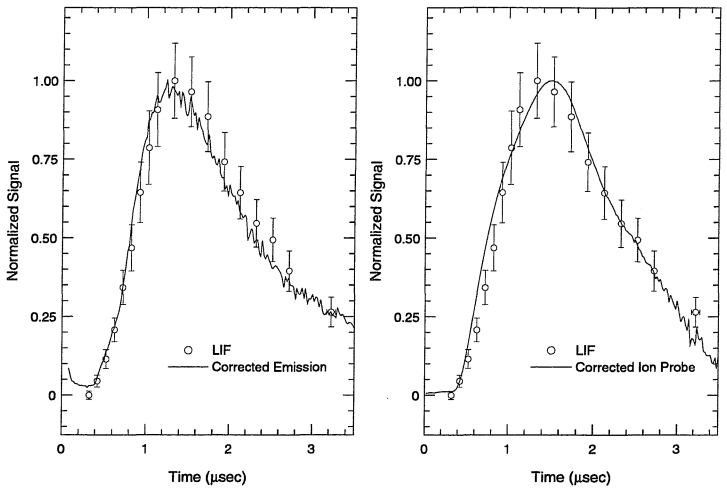

Figure 5.14: (Left) LIF data compared with emission data after correcting for decay in the excited-state populations. (Right) LIF data compared with ion probe data after correcting for decay in the ionization fraction.

in equation 5.38 is integrated over the interval $0 < t < t_p$ one obtains the average temperature

$$\langle T_s \rangle = T_0 + (T_f - T_0)\frac{1}{1+n}, \tag{5.42}$$

which gives $\langle T_s \rangle$ = 158,000 K for the parameters used to fit the experimental axial density profiles. The model used to generate this plume is therefore self-consistent, and the resulting TOF profile suggests a comparable plasma temperature to that observed experimentally.

5.5 Influence of the substrate on the expanding plume

In Chapter 3 PLIF data was presented which suggested that for time delays greater than about 3 μs, a build-up in Si density near the substrate occurs (see Figure 3.10). This data provides evidence that the sticking probability of plume atoms onto the unheated Si (100) substrate is less than unity. Figure 5.16 shows the plume density along the axis if an Si plume after 5 μs with a substrate located 3 cm from the target. Experimental data obtained using PLIF imaging is compared with simulation

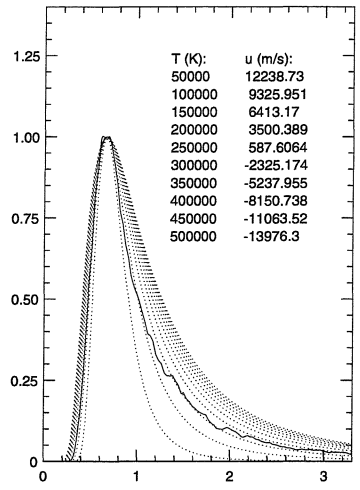

Figure 5.15: Time-of-flight profile acquired in simulation assuming a time-dependent source temperature described by equation 5.36. The probe is 1.0 cm from the target.

data, assuming a diffusely reflecting substrate with a sticking probablity of 0.75. The simulation is otherwise identical to the one that produced the images and data appearing in Figures 5.10 and 5.15. Certain qualitative features, including the rapid drop in density near the target and the build-up in density near the substrate are similar. This value for the sticking probability is consistent with value of 0.76 $\pm$ .05 determined elsewhere for Ba atoms on an MgO substrate [95].

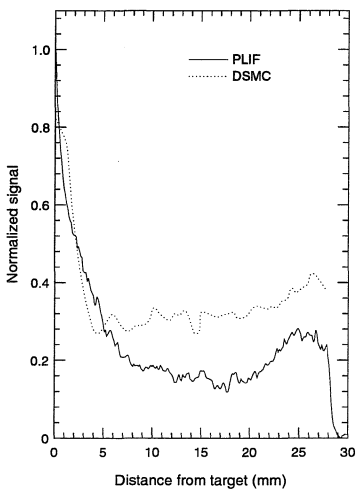

Figure 5.16: Normalized density profiles along the axis of an Si plume after 5 μs. An unheated Si (100) substrate is present 3 cm from the target. Compared are PLIF data and simulation data assuming a diffusely reflecting substrate with a sticking probability of 0.75.

5.6 Summary

In this chapter the physics of target heating are investigated by numerically solving the heat flow equation within an Si target which experiences surface heating by intense (15-250 MW/cm^2) laser radiation. The model includes melting and vaporization, whereby an effusion plume is generated at a rate consistent with the surface vapor pressure. The 1-D plume is modeled assuming a shifted-Maxwellian velocity distribution, and a characteristic width equal to the center-of-mass distance from the target, which is determined by momentum conservation. The temperature of the plume is then determined by energy conservation, and the ionization fraction in the plume is estimated using the Saha equation. Details such as multi-photon ionization and electron impact ionization are ignored. Laser heating of the free electrons in the plume via inverse Bremsstrahlung (IB) absorption is assumed to couple energy into the plasma bulk rapidly, an approximation which neglects detailed energy transfer among different species in the plume.

The results show that for a laser intensity greater than about 50 MW/cm^2, IB absorption quickly leads to plasma breakdown. This is evidenced by a rapid increase in the plume temperature and ionization fraction, and by a rapid drop in the target's surface temperature due to shielding by the plasma. This model therefore explains quantitatively how atomic velocities near 1 cm/μs are attained. If breakdown occurs early in the laser pulse, then the temperature of the plume rises rapidly to more than 100,000 K, and then asymptotically approaches an upper-bound value when IB absorption is equal to radiative losses, which are modeled here as emissive. This upper bound on plasma temperature might explain why increases in laser fluence often do not result in proportional increases in the kinetic energy of plume atoms [26].

Since the characteristic width of the plasma immediately after the laser pulse is estimated at only a few microns, the plume's creation is modeled as effusion from a hot source located at the target surface, with an area equal to that of the laser spot. The free parameters in this model, specifically the source temperature T_s and the number of monolayers N_m ablated, are determined by comparing simulated plumes to real

ones. The number of monolayers in the plume is estimated by comparing forward-peaking, and the temperature is determined by comparing axial density profiles. It is shown that a steady effusion from a time-dependent source temperature of the form

$$T_s(t) = T_0 - (T_0 - T_f)\left(\frac{t}{t_p}\right)^n \tag{5.43}$$

for $0 < t < t_p$ results in a plume which compares well with experiment, if a total of ≈ 2 monolayers desorbed. This empirical law can be justified by examining the time-dependent particle and energy flux passing through an imaginary bounding surface of a heated plasma which remains in thermal equilibrium as atoms escape into vacuum. Because energy and particle number are conserved in the model, it is similar to the expansion of a heated gas intially at the time-average temperature $\langle T_s \rangle$. TOF profiles acquired experimentally and in simulation suggest an initial plasma temperature near 150,000 K for both Cu and Si plumes.

Chapter 6 DSMC simulations of expansions into a background gas

6.1 Introduction

Having demonstrated in the previous chapter that the creation of a PLA plume may be modeled as a process similar to effusion but with a time-dependent source temperature, the model is used in this chapter to study PLA into a background gas using the DSMC method. Of interest are the temporal and spatial evolution of the density, temperature, and flow velocity of the background gas as the ablation plume expands, and the influence of the background gas on the particle flux and energy per particle incident onto the substrate. It has been suggested [96] that the expanding material displaces the background gas analogous to a snowplow, compressing it to high density along the contact front. The magnitude of the density increase in the background gas at the contact front and any influence on the expansion velocity of the plume have not been measured experimentally. This effect is studied here in simulations as 2 monolayers of Si expands into an Ar background gas at 0-100 mTorr.

It has been observed experimentally using an ion probe that the plume splits into fast and slow components in the presence of a background gas [28, 29, 30]. One explanation of this effect invokes differences in the collision cross sections for ion-neutral and neutral-neutral collisions, whereby ions more easily penetrate through the gas. In this scenario, charge exchange is then responsible for the existence of slow ions and fast neutrals in the plume. Plume splitting can be explained more simply, however, without including ions in the model and without invoking two distinct collision cross sections. This alternative explanation becomes apparent upon examination of DSMC simulation results.

If the background gas affects the expansion of the plume, it might be expected

that the particle flux and energy per particle incident onto the substrate might also be affected. Simulations show how particle flux, average energy per incident particle, and forward-peaking in the film density vary with background gas pressure. Particularly interesting are data regarding the flux of background gas molecules on the substrate. At a temperature of 300 K, energies exceeding 0.5 eV are not expected, so the presence of these energetic particles indicates the influence of plume-gas collisions. This work is relevant because a background gas is often used during PLD, and many recent PLD applications apparently depend on gas phase collisions. ZnTe films highly doped with N atoms, for example, have recently been grown by ablating ZnTe into N_2. Because of the large binding energy of N_2 it is unclear how the molecules become dissociated and incorporated into the film. It is possible that high temperature within the background gas, heated by the expanding plume, may be sufficient to dissociate a small fraction of N_2 molecules, resulting in energetic N atoms which then bombard the substrate. Alternatively, energetic N_2 molecules, produced via in-flight collisions with Zn and Te, may simply dissociate upon impact with the substrate. The temperature within an Ar background gas, and the energy per Ar atom incident onto the substrate during the expansion of Si offer important clues about how these ZnTe films may become implanted with N atoms.

The presence of a background gas has also been shown to influence the stoichiometry of deposited films. A background gas containing O_2 is often used, for example, to deposit both oxide films [12, 13, 14, 15, 76] and YBCO films [16]. Although the role of O_2 in some of these experiments may simply be to oxidize the substrate and/or target surface, it was observed earlier using PLIF imaging of SiO that in-flight chemistry occurs within the plume. Since it is extremely difficult to treat chemistry in a non-equilibrium rarified environment using any method other than DSMC, this technique provides a unique opportunity to study in-flight chemistry during PLD. For this reason, the expansion of Si into a background gas mixtures containing O_2 at 10 mTorr-100 mTorr is studied, including vibrational and rotational excitation of the O_2 molecules, and the reaction $Si + O_2 \rightarrow SiO + O$.

6.2 Simulation parameters

Despite the validity of the DSMC method for simulating the expansion of a plume into any gas pressure, the range of gas pressure for which the technique is practical is limited by statistical considerations. If at total of N simulation particles are used, the number representing target atoms is given by

$$N_t = N\frac{r_s^2 d_m N_m \rho}{r_s^2 d_m N_m \rho + PR^2 L/kT} \tag{6.1}$$

and the number representing gas molecules is

$$N_g = N\frac{PR^2 L/kT}{r_s^2 d_m N_m \rho + PR^2 L/kT}, \tag{6.2}$$

where R and L are the dimensions of the simulated volume. By inspection, as the pressure increases, the number of simulation particles representing target atoms decreases, requiring more runs to be averaged to provide statistically acceptable results. Provided in the table below are values for the fraction of simulation atoms which represent target atoms over a wide range of gas pressure and monolayers ablated, assuming a cylindrical volume with dimensions $R = 1.5$ cm and $D = 3.0$ cm as in Chapter 4.

N_m/P(mTorr)	0.1	1.0	10	100
0.1	.11153	.01239	.00125	.00012
1.0	.55660	.11153	.01239	.00125
10.0	.92621	.55660	.11153	.01239

In the table below are the results when the dimensions are reduced to $R = 1.0$ cm and $D = 2.0$ cm. Since these dimensions improve the statistical efficiency at higher pressures by a factor of 4, they are used in most of the simulations that follow.

N_m/P(mTorr)	0.1	.01	10	100
0.1	.29759	.04064	.00421	.00042
1.0	.80904	.29759	.04064	.00421
10.0	.97694	.80904	.29759	.04064

In general, the DSMC method works well only if at least a few simulation particles occupy each subcell. If the dimension of each subcell is comparable to a mean free path, the number of simulation particles per subcell N_c in a gas is given by

$$N_c = \frac{N_g}{V}\left(\frac{kT}{\sqrt{2}\sigma P}\right)^3, \tag{6.3}$$

where N_g is the number of simulation gas particles and V is the volume enclosing the gas. This quantity decreases rapidly with pressure, and the maximum practical pressure can be obtained by setting N_c to about 10. Assuming a 300 K gas, the pressure must therefore satisfy $P < 5 \times 10^{-3}(N_g/V)^{1/3}$, which is about 100 mTorr if, for example, 200,000 simulation gas particles and a cylindrical volume with dimensions $R = 1$ cm and $D = 2$ cm are assumed.

To simulate the expansion of a plume into a background gas, the dimension of the subcells near the target must be comparable to the mean free path in the plume, which is generally smaller than the mean free path in the gas. Assuming a plume width near 200 μm after laser heating, the mean free path in the early plume is about $100/\mathrm{N}_m$ μm. If a cylindrical volume is divided uniformly into concentric subcells having this dimension then the average number of simulation atoms per subcell is given by

$$N_c = 1 \times 10^{-8}\frac{N_g}{RDN_m^2} \tag{6.4}$$

This quantity is shown in the table below for a wide range of gas pressures and monolayers ablated, always assuming a total of 400,000 simulation particles and an $R = 1$ cm, $D = 2$ cm cylindrical volume. Only ablation of a few monolayers into a few mTorr of background gas provides statistical balance between both the plume and the gas.

N_m/P(mTorr)	0.1	1.0	10.0	100.0
0.1	1404.8	1918.7	1991.5	1999.1
1.0	3.8191	14.048	19.187	19.915
10.0	.00461	.03819	.14048	.19187

6.3 Expansion of Si into Ar

Shown in Figure 6.1 are time-sequence mesh plots spaced by 250 ns depicting the first 1.0 μs of expansion into vacuum of a 2 monolayer Si plume. The plume is generated assuming steady effusion during a 30 ns period, using equation 5.36 to describe the time-dependent source temperature with T_0 = 200,000 K, T_f = 300 K, and n = 3.8. These parameters were shown earlier to produce a plume which compares well with an experimental Si plume, diagnosed using PLIF imaging. In each of these plots the label "axial position" denotes the distance from the target in units of cell width, which in this case is 0.5 mm. Similarly, the label "radial position" denotes the radial cell position, with the axis of symmetry at cell 20. The width of each radial cell is also 0.5 mm.

Shown next, in Figure 6.2, are similar time sequence mesh plots of Si density when the plume expands into 10 mTorr of argon. The literal difference between these two cases is shown in Figure 6.3. Two recessed regions along the sides suggest that the plume becomes less forward-peaked in the presence of a background gas, and the two large peaks along the axis suggest that the presence of background gas reduces the density of the plume in two regions. One region is the leading edge of the plume, indicating a slower plume expansion. This effect was observed experimentally in the PLIF data presented earlier. The second region coincides with the location of a peak in the background gas density after 250 ns produced by a snowplow effect (Figure 6.4). This density peak serves loosely as a wall which separates the expanding plume into two components. Although this effect has been observed experimentally [28, 29, 30], this is believed to be the first evidence of this effect reported using DSMC simulation.

Unfortunately, a double-humped density profile is not observed in the PLIF images of Si density acquired during ablation of Si into 10 mTorr Ar presented earlier. These images show the plume only after 1.0 μs, however, when the effect is not as apparent. PLIF images of Si density after 1.0 μs also suggest that Si atoms continue to desorb from the target well after the laser pulse, resulting in a higher Si density near the target than the ablation model used in the simulation predicts. This might possibly mask the plume-splitting effect.

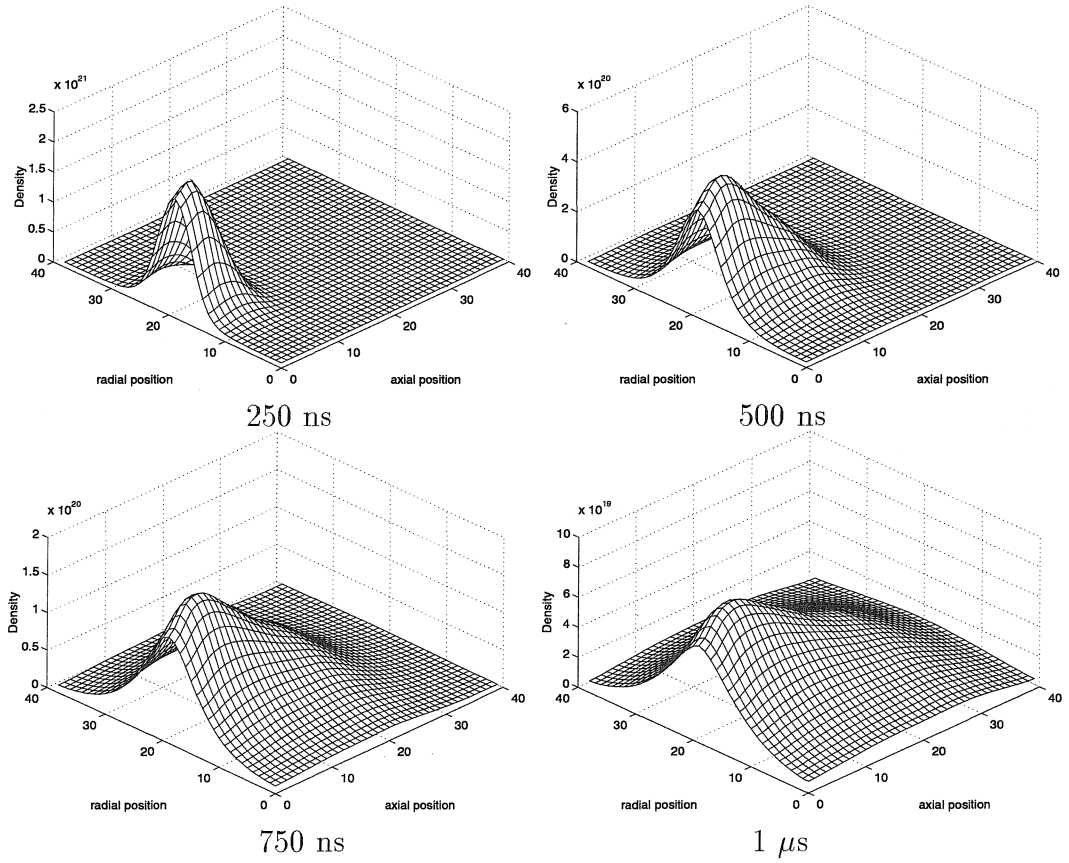

Figure 6.1: Time sequence mesh plots of Si density during a simulated Si plume expansion into vacuum. Each cell has a width of 0.5 mm, so an "axial position" of 40 corresponds to a distance 2.0 cm from the target.

Because the peak diminishes rapidly, and the mean free path in a 10 mTorr gas is about equal to the target-substrate spacing, the most significant interaction of the plume with the low-pressure gas occurs early in the expansion phase and then the plume expands nearly collisionlessly to the substrate. Collisionless expansion is evidenced in plots of radial and axial flow speeds of Si in Figure 6.5. The brevity

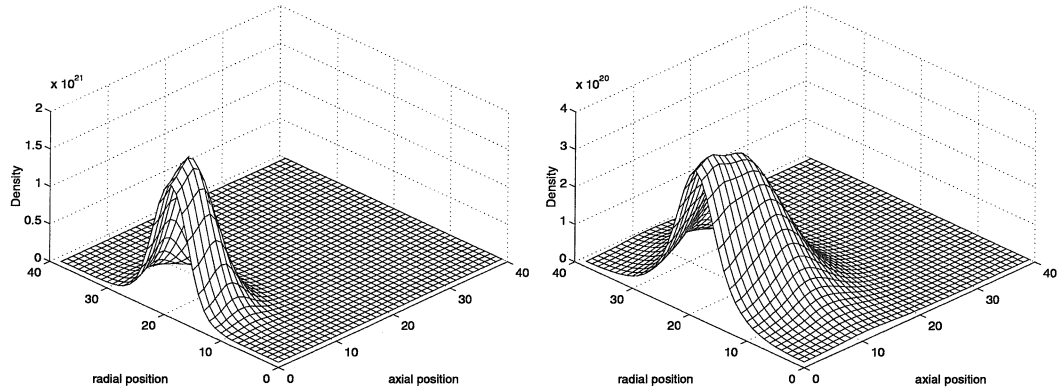

Figure 6.2: Time sequence mesh plots of Si density during a simulated Si plume expansion into 10 mTorr Ar.

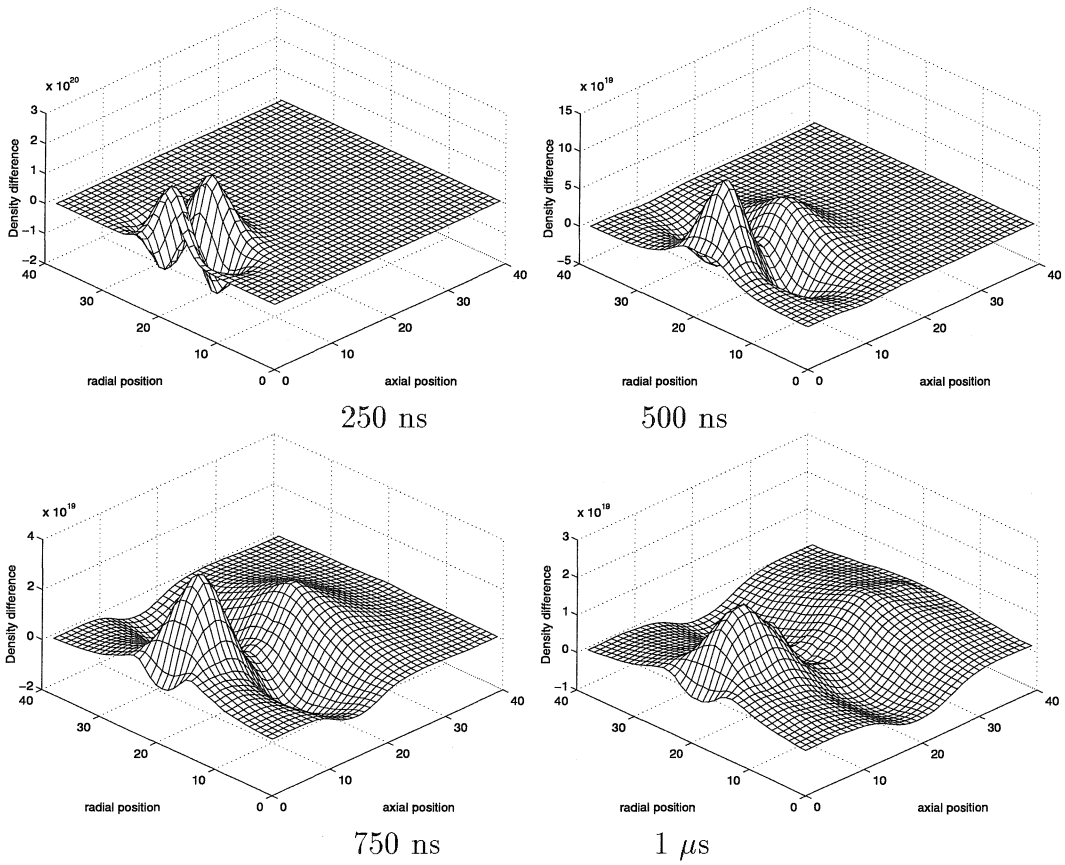

Figure 6.3: Time sequence mesh plots of the difference in Si density between plumes expanding into vacuum and 10 mTorr Ar.

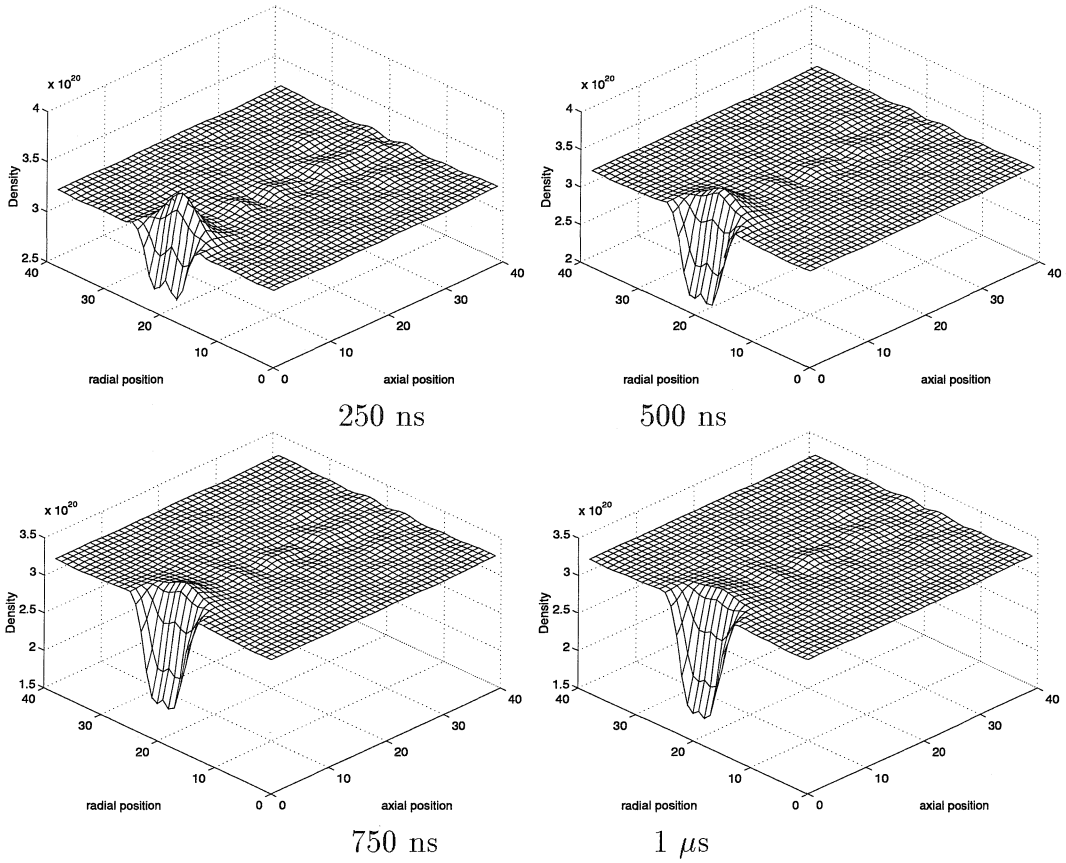

Figure 6.4: Time sequence mesh plots of Ar density during a simulated Si plume expansion into 10 mTorr Ar.

of the interaction is evidenced in Figure 6.8 where the total energy of both target atoms and background gas atoms are shown as functions of time. The gas energy rises rapidly during the first 250 ns of expansion and then remains constant until about 1 μs. A corresponding drop in the plume energy indicates an energy transfer from the plume to the gas during this brief 250 ns period. The increase in gas energy is manifested in a large axial flow velocity and temperature along the contact front, quantities which are plotted in Figures 6.6 and 6.7, repectively. The Ar flow speed in each cell is defined by $\vec{u} = \langle \vec{v} \rangle$ where $\langle\rangle$ denotes an average over all the Ar simulation particles in a cell. The peak axial flow speed near $u_z = 800$ m/s at 250 ns exceeds the 320 m/s sound speed in the 300 K background gas, indicating a supersonic expansion. The perpendicular temperature of the argon, defined in each cell by

$$T_{perp} = \frac{m}{k}(\langle {v_z}^2 \rangle - {u_z}^2), \tag{6.5}$$

is greatest early in the expansion. This parameter has a peak value near 15,000 K at 250 ns.

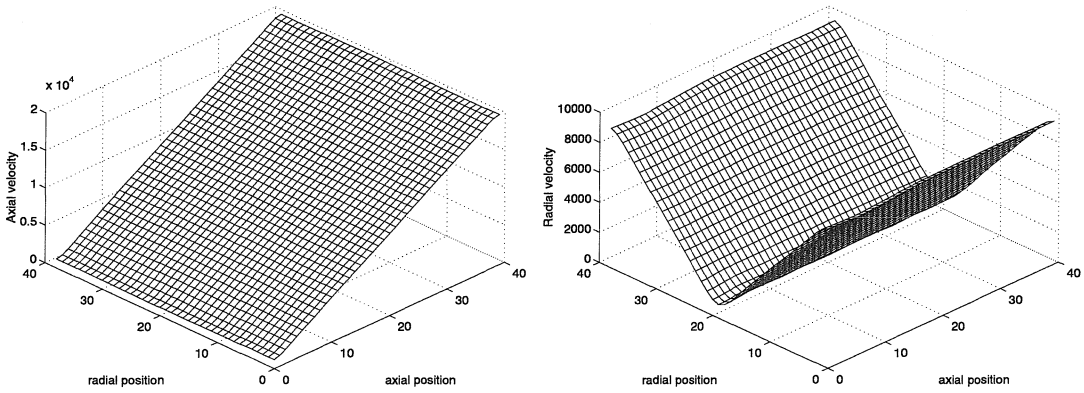

Figure 6.5: Mesh plots of Si axial (left) and radial (right) flow speed at t = 1 μs during a simulated Si plume expansion into 10 mTorr Ar. Plots indicate collisionless expansion.

After about 1.0 μs the energy in both the plume and the background gas gradually drop, the plume energy asymptotically approaching zero while the gas energy decays to its equilibrium value. Since plume particles are continuously recondensing onto the substrate and other surfaces, the decay in plume energy is not surprising. The

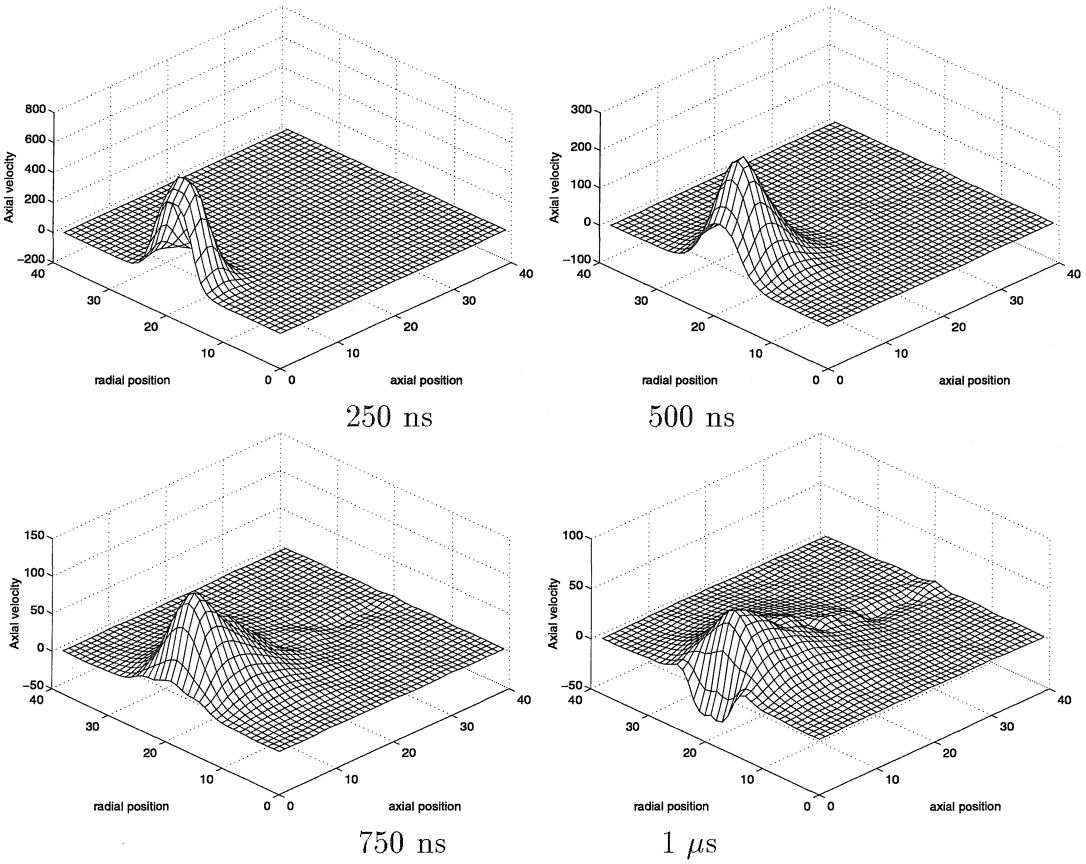

Figure 6.6: Time sequence mesh plots of Ar axial flow speed during a simulated Si plume expansion into 10 mTorr Ar.

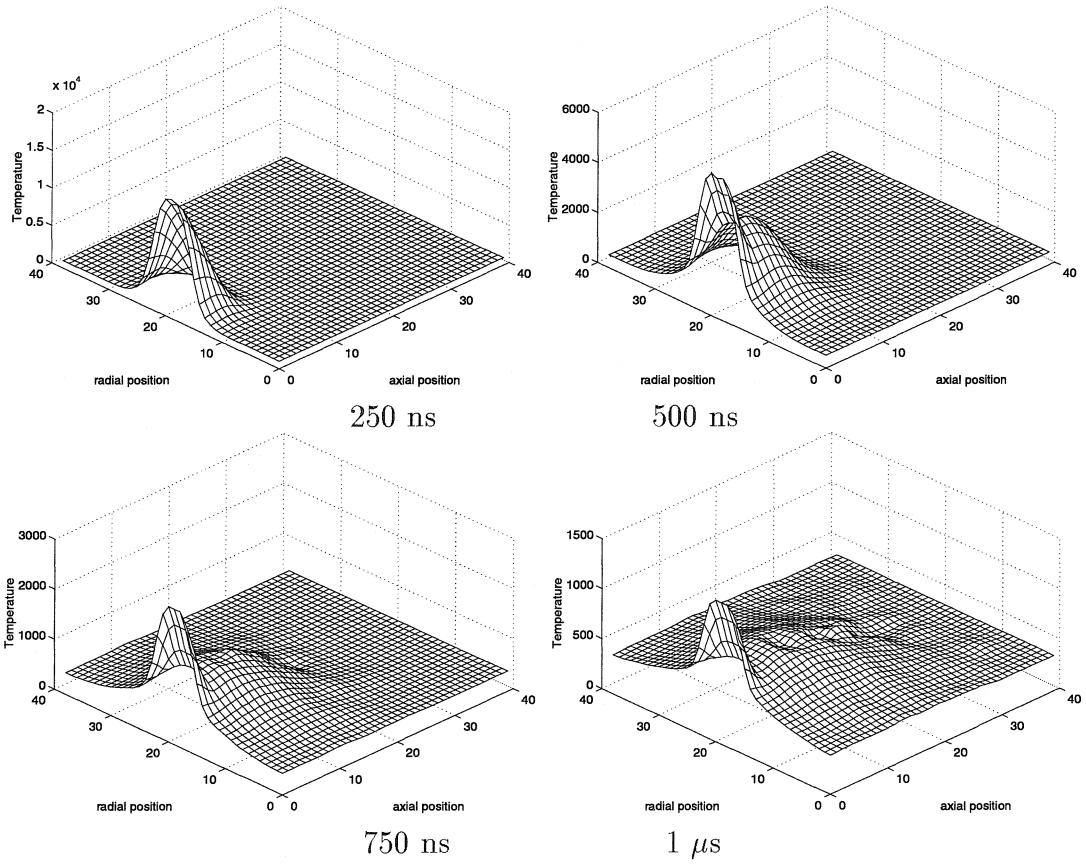

Figure 6.7: Time sequence mesh plots of Ar axial temperature during a simulated Si plume expansion into 10 mTorr Ar.

simulation explicitly conserves gas particles, however, except for those incident onto the substrate with an energy exceeding 0.5 eV. These results therefore suggest that the decay in gas energy after 1.0 μs results from the recondensation of a small number of very energetic gas atoms onto the substrate. Figure 6.8 shows how a pulse of Ar, having an average axial energy as high as 15 eV is incident onto the substrate. The Ar particle flux is about 1% that of the Si. The temperature plots in Figure 6.7 are therefore misleading, suggesting a gas in thermal equilibrium at a temperature as high as 15,000 K when actually only a few gas particles have an energy significantly above the 0.04 eV mean energy of the 300 K bulk.

It is interesting to consider that if N_2 replaced Ar as the background gas, and Zn and Te replaced Si, it is plausible that N_2 molecules with a kinetic energy of 15 eV could dissociate upon impact with the substrate, producing up to 2% doping of a ZnTe film. It is also plausible that N_2 could dissociate during in-flight collisions and then travel to the substrate.

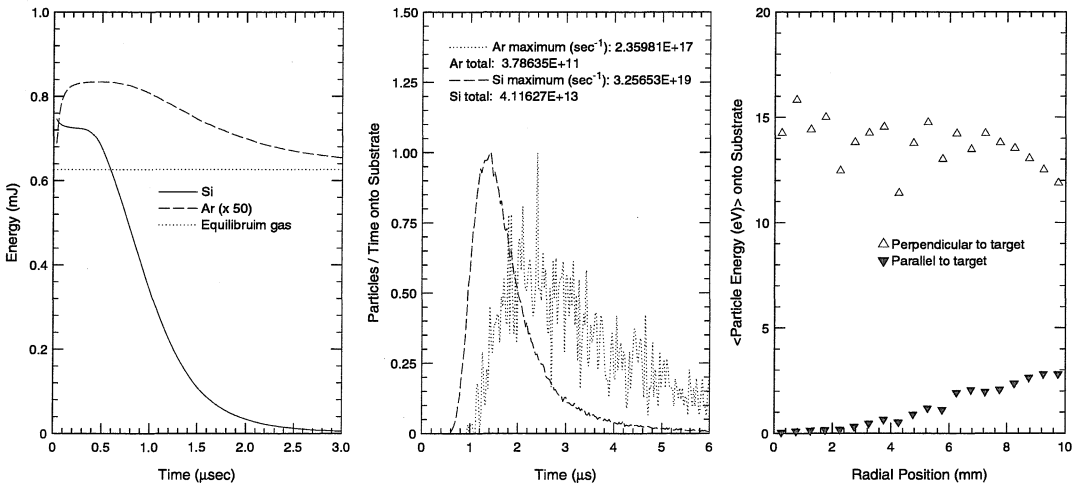

Figure 6.8: (Left) Total energy of Si atoms and Ar atoms in the simulation volume vs. time for 10 mTorr pressure. Data indicates a brief energy exchange during the initial 250 ns of expansion. (Center) Si and Ar particle flux onto substrate vs. time. (Right) Average axial energy of Ar atoms incident onto the substrate. Data suggests that a pulse of energetic Ar closely follows the Si plume.

If the background gas pressure is increased to 100 mTorr, the energy exchange between the plume and background gas occurs in two separate phases. The first phase involves a rapid compression, as described earlier, which separates the plume

into two components. The much slower second phase is a thermal heating of the gas by the slow component of the plume. These two phases are evident in Figure 6.9. The energy transfer during compression at this background pressure is negligible, and over within the first 100 nsec of the plume's expansion. The background gas density throughout the simulation is therefore constant. In contrast, thermal heating lasts until about 1.5 μs.

Figure 6.9 also shows how a much longer pulse of Ar atoms, having an axial energy near 5 eV, arrives at the substrate after the fast Si component. At this gas pressure, the total number of Ar atoms exceeds the number of Si atoms, and the radial energy is almost equal to the axial energy, suggesting that the Ar atoms arriving at the substrate are nearly thermal. The plot includes only Ar atoms which stick to the substrate (axial energies exceeding 0.5 eV), however, so the temperature of the Ar atoms cannot be easily deduced from this data. Instead Figure 6.10 shows the temperature of the Ar gas at 1.0 μs, 2.0 μs, and 3.0 μs. The data suggests that thermal heating by the plume has raised the argon temperature to nearly 600 K near the substrate.

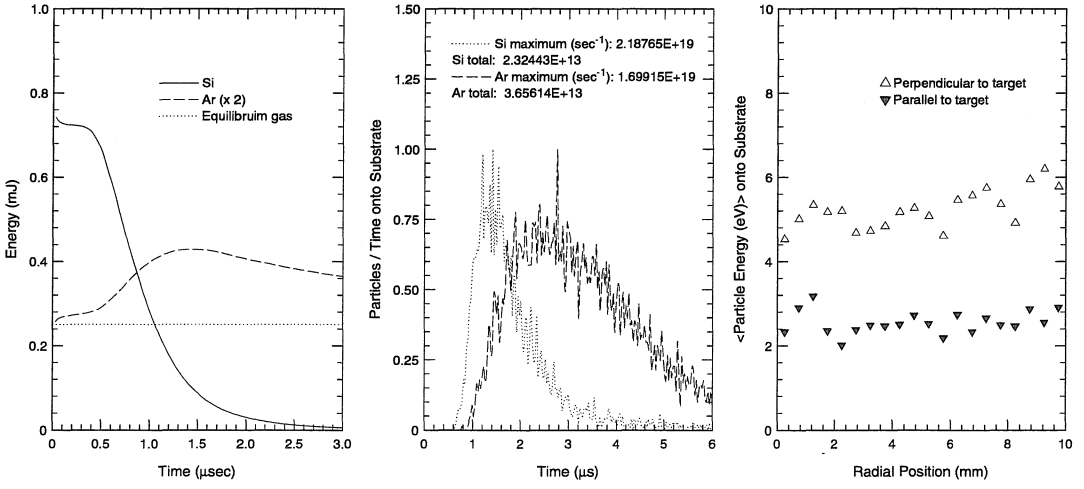

Figure 6.9: (Left) Total energy of Si atoms and Ar atoms in the simulation volume vs. time for 100 mTorr pressure. Data indicates a brief energy exchange during the initial 250 ns of expansion, followed by a longer period of gas heating lasting several μs. (Center) Si and Ar particle flux onto substrate. (Right) Average axial energy of Ar atoms incident onto the substrate vs. time. Parallel and perpendicular components are nearly thermal.

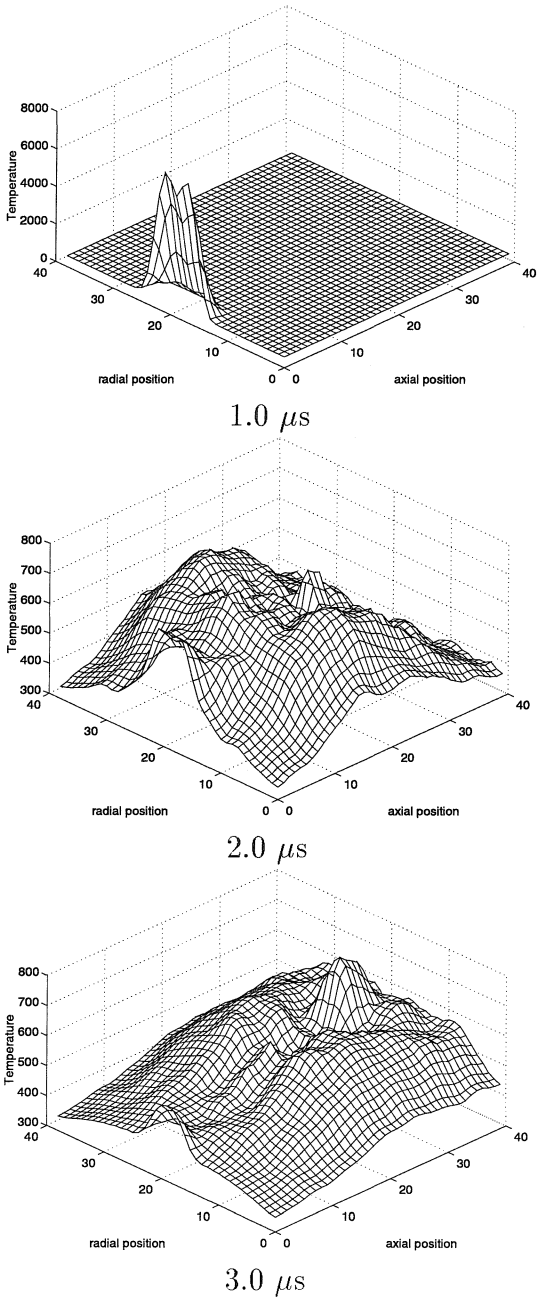

Figure 6.10: Mesh plots of Ar axial temperature during a simulated Si plume expansion into 100 mTorr Ar.

Figure 6.11 compares the expansion of Si into 100 mTorr Ar with expansion into vacuum on the long time scale of thermal heating. For times less than 1.0 μs the density of the slow component of Si, held in compression against the target, is so large that it renders invisible the presence of the fast component. As this slow component expands, the density everywhere is about an order of magnitude greater than in vacuum for the same time delay. The existence of the fast component at this pressure is evidenced by examining the particle flux and energy per particle incident onto the substrate. Figure 6.12 compares these quantities for Si expansion into vacuum, 10 mTorr, and 100 mTorr. The expansion of the fast component of the plume appears to be virtually uneffected by the presence of the background gas, although the average energy per atom does decrease about 10% for 10 mTorr and about 20% for 100 mTorr. A slight decrease in forward-peaking between vacuum and 10 mTorr conditions explains the 12% decrease in the total number of Si atoms deposited onto the substrate, however, this does not explain the factor of 2 decrease in the amount of Si reaching the substrate at 100 mTorr. This decrease is more likely due a corresponding decrease in the fraction of Si atoms in the fast component of the plume. A plot showing the decrease in the total number of Si particles incident onto the substrate in the interval $0 < t < 6\mu$s as a function of Ar pressure is provided. The rapid drop near 100 mTorr explains why most PLD applications do not use pressures significantly greater than this value.

6.4 Ablation of Si_xGe_{1-x} into vacuum and Ar

It is interesting to investigate the expansion behavior of a multi-component target material such as Si_xGe_{1-x} into both vacuum and a background gas, and compare the particle flux and energy per particle incident on the substrate for the two species. Because of differences between the two species' collision cross sections and mass, it is expected that in-flight segregation may occur, which might effect the stoichiometry of a deposited film. Shown in Figure 6.13 are images of the Si and Ge densities after a delay of 1.0 μs when 2 monolayers of $Si_{0.5}Ge_{0.5}$ is ablated. The germanium component

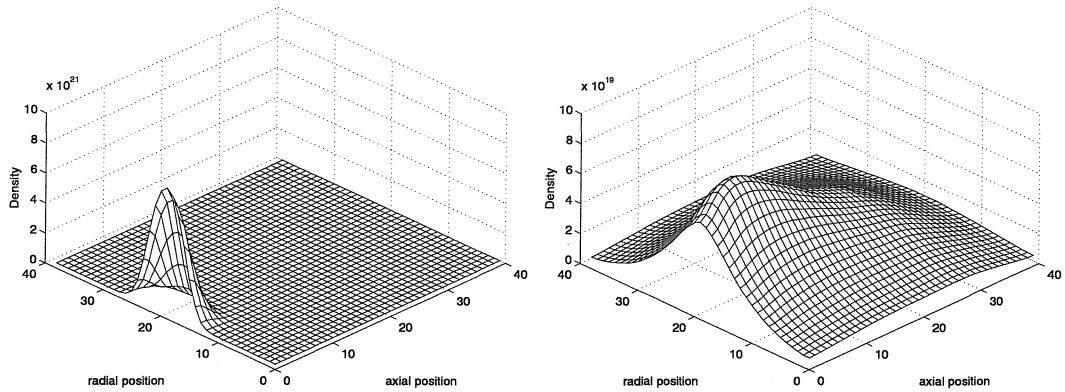

1.0 μs

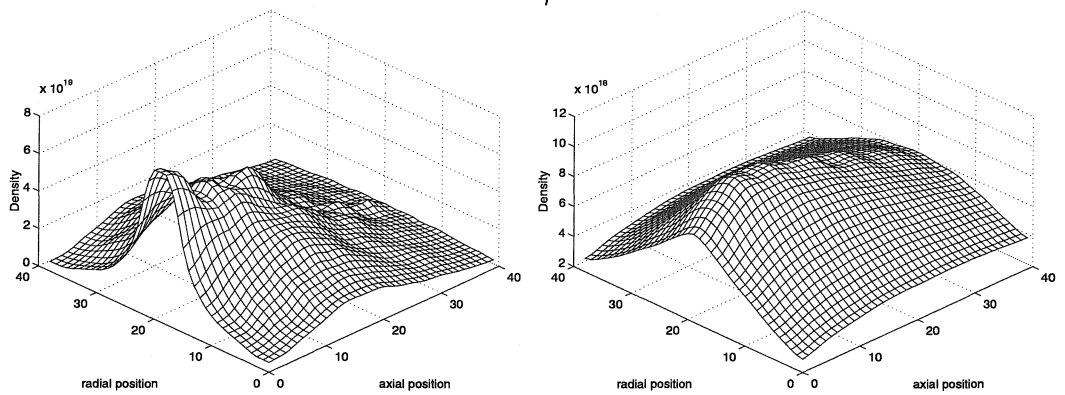

2.0 μs

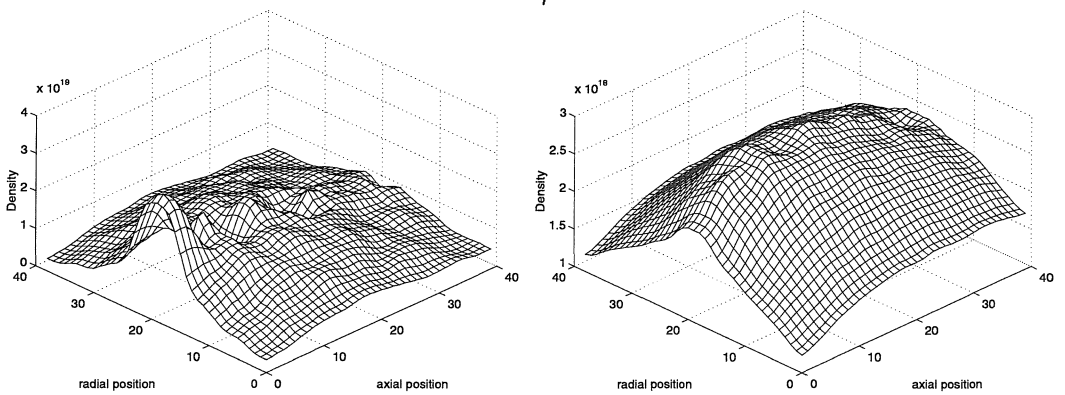

3.0 μs

Figure 6.11: Time sequence mesh plots of Si density during a simulated Si plume expansion into (left column) 100 mTorr Ar, and (right column) vacuum.

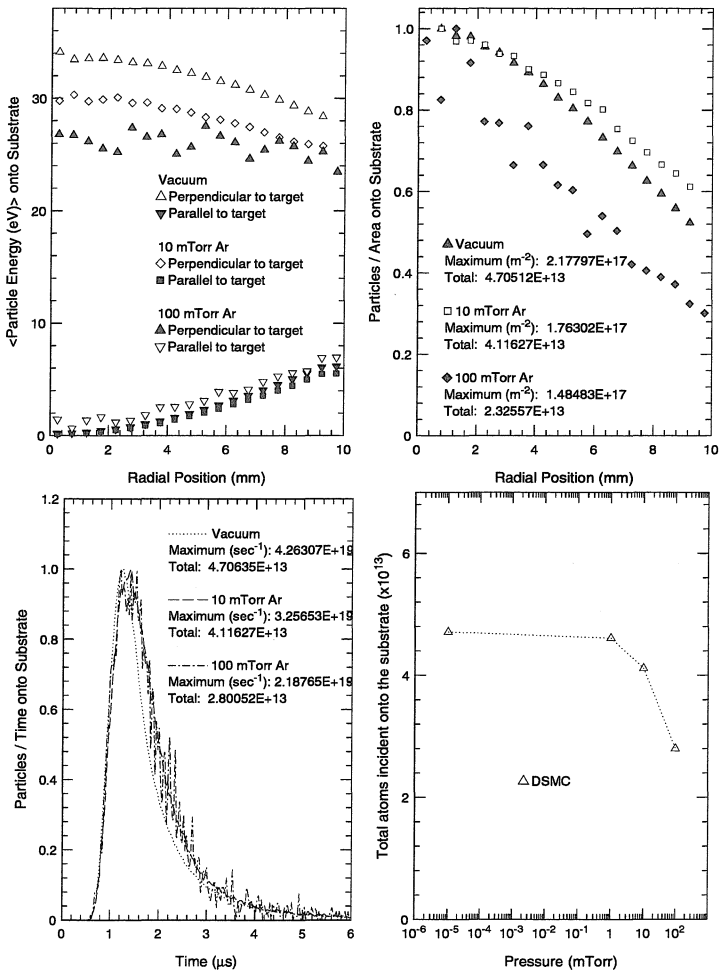

Figure 6.12: A comparison of Si particle flux onto the substrate and energy per particle for ablation into vacuum, 10 mTorr Ar, and 100 mTorr Ar.

of the plume is more forward-peaked than the Si component. This segregation effect is consistent with previous DSMC simulations [97] involving two species which differ only in mass. The enhanced forward-peaking of the heavier species can therefore be explained by considering that the slower speed of the heavier species results in a higher density during the early expansion. This results in a greater number of collisions and therefore greater forward-peaking.

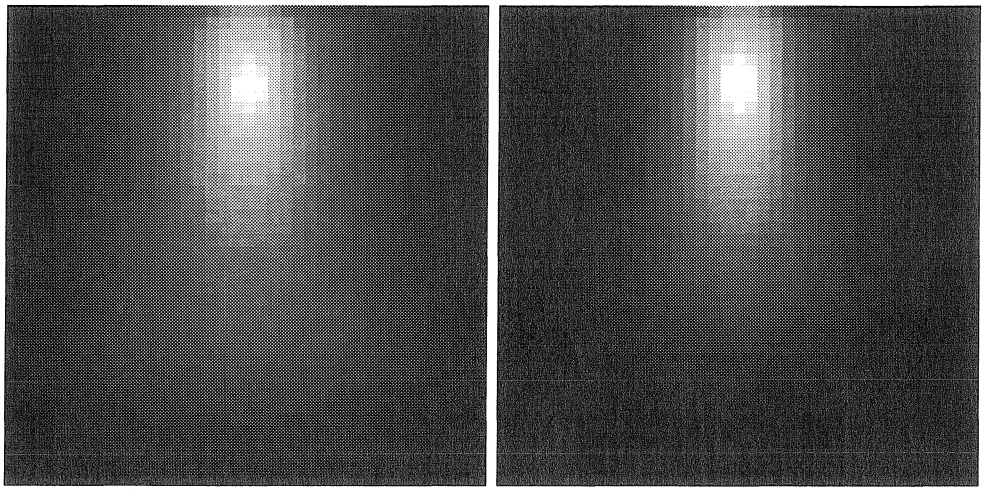

Figure 6.13: A comparison of Si and Ge plumes after a 1.0 μs delay during ablation of $Si_{0.5}Ge_{0.5}$ into vacuum.

The consequences of this effect are evident in Figure 6.14, where the properties of Si and Ge atoms incident onto the substrate are shown. These data include substrate impacts during the interval $0 < t < 6\mu s$. While the Ge deposition is significantly more forward-peaked than the Si, it is slightly less forward-peaked than it would be if the plume contained only Ge. Similarly, the Si deposition is slightly more forward-peaked than when a pure Si plume is ablated. Assuming a sticking probability of 1 for each species, the average stoichiometry of the deposited film when Si and Ge are ablated simultaneously in equal quantity can be described by $Si_{0.42}Ge_{0.58}$. At the center of the film, the concentration of Si is even lower, the stoichiometry described by $Si_{0.36}Ge_{0.64}$.

The film stoichiometry resulting from the ablation of $Si_{0.5}Ge_{0.5}$ differs significantly from that expected if the Si and Ge are ablated in equal quantities *sequentially* from

the target. Sequential ablation might be accomplished, for example, by using a rotating target consisting of pieces of pure Si and Ge. In this case, the average film stoichiometry would be described by $Si_{0.40}Ge_{0.60}$, and by $Si_{0.31}Ge_{0.69}$ at the center. Sequential ablation of Si and Ge therefore results in a film whose stoichiometry differs more from that of the target material than when both species are ablated simultaneously.

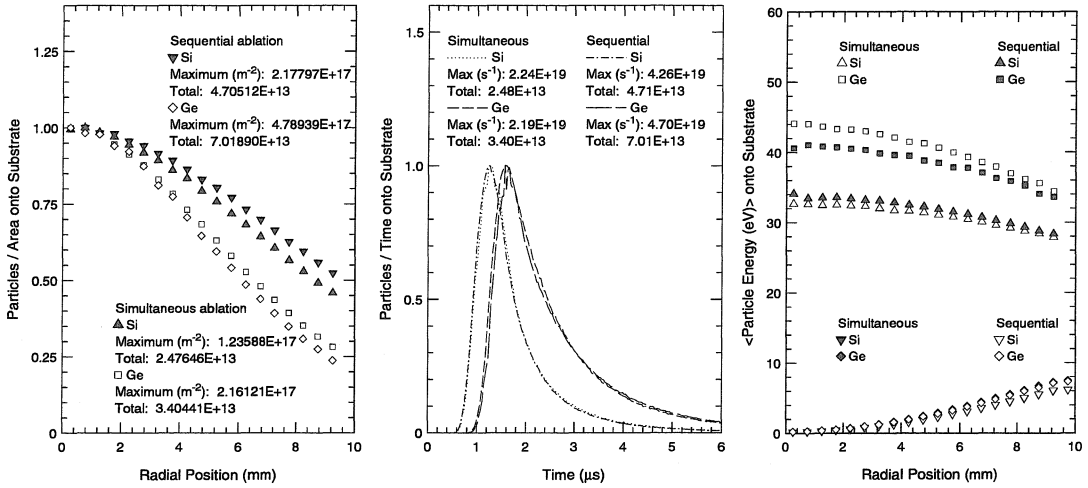

Figure 6.14: A comparison of Si and Ge particle flux onto the substrate and energy per particle for ablation into vacuum of both $Si_{0.5}Ge_{0.5}$ and equal quantities of pure Si and Ge.

The difference in average Si and Ge energies incident onto the substrate indicate that the *velocities* of the two species, rather than the energies, become more comparable as the plume expands. In this particular simulation, the ratio of each species average axial energy onto the substrate ($E_{ge}/E_{si} \approx 1.35$) is about equal to the ratio of their axial speed $(E_{ge}m_{si}/E_{si}m_{ge})^{1/2}$, however, because the forward-peaking of the heavier species increases more rapidly than that of the lighter species as the total number of ablated monolayers increases, the ratio of the axial speeds is expected to be even closer to unity if more than two monolayers are ablated. It is observed experimentally that the velocities of different species rather their energies are comparable during the ablation YBCO.

It is interesting to examine the influence of a background gas on the stoichiometry of Si_xGe_{1-x} films when an $Si_{0.5}Ge_{0.5}$ target is ablated, and when equal quantities of Si

and Ge are ablated sequentially. Figure 6.15 compares the particle flux of each species onto the substrate for both cases. The data suggest that the Si, the lighter species, is more influenced by the background gas. As a consequence, the average stoichiometry of the deposited film, again assuming a sticking probablity one 1 for each species, is described by $Si_{0.43}Ge_{0.57}$ for simulataneous ablation of Si and Ge, and $Si_{0.41}Ge_{0.59}$ for sequential ablation. At the center of the film, the stoichiometries are $Si_{0.40}Ge_{0.60}$ for simulataneous ablation, and $Si_{0.36}Ge_{0.64}$ for sequential ablation. A comparison of these results to those for ablation into vacuum indicates that the film is more enriched with Si (the lighter species) during both sequential and simulatanous ablation into 10 mTorr Ar, and that this effect is most pronounced at the center of the film.

Curiously, experimental data suggests that Sn concentration in Sn_xGe_{1-x} alloys increases with Ar background pressure during the sequential ablation of Sn and Ge [98]. In this case Sn is the *heavier* species, so this data contrasts with the DSMC simulation data for ablation of Si and Ge into Ar. It is possible, however, that the sticking probability for Ge and/or Sn depends on the incident energy, and that differences resulting from the reduced incident energies with the Ar present may offset the gas phase segregation effect, explaining the increase in Sn concentration with Ar pressure. This possibility was not investigated.

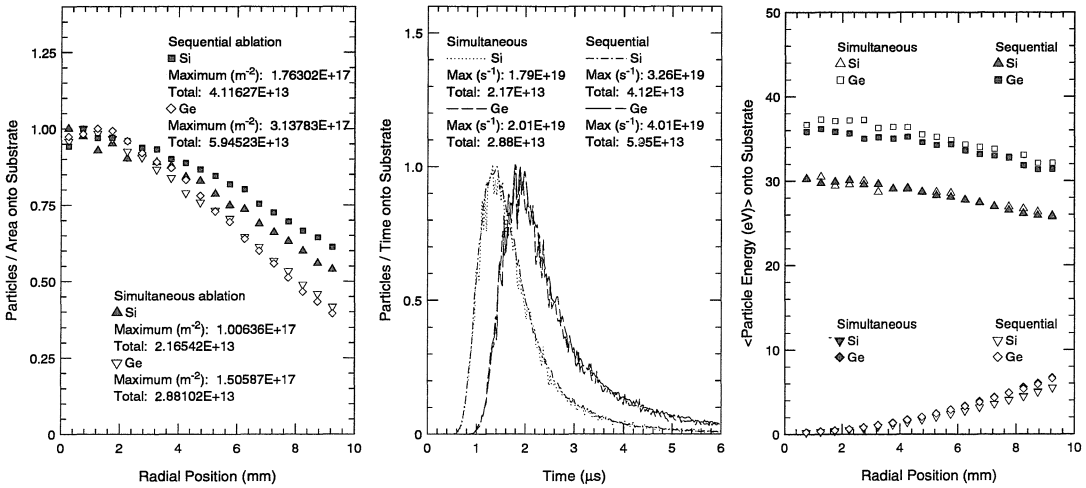

Figure 6.15: A comparison of Si and Ge particle flux onto the substrate and energy per particle for ablation into 10 mTorr Ar of both $Si_{0.5}Ge_{0.5}$ and equal quantities of pure Si and Ge.

6.5 Expansion of Si into O_2

Diatomic molecules like O_2 and N_2 store internal energy in rotational and vibrational modes which becomes accessible during collisions. In thermal equilibrium, internal quantum states are populated according a Boltzmann distribution, however, the population densities of these states during unsteady, super-sonic flow are much more complex. A technique for including energy transfer among rotational, vibrational, and translational degrees of freedom using DSMC simulation is well known [70, 63], so this method offers a unique opportunity to study the influence of the internal degrees of freedom in diatomic molecules during PLA. The technique assumes that the rotational levels form a continuum, so rotational energy is stored in 2 internal degrees of freedom. The vibrational levels, however are usually more widely spaced, and often do not satisfy $\Delta E_v/k = T_{vib} \ll T$. The vibrational energy level spacings in O_2, for example, may be described using the value T_{vib} = 2256 K [63]. These levels must therefore be treated discretely.

A technique has also been developed [63] for including binary chemical reactions of the form $A + B \rightarrow C + D$ when the reaction rate has an Ahrrenius form, given by

$$k(T) = \Lambda T^{\eta} e^{-E_a/kT}, \tag{6.6}$$

where Λ, η, and E_a are parameters specific to a particular reaction. Details describing how a reaction cross section is obtained for a selected collision pair, and this cross section is then used to statistically treat chemical reactions in a gas are provided in Appendix B.

Although the results which follow are intended to demonstrate the more general ability to study *any* set of reactions of interest, focus is placed on the reaction Si + O_2 $\rightarrow$ SiO + O because PLIF data suggesting in-flight production of SiO as Si expands into air was presented earlier, and because this is the simplest bi-molecular pathway to the production of SiO in this system. The change in free energy per particle for this reaction is ΔG^0 = -3.12 eV [79], indicating that the reaction is exothermic. In

equilibrium, the mole fractions of the reactants and products satisfy

$$\frac{[SiO][O]}{[Si][O_2]} = e^{-\Delta G^0/kT} = K_p \tag{6.7}$$

At 2500 K, this fraction becomes K_p = 2 x 10^6, so in a simulation with 400,000 simulation particles, all of the Si and O_2 particles should be coverted to SiO and O particles. The reverse reaction SiO + O $\rightarrow$ Si + O_2 may therefore be ignored.

Experimental measurements of η and E_a are unavailable, and known measurements of Λ differ significantly [99, 100]. Experiments done at 300 K in 4-5 Torr Ar suggest a value of 9.8 x 10^{-6} while measurements in 1 Torr He suggest 2.7 x 10^{-4}. Instead, a comparison may be made to the reaction Si + NO $\rightarrow$ SiO + N, which has been studied more thoroughly [101]. This work was done at 1660-3660 K in a background of Ar at 340-1140 Torr, where an activation energy E_a = 0.153 eV and a reaction rate Λ = 5.3 x 10^{-5} were determined. The value η = 1 is assumed. For lack of better experimental data, these values are used in the following simulation to approximate Ahrrenius coefficients for the reaction Si + O_2 $\rightarrow$ SiO + O. This warrants caution when examining qualitative properties of the flow, but since a long list of other reactions (e.g. O_2 $\rightarrow$ O + O, SiO $\rightarrow$ Si + O, O_2 + O $\rightarrow$ O_3, etc.) are neglected entirely, concern about uncertainties in the reaction coeeficients for the reaction Si + O_2 $\rightarrow$ SiO + O seems premature. The results which follow merely serve to demonstate the plausiblity of obtaining useful information about reactive pulsed laser deposition using the DSMC method. With a more complete list of possible reactions included, realistic estimates of flow properties and reaction product concentrations are expected.

The dimensions of the cylindrical volume for this simulation are reduced to D = 1.5 cm and R = 0.75 cm, and a cell width of 0.25 mm is used. Each cell is divided into 100 subcells and an initial time step of 1 ns is chosen to satisfy the requirements of the DSMC method. As before, the simulation considers the interval $0 < t < 6\mu$s.

Figure 6.16 shows time sequence images of Si density as a 2-monolayer plume of Si expands into 10 mTorr of O_2. Each image depicts the 1.5 cm region between the

target and substrate, with the 2.0 mm ablation spot at the top, and the width of each image is also 1.5 cm. The results are very similar those when 10 mTorr Ar is used, but with a slightly lower peak density. Clearly evident is the fast and the slow component of the plume. The density of O_2 during this period is shown next in Figure 6.17. These images only show the 0.5 cm interesting region near the target, since the density is uniform elsewhere. The snowplow effect is evident as before, however, these images demonstrate how the Si plume pushes the O_2 out more *radially* as a high density pocket of O_2 forms on-axis. This explains how the plume becomes less forward-peaked with the introduction of the background gas.

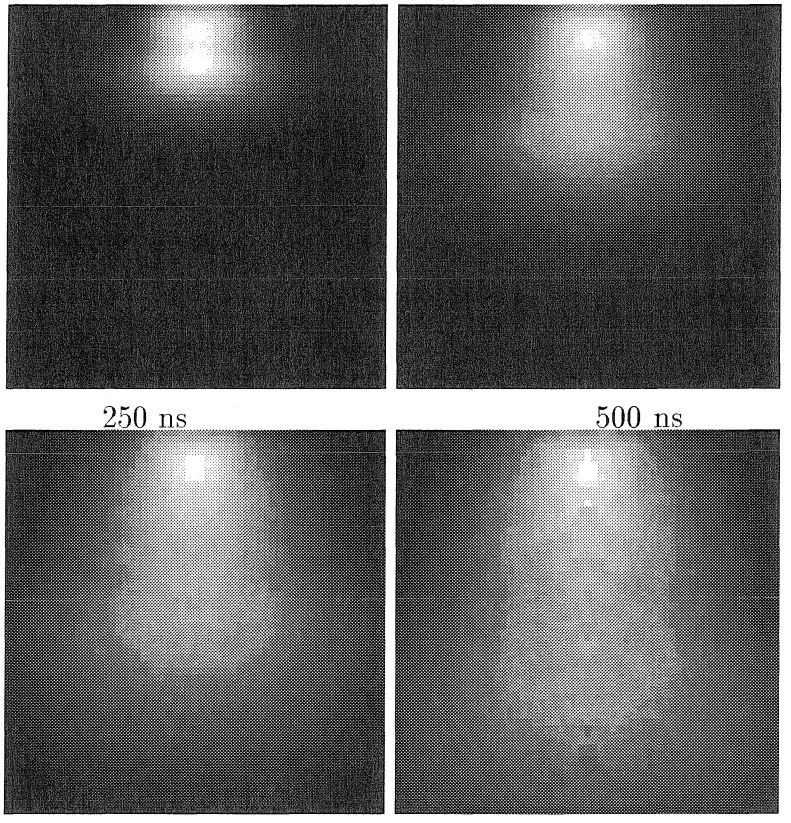

Figure 6.16: Si density during a simulated Si plume expansion into 10 mTorr O_2. The image depicts the 1.5 cm x 1.5 cm region between the target and the substrate.

It is interesting to compare the several temperature parameters for the O_2 gas. In Figures 6.18, 6.18, and 6.18 show the perpendicular, parallel, and rotational temperatures at several times. The regions where these temperatures differ indicate the

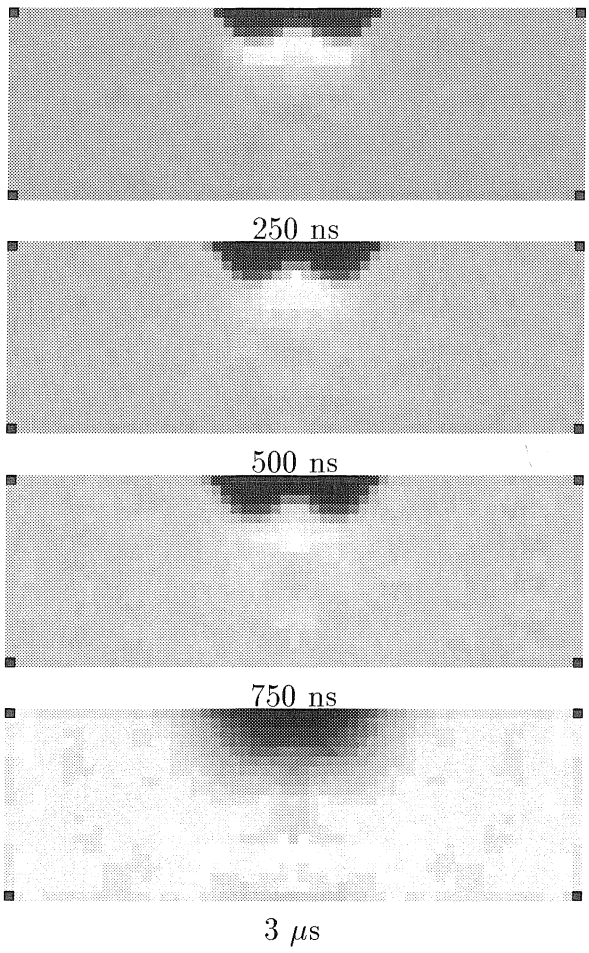

Figure 6.17: O_2 density during a simulated Si plume expansion into 10 mTorr O_2. The image shows the 1.5 cm x 0.5 cm region near the target.

presence of a fast, collisionless, non-thermal component of O_2 gas traveling toward the substrate. When this fast component of the O_2 is ignored, it appears that the temperature of the bulk of the gas remains near 300 K everywhere, except very near the ablation spot. This is evident when the *rotational* temperature of the O_2 is examined. This conclusion is consistent with an earlier finding that the dominant energy transfer from the plume to a background of Ar at 10 mTorr occurs via collisions between fast Si and O_2 molecules, and occurs within the first few hundred nanoseconds of expansion.

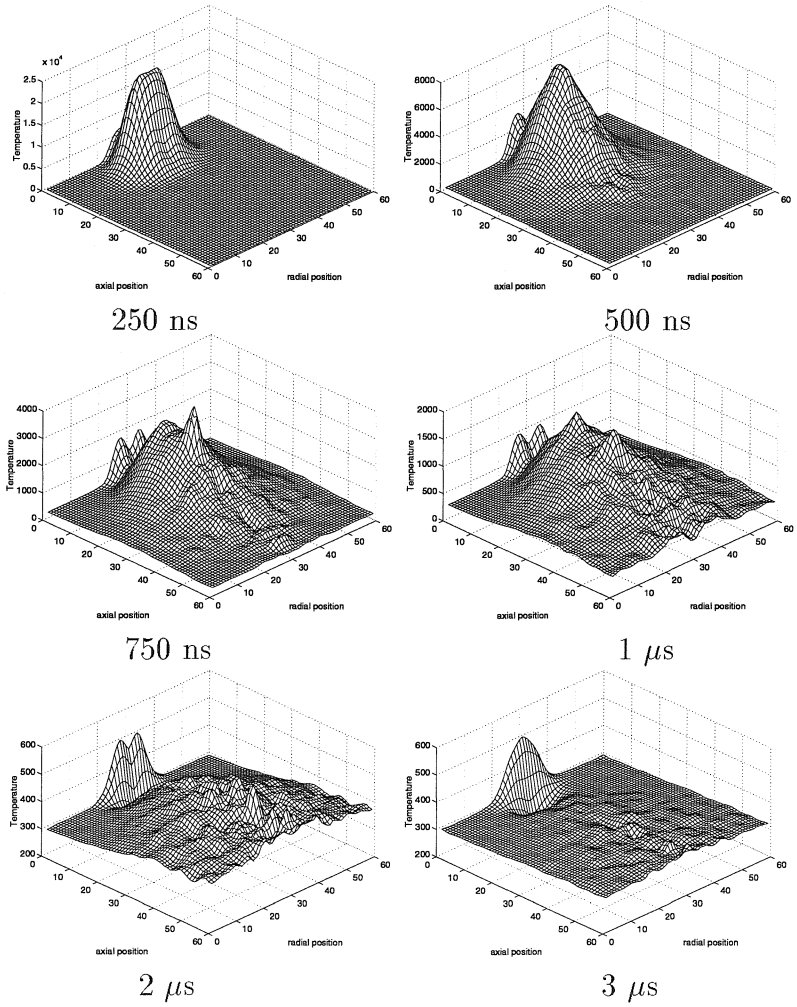

Figure 6.18: Time sequence mesh plots of O_2 axial temperature during a simulated Si plume expansion into 10 mTorr O_2.

The reaction cross section for Si + O_2 → SiO + O is maximum when E_c, the combined energy of the Si and O_2 pair in the center-of-mass reference frame, satisfies

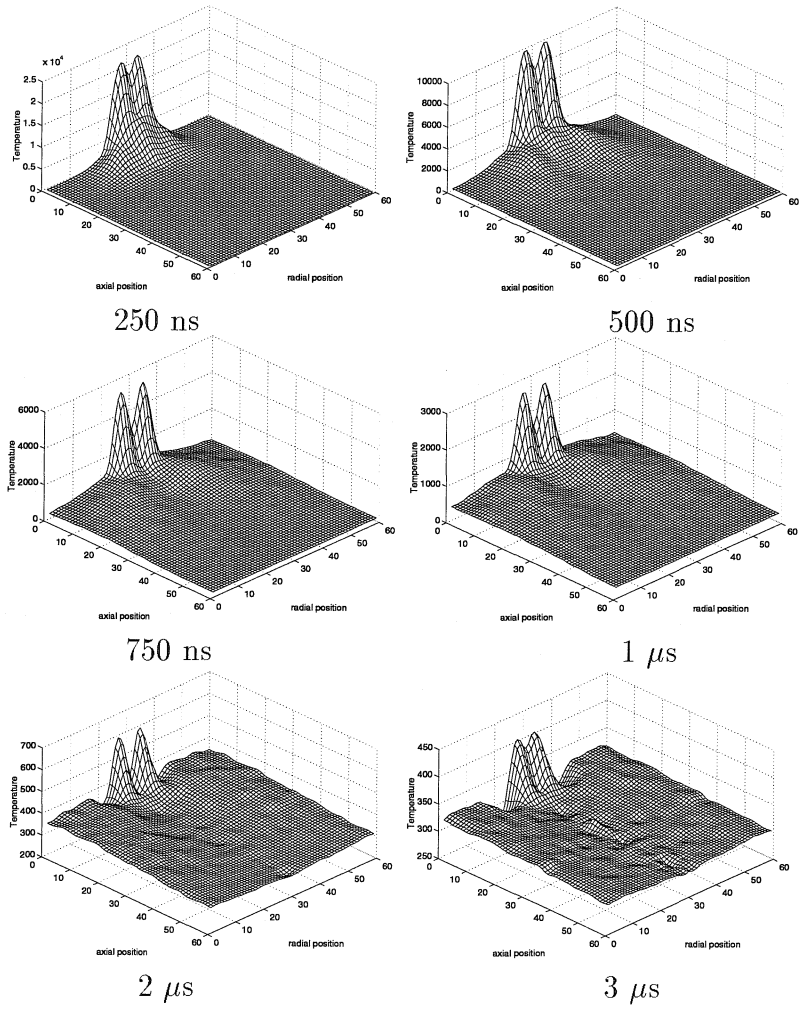

Figure 6.19: Time sequence mesh plots of O_2 radial temperature during a simulated Si plume expansion into 10 mTorr O_2.

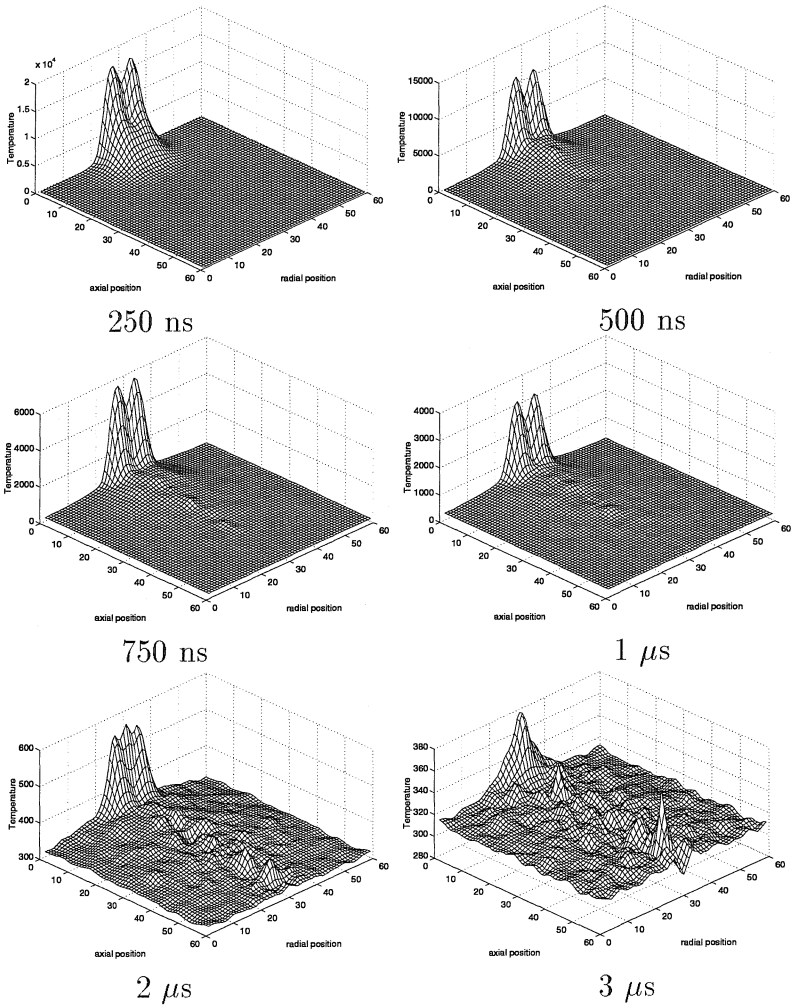

Figure 6.20: Time sequence mesh plots of O_2 rotational temperature during a simulated Si plume expansion into 10 mTorr O_2.

$E_c \approx 10E_a$ (equation 0.114). If the activation energy of this reaction is about 0.15 eV, then SiO production should occur primarily where E_c is nearest to 1-2 eV, an energy much smaller than the characteristic energy of the expanding Si atoms. Simulation results suggest that, on average, the reaction cross section is only about 5-10% as large as the collision cross for Si and O_2. The density of SiO is therefore small, resulting in very noisy images for times greater than 1 μs, even when the results of 40 simulations are averaged and processed through a median filter. Images depicting the relative density of SiO for times less than 1 μs are in Figure 6.21. SiO appears to be produced primarily off-axis. Since the velocity of the more radially expanding off-axis Si atoms is smaller than that of axially directed on-axis Si atoms, a higher percentage of off-axis collisions between Si and O_2 result in SiO. This effect is offset, however, by the greater number of collisions on-axis due to a higher density of both Ar and O_2, however, so it is not obvious *a priori* where the most SiO production should occur.

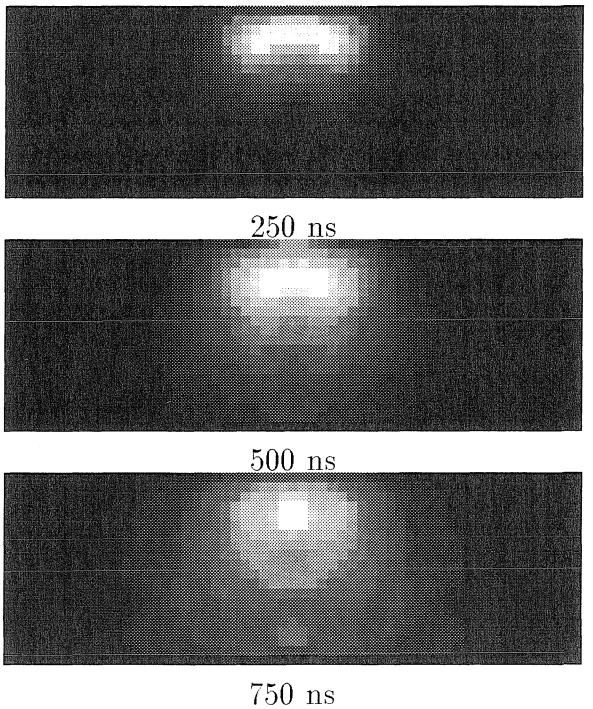

Figure 6.21: SiO density during a simulated Si plume expansion into 10 mTorr O_2. The image shows the 1.5 cm x 0.5 cm region near the target.

The radial distribution of particle flux and energy per particle incident onto the

substrate for each of the three species Si, O_2, and SiO is shown shown in Figure 6.22. In order to discount the continuous flux of 300 K O_2 incident onto the substrate, only O_2 molecules with an energy exceeding 0.5 eV are allowed to stick, the rest specularly reflect. The total flux of SiO onto the substrate is about 10% of the flux of O_2, and the average energy per SiO particle of 15 eV is 36.5% greater than the average value of 11 eV for O_2 molecules. Since the mass of SiO is about 37.5% greater than that of O_2, this result is consistent with the earlier finding that particle velocities, rather than particle energies, tend to become more similar during PLA.

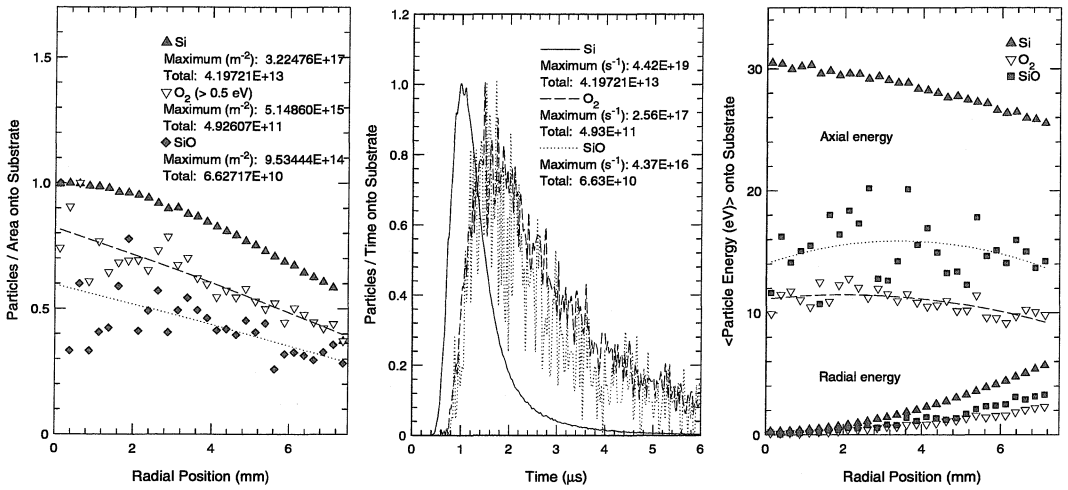

Figure 6.22: (Left) Surface density of Si, O_2, and SiO on the substrate as a function of radial position for ablation of Si into 10 mTorr O_2. (Center) Impact rate as a function of time. (Right) Average axial and radial energy per particle incident onto the substrate.

A second simulation, in which a 5-monolayer plume expands into 100 mTorr O_2 was also performed. The density of the Si at several time delays is shown in Figure 6.23, focusing on the 5 mm region near the target. The fast plume component is seen to separate from the slow component, and later a contact front forms as the slow component expands. A distinct contact front was not observed in an earlier simulation of a 2-monolayer plume expanding into 100 mTorr Ar.

The density of O_2 is shown next in Figure 6.24, followed by the SiO density in Figure 6.25. Similar to the results at lower pressure, the O_2 in this case achieves high density on-axis by 250 nsec, and the Si then begins to displace the O_2 around this

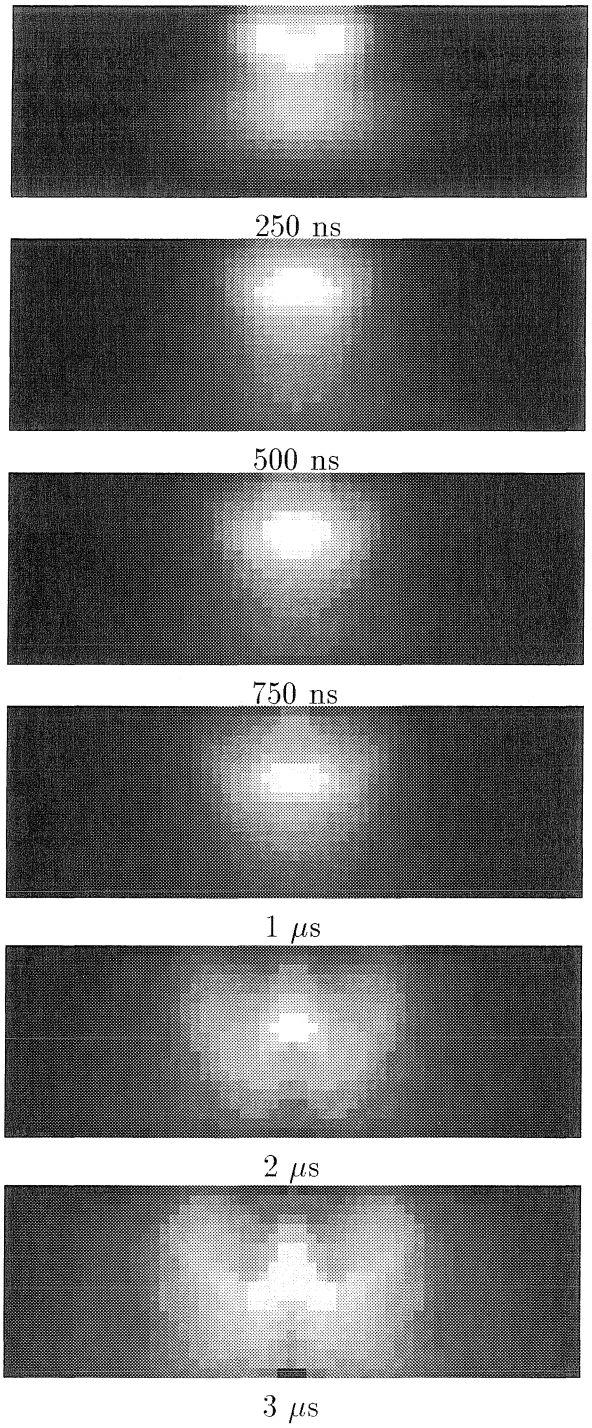

Figure 6.23: Si density during a simulated Si plume expansion into 100 mTorr O_2. The image shows the 1.5 cm x 0.5 cm region near the target.

compressed region. The reaction product SiO appears to first form at the sides of the expanding plume, consistent with the results at lower O_2 pressure, but by 3 μs the SiO appears distributed around the perimeter of the forming contact front. A comparison of these simulation data with the PLIF data shown in Figure 3.5 reveals interesting qualitative agreement. Like the DSMC results, the PLIF data also suggests that SiO is formed primarily at the sides of the plume, however, the order-of-magnitude difference in background gas pressure for the two cases warrants caution when making a more detailed comparison.

Shown in Figures 6.26, 6.27, and 6.28 are the axial, radial, and rotational temperatures of the O_2, respectively. The presence of a fast non-thermal O_2 component is once again evidenced by differences among these temperatures. In this case, however, thermal heating of the O_2 is suggested when this contribution is ignored. Consistent with the earlier finding that the dominant energy transfer from the plume to a 100 mTorr background gas is thermal heating, the rotational temperature of the O_2 is observed to rise well above 300 K along a conical surface whose tip is at the ablation spot. This temperature rise occurs on a μs time scale.

Finally, Figure 6.29 provides information about the particle flux onto the substrate for the ablation of 5 monolayers of Si into 100 mTorr O_2.

6.6 Conclusions

In this chapter the DSMC method is used to study the expansion of an Si into both Ar and O_2 at 10 mTorr and 100 mTorr, and to study the expansion of an $Si_{0.5}Ge_{0.5}$ alloy into both vacuum and 10 mTorr Ar.

When Si expands into Ar, the plume is observed to split into two components, one which travels collisionlessly toward the substrate, and the other which is retarded by the background gas. The separation results from a rapid buildup in the background gas density at the contact front during the first 250 ns of expansion, which physically divides the plume. When the particle flux onto the substrate during expansion into Ar at 10 mTorr is compared with that for ablation into vacuum, the number of fast Si

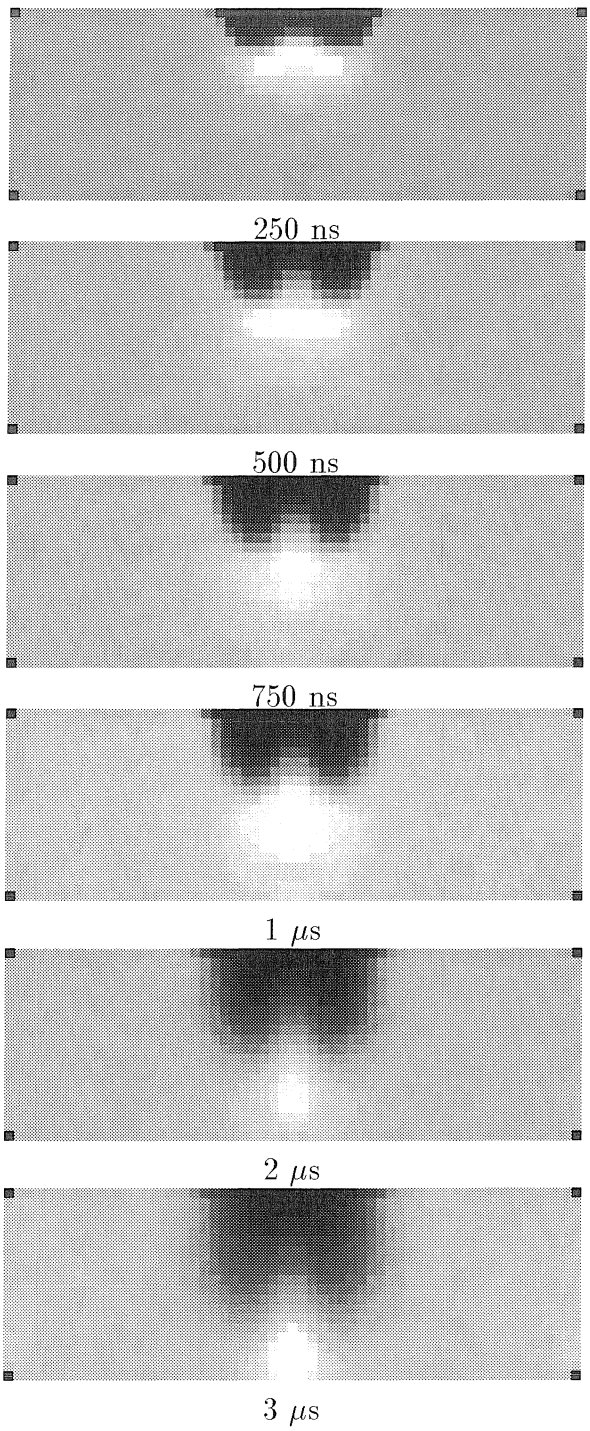

Figure 6.24: O_2 density during a simulated Si plume expansion into 100 mTorr O_2. The image shows the 1.5 cm x 0.5 cm region near the target.

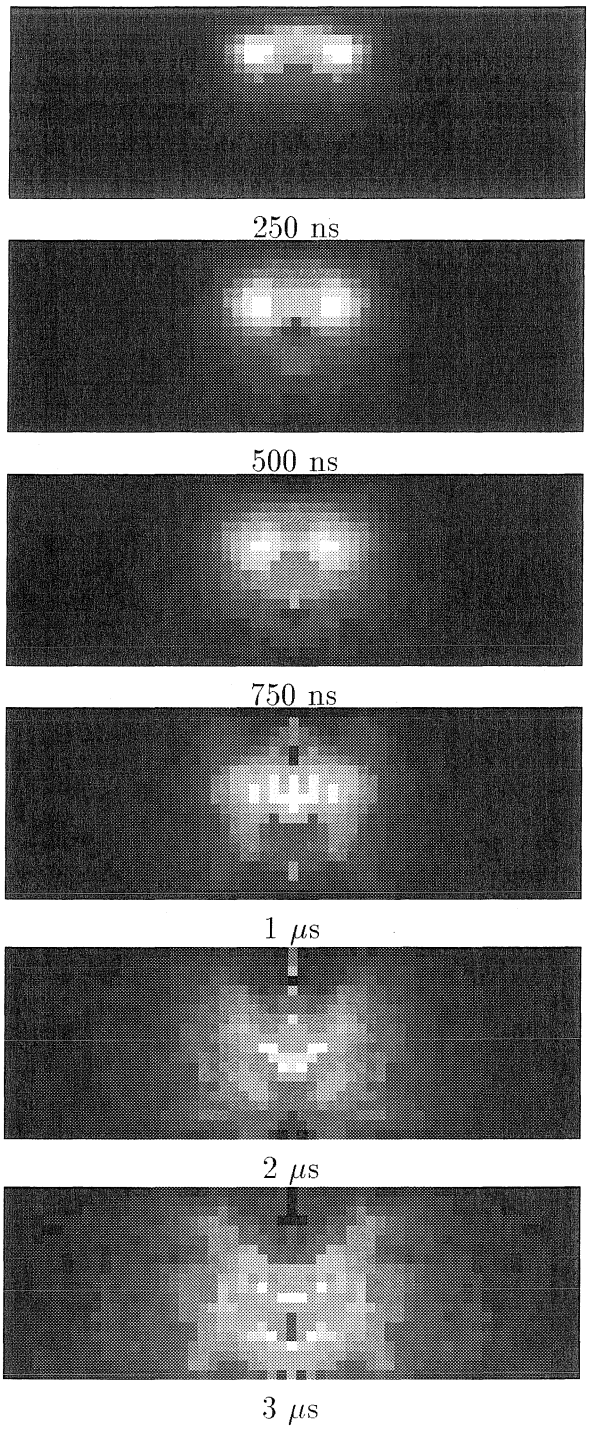

Figure 6.25: SiO density during a simulated Si plume expansion into 100 mTorr O_2. The image shows the 1.5 cm x 0.5 cm region near the target.

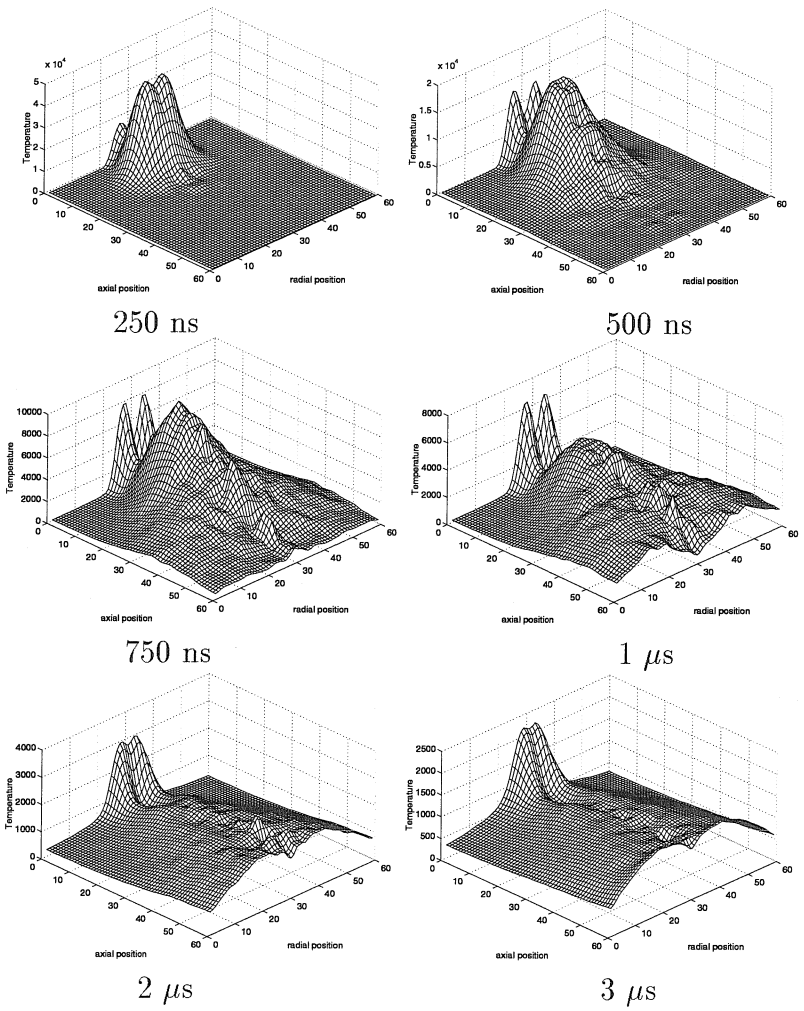

Figure 6.26: Time sequence mesh plots of O_2 axial temperature during a simulated Si plume expansion into 100 mTorr O_2.

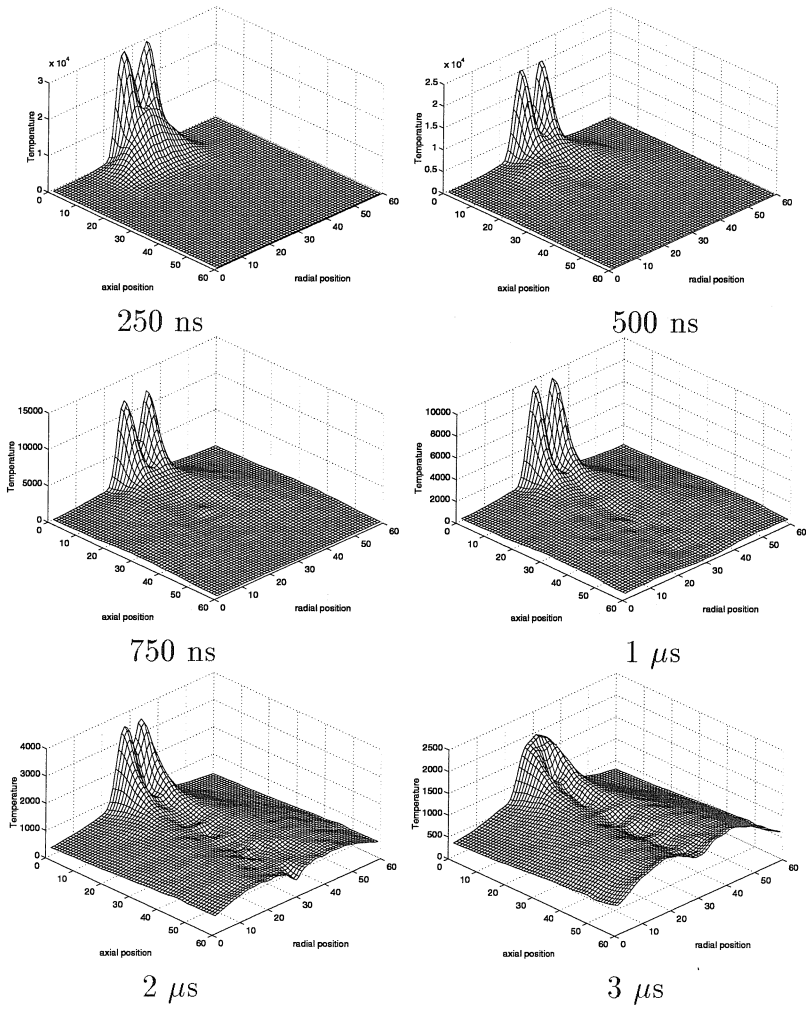

Figure 6.27: Time sequence mesh plots of O_2 radial temperature during a simulated Si plume expansion into 100 mTorr O_2.

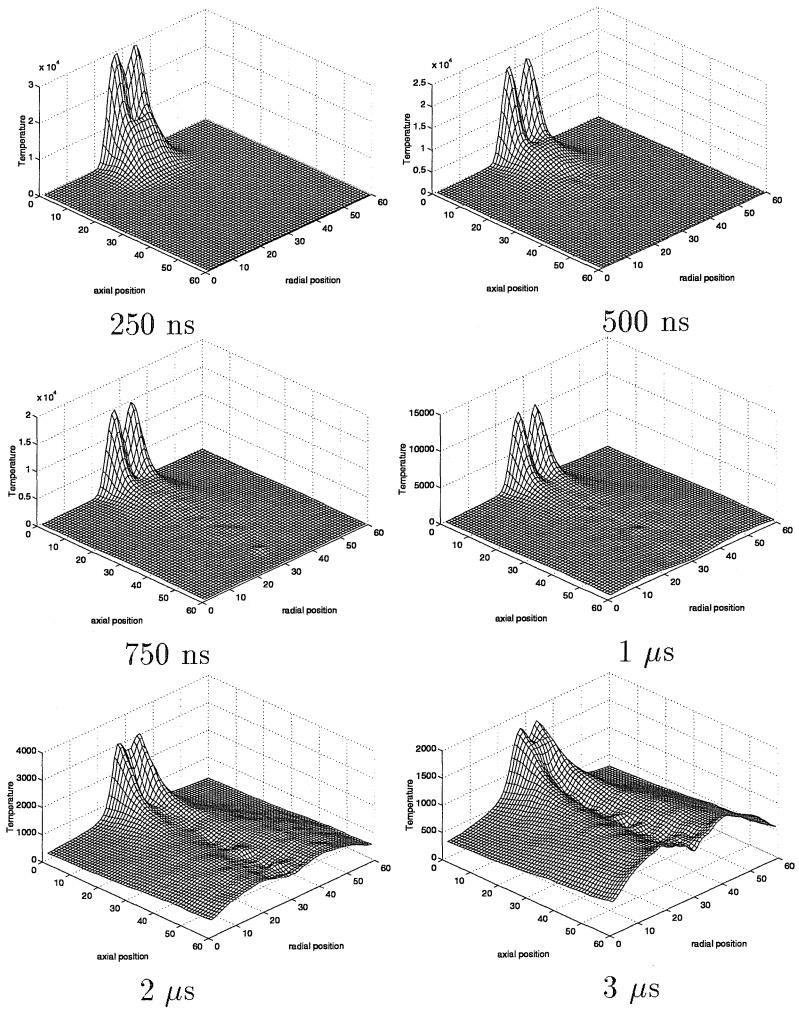

Figure 6.28: Time sequence mesh plots of O_2 rotational temperature during a simulated Si plume expansion into 100 mTorr O_2.

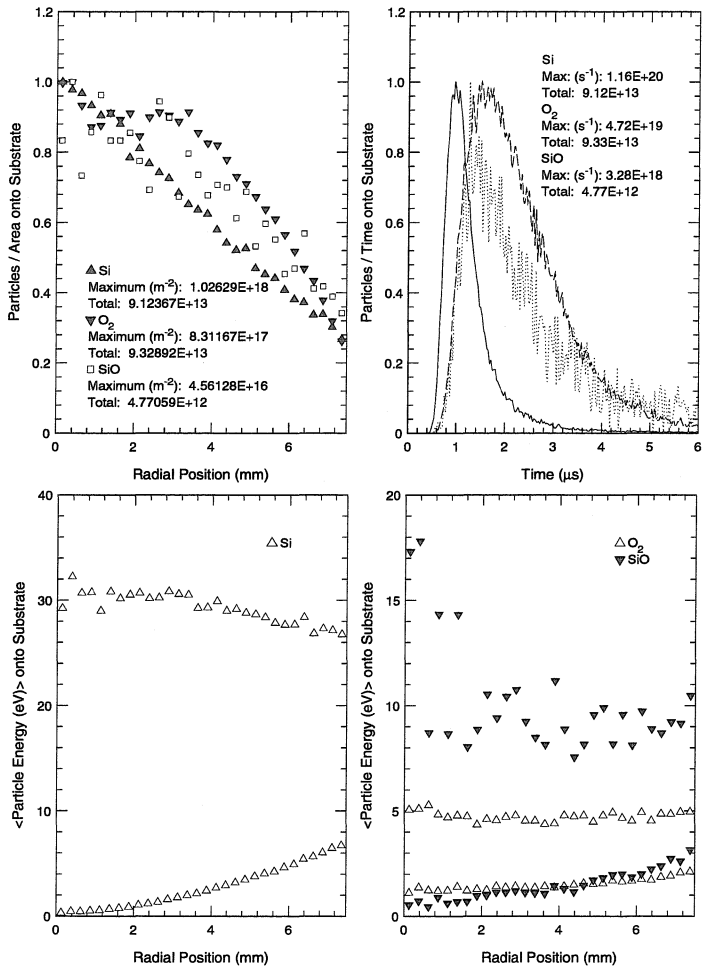

Figure 6.29: Surface density of Si, O_2, and SiO on the substrate as a function of radial position for ablation of Si into 100 mTorr O_2. Also shown are impact rates as functions of time for each species, and average axial and radial energy per particle incident onto the substrate.

atoms incident is diminished by about 10%, the average energy per particle by about 4 eV, and the resulting film is slightly less forward-peaked. At an Ar pressure of 100 mTorr, the number of Si atoms in the fast component of the plume diminishes by a factor of 2 and the energy per atom falls about 20%, from about 32 eV to about 26 eV.

At an Ar pressure of 10 mTorr, the energy exchange between the plume and background gas occurs mostly during this early period, resulting in a fast (10-15 eV) Ar component and very little thermal heating of the gas bulk. A pulse of energetic Ar molecules, consisting of about 1% the number of Si atoms in the fast plume component, are incident onto the substrate shortly after the fast Si component arrives. At 100 mTorr, the dominant energy transfer mechanism from the plume to the background gas becomes thermal heating on a μs time scale. The energy per particle in the fast Ar component drops to about 5 eV at this pressure. This high energy background gas flux is interesting because it may play an important role in surface preparation or annealing of the growing film during PLD.

When a 10 mTorr O_2 background gas is used instead of Ar, a fast (11 eV) O_2 component is observed to be incident onto the substrate shortly after the fast Si component arrives. This pulse of high energy background gas also includes 15 eV SiO molecules, formed in the gas-phase by the reaction $Si + O_2 \rightarrow SiO + O$. The number of these molecules is about 10% the number of fast O_2 molecules. Heating of the O_2 on a μs time scale when the background pressure is increased to 100 mTorr is evident in a rotational temperature increase in the O_2 along a conical surface whose tip is at the location of the ablation spot. SiO is observed to form primarily at the *sides* of the expanding plume and is later seen primarily along the contact front between Si and O_2. These results are qualitatively similar to those obtained during PLIF imaging of an Si plume expanding into air at 1 Torr.

Although the results obtained from the simulations discribed in this chapter are interesting, the real purpose of this work is to demonstrate the potential of the DSMC to study the expansion of plumes with a much wider range of compositions into rarified background gas mixtures, including any number of target and/or gas species, and any

number of chemical reactions. The hope is that future work will prove this method to be useful for providing quantitative estimates of parameters relevant to the deposition of interesting films.

Appendix A Overview of a closed two-level system

A.1 Interaction of an electromagnetic field and an isolated two level molecule.

Consider a molecule, described by a wave function Ψ satisfying $\Psi = \sum c_n \Phi_n$ where the set Φ_n are time-independent eigenfunctions of some time-independent Hamiltonian H_0, that is $H_0\Phi_n = E_n\Phi_n$. Under the influence of some time-dependent perturbation in the Hamiltonian, $\tilde{V}(t)$, the coefficients c_n satisfy the equation

$$i\hbar\dot{c}_n(t) = E_n c_n(t) + \sum \langle \Phi_n | \tilde{V}(t) | \Phi_m \rangle c_m. \tag{0.8}$$

If the perturbation is caused by a weak electromagnetic wave with a sufficiently long wavelength to justify the dipole approximation, the perturbation potential can be described in terms of the molecular dipole moment $\vec{\mu}$ and the electric field vector $\vec{E}(t)$ by

$$\tilde{V}(t) = -\vec{\mu} \cdot \vec{\mathcal{E}}(t), \tag{0.9}$$

where the electric field strength can be written as

$$\vec{\mathcal{E}}(t) = \frac{1}{2}\vec{\mathcal{E}}_0 e^{-i\omega t} + c.c. \tag{0.10}$$

For a frequency ω sufficiently near a transition frequency in the molecule, the molecule can be treated as a two-level system, with time-dependent eigenstate amplitudes $c_1(t)$ and $c_2(t)$ which satisfy

$$i\hbar\dot{c}_1(t) = E_1 c_1 - \frac{1}{2} e c_1 \vec{\mu}_{12} \cdot (\vec{\mathcal{E}}_0 e^{-i\omega t} + \vec{\mathcal{E}}_0^* e^{i\omega t}) \tag{0.11}$$

and

$$i\hbar\dot{c}_2(t) = E_2 c_2 - \frac{1}{2} e c_2 \vec{\mu}_{21} \cdot (\vec{\mathcal{E}}_0 e^{-i\omega t} + \vec{\mathcal{E}}_0^* e^{i\omega t}), \tag{0.12}$$

where $\vec{\mu}_{nm} = \langle \Phi_n | \vec{\mu} | \Phi_m \rangle$. In general, the electric field vector $\vec{E}_0$ is complex to include the possibility of a circularly polarized field. The behavior of the eigenstate amplitudes can be seen more clearly by tranforming them to a reference frame that is rotating at a rate $\omega_1 = E_1/\hbar$, a frame in which c_1 is stationary when no perturbation is applied. This is achieved by letting $c_n \rightarrow c_n e^{-i\omega_1 t}$. Equations 0.11 and 0.12 then become

$$i\dot{c}_1(t) = \frac{e}{2\hbar} c_2 \vec{\mu}_{12} \cdot (\vec{\mathcal{E}}_0 e^{-i\omega t} + \vec{\mathcal{E}}_0^* e^{i\omega t}) \tag{0.13}$$

and

$$i\dot{c}_2(t) = \omega_{21} c_2 - \frac{e}{2\hbar} c_1 \vec{\mu}_{21} \cdot (\vec{\mathcal{E}}_0 e^{-i\omega t} + \vec{\mathcal{E}}_0^* e^{i\omega t}), \tag{0.14}$$

where $\omega_{21} = (E_2 - E_1)/\hbar$. In this rotating frame, when no perturbation is applied, c_1 is fixed in time but c_2 rotates at a rate ω_{21}. It is therefore convenient to consider c_2 in a reference frame that is rotating at a rate ω_{21} by employing the transformation $c_2 \rightarrow c_2 e^{i\omega_{21} t}$. Equations 0.13 and 0.14 become

$$i\dot{c}_1(t) = \frac{e}{2\hbar} c_2 \vec{\mu}_{12} \cdot (\vec{\mathcal{E}}_0 e^{-i(\omega+\omega_{21})t} + \vec{\mathcal{E}}_0^* e^{i(\omega-\omega_{21} t)} \tag{0.15}$$

and

$$i\dot{c}_2(t) = (\omega_{21} - \omega) c_2 - \frac{e}{2\hbar} c_1 \vec{\mu}_{21} \cdot (\vec{\mathcal{E}}_0 e^{-i(\omega-\omega_{21})t} + \vec{\mathcal{E}}_0^* e^{i(\omega+\omega_{21})t}). \tag{0.16}$$

If the radiation frequency is near the transition frequency ($\omega \approx \omega_{21}$) then both c_1 and c_2 have a slow and a fast rotating term. Since the coefficients c_1 and c_2 would be solved by integration of equations 0.15 and 0.16, the rapidly oscillating terms would average to zero on the time scale of the slow terms, leaving only the contribution from the slow terms. In this rotating wave approximation, the fast terms can be discarded, and the slow terms then expanded in a power series. This leaves

$$i\dot{c}_1(t) = \frac{e}{2\hbar} c_2 \vec{\mu}_{12} \cdot \vec{\mathcal{E}}_0^* (1 - i\Delta t + \Delta^2 t^2 + ...) \tag{0.17}$$

and

$$i\dot{c}_2(t) = (\omega_{21} - \omega)c_2 - \frac{e\pi}{h}c_1\vec{\mu}_{21} \cdot \vec{\mathcal{E}}_0(1 + i\Delta t - \Delta^2 t^2 + ...), \tag{0.18}$$

where $\Delta = \omega_{21} - \omega$ is a measure of detuning of the electromagnetic wave from resonance. If $\Delta t \ll 1$ then equations 0.18 and 0.18 then reduce to

$$i\dot{c}_1(t) = \frac{e}{2\hbar}c_2\vec{\mu}_{12} \cdot \vec{\mathcal{E}}_0^* \tag{0.19}$$

and

$$i\dot{c}_2(t) = \Delta c_2 - \frac{e\pi}{h}c_1\vec{\mu}_{21} \cdot \vec{\mathcal{E}}_0. \tag{0.20}$$

A.2 Population rate equations for an ensemble of molecules in a closed two level system

For an ensemble of identical molecules, it is convenient to define a density matrix which satisfies $\rho_{ij} = \langle c_i c_j^* \rangle$. The brackets denote an average over all the molecules in the ensemble. For N molecules, $N\rho_{nn}$ represents the average number found in eigenstate Φ_n. After substituting the equations for c_1 and c_2 from equations 0.19 and 0.20, the components of the density matrix can be shown to satisfy

$$\dot{\rho}_{12}(t) = i\Delta\rho_{12} + i\frac{e}{2\hbar}\vec{\mu} \cdot \vec{\mathcal{E}}_0^*(\rho_{22} - \rho_{11}) \tag{0.21}$$

and

$$\dot{\rho}_{22}(t) = i\frac{e}{2\hbar}\vec{\mu} \cdot (\vec{\mathcal{E}}_0\rho_{12} - \vec{\mathcal{E}}_0^*\rho_{21}), \tag{0.22}$$

where $\vec{\mu} = \vec{\mu}_{12} = \vec{\mu}_{21}^*$. The time dependent behavior of remaining matrix elements follow from the relations $\dot{\rho}_{11} = -\dot{\rho}_{22}$ and $\rho_{21} = \rho_{12}^*$.

Equations 0.21 and 0.22 describe the time evolution of the density matrix components in an isolated two-level system under the influence of an oscillatory electric field near resonance. If no field exists, that is if $\vec{\mathcal{E}}_0 = \vec{\mathcal{E}}_0^* = 0$, then these equations predict that the populations of each state will remain constant, and the off-diagonal

matrix elements will rotate at the detuning frequency Δ.

In a physically real two-level system, excited molecules tend to relax to the ground state in the abscence of an electric field. Quantum field theory describes this process as an interaction of the excited molecule with the zero-point electric field, resulting in spontaneous relaxation from the upper to lower state. This effect can be modeled by introducing a spontaneous emission rate A_{21} given by

$$A_{21} = \frac{|\vec{\mu}|^2 \omega_{21}^3}{3\epsilon_0 \pi \hbar c^3}, \tag{0.23}$$

where $|\vec{\mu}|^2 = e^2 |\langle \Phi_1 | \vec{r} | \Phi_2 \rangle|^2$. The off-diagonal matrix elements, which contain phase relationships between the two eigenfunctions averaged over the ensemble of molecules, must also be allowed to relax as coherence is lost among atoms, due to each atom's independent interaction with the zero-point electric field. Equations 0.21 and 0.22 can be modified to include these considerations by writing

$$\dot{\rho}_{12}(t) = i\Delta\rho_{12} + i\frac{e}{2\hbar}\vec{\mu} \cdot \vec{\mathcal{E}}_0^*(\rho_{22} - \rho_{11}) - \beta\rho_{12} \tag{0.24}$$

and

$$\dot{\rho}_{22}(t) = i\frac{e}{2\hbar}\vec{\mu} \cdot (\vec{\mathcal{E}}_0\rho_{12} - \vec{\mathcal{E}}_0^*\rho_{21}) - A_{21}\rho_{22}. \tag{0.25}$$

The damping rate for off-diagonal matrix elements (β) is presumed to be sufficiently large that the steady-state solution for those quantities is valid, that is $\dot{\rho}_{21} = \dot{\rho}_{12} \approx 0$. This assumption implies that the off-diagonal elements follow the population difference according to

$$\rho_{12}(t) = \frac{i\frac{e}{2\hbar}\vec{\mu} \cdot \vec{\mathcal{E}}_0^*(\rho_{22} - \rho_{11})}{\beta - i\Delta} \tag{0.26}$$

and

$$\rho_{21}(t) = \frac{-i\frac{e}{2\hbar}\vec{\mu} \cdot \vec{\mathcal{E}}_0(\rho_{22} - \rho_{11})}{\beta + i\Delta}. \tag{0.27}$$

A substitution of equations 0.26 and 0.27 into equation 0.25 results in a population

rate equation for the upper state given by

$$\dot{\rho}_{22}(t) = -A_{21}\rho_{22} - R_{21}\rho_{22} + R_{12}\rho_{11}, \tag{0.28}$$

where the stimulated emission/absorption rate is given by

$$R_{21}(\Delta) = R_{12}(\Delta) = \frac{|\frac{\vec{\mu}\cdot\vec{\mathcal{E}}_0}{\hbar}|^2\frac{\beta}{2}}{(\Delta^2+\beta^2)}. \tag{0.29}$$

For a gas of collisional molecules subject to linearly polarized radiation, the orientation of the complex dipole moment with the electric field vector can be assumed, on average, to be random so that if $\vec{\mathcal{E}}_0 = \mathcal{E}_0\hat{n}$, then

$$|\vec{\mu}\cdot\vec{\mathcal{E}}_0|^2 = \langle|\vec{\mu}\cdot\hat{n}|^2\rangle\mathcal{E}_0^2 = \frac{1}{3}|\vec{\mu}|^2\mathcal{E}_0^2. \tag{0.30}$$

The brackets $\langle\rangle$ denote an ensemble average over all the molecules. The orientation-averaged stimulated emission (absorption) rate is then given by

$$R_{21}(\Delta) = R_{12}(\Delta) = \frac{\beta}{6\hbar^2}\frac{|\vec{\mu}|^2\mathcal{E}_0^2}{(\Delta^2+\beta^2)}. \tag{0.31}$$

From equation 0.28, the relation $\dot{\rho}_{11} = -\dot{\rho}_{22}$, and $N_i = N\rho_{ii}$, the population rate equations for a closed two-level system can be written as

$$\dot{N}_2(t) = -A_{21}N_2 - R_{21}N_2 + R_{12}N_1 \tag{0.32}$$

and

$$\dot{N}_1(t) = A_{21}N_2 + R_{21}N_2 - R_{12}N_1. \tag{0.33}$$

A.3 Effect of degeneracy on the population rate equations

The spacing between energy levels in a molecule is often dependent on some quantized angular momentum vector $\vec{J}$, which results in a set of $2J+1$ energetically degenerate states foe a level described by quantum number J. Since the two levels in the model under consideration may depend on different angular momentum quantum numbers, they will, in general, have different degeneracies g_1 and g_2. Equations 0.32 and 0.33 can be applied to the populations of each degenerate state by letting, for example, A_{2i1j} denote the spontaneous emission rate from the substate (i) in the upper level to substate (j) in the lower level. This results in g_1 equations for the lower substate populations and g_2 equations for the upper substate populations of the form

$$\dot{N}_{2i}(t) = \sum_{j}^{g1} \{-A_{2i1j}N_{2i} - R_{2i1j}N_{2i} + R_{1j2i}N_{1j}\} \tag{0.34}$$

and

$$\dot{N}_{1i}(t) = \sum_{j}^{g2} \{A_{2j1i}N_{2j} + R_{2j1i}N_{2j} - R_{1i2j}N_{1i}\}\,. \tag{0.35}$$

Each set of equations can be summed to give rate equations for the combined upper and lower level populations, that is $\dot{N}_1(t) = \sum_i^{g2} \dot{N}_{2i}(t)$ and $\dot{N}_2(t) = \sum_i^{g1} \dot{N}_{1i}(t)$. This gives

$$\dot{N}_2(t) = -\sum_{i}^{g2} N_{2i} \left\{ \sum_{j}^{g1} (A_{2i1j} - R_{2i1j}) \right\} + \sum_{j}^{g1} N_{1j} \left\{ \sum_{i}^{g2} R_{1j2i} \right\} \tag{0.36}$$

and

$$\dot{N}_1(t) = \sum_{j}^{g2} N_{2j} \left\{ \sum_{i}^{g1} (A_{2j1i} + R_{2j1i}) \right\} - \sum_{i}^{g1} N_{1i} \left\{ \sum_{j}^{g1} R_{1i2j} \right\}. \tag{0.37}$$

The dependence of R_{21}, R_{12}, and A_{21} on the particular substate pair is contained in the quantity $|\vec{\mu_{ij}}|^2$. It can be shown that by spatial symmetry this quantity satisfies

$$\sum_{i}^{g2}\sum_{j}^{g1} |\vec{\mu}_{ij}|^2 = \sum_{j}^{g1}\sum_{i}^{g2} |\vec{\mu}_{ij}|^2 = g_1 \sum_{i}^{g2} |\vec{\mu}_{ij}|^2 = g_2 \sum_{i}^{g1} |\vec{\mu}_{ij}|^2, \tag{0.38}$$

and therefore the rate equations 0.32 and 0.33 are recovered, with the understanding that

$$A_{21} = \frac{1}{g_2}\frac{\omega_{21}^3}{3\epsilon_0\pi\hbar c^3}S_{21}, \tag{0.39}$$

$$R_{21}(\Delta) = \frac{1}{g_2}\frac{\mathcal{E}_0^2}{6\hbar^2}\frac{\beta}{(\Delta^2+\beta^2)}S_{21}, \tag{0.40}$$

and

$$R_{12}(\Delta) = \frac{1}{g_1}\frac{\mathcal{E}_0^2}{6\hbar^2}\frac{\beta}{(\Delta^2+\beta^2)}S_{21}, \tag{0.41}$$

where S_{21} is called the linestrength of the transition and is defined by

$$S_{21} \equiv S_{12} \equiv \sum_i^{g2}\sum_j^{g1}|\vec{\mu_{ij}}|^2. \tag{0.42}$$

A.4 The effects of broadening and pump laser linewidth on R_{21}

The stimulated emission rate R_{21} given in equation 0.40 is frequency-dependent, and can be written as

$$R_{21}(\nu) = \frac{1}{g_2}\frac{\mathcal{E}_0^2}{12\hbar^2}, S_{21}L(\nu) \tag{0.43}$$

where $L(\nu)$ is a normalized Lorentzian lineshape function given by

$$L(\nu) = \frac{\frac{\delta\nu_0}{\pi}}{(\nu-\nu_{21})^2-\delta\nu_0^2}. \tag{0.44}$$

The linewidth of this lineshape function $\delta\nu_0$, related to the dephasing collision rate β by $\beta = 2\pi\delta\nu_0$, reflects a quantum mechanical limit obtained from quantum field theory. In general, this natural linewidth can be related to the spontaneous emission rates associated with each of the two states of the system under consideration by

$$\delta\nu_0 = \frac{1}{4\pi}(A_2 + A_1), \tag{0.45}$$

where A_2 and A_1 are obtained by summing spontaneous emission rates over all allowed transitions from the respective state, that is

$$A_2 = \sum_m A_{2m} \tag{0.46}$$

and

$$A_1 = \sum_m A_{1m}. \tag{0.47}$$

In a closed, two-level system for example, $\delta\nu_0 = \frac{1}{4\pi}A_{21}$.

In a real system, elastic collisions among atoms may contribute to the dephasing rate of off-diagonal matrix elements when the pressure of the system is non-zero. Such collisions can be included in the stimulated emission rate by introducing a second linewidth $\delta\nu_c$ such that $\delta\nu = \delta\nu_0 + \delta\nu_c$. The resulting lineshape $L(\nu)$ is then broader, but retains its Lorentzian form, a consequence of combining two homogeneous broadening mechanisms.

The molecular velocity of a molecule along the direction of propagation of the radiation field introduces a Doppler shift in its resonant frequency, given by

$$\nu_{21}^{'} = \nu_{21}(1 \pm \frac{v}{c}), \tag{0.48}$$

where v is the velocity of the particular molecule experiencing the applied field. Quite often, the technique of LIF is applied to the study of a gas at temperature T with no center-of-mass flow velocity along the direction of laser beam propagation. In this special case, the fraction of N molecules with a velocity v on this axis in the interval $v + dv$ is

$$df(v) = \left(\frac{m}{2\pi kT}\right)^{\frac{1}{2}} e^{-mv^2/2kT} dv. \tag{0.49}$$

The fraction of atoms resonant in the interval $\nu + d\nu$ is therefore

$$df(\nu) = \left(\frac{m}{2\pi kT}\right)^{\frac{1}{2}} e^{-mc^2(\nu-\nu_{21})^2/2kT\nu_{21}^2} \left(\frac{c}{\nu_{21}} d\nu\right). \tag{0.50}$$

Neglecting collisional broadening, the absortion or stimulated emission rate is pro-

portional to the number of resonant molecules, so $R_{12}(\nu)$ and $R_{21}(\nu)$ would be proportional to the normalized lineshape function

$$D(\nu) = \frac{c}{\nu_{21}} \left(\frac{m}{2\pi kT} \right)^{\frac{1}{2}} e^{-mc^2(\nu-\nu_{21})^2/2kT\nu_{21}^2} \tag{0.51}$$

rather than $L(\nu)$. This lineshape function has a FWHM given by

$$\delta\nu_D = 2\frac{\nu_{21}}{c} \left(\frac{2kT}{m} Ln(2) \right)^{1/2} \tag{0.52}$$

and reflects the in-homogeneous broadening of the stimulated emission rate lineshape function caused by velocity-dependent Doppler shifts in a collisionless gas.

To simultaneously include the effects of Doppler broadening and collisional broadening in the study of laser light absorption by a gas, the convolution integral of the two lineshapes must be calculated. A lineshape function $S(\nu)$ can be defined by

$$S(\nu) = \int_{-\infty}^{\infty} D(\nu')L(\nu,\nu')d\nu', \tag{0.53}$$

where $L(\nu,\nu')$ is a Lorentzian lineshape centered at ν'. The result is called a Voight profile, defined by

$$S(\nu) = \frac{1}{\pi^{\frac{3}{2}}} \frac{b^2}{\delta\nu_0} \int_{-\infty}^{\infty} \frac{dy\ e^{-y^2}}{(y+x)^2+b^2}, \tag{0.54}$$

where

$$x = 2\sqrt{Ln(2)} \frac{\delta\nu_0 - \nu}{\delta\nu_D} \tag{0.55}$$

and

$$b = 2\sqrt{Ln(2)} \frac{\delta\nu_0}{\delta\nu_D}. \tag{0.56}$$

The stimulated emission rate is then given by

$$R_{21}(\nu) = \frac{1}{g_2} \frac{\mathcal{E}_0^2}{12\hbar^2} S_{21} S(\nu). \tag{0.57}$$

As before, $R_{12}(\nu) = \frac{g_2}{g_1} R_{21}(\nu)$.

For a gas at sufficiently low temperature and with sufficiently high density, it can

be shown that the Voight lineshape $S(\nu)$ reduces to the Lorentzian lineshape function $L(\nu)$, refered to as the collisionally broadened limit. In contrast, the Voight lineshape appropriate for a high temperature rarified gas reduces to the Doppler lineshape function $D(\nu)$. These two limits can be reached more directly by considering that when the width of one lineshape is significantly greater than the width of the other, the narrower lineshape can be treated as a delta function in the convolution integral of equation 0.54, making use of the fact that

$$\int_{-\infty}^{\infty} f(\nu')\delta(\nu - \nu')d\nu' = f(\nu). \tag{0.58}$$

This simplifying view of convolution integrals is important when further considering that in general, no radiation field is perfectly monochromatic and an additional lineshape function $\mathcal{L}(\nu)$ should be introduced to correctly evaluate the lineshape function for the stimulated emission rate, that is

$$S(\nu) = \int_{-\infty}^{\infty}\int_{-\infty}^{\infty} D(\nu')L(\nu,\nu')\mathcal{L}(\nu',\nu)d\nu' d\nu. \tag{0.59}$$

If the laser lineshape function is sufficiently narrow compared to either the Doppler or collisional lineshape function, it can effectively be treated as a delta function, and the stimulated emission rate can be described by equation 0.43 using the Voight profile in equation 0.54. It is convenient to define the laser intensity as $I_0 = \frac{1}{2}\epsilon_0 c\mathcal{E}_0^2$, which allows the stimulated emission rate $R_{21}(\nu)$ to be written

$$R_{21}(\nu) = \frac{c^2}{8\pi h\nu_{21}^3} I_0 A_{21} S(\nu). \tag{0.60}$$

In the opposite limit where the laser linewidth exceeds both the collision linewidth and the Doppler linewidth, the intensity I_0 appearing in the above equation can be regarded as the coefficient used in the equation describing the laser's intensity per unit frequency interval $d\nu$, that is,

$$I(\nu) = I_0\mathcal{L}(\nu), \tag{0.61}$$

with the lineshape $S(\nu)$ replaced by $\mathcal{L}(\nu)$. It can be shown that this limit applies when performing PLIF imaging on a PLA plume that expands into vacuum or a very low pressure background gas while the former limit applies when the background gas pressure is sufficiently high.

A.5 Thermal population of molecular levels with no radiation field

The solutions to the population rate equations 0.32 and 0.33 depend on the choice of initial conditions. For a system in thermal equilibrium, the probability that an atom or molecule can be found in some quantum state with energy E_n is given by

$$P(n) = \frac{g_n e^{\frac{-E_n}{kT}}}{Z(T)}, \tag{0.62}$$

where T denotes the equilibrium temperature, the partition function $Z(T)$ is defined by

$$Z(T) = \sum g_n e^{\frac{-E_n}{kT}}, \tag{0.63}$$

and g_n is the degeneracy of the state described by quantum number n. For an ensemble of N molecules, the population expected to be found in each level of a two-level subsystem, in thermal equilibrium, would therefore be

$$N_1^0 = N g_1 \frac{e^{\frac{-E_1}{kT}}}{Z(T)} \tag{0.64}$$

and

$$N_2^0 = N g_2 \frac{e^{\frac{-E_2}{kT}}}{Z(T)}, \tag{0.65}$$

and the total number of molecules in the subsystem would be

$$N_{sub} = N \frac{g_1 e^{\frac{-E_1}{kT}}}{Z(T)} (1 + \frac{g_2}{g_1} e^{\frac{-(E_2 - E_1)}{kT}}). \tag{0.66}$$

For sufficiently low temperature, $E_2 - E_1 \gg kT$ and the population in the excited state in thermal equilibrium can be neglected. Under this assumption, all of molecules in the two-level subsystem begin in the lower state so that

$$N_{sub} \approx N_1^0 = N\frac{g_1 e^{\frac{-E_1}{kT}}}{Z(T)}. \tag{0.67}$$

For a system not in thermal equilibrium, but whose state populations are initialized by some thermal mechanism, the lower state would still be expected to be significantly more populated than the upper state prior to a resonant laser pulse, although equation 0.67 cannot rigorously be used to relate the population of the lower state to the total number of atoms or molecules in the ensemble.

A.6 Solutions of the population rate equations

The solutions of the population rate equations 0.32 and 0.33 are easily obtained analytically. Using the assumption $N_2 = 0$ they are

$$N_2(t) = N_1^0\frac{R_{12}}{A_{21} + R_{21} + R_{12}}(1 - e^{-(A_{21}+R_{21}+R_{12})t}) \tag{0.68}$$

and

$$N_1(t) = N_1^0 - N_2(t). \tag{0.69}$$

The steady state solutions ($t \to \infty$) of the rate equations are therefore

$$N_2(t \to \infty) = N_1^0\frac{R_{12}}{A_{21} + R_{21} + R_{12}} \tag{0.70}$$

and

$$N_1(t \to \infty) = N_1^0\frac{A_{21} + R_{21}}{A_{21} + R_{21} + R_{12}}. \tag{0.71}$$

Following the application of the laser field, the population of the upper state then satisfies

$$N_2(t) = N_1^0\frac{R_{12}}{A_{21} + R_{21} + R_{12}}(1 - e^{-(A_{21}+R_{21}+R_{12})t_p})e^{-A_{21}t}, \tag{0.72}$$

where t_p denotes the duration of the applied laser pulse. Since atoms are conserved, the lower state population satisfies $N_1(t) = N_1^0 - N_2(t)$.

These solutions reveal that both during the laser pulse and after it, the upper state population is directly proportional to the population of the *lower* level immediately prior to the application of the field. This is important because the LIF signal $\mathcal{S}(\vec{x})$ gathered from time t_1 to time t_2 will satisfy

$$\mathcal{S}(\vec{x}) \propto \int_{t_1}^{t_2} A_{21} N_2(\vec{x}, t) dt \propto N_1^0(\vec{x}). \tag{0.73}$$

A.7 Linear vs. saturated laser intensity

The upper state population at the instant the field terminates can be written as

$$N_2(t_p) = N_1^0 \frac{g_2}{g_1 + g_2} (1 - e^{-A_{21}(1+\kappa(\nu))t_p}) \frac{\kappa(\nu)}{1 + \kappa(\nu)}, \tag{0.74}$$

where

$$\kappa(\nu) = \frac{R_{21}(\nu) + R_{12}(\nu)}{A_{21}} = \frac{I_0 c^2}{8\pi h \nu_{21}^3} \frac{g_1 + g_2}{g_1} S(\nu). \tag{0.75}$$

The dimensionless parameter $\kappa(\nu)$ may be used to identify limiting regimes for the dependence of the upper state population on the applied laser intensity I_0. If $\kappa(\nu) \ll 1$ then equation 0.74 reduces to

$$N_2(t_p) = N_1^0 \frac{g_2}{g_1 + g_2} (1 - e^{-A_{21} t_p}) \kappa(\nu). \tag{0.76}$$

Since $\kappa(\nu)$ is proportional to I_0, in this weak field limit the upper state population is directly proportional to the intensity of the applied laser field as well as the density of atoms or molecules in the lower state prior to the laser pulse. For the purpose of PLIF imaging, spatial variations in laser sheet intensity as well as pulse-to-pulse energy fluctuations therefore affect the signal levels. To account for this dependence, the PLIF signal acquired with each pulse must be normalized to the laser energy, or else averaged over several pulses to minimize the effects of pulse-to-pulse laser energy

fluctuations. The resulting PLIF images must then be normalized by the spatial intensity profile of the pump laser, presumably a time-independent function.

If $\kappa(\nu) \gg 1$ then the upper state population immediately following the laser pulse may reduce to two additional limiting forms, the long pulse limit or the short pulse limit. The short pulse limit, defined by $A_{21}(1+\kappa(\nu))t_p \ll 1$ allows the exponent in equation 0.74 to be expanded as

$$e^{-A_{21}(1+\kappa(\nu))t_p} \approx 1 - A_{21}(1+\kappa(\nu))t_p + ... \tag{0.77}$$

Retaining only the leading term, equation 0.74 then reduces to

$$N_2(t_p) = N_1^0 \frac{g_2}{g_1+g_2} A_{21} t_p \kappa(\nu). \tag{0.78}$$

As in the weak field limit, the strong field/short pulse limit results in an upper state population that is directly proportional to the laser intensity. For this reason, both of these regimes are commonly referred to as linear and require the same normalization of LIF signal to pump laser intensity. This particular regime is impossible, regardless of laser intensity, if $A_{21}t_p > 1$.

In contrast, the strong field/long pulse limit permits the reduction of equation 0.74 to

$$N_2(t_p) = N_1^0 \frac{g_2}{g_1+g_2}, \tag{0.79}$$

which shows that the upper-state population is pumped to some maximum value, about half the total population, which is independent of laser intensity and pulse duration. Fluorescence from a saturated interaction volume is therefore maximized, since about half of the atoms initially in the lower state contribute to the signal instead of only a few percent as with linear laser intensity. Furthermore, regions of the interaction volume pumped into saturation require no normalization to account for pulse-to-pulse energy fluctuations or spatial variations in intensity across the pump laser sheet. These facts, in principle, make the use of saturated laser intensity an attractive alternative to using linear laser intensity in some applications.

Another advantage to using saturated laser intensity occurs when the region being probed is optically thick at the frequency of the pump laser, evidenced by significant attenuation as the pump laser penetrates into the interaction volume. To understand this phenomenon, consider that the *coherent* laser energy density in the interaction volume must satisy

$$\frac{d\rho(x,t)}{dt} = h\nu(R_{12}N_1(x,t) - R_{21}N_2(x,t)) \tag{0.80}$$

so that if $I(x,t) = c\rho(x,t)$ and

$$\frac{d\rho(x,t)}{dt} = \frac{1}{c}\frac{d\rho(x,t)}{dt}, \tag{0.81}$$

then

$$\frac{dI(x,t)}{dx} = h\nu(R_{12}N_1(x,t) - R_{21}N_2(x,t)) \tag{0.82}$$

If the laser intensity is linear, then $N_2 \ll N_1$ and

$$\frac{dI(x,t)}{dx} \approx -h\nu(R_{12}N_1(x,t) = -\frac{1}{\lambda}I(x,t), \tag{0.83}$$

or

$$I(x,t) = I(o,t)e^{-\frac{x}{\lambda}}, \tag{0.84}$$

where the scale length of attenuation λ is given by

$$\lambda = \frac{4\pi\nu^2}{c^2 A_{21} S(\nu) N_1(x,t)}. \tag{0.85}$$

When pumping a transition with a sufficiently large absorption rate, in a plume with sufficiently high density, this attenuation length can become smaller than the scale length of the plume. This significantly complicates PLIF imaging because the sheet intensity then varies along the length of propagation. Worse still, the variation becomes time-dependent if the density is time-dependent. In contrast, if the laser intensity is sufficiently high to saturate the upper-level during the laser pulse, then

$R_{12}N_1(x,t) \approx R_{21}N_2(x,t)$ so that

$$\frac{dI(x,t)}{dx} \approx 0, \tag{0.86}$$

implying that the pump laser is unattenuated in the saturated regime. Problems with optical thickness, which can make LIF difficult if not impossible in the linear regime, can therefore be minimized using saturated laser energy.

PLIF imaging in the saturated regime, however, introduces a host of potential errors that do not exist when operating in the linear regime. One such error can occur when integrating LIF signal during the time that the laser is first turned on. Although the steady state solution to the upper-state population is independent of laser intensity, the time required to achieve steady state does depend on laser intensity and therefore the LIF signal during this time, which is proportional to the upper-state population, depends on laser intensity. If this time is a significant fraction of the pulse duration, then even for a fixed density of resonant atoms, a significant variation in LIF signal will result when pump laser intensity varies in space along the cross section of the pump laser sheet. This artifact can be minimized by time-integrating the LIF signal only following the anticipated time required for the upper state to reach steady state, or by ensuring that the saturation time is a negligible fraction of the pulse duration. Alternatively, the rate equation describing the upper state of the LIF system can be solved as a function of pump laser intensity. The integral of this solution over time can then be used to normalize the LIF signal. In principle this method correctly reduces to either the linear or saturated limits, however, it requires quantitative knowledge about the pump laser intensity, since the rate equations are sensitive to a threshold intensity I_0 unique to the specific LIF scheme used.

A more problematic source of error when considering PLIF in the saturated laser intensity regime is introduced by temporal, spatial, and spectral wings in the intensity profile of the pump laser. Although the laser pulse is usually modeled as a step function in time, in reality the pulse is complex, consisting of several temporal pulses with wings where the intensity may drop well below the threshold where the strong

field limit is valid. During these periods, the upper-state population will depend on laser intensity and therefore the contribution to the time-integrated LIF signal during the temporal wings of the laser pulse introduce error under the saturated laser intensity approximation. This same problem arises due to spatial wings in the intensity profile of the pump laser. If the intensity at the spatial peak of a focused laser beam is sufficient to saturate a transition of interest, the intensity in some region of the spatial wings of the profile is certainly not. The contribution to the LIF signal from spatial regions illuminated by the wings of the intensity profile therefore also introduce error. Finally, in an interaction volume where the resonant frequency varies (due to Doppler shift) over a range which is wider than the spectral width of the pump laser, the intensity of the pump laser in regions of the spectral wings is weak even if the intensity at the spectral peak is sufficient to saturate the transition. Again, this results in error if the saturated intensity approximation is applied to PLIF signal detected from regions illuminated by the spectral wings of the pump laser profile.

A.8 Power broadening in the long pulse limit

In the long pulse limit, defined here by $A_{21}(1+\kappa(\nu))t_p > 1$, equation 0.75 can be used to estimate the threshold intensity I_s which divides the linear regime from the saturated regime. This intensity is given by

$$I_s \approx \frac{g_1}{g_1+g_2}\frac{8\pi^2 h\nu_{21}^3 \delta\nu_0}{c^2}, \tag{0.87}$$

where $\delta\nu_0$ is the spectral linewidth of the pump laser, neglecting collisional and Doppler broadening, and the peak magnitude of the lineshape function $\mathcal{L}(\nu)$ is given by $1/\pi\delta\nu_0$. If the pump laser intensity used is well below this threshold value, then the resulting LIF signal will be linearly dependent on laser intensity, and if the pump laser intensity is greater than this threshold value, the LIF signal will be independent of laser intensity, reflecting the existence of a saturated upper state. Even without varying the laser intensity to directly verify its influence on LIF signal, the spectral

linewidth of the LIF signal may be used to detect whether the pump laser intensity is linear or nonlinear.

To see how this works, consider that equation 0.74, the general solution for the upper-state population immediately after the application of the pump laser pulse, can be written as

$$N_2(\nu) = N_1^0 \frac{I_0 c^2}{8\pi h \nu_{21}^3} \frac{g_2}{g_1} \mathcal{S}(\nu), \tag{0.88}$$

where the dependence of $N_2(\nu)$, and therefore LIF signal, on pump laser frequency is contained in the normalized lineshape function

$$\mathcal{S}(\nu) = \alpha \frac{S(\nu)}{\alpha + S(\nu)} \tag{0.89}$$

with

$$\alpha = \frac{8\pi h \nu_{21}^3}{I_0 c^2} \frac{g_1}{g_1 + g_2}. \tag{0.90}$$

In general, this lineshape function is difficult to simplify, since $S(\nu)$ is a convolution integral given by equation 0.54. For the purpose of illustrating the qualitative influence of laser power on its shape, however, it is convenient to consider a regime in which $S(\nu)$ is a Lorentzian function $\mathcal{L}(\nu)$ with a HWHM $\delta\nu_0$, as in the case of a PLA plume collisionlessly expanding into vacuum where $\mathcal{L}(\nu)$ is the lineshape of the pump laser. It can be shown that in this case the lineshape $\mathcal{S}(\nu)$ is also Lorentzian, with a HWHM $\delta\tilde{\nu}_0$ given by

$$\delta\tilde{\nu}_0 = \delta\nu_0 \sqrt{1 + \frac{1}{\pi\alpha\delta\nu_0}}. \tag{0.91}$$

For sufficiently low pump laser intesity, $\delta\tilde{\nu}_0$ reduces to the width of the pump laser lineshape, $\delta\nu_0$, which is independent of laser intensity. However, with increased laser intensity, the linewidth grows, an effect commonly refered to as power broadening. For lineshape functions $S(\nu)$ which are not Lorentzian, power broadening at high laser intensity is similar, although a solution for the linewidth cannot as easily be put into closed form. Evidence of LIF signal with a spectral linewidth greater than the the width of $S(\nu)$ indicates a pump laser intensity which is nonlinear.

Appendix B The DSMC method

B.1 Generation of a background gas

The velocity distribution function appropriate for an equilibrium gas is given in Cartesian coordinates by

$$f(v_x, v_y, v_z)dv_x dv_y dv_z = \frac{1}{\pi^{3/2} v_p^3} e^{\frac{-(v_x^2+v_y^2+v_z^2)}{v_p^2}}, dv_x dv_y dv_z \tag{0.92}$$

with $-\infty < v_x, v_y, v_z < \infty$, and $v_p = \sqrt{2kT/m}$. There are several Monte Carlo methods available to generate an ensemble of particles consistent with this function. One could generate each velocity component seperately by direct integration using

$$\frac{2}{\sqrt{\pi}} \int_{-\infty}^{\frac{|v|}{v_p}} e^{-u^2} du = \mathrm{erf}(\frac{|v|}{v_p}) = \mathcal{R}, \tag{0.93}$$

where $\mathcal{R}$ is a random number satisfying $0 < \mathcal{R} < 1$. The speed component $|v_i|$ can then be obtained from tabulated error function data, with the sign of v_i determined using a second random number. This method is computationally inefficient because a data table must be searched to find the value $|v_i|$ that best satisfies equation 0.93.

For Monte-Carlo simulations, the best method is the one that is most computationally efficient, even if somewhat indirect. To this end, one can obtain each velocity component by integration if it is treated as a one-dimensional projection from a two-dimensional velocity. In a two dimensional subspace, the probability $P(v)dv$ of a particle having a speed between v and $v + dv$ is given by

$$P(v)dv = \frac{v}{v_p} e^{-\frac{v^2}{v_p^2}} dv, \tag{0.94}$$

which can be integrated to give

$$\int_0^\infty P(v)dv = 1 - e^{\frac{v^2}{v_p}^2} = \mathcal{R}_1, \tag{0.95}$$

so that $v = v_p\sqrt{-log(\mathcal{R}_1)}$ for the velocity in the two dimensional space. Since the orientation in this subspace is random, it can be chosen as as the x, y plane so that

$$v_x = v_p\sqrt{-log(\mathcal{R}_1)}sin(2\pi\mathcal{R}_2) \tag{0.96}$$

and

$$v_y = v_p\sqrt{-log(\mathcal{R}_1)}cos(2\pi\mathcal{R}_2). \tag{0.97}$$

The velocity component v_z may be treated as a projection from a virtual two-dimensional subspace, giving

$$v_z = v_p\sqrt{-log(\mathcal{R}_3)}cos(2\pi\mathcal{R}_4). \tag{0.98}$$

This method only requires four random numbers to generate all three velocity components and requires no look-up tables.

Positions for gas particles are generated by integrating the cylindrical spatial distribution function

$$P(r, z)drdz = \frac{2}{R^2D}rdrdz, \tag{0.99}$$

where R is the radius of the cylindrical volume. This gives $r = R\sqrt{\mathcal{R}_1}$ or $x = R\sqrt{\mathcal{R}_1}cos(2\pi\mathcal{R}_2)$ and $y = R\sqrt{\mathcal{R}_1}sin(2\pi\mathcal{R}_2)$. The axial position is given by $z = D\mathcal{R}_3$ where D is the cylinder's length. The position of each particle therefore requires three random numbers.

B.2 Generation of plume particles

The velocity distribution function appropriate for an ensemble of particles generated by thermal effusion is given by

$$f(v_x, v_y, v_z)dv_x dv_y dv_z = \frac{2v_z}{\pi v_p^4} e^{\frac{-(v_x^2+v_y^2+v_z^2)}{v_p^2}}, dv_x dv_y dv_z \tag{0.100}$$

with $-\infty < v_{x,y} < \infty$ and $0 < v_z < \infty$. The velocity components v_x and v_y may be obtained for each particle using the method previously described for a background gas, while the z component of velocity may be obtained by direct integration, giving $v_z = v_p\sqrt{-log(\mathcal{R}_3)}$. Only three random numbers are required to specify all three velocity components.

The position of each plume particle is initialized to $x = r_s\sqrt{\mathcal{R}_1}cos(2\pi\mathcal{R}_2)$ and $y = r_s\sqrt{\mathcal{R}_1}sin(2\pi\mathcal{R}_2)$, with $z = v_z\Delta t\mathcal{R}_3$. The z position is not initialized to exactly zero to account for the uncertaintly in when during the time step the particle was desorbed.

B.3 Treatment of collisions using DSMC

The treatment of collisions is the heart of the DSMC method. At each time step a number of collision pairs, given by

$$N_{pairs} = \frac{N^2 F(\sigma v_r)_{max}\Delta t}{2V_c}, \tag{0.101}$$

is randomly selected in each cell, where N is the number of simulation particles in the cell, F is the number of real atoms that each simulation atom represents, $(\sigma v_r)_{max}$ is the greatest value of collision cross section $\times$ relative velocity experienced in the cell, Δt is the time step, and V_c is the volume of the cell. Bird recommends that the quantity N^2 be replace by $N\bar{N}$ to account for statistical fluctuation, however, for very unsteady flow $\bar{N}$ is not well-defined.

Having randomly selected N_{pairs} collision pairs, a pair is "accepted and a collision

executed if $\mathcal{R} < \sigma v_r/(\sigma v_r)_{max}$, otherwise the pair is "rejected and the two particles are not disturbed. The quantity $(\sigma v_r)_{max}$ is a parameter that is updated for each cell every time step after first being initialized to a some reasonable value. For optimum computational efficiency, the initial value should be small enough that at least a few updates occur in each cell during the simulation.

VHS cross sections are based on the empirical observation that the viscosity μ of a typical gas is related to the temperature by $\mu(T) = \mu_{ref}(T/T_{ref})^{\omega}$ where μ_{ref} is the viscosity at some reference temperature T_{ref}. This functional form of the viscosity has theortical foundations in Chapman-Enskog theory, which considers perturbations of the distribution function about a Maxwellian. The parameters ω and μ_{ref} may be obtained for a wide variety of atoms [79].

It can be shown that the diameter of a VHS molecule is given by

$$d = \frac{15}{8}\frac{(m/\pi)^{1/2}(kT_{ref})^{\omega}}{\Gamma(9/2-\omega)\mu_{ref}E_t^{\omega-1/2}}, \tag{0.102}$$

where $E_t = m_r v_r^2/2$ is the relative translational energy of a collision pair with m_r defined as the reduced mass of the pair. The cross section σ is then $\sigma = \pi d^2$. For collisions among unlike molecules, the mean collision diameter may be used so that $\sigma = \pi(d_1 + d_2)^2/4$.

B.4 The Larsen-Borgnakke model

When molecules with rotational and/or vibrational energy collide, translational momentum is conserved but total translational energy is not. The Larsen-Borgnakke method provides a computationally efficient way to treat collisions among such molecules. The close spacing of rotational energy levels ($\Delta E_r << kT$) allows the rotational energy of a diatomic molecule to be treated as if the molecule has two internal degrees of freedom, each of which tends to acquire an energy $kT/2$ in equilibrium. When a molecule with two internal degrees of freedom having a combined energy E_{int}^1 collides

with another atom, its internal energy after the collision $E_{int}^{1'}$ can be determined by

$$E_{int}^{1'} = (E_{int}^{1} + E_t)(1 - \frac{\mathcal{R}}{5/2 - \omega_{21}}), \tag{0.103}$$

where ω_{21} is the average of the parameters ω_1 and ω_2 appropriate for each molecule and E_t is the relative translational kinetic energy of the pair before the collision. Equation 0.103 which is valid whether or not the second molecule has internal energy, has been rigorously proven to produce the correct equipartition of energy. If the second molecule has no internal modes then $E_t' = E_t + E_{int}^{1} - E_{int}^{1'}$, however, if the second molecule also has two internal degrees of freedom, its internal energy after the collision is then given by

$$E_{int}^{2'} = (E_{int}^{2} + E_t')(1 - \frac{\mathcal{R}}{5/2 - \omega_{21}}) \tag{0.104}$$

and $E_t = E_t' + E_{int}^{2} - E_{int}^{2'}$.

In general one or both of the molecules may have more than two internal rotational degrees of freedom. The energy $E_{int}^{1'}$ of molecule with ζ_1 internal modes after a collision can be determined by sampling from the normalized probablity

$$P(E_{int}^{1'}) = \frac{\zeta_1/2 - \omega_{21} + 1/2}{\zeta_1/2 - 1}\left(\frac{E_{int}^{1'}}{E_{int}^{1} + E_t}\right) + \frac{\zeta_1/2 - \omega_{21} + 1/2}{3/2 - \omega_{21}}\left(1 - \frac{E_{int}^{1'}}{E_{int}^{1} + E_t}\right), \tag{0.105}$$

leaving $E_t' = E_t + E_{int}^{1} - E_{int}^{1'}$ for translational energy. If the second molecule has $\zeta_2 > 2$ internal rotational modes then the energy $E_{int}^{2'}$ can then be determined by sampling from the normalized probablity

$$P(E_{int}^{2'}) = \frac{\zeta_2/2 - \omega_{21} + 1/2}{\zeta_2/2 - 1}\left(\frac{E_{int}^{2'}}{E_{int}^{2} + E_t'}\right) + \frac{\zeta_2/2 - \omega_{21} + 1/2}{3/2 - \omega_{21}}\left(1 - \frac{E_{int}^{2'}}{E_{int}^{2} + E_t'}\right) \tag{0.106}$$

or, if $\eta_2 = 2$, by using equation 0.104. The translational energy afterward is then $E_t = E_t' + E_{int}^{2} - E_{int}^{2'}$.

Unlike rotational levels, the spacings between vibrational levels are not closely spaced, so treatment of vibrational energy transfer requires a slightly different ap-

proach, but the sequential assigment of energy to successive internal modes remains the same. Suppose, for example, equation 0.103 is used to determine the rotational energy of the first molecule after the collision, leaving energy E_t'. The vibrational level of this molecule after the collision i' can be determined by sampling from the normalized probability

$$P(i') = 1 - \frac{i\Delta E_v}{E_t' + i\Delta E_v}, \tag{0.107}$$

where ΔE_v denotes the energy spacing between vibrational levels. This process leaves $E_t = E_t + (i - i')\Delta E_v$ which can be used in the place of E_t' in equation 0.104 or equation 0.106 to determine the rotational energy of the second molecule, whose vibrational energy can then be determined. Having assigned the final rotational and vibrational energy for each molecule, the final energy E_t is then divided between the two particles such that momentum is conserved.

As a DSMC simulation progresses, the rotational temperature of a diatomic gas is simply obtained by assuming 2 thermal degrees of freedom, that is $T_{rot} = E_r$ / k. The vibrational temperature is not as easily obtained. However if one assumes that the vibrational levels are populated according to a Boltzmann distribution, then the population of state i should satisfy

$$ln(N_i) = C - \frac{iE_v}{kT}, \tag{0.108}$$

where C is a constant. A least-square fit to this function using all levels for which $N_i > 0$ can therefore be used to define a vibrational temperature.

B.5 Bi-molecular chemical reactions

A typical bi-molecular chemical reaction takes the form $A + B \leftrightarrow C + D$ and the rate equation governing the concentration of species A is given by

$$\frac{dn_A}{dt} = k_1 n_A n_B - k_2 n_C n_D, \tag{0.109}$$

where k_1 and k_2 take the form

$$k(T) = \Lambda T^{\eta} e^{\frac{-E_a}{kT}}, \tag{0.110}$$

where Λ and η are constants and E_a is the reaction's activation energy. These parameters are tabulated for a wide variety of reactions. Bird has demonstrated that a reaction cross section of the form

$$\sigma_R = \sigma C_1 (E_c - E_0)^{C_2} (1 - E_0/E_c)^{3/2-\omega_{12}+\bar{\zeta}} \tag{0.111}$$

produces a forward reaction rate of the form in equation 0.110 if $E_c > E_a$, $C_2 = \eta - 1 + \omega_{12}$, and

$$C_1 = \frac{\sqrt{\pi}\Lambda\epsilon}{2\sigma_{ref}} \frac{\Gamma(\bar{\zeta} + 5/2 - \omega_{12})}{\Gamma(\bar{\zeta} + 3/2 + \eta)} \left(\frac{m_r}{2kT_{ref}}\right)^{1/2} \frac{T_{ref}^{1-\omega_{12}}}{k^{\eta-1+\omega_{12}}}, \tag{0.112}$$

where E_c is the sum of the translational, rotational, and vibrational energies of both colliding molecules, $\bar{\zeta}$ is the average number of internal degrees of freedom contributing to E_c, and ϵ is a symmetry factor that equals one if $\zeta_1 = \zeta_2$, otherwise equals two. The probability of a reaction, assuming $E_c > E_a$ is then given by

$$\frac{\sigma_R}{\sigma} = \frac{\sqrt{\pi}\Lambda\epsilon T_{ref}^{\eta}}{2\sigma_{ref}(kT_{ref})^{\eta-1+\omega_{12}}} \frac{\Gamma(\bar{\zeta} + 5/2 - \omega_{12})}{\Gamma(\bar{\zeta} + 3/2 + \eta)} \left(\frac{m_r}{2kT_{ref}}\right)^{1/2} \frac{(E_c - E_a)^{\eta+\bar{\zeta}+1/2}}{E_c^{\bar{\zeta}+3/2-\omega_{21}}}. \tag{0.113}$$

A sample from this distribution determines whether a selected pair chemically reacts before the available energy is redistributed. If so, the energy is reduced by E_a and the collision is completed as previously described. By inspection, the probability for a reaction is maximum for

$$E_c = \frac{\bar{\zeta} + 3/2 - \omega_{21}}{1 - \omega_{21} - \eta} E_a \tag{0.114}$$

and drops to zero if E_c is much greater than or much less than this value. Typically $\sigma_R/\sigma \ll 1$ for all E_c.

Bibliography

[1] D. Dijkkamp, T. Venkatesan, X. Wu, and S. A. Shaheen, Appl. Phys. Lett. **51**, 619 (1987).

[2] A. Inam *et al.*, Appl. Phys. Lett. **53**, 908 (1988).

[3] R. Farrow *et al.*, J. Phys. D. **12**, (1979).

[4] J. Cheung and D. Cheung, J. Vac. Sci. Technol. **24**, 182 (1982).

[5] J. T. Cheung and H. Sankur, CRC Crit. Rev. in Sol. State and Mat. Sci. **15**, 63 (1988).

[6] T. Venkatesan, X. D. Wu, A. Inam, and J. B. Wachtman, Appl. Phys. Lett. **52**, 1193 (1988).

[7] R. B. Laibowitz, R. H. Koch, P. Chaudhari, and R. J. Gambino, Physica B, C **148**, 182 (1987).

[8] O. Auciello and R. Ramesh, MRS Bulletin **21**, 31 (1996).

[9] E.W.Chase, T. Venkatesan, C. Chang, and B. Wilkens, J. Mater. Res. **4**, 1326 (1989).

[10] S. Gapanov, B. Luskin, B. Nesterov, and N. Salashchenko, Sov. Tech. Phys. Lett. **3**, 234 (1977).

[11] A. Puretzky, D. Geohehgan, G. Jellison, and M. McGibbon, Appl. Surf. Science **96**, 859 (1996).

[12] A. Slaoui, E. Fogarassy, C. Fuchs, and P. Siffert, J. Appl. Phys. **71**, 590 (1991).

[13] E. Fogarassy, A. Slaoui, C. Fuchs, and J. P. Stoquert, Appl. Surf. Science **54**, 180 (1991).

[14] T. P. Chen, T. I. Bao, and L. I, Appl. Phys. Lett. **63**, 2475 (1993).

[15] T. Szorenyi, P. Gonzalez, and M. Fernandez, Thin Solid Films **193**, 619 (1990).

[16] A. Gupta, J. Appl. Phys. **73**, 7877 (1993).

[17] C. Rouleau *et al.*, Appl. Phys. Lett. **17**, 2545 (1995).

[18] I. Mihailescu, N. Chitica, L. Nistor, and V. Teodorescu, J. Appl. Phys. **74**, 5781 (1993).

[19] I. Mihailescu, A. Lita, V. Teodorescu, and A. Luchas, J. Mat. Science **31**, 2839 (1996).

[20] L. C. Chen, in *Particulates generated by pulsed laser ablation*, edited by D. B. Chrisey and G. K. Hubler (John Wiley and Sons, Inc., New York, 1994), pp. 167–198. See Ref. [102].

[21] J. Dubowski, Proc. Soc. Photo-Opt. Instrum. Eng. **97**, 668 (1986).

[22] D. Lubben, S. A. Barnett, K. Suzuki, and S. Gorbatkin, J. Vac. Sci. Technol. **B3**, 968 (1985).

[23] R. Kelly and R. W. Dreyfus, Nucl. Instr. and Meth. in Phys. Res. B **32**, 341 (1988).

[24] J. P. Zheng, Z. Q. Huang, D. T. Shaw, and H. S. Kwok, Appl. Phys. Lett. **54**, 280 (1989).

[25] D. Geohegan, in *Diagnostics and characteristics of laser-produced plasmas*, edited by D. B. Chrisey and G. K. Hubler (John Wiley and Sons, Inc., New York, 1994), pp. 115–166. See Ref. [102].

[26] R. J. von Gutfeld and R. W. Dreyfus, Appl. Phys. Lett. **54**, 1212 (1989).

[27] K. Fukushima, Y. Kanke, and T. Morishita, J. Appl. Phys. **74**, 6948 (1993).

[28] D. Geohegan, Appl. Phys. Lett. **1992**, 2732 (1992).

[29] D. Geohegan and A. Puretzky, Appl. Surf. Science **1996**, 131 (1996).

[30] D. Geohegan, Thin Solid Films **220**, 138 (1992).

[31] D. Geohegan and A. Puretzky, Appl. Phys. Lett. **67**, 197 (1996).

[32] L. D. Landau and E. M. Lifshitz, *Fluid Mechanics* (Pergamon Press, Inc., New York, 1987).

[33] T. Okada, Y. Nakata, W. K. A. Kumuduni, and M. Maeda, Appl. Surf. Science **79**, 136 (1994).

[34] D. Fried, S. Jodeh, and G. Reck, J. Appl. Phys. **75**, 522 (1993).

[35] T. Okada, N. Shibamaru, Y. Nakayama, and M. Maeda, Appl. Phys. Lett. **60**, 941 (1991).

[36] C. E. Otis and R. W. Dreyfus, Phys. Rev. Lett. **67**, 2102 (1991).

[37] T. Okada, Y. Nakayama, W. Kumunudi, and M. Maeda, Appl. Phys. Lett. **61**, 2368 (1992).

[38] R. W. Dreyfus, J. Appl. Phys. **69**, 1721 (1991).

[39] D. L. Pappas, K. L. Saenger, J. J. Cuomo, and R. W. Dreyfus, J. Appl. Phys. **72**, 3966 (1992).

[40] R. W. Dreyfus, R. Kelly, and R. E. Walkup, Nucl. Instr. and Meth. in Phys. Res. B **23**, 557 (1987).

[41] P. W. Milonni and J. H. Eberly, *Lasers* (John Wiley and Sons, New York, 1988).

[42] A. D. Sappey and T. K. Gamble, Appl. Phys. Lett. **72**, 5095 (1992).

[43] D. P. Butt, P. J. Wantuck, and A. D. Sappey, J. Appl. Phys. **77**, 1411 (1994).

[44] D. K. Zerkle and A. D. Sappey, IEEE Transactions on Plasma Physics **24**, 37 (1996).

[45] M. A. Capelli, P. H. Paul, and R. K. Hanson, Appl. Phys. Lett. **56**, 1715 (1990).

[46] D. G. Goodwin, D. L. Capewell, and P. H. Paul, in *Film Synthesis and Growth using Energetic Beams*, edited by H. A. Atwater, J. T. Dickinson, D. H. Lowndes, and A. Polman (Materials Research Society, Pittsburgh, PA, 1995), pp. 33–38, mRS Proceedings Volume 388. See Ref. [103].

[47] P. H. Paul, D. L. Capewell, and D. G. Goodwin, in *Laser-Induced Thin Film Processing*, edited by J. J. Dubowski (SPIE, Bellingham, WA, 1995), pp. 39–48, sPIE Proceedings Volume 2403. See Ref. [104].

[48] H. Wang, A. P. Saltzberg, and B. R. Weiner, Appl. Phys. Lett. **59**, 935 (1991).

[49] T. Okada, N. Shibamaru, Y. Nakayama, and M. Maeda, Jpn. J. Appl. Phys. **31**, L367 (1992).

[50] R. K. Singh, J. Non-Crys. Sol. **178**, 199 (1994).

[51] D. L. Lin, X. Li, and Z. D. Liu, J. Appl. Phys. **72**, 4227 (1992).

[52] D. Sibold and H. M. Urbassek, Phys. Fluids A **4**, 165 (1992).

[53] R. Kelly, Phys. Rev. A **46**, 860 (1992).

[54] T. Ytrehus, in *Rarefied Gas Dynamics*, edited by J. L. Potter (American Institute of Aeronautics and Astronautics, Princeton. NJ, 1976), pp. 1197–1212, proceedings of the 10th International Symposium Volume 51.

[55] R. Kelly, J. Chem. Phys. **92**, 5047 (1990).

[56] R. Kelly and A. Miotello, in *Mechanisms of pulsed laser sputtering*, edited by D. B. Chrisey and G. K. Hubler (John Wiley and Sons, Inc., New York, 1994), pp. 55–87. See Ref. [102].

[57] D. Sibold and H. M. Urbassek, J. Appl. Phys. **73**, 8544 (1993).

[58] D. Sibold and H. M. Urbassek, Appl. Phys. B **55**, 391 (1992).

[59] D. Sibold and H. M. Urbassek, Phys. Rev. A **73**, 6722 (1991).

[60] A. Vertes, R. W. Dreyfus, and D. E. Platt, IBM J. Res. Develop. **38**, 3 (1994).

[61] C. L. liu *et al.*, in *Film Synthesis and Growth using Energetic Beams*, edited by H. A. Atwater, J. T. Dickinson, D. H. Lowndes, and A. Polman (Materials Research Society, Pittsburgh, PA, 1995), pp. 133–138, mRS Proceedings Volume 388. See Ref. [103].

[62] M. Aden, E. W. Kreutz, and A. Voss, J. Phys. D. **26**, 1545 (1993).

[63] G. A. Bird, *Molecular Gas Dynamics and the Direct Simulation of Gas Flows* (Oxford University Press, New York, 1994).

[64] D. Sibold and H. M. Urbassek, J. Appl. Phys. **73**, 8544 (1993).

[65] D. Sibold and H. M. Urbassek, J. Vac. Sci. Technol. **11**, 676 (1993).

[66] I. Noorbatcha, R. Lucchese, and Y. Zeiri, Surf. Sci. **200**, 113 (1987).

[67] I. Noorbatcha and R. Lucchese, J. Chem. Phys. **86**, 5816 (1987).

[68] J. C. S. Kools, J. Appl. Phys. **74**, 6401 (1993).

[69] D. L. Capewell and D. G. Goodwin, in *Laser-Induced Thin Film Processing*, edited by J. J. Dubowski (SPIE, Bellingham, WA, 1995), pp. 49–59, sPIE Proceedings Volume 2403. See Ref. [104].

[70] C. Borgnakke and P. S. Larsen, J. Comput. Phys. **18**, (1975).

[71] M. Allen, K. McManus, D. Sonnenfroh, and P. Paul, Appl. Opt. **34**, 6287 (1995).

[72] P. Paul, Opt. Lett. **19**, 998 (1994).

[73] P. Paul, I. Vancruningen, and R. Hanson, Exp. Fluid **9**, 241 (1990).

[74] R. Hanson, J. Seitzman, and P. Paul, Appl. Phys. B **50**, 441 (1990).

[75] W.L.Weise and J. R. Fuhr, *NIST Database for Atomic Spectroscopy* (NIST Standard Reference Data, Gaithersburg, MD, 1995).

[76] M. Tsuji, N. Itoh, and Y. Nishimura, Jpn. J. Appl. Phys. **31**, 2536 (1992).

[77] F. Vega, C. Alfonso, and J. Solis, Appl. Surf. Science **69**, 403 (1993).

[78] C. Kittel, *Introduction to Solid State Physics* (John Wiley and Sons, Inc, New York, 1986]).

[79] R. J. Kee *et al.*, *A fortran computer code package for the evaluation of gas-phase, multicomponent transport properties* (SAND86-8264, Sandia, CA, 1986).

[80] K. L. Saenger, in *Angular distribution of ablated material*, edited by D. B. Chrisey and G. K. Hubler (John Wiley and Sons, Inc., New York, 1994), pp. 199–225. See Ref. [102].

[81] J. S. D. Groot *et al.*, Phy. Fluids B **4**, 701 (1992).

[82] D. F. Edwards, in *Silicon (Si)* (Academic Press, Inc., New York, 1985), pp. 547–569.

[83] P. U. T. P. R. Center, *Thermophysical properties of matter* (IFI/Plenum, New York, 1970-[79]).

[84] *CRC Handbook of Chemistry and Physics* (CRC Press, Inc., West Palm Beach, FL, 1996).

[85] F. P. Incropera and D. P. DeWitt, *Introduction to Heat Transfer* (John Wiley and Sons, Inc., New York, 1996).

[86] P. S. Peercy, J. Y. Tsao, and M. O. Thompson, J. Mater. Res. **5**, 1463 (1990).

[87] T. Venkatesan, in *Pulsed Laser Deposition : Future Trends*, edited by D. B. Chrisey and G. K. Hubler (John Wiley and Sons, Inc., New York, 1994), pp. 313–322. See Ref. [102].

[88] R. K. Singh, J. Electron. Mater. **25**, 125 (1996).

[89] K. R. Chen *et al.*, in *Film Synthesis and Growth using Energetic Beams*, edited by H. A. Atwater, J. T. Dickinson, D. H. Lowndes, and A. Polman (Materials Research Society, Pittsburgh, PA, 1995), pp. 27–32, mRS Proceedings Volume 388. See Ref. [103].

[90] F. F. Chen, *Plasma Physics and Controlled Fusion* (Plenum Press, Inc., New York, 1990).

[91] G. Schmidt, *Physics of High Temperature Plasmas* (Academic Press, Inc., New York, 1979).

[92] S. Foltyn, in *Surface Modification of Materials by Cumulative Laser Irradiation*, edited by D. B. Chrisey and G. K. Hubler (John Wiley and Sons, Inc., New York, 1994), pp. 89–113. See Ref. [102].

[93] *Atomic Energy Levels*, edited by C. E. Moore (National Bureau of Standards, Washington D. C., 1971).

[94] *Experimental Transition Probabilities for Spectral Lines of Seventy Elements*, edited by C. Charles H. and W. R. Bozman (National Bureau of Standards, Washington D. C., 1962).

[95] C. Gabbanini, S. Gozzini, and A. Lucchesini, Appl. Phys. Lett. **67**, 715 (1995).

[96] V. Baranov *et al.*, Phys. Rev. E **48**, 1324 (1993).

[97] H. M. Urbassek and D. Sibold, Phys. Rev. Lett. **70**, 1886 (1993).

[98] M. Taylor, G. He, and C. S. an H. Atwater, in *Film Synthesis and Growth using Energetic Beams*, edited by H. A. Atwater, J. T. Dickinson, D. H. Lowndes, and A. Polman (Materials Research Society, Pittsburgh, PA, 1995), pp. 97–102, mRS Proceedings Volume 388. See Ref. [103].

[99] P. Swearengen, S. Davis, and T. Niemczyk, Chem. Phys. Let. **55**, 274 (1978).

[100] D. Husain and P. Norris, J. Chem. Soc. Faraday Trans. 2 **74**, 93 (1978).

[101] H. Mick, H. Matsui, and P. Roth, J. Phys. Chem. **97**, 6839 (1993).

[102] *Pulsed Laser Deposition of Thin Films*, edited by D. B. Chrisey and G. K. Hubler (John Wiley and Sons, Inc., New York, 1994).

[103] in *Film Synthesis and Growth using Energetic Beams*, edited by H. A. Atwater, J. T. Dickinson, D. H. Lowndes, and A. Polman (Materials Research Society, Pittsburgh, PA, 1995), mRS Proceedings Volume 388.

[104] in *Laser-Induced Thin Film Processing*, edited by J. J. Dubowski (SPIE, Bellingham, WA, 1995), sPIE Proceedings Volume 2403.